TUNABLE LIQUID CRYSTAL BEAM STEERING DEVICE BASED ON PANCHARATNAM PHASE IN FRINGE-FIELD SWITCHING-MODE

A dissertation submitted to

Kent State University in partial

fulfillment of the requirements for the

degree of Doctor of Philosophy

By

Comrun Yousefzadeh

August 2021

Dissertation written by

Comrun Yousefzadeh

B.S., Shahid Beheshti University, Tehran, Iran 2012

M.S., Cleveland State University, Cleveland, USA 2016

M.S., Kent State University, Kent, USA 2018

Ph.D., Kent State University, 2021

Approved by

Dr. Philip Bos, Chair, Doctoral Dissertation Committee

Dr. Hiroshi Yokoyama, Members, Doctoral Dissertation Committee

Dr. Deng-Ke Yang

Dr. James Gleeson

Dr. Bjorn Lussem

Accepted by

Dr. Antal Jakli, Director, Materials Science Graduate Program

Dr. Mandy Munro-Stasiuk, Interim Dean, College of Arts and Sciences

TABLE OF CONTENTS

LIST OF FIGURES

LIST OF TABLES

ACKNOWLEDGEMENT

First and foremost, I cannot express enough gratitude to my advisor, Prof. Philip Bos for his continuous support, guidance, extensive knowledge and patience throughout my studies. Soon after I joined his team, I realized the exciting combination of leadership and hard work in his attitude and was very impressed witnessing how he has devoted his career to enhance the current technology in the field of liquid crystal. Through our regular morning meetings, I often received impactful feedback. Whenever a roadblock was encountered, he generously offered his expertise and his time to provide sufficient resources for us in order to effectively tackle the problem. He has gone above and beyond the standards to ensure a productive environment in the lab. Not only has he taught me technical matters, but also many professional skills such as how to present my ideas clearly and even beyond this, he taught me life lessons such as how one can always be humble, no matter how far we advance in our field. My appreciation to Dr. Bos simply goes beyond words.

Secondly, I would like to thank all of the faculties and staff at the Advanced Materials and Liquid Crystal Institute for their support and help throughout my studies. I thank all members of the committee for their precious time. I thank Dr. Yokoyama, Dr. Yang, Dr. Jonathan Selinger, Dr. Robin Selinger, Dr. Antal Jakli, Dr. Oleg Lavrentovich, Dr. Liang-Chy Chen and Dr. Peter Palffy-Muhory for sharing their invaluable knowledge throughout my courses and providing excellent guidance that was essential to this work. I also thank Douglas Bryant for his assistance with cleanroom related work.

Next, I would like to thank all collaborators to my research, Dr. Andre Van Rynbach who made a significant time investment to this work with a bright mind. I would like to thank Dr. Lu Lu and Dr. Nicholas Diorio from Facebook Reality Labs for their support and insight. Frequent discussions with these collaborators often directed my work. I thank Dr. Achintya Bhowmik and Dr.Yanli Zhang for their assistance with the Zemax project. Also, I had an excellent opportunity to intern at Apple, Inc which provided me a variety of unique skills and expanded my knowledge in the field of Optics and Display. My special thank goes to Dr. Zhibing Ge, Dr. Xiaokai Li and Dr. Yuan Chen at Apple whose expertise and immense knowledge was very beneficial for me.

Additionally, I would like to thank my amazing friends and fellows in AMLCI. I thank current and former members of Boslab including Dr. Afsoon Jamali, Dr. Colin McGinty, Dr. Junren Wang, Dr. Xiayu Feng, Amit Bhowmick, Brandon Vreeland and Frankie Xi. Especially, I thank Dr. Michael Varga, Dr. Mohammad Salili, Dr. Ahlam Nemati, Dr. Sasan Shadpour, Yousef Golestani and all other awesome friends with whom I made memories and went through ups and downs during this journey.

Finally, I thank all of my family and friends for their unconditional support without which it would not have been possible for me to complete this chapter of my life. Specifically, I thank my parents, my partner and my dearest sister, Bahare Yousefzadeh who were all the main source of motivation for me and were my reasons to continue throughout my life especially when times were tough.

Comrun Yousefzadeh

July 2021, Kent, Ohio

CHAPTER 1 – INTRODUCTION

1.1 REVIEW OF THE DEMAND AND PAST TECHNOLOGIES

An increasing demand for fast and efficient random access pointing within emerging applications such as LiDAR [1-4], space based optical communications [5-8], displays [9-12], microscopy [13], optical tweezers [14] and autonomous vehicles has led to more investigation on beam steering approaches. For instance, this capability is crucial for LiDAR remote sensing for ecosystem studies, laser scanning of forest resources, space station navigation and etc [15-17] . Currently, mechanical approaches such as Gimbals, fast steering mirrors (FSMs), Risley prisms, lenslet arrays, micro electromechanical systems (MEMs) and rotating polygons are largely being used in to fulfill this requirement [18]. However, mechanical approaches have some issues such as mechanical complexity, pointing stability that requires some settle time, being expensive, bulky and heavy. Although the electrical approaches have some challenges such as efficiency, aperture size, response time and long-time durability, there is still a need to replace mechanical steering devices with electrical approaches to address existing issues.

Electro-optic (EO) beam steering offers several important advantages over traditional mechanical steering approaches. These advantages include a lower cost, faster steering rates, compactness, lightweight, high volume production, and random access beam pointing capability. While progress towards replacing mechanical steering approaches has been promising, challenges remain to achieve large aperture sizes with tunable steering directions. As a result, various non-mechanical beam steering devices

have been seriously considered over the last few decades as an alternative to current mirror- and gimbal-based systems. Particularly, liquid crystals (LC) have been considered because of their high birefringence. Additionally, well-established techniques of liquid crystal displays and the well-known fabrication methods makes them an excellent candidate.

LC refers to a state of matter that possess some characteristics of the liquids such as fluidity and formation and some characteristics of the crystals such as optical anisotropy and molecular orders. LCs are elongated rod-shaped molecules that exhibit optical anisotropic features. Particularly, LCs in nematic phase have long-range orientational order but no positional order. These self-assembled anisotropic molecules whose long axis tends to stay in parallel to each other, can align in a preferred direction, so called “director”, which is defined by a unity vector n(r). Direction of the director can be defined by boundary conditions imposed by substrates that sandwich the cell (pre-alignmnet). However, upon the presence of an electric field, the molecules tend to rotate to align their long axis to that electric field direction. Therefore, the director can be switched between the two arbitrary directions in volage on and voltage off states. This is the basis of an electro-optical LC device [19].

Liquid-crystal-based optical phased arrays (OPA) [20-22], volume holographic grating [23, 24], Pancharatnam-based and vertically aligned, continuous phase, optical phased array (V-COPA) [25-27], Decentered microlens arrays [28] and potential emerging approaches [29-31] are among the researched candidates. While OPA beam

steering is the most mature of the options, it is limited in transmission efficiency for steering angles above about ± 1 degree due to the fringing fields at the 2π phase resets. Many of the non-mechanical beam steering devices explored to date use LC for their inherent birefringence and responsiveness to electric fields.

There has been work on liquid crystal based Pancharatnam Phase Devices (PPDs) since 2005 [27, 32-46]. Honma and Nose [32] used the Pancharatnam concept to build a liquid crystal Fresnel zone plate with a fixed focal length. Crawford et al. [33] proposed a surface patterning method to fabricate PPDs using polarization holography. Escuti et al. used PPDs to build a modulator for unpolarized incident light with high contrast ratio (600:1) and 2ms switching time for a monochromatic light [47].

Although PPDs can diffract light with very high efficiency, they are not inherently tunable. They are usually combined with large angle step steering devices because of the deflection angle limitation of this type which arises when 2π resets exist along the aperture [21]. Dynamic beam steering with these devices is currently only accomplished in a stepwise fashion, whereby several PPDs are stacked in series with polarization switches in between each layer. As the switches toggle the light between right and left circularly polarized light, consecutive diffraction angles either add or subtract to give the final steering angle of the stack. This approach is practically limited because each successive stage of steering reduces the efficiency from transmission losses and beam walk-off. Research on continuous steering with high diffraction efficiency in PPD was the topic of interest to Lei Shi et al. [26, 48]. In order to overcome the tunability challenge, they created a beam steering device called the Vertically Aligned Continuous

Optical Phased Array (V-COPA). While the VCOPA approach provides a defect-free topology where a continuous tuning is allowed, it suffered from a slow response time on the order of seconds which makes the device impractical for applications where a rapid response is critical. In contrast to this approach, but similar to our proposed device that is introduced later in this chapter [49], conventional FFS LCD devices have much faster response time in the order of several milliseconds. Although the response time depends on several factors such as cell gap, electrodes spacing, rubbing angle, LC material, S.H. Lee. et al. [50] showed that a response time of around 10 ms is expected for a FFS mode device with negative dielectric anisotropy.

1.2 FUNDAMENTAL PRINCIPLE OF LC BEAM STEERING

The physics of beam steering can be explained by considering a simple example of glass prism. In a prism, the light passing through the thicker part of the prism is delayed with respect to the light that is passing through the thinner part because the light travels more slowly in the prism than air due to the difference in their index of refraction. Therefore, the exiting phase of the light will steer to an angle to account for this relative delay. In the simple case of prism, the deflection angle can be related to the aperture and optical path difference (OPD). Different steering angles can be achieved by changing the thickness of the prism. But, large steering angles need thicker prisms. However, by introducing 2π phase resets, we can significantly reduce the required thickness since there will be no difference between 0, 2π, 4π,… phase shift from a phase point of view. Therefore, the unfolded phase profile resulted from both approaches looks the same and will steer to the same angle. The latter approach is based on blazed transmission grating

where the modulo phase shift creates a periodic sawtooth phase profile. The steering parameters in this case can be electrically controlled and is governed by grating equation:

$$\sin\theta = m\frac{\lambda}{\Lambda} \tag{1.1}$$

Where θ, is the deflection angle, λ is the wavelength of light and Λ is the periodicity of the grating. Two main methods can be employed to steer the light. One is to change the grating period in which the phase difference is fixed and the period varies along the aperture while the other is to change the amount of phase shift each module can have. Liquid crystal beam steering devices have been created based on both of these approaches. [20, 21, 51-53]

It should be noted that LC beam steering can be classified into a few numbers of different approaches such as volume holograms which can potentially steer light into large angles with high efficiency [54-56], birefringent prisms [57], Pancharatnam Phase Devices (PPD) [58] which is the base approach of this dissertation and other scientifically emerging methods have been investigated [59, 60].

S. Pancharatnam was the one who first realized the so called Pancharatnam phase phenomena and described it in his fascinating paper in 1956 [61]. Later on, M.V Berry followed this work and showed that Pancharatnam phase of light depends on the trajectory of wave polarization on Poincare sphere and for a cyclic evolution of polarization, it forms a closed curve on Poincare sphere. [62, 63]

In PPDs, LC director form a continuous rotation in a plane parallel to the substrates. This creates a periodic cycloidal shape that is shown in figure 1.2. Also, they are often being made to be a half wave retarder for a specific wavelength called “design

wavelength" and a circularly polarized light is used as input so that the exiting light is also circularly polarized (with different handedness). This way the exiting light can constructively interfere to steer to an angle with maximum efficiency [64]. The phase of the light exiting from a half-wave retarder PPD is twice the orientation angle β of the optical axis with respect to a fixed lab axis, or Γ=2 β [21, 65, 66]. Noteworthy, the local director axis of LC is the local optic axis. Because the PPD acts as a half-wave retarder, the output beam obtains the opposite polarization handedness to the input light. Additionally, the relative phase shift of the circularly polarized light exiting the aperture at two points separated by x, will be:

$$\Gamma=2\,\beta(x) \tag{1.2}$$

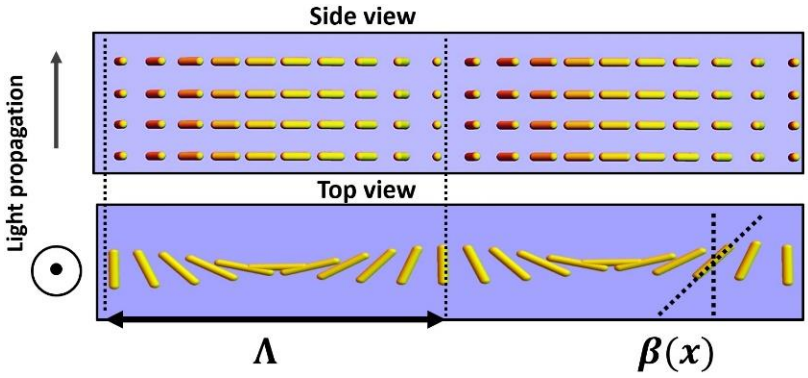

Figure 1.2 Front and top views of the director structure in a beam steering PPD device. Different colors in the picture depicts opposite sides of LC molecules.

The light passing through first LP and QWP in figure 1.2, is circularly polarized and can be described by Jones calculas notation as:

$$E_{in} = \begin{pmatrix} E_{x_{in}} \\ E_{y_{in}} \end{pmatrix} \tag{1.3}$$

$$E_{in} = \begin{pmatrix} E_{x_{in}} \\ i\,E_{x_{in}} \end{pmatrix} \tag{1.4}$$

Assuming it's right hand circular polarized light, E_{xin} and E_{yin} are the x and y components of the incoming light electric field, respectively. The transmitted light through a HWP is then described as:

$$E_{out=} \begin{pmatrix} \cos\beta & -\sin\beta \\ sin\,\beta & \cos\beta \end{pmatrix} \begin{pmatrix} 1 & 0 \\ 0 & e^{i\phi} \end{pmatrix} \begin{pmatrix} \cos\beta & \sin\beta \\ -sin\,\beta & \cos\beta \end{pmatrix} \begin{pmatrix} E_{x_{in}} \\ i\,E_{x_{in}} \end{pmatrix} \tag{1.5}$$

Where β is the relative angle between the slow axis of the HWP and x-axis and ϕ is the phase retardation of the HWP which is equal to π. Doing the math, the above equation can be represented as :

$$E_{out=} \begin{pmatrix} E_{x_{in}} e^{2i\beta} \\ -i\,E_{x_{in}} e^{2i\beta} \end{pmatrix} \tag{1.6}$$

The most interesting result from the above model is that not only the transmitted light is a left hand circular polarizer, but also has an additional common phase factor $e^{2i\beta}$. Seemingly, the phase of the transmitted light can be controlled by the azimuthal angle β where a horizontal 0 to π change of β means a 2π change in the spatial phase of the output light phase across the aperture. By repeating this periodic rotation pattern, a a continuous phase LC grating can be achieved that potentially can have no resets. Therefore, it is possible to form a constant large phase gradient with a thin cell gap that is only half-wave thick. As mentioned earlier, this type of devices has been investigated with an increasing interest since 2005 and has often acquired different names including Geometrical Phase (GP), liquid crystal Polarization grating (LCPG),…. But throughout this dissertation, we refer to it as Pancharatnam Phase Device (PPD) to emphasize the

fundamental difference of this phase-based approach from other approaches and avoid any confusion with conventional gratings and other devices with geometrical optics basis.

For a better understanding of how polarization state of the light evolve through the PPD device, the following example visualize the effect by considering evolution of polarization state at different locations across the aperture. Let's consider the circularly polarized light as a group of vectors numbered 1 to 8. Since the circularly polarized light can be treated as linear polarized light at any instantaneous time, we can consider the vectors below as the linearly polarized light vector that rotates at 8 different time instances (1 to 8) . At the time the circular light hit the half wave plate, the vectors are reflected about the optic axis of the molecule (which is axis of the half wave plate) shown in blue line. Figure 1.3 shows this circular light before and after the LC layer at 4 different locations with 4 different orientation of the optic axis.

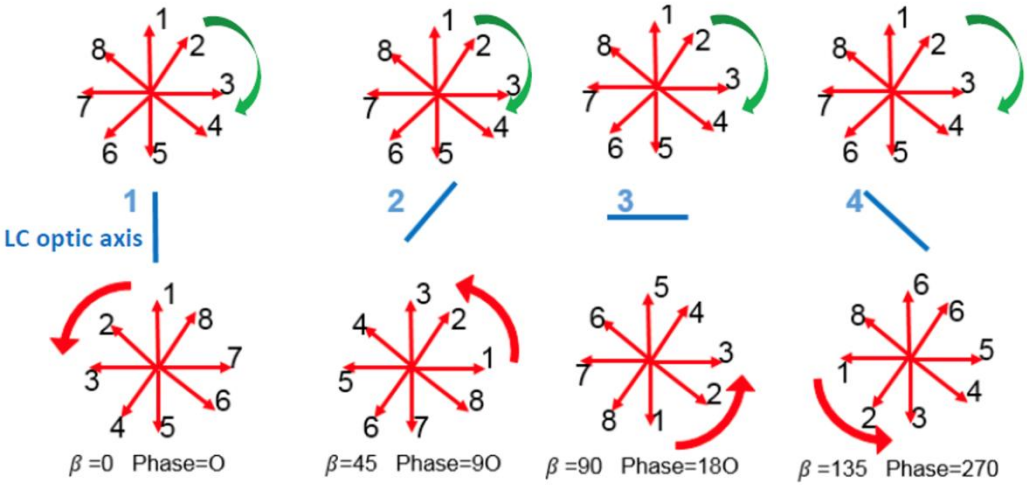

Figure 1.3 Illustration of polarization state of a circular light before and after passing a PPD at four locations with different LC optic axis orientations

For example, at the location (1):

- vector 1 remains the same because it aligns with the optic axis.

-vector 2 reflects about the vertical (optic) axis and replaces with vector 8 and vice versa

-vectors 3 and 7 are switches in a similar way

-vectors 4 and 6 also switches by reflection about optic axis

-finally, vector 5 remains the same similar to vector 1.

Repeating that argument for locations 1-4 shown above, the output light comes out of the PPD is oppositely circularly polarized to that input light at all locations but there is a phase shift in the circular polarized light which is twice as the angle β. This simplified visualization helps having a better understanding of this fairly complex phenomena.

1.3 NOVEL APPROACHES AND REPLACEMENT CANDIDATES

More recently, developments in liquid crystal polarization gratings (LCPG) [18, 34, 40] and polarization volume gratings (PVG) [24, 56] have shown large aperture and wide angle steering ability with a relatively simple fabrication process [40, 67]. Reflective polarization gratings with a deflection angle twice that of a transmissive grating have been introduced [68-70]. In an attempt to reduce the response time, a polymerizable LCPG combined with a ferroelectric liquid crystal (FLC) phase shutter for near-infrared (NIR) [71-73] has been demonstrated. Also, a polymer-stabilized twisted nematic diffractive waveplate for mid-wave infrared (MWIR) [74] was introduced. Moreover, recent developments in long-wave infrared devices [75] shows a promising

future for the technology of liquid crystal diffractive waveplates to cover the entire infrared spectrum.

As another example, electro-optical laser scanners based on waveguides with liquid crystal cladding layer [4]. The architecture of the device, allows for high steering angles up to 80 degrees with sub-milisecond response time (<500 μm) due to the very thin layer of LC required as cladding. The geometry exploit benefits of large birefringence acquired with low driving voltage as well as fast electro-optic response of LC. Therefore, the deflection angle can be also tuned by changing the effective index of the waveguide. Since the device realize a true-time delay, there would be no 2π resets which eliminated the loss due to fringing field. The device can be designed for both in-plane and out of plane beam steering. The latter case has more limitations on deflection angle. However, one main drawback is that the aperture size which is usually limited because the light beam has to be narrow to couple to a guiding mode. Analog devices has purchased this technology and by further improvements on current loss ratio, it is expected to see that this approach will be considered more for mid-IR range steering and small beam applications. [18]

Nevertheless, most of the approaches mentioned above rely on passive steering and active switching of polarization state. A dynamically tunable device with high efficiency and a fast response time would greatly enhance the functionality by replacing many switches in series with a single stage device to steer to a laser across the full field of regard. This would increase the throughput efficiency, reduce the device size, and increase the usable clear aperture.

1.4 OUR APPROACH (FFS-PPD)

It is the goal of this project to electrically adjust the value of $\beta(x)$ in local areas so that a phase difference is directly imposed on the output light by PPD. Here, we propose a unique liquid crystal device in fringe field switching (FFS) mode based on Pancharatnam Phase Device [49, 76-78]. Our FFS-PPD beam steering can provide both tunability and a fast response times in a format scalable to large apertures. This architecture employs a linear array of phase control elements (PCEs) to locally control the orientation of the liquid crystal director into a cycloidal pattern to deflect transmitted light. The PCEs are comprised of a fringe field switching electrode structure that can provide a variable in-plane electric field. Each PCE has sub-elements that provide an in-plane electric field that causes the director to rotate away from its zero voltage value and has two key aspects. One is to create an in-plane field along both cell substrates to cause the director between the substrates to be rotated uniformly, about the z direction, by an angle, whose magnitude is defined by the amplitude of the field. And the other is to be able to set the sign of the rotation angle.

Considering the first objective, to be able to electrically adjust the value of $\beta(x)$, the approach will be to provide a device that has electrical phase control elements (PCE) that can define $\beta(x)$. In more detail, in FFS-PPD design we will consider to set the angle $B(x)$ through the balance of torques on the local liquid crystal director field between the

surface torque and the electrical torque. The overview design of a PCE is shown in figure 1.4.

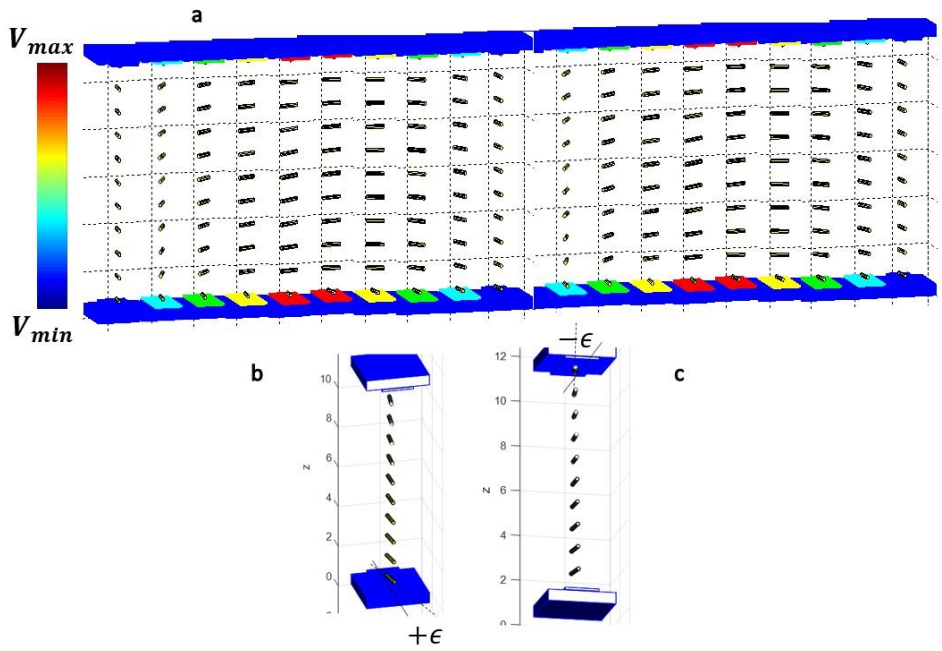

Figure 1.4 a) device configuration (side view) where the color of the sub-elements of each PCE are related to the strength of the electric field they provide with blue being 0V and red being maximum voltage. b,c) at an applied voltage the director is following electric field while is still subject to boundaries.

Figure 1.4 shows that each PCE consists of a pair of sub-elements located on interior side of both surfaces of the device that are capable of providing an in-plane electric field. The surface boundary condition, that defines the director orientation in the absence of an electric field, is set to a value along an axis defined as + ϵ on one surface (figure 1.4 b) and - ϵ on the other (figure 1.4 c), where the angle is measured from a lab reference axis in the plane of the layer , here defined an axis that will be called the

"symmetry axis" . Detailed explanation of the system is discussed in the following chapters.

1.5 SCOPE OF DISSERTATION

In the first chapter, background, previous approaches including some novel technologies is briefly discussed. We discussed about the fundamental of beam steerings. Also, we introduced FFS-PPD approach to distinguish it among other candidates. Chapter 2 elaborate the concept of FFS-PPD device as a tunable, FFS mode beam steering based on Pancharatnam phase. Fundamental principle of PPDs is explained here. Device configuration, boundary conditions and voltage activating methods are introduced. This chapter also includes different modeling methods that is used throughout this work and will finally explores some issues associated with this design and how we are trying to overcome the limitations to maximize the usage. This leads to design goals and desired optical power efficiency that will be explained.

Chapter 3 focuses on optimization of the device design by minimizing any potential source of efficiency loss. Electrode and gap spacing, cell thickness, voltage method, surface anchoring energy,… are separately optimized through modeling and effect of each parameter is investigated in details. Based on the optimized parameters, an optical power efficiency will be predicted in comparison to starting point device.

Chapter 4 considers fabrication process of the device. After promising results predicted by modeling, fabrication started to build this device for the first time. As a first-time work, many unexpected challenges raised during the process development that in

some cases directed us to a different route in order to overcome those challenges. Although the cell preparation method is based on standard photolithography process, we empirically customized conventional layer deposition methods such as sputtering and spin coating, and many other steps for our specific needs. Both mechanical and optical prospects of these challenges are discussed in this chapter. After successful completion of building the device, characterization methods were employed to test the device. These methods are studied in this chapter. Finally, a fundamental working principle of the device was tested and shown compatible result with modeling expectation for a high efficiency device. This resulted in proof of concept that paves the way for future investigations in this approach.

In chapter 5, lens applications of Phancharatnam phase device is considered. We will provide a guideline under which a Pancharatnam Phase Lens (PPL) can be considered achromatic for human eye, hence, can be used for practical applications such as head mounted displays (HMDs), augmented/virtual reality (AR/VR) and 3D systems. Experimental data verifies our proposed guidelines and establish a criteria to evaluate chromaticity issue of PPD lens.

In Chapter 6 we discuss characterization methods of a Fresnel segmented phase profile (SPP) lens. The concept and early results were introduced and published by previous students [79-81]. Here, we show more careful calculation of the voltage profile based on the dynamic phase profile of the lens. Experimental data will be compared with ideal lens characteristics based on the modeling. Consistency of the experimental data such as point

spread function (PSF) and modulation transfer function (MTF) of the lens with expectations from an ideal lens brings very promising result. Finally, MTF of the sample lenses will be calculated under different rotational angles for off-axis light.

Chapter 7 summarizes the context of this dissertation. Detailed conclusion of the most important parts of each chapter will be presented in this chapter. Also, future works and room for improvement will be discussed as well.

CHAPTER 2 - DEVICE CONCEPT OF A TUNABLE, FFS MODE BEAM STEERING BASED ON PPD

INTRODUCTION

As described in section 1.2, PPDs are usually designed as half-wave retarders with a cycloidal anisotropy pattern written into an LC polymer. The optical axis of the birefringent material in these devices is perpendicular to the light propagation vector and rotates by an angle β that varies linearly with x position across the aperture For a distance Λ over which the optical axis of the LC director rotates by 180° in this cycloidal pattern, the PPD will diffract circularly polarized light of wavelength λ to an angle of $\theta = \pm \sin^{-1}\frac{\lambda}{\Lambda}$ with the sign depending on if the light is right or left handed circularly polarized. As explained in section 1.2 the phase of the light exiting from a half-wave retarder PPD is twice the orientation angle β of the optical axis with respect to a fixed lab axis, or $\Gamma = 2\,\beta$. In the case of a linear change of phase across the aperture, the incident phase front becomes tilted and consequently deflects the output light. PPDs are designed as half-wave retarders whereby circular polarized light obtains the opposite polarization handedness at the output from the input. Therefore, the optical path difference (OPD) should meet the half-wave condition.

$$OPD=\Delta n*d=\lambda/2 \qquad (2.1)$$

In the next section, we will discuss the design and specifications of FFS-PPD device.

2.2 DEVICE CONCEPT

2.2.1 Device Configuration

The design concept for FFS-PPD device is to have individual PCEs control the sign and magnitude of the in-plane rotation angle of the director, $\beta(x)$, in a local area through the application of an electric field. High efficiency beam steering with a PPD requires a uniform director angle throughout the thickness of the cell and the ability to set this rotation angle, β, so that any value between -90 and +90 degrees is achievable.

To create a dynamically tunable PPD, we use a linear array of PCEs to locally control the orientation of the LC director and hence create a linear optical phase change across the aperture for transmitted light. The PCEs in close proximity to a ground plane comprise a Fringe Field Switching (FFS) electrode structure that can provide a variable in-plane electric field to locally address the LC director. The underlying operation is therefore based on using individual PCEs to control the sign and magnitude of the in-plane rotation angle of the director, $\beta(x)$, through the application of local electric fields.

The basic structure for the PCEs consists of an FFS electrode architecture composed of a series of linear electrodes separated from a ground plane by a thin insulator layer . Each PCE consists of a pair of sub-elements located on the interior sides of both surfaces of the device that are capable of providing an in-plane electric field. The layers going from the glass substrate to the LC are shown in figure 2.1. The presence of a ground plane so close to the charged electrodes helps create strong electric fields in the vicinity of the electrode edges. These fields exert a torque on liquid crystal molecules causing rotation against the elastic torque from the surfaces. In figure 2.1, the cell

thickness is indicated by d, W is width of an electrode and L is width of a gap. The electrodes shown as black rectangles are typically transparent indium tin oxide (ITO). The insulator layer of SiO2 is around 150 nm thick and the alignment layer is either a commercial polyimide or photo-alignment material.

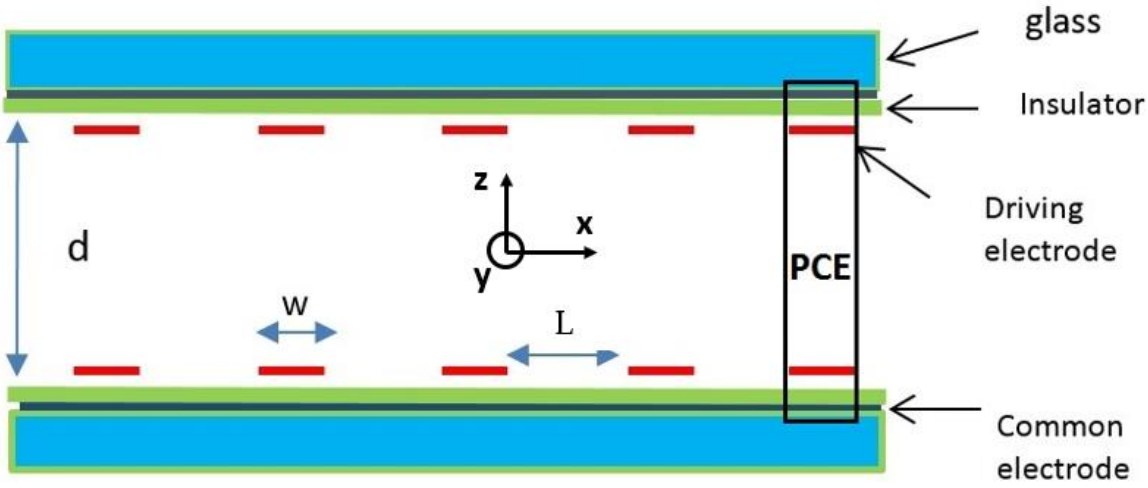

Figure. 2.1. Side view of the cell configuration

The important aspect of a PCE is its ability to provide a strong electric field to provide a torque that causes the director to rotate, about the layer normal, away from the symmetry axis. Since an in-plane rotation of the director profile is desired, the use of negative dielectric LC material is advantageous given the fringe field electric lines in this device are primarily directed perpendicular to the alignment plane. A positive LC material would tilt upward with the fringe fields near the electrode edges, which would counteract the desired PPD pattern and reduce device efficiency [82]. However, in thin cells the surfaces tend to hold the director in the plane of the cell and positive materials

could be considered. As the liquid crystal considered here, has a negative dielectric anisotropy, the symmetry axis is parallel to the electric field. All aspects of the basic structure are well known and commonly used in the display industry.

2.2.2 Boundary Conditions

The surface boundary conditions along the top and bottom electrode layers set the director orientation in the absence of an electric field. Here, we align the director angle to be along an axis defined as + ϵ on one surface and - ϵ on the other in relation to a defined axis of symmetry (Figure. 2.2). This boundary condition sets an intrinsic bias for the sign of the angle and hence the direction, i.e. clockwise or counterclockwise, it will rotate when an electric field is applied from the strong fringing fields. As a result, the sign of the angle of rotation of the director away from the symmetry axis is determined by the electric field applied to the top or bottom electrodes.

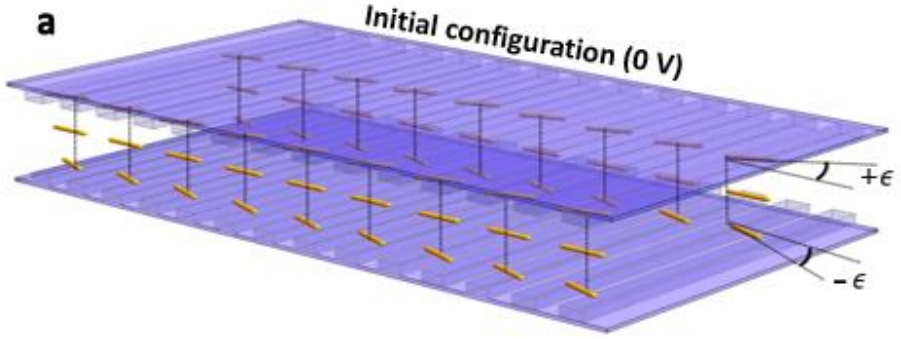

Figure 2.2 The alignment layer rubbing direction of +ε and –ε is shown on the top and bottom substrates, respectively

2.2.3 Activation Using Two-Step Voltage Method

To reach from an initial configuration with boundary conditions defined by the rubbing angles on the top and bottom substrates to a cycloidal pattern, we apply voltages using a "two-step method". In this method, we bias the rotation direction of the molecules for a positive rotation sense using the top electrodes and a negative sense with the bottom electrodes. For example, if it is desired to have a positive angle of rotation, the electrode surface with a positive bias angle (i.e. electrodes +1 to +7 on the top substrate) $+\epsilon$ is activated first. The magnitude of the field from the selected sub-element is increased until the electric torque on the molecules overcomes the elastic coupling forces to the director on the opposite surface and rotates all the molecules throughout the thickness to a positive angle (first step). In the second step, the other sub-element on the opposite surface is activated causing the director field between the sub elements of the PCE to uniformly rotate to the positive direction (2nd step). Similarly, applying the same process but to the $-\epsilon$ surface first (i.e. electrodes -8 to -14) causes the director field to rotate in the negative direction. The final rotation angle determined by the balance of torques between the electric torque and the surface anchoring torque. Therefore, by controlling the magnitude of the electric field generated by the PCE, the desired magnitude of the rotation angle can be achieved.

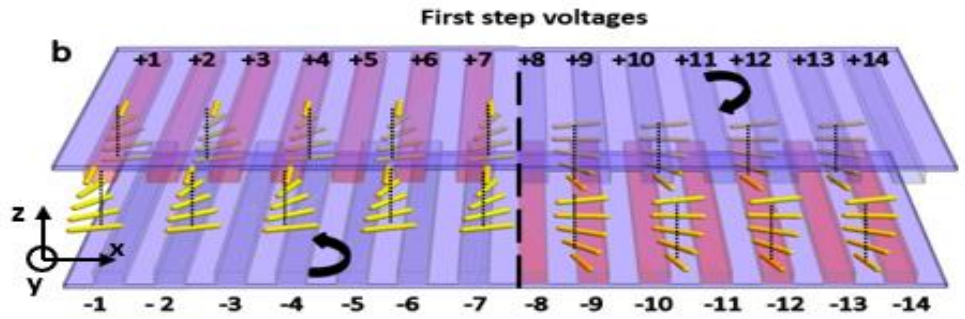

Figure 2.3 The first step of the two-step method sets the sign of the rotation angle based on activating either the top or bottom electrodes.

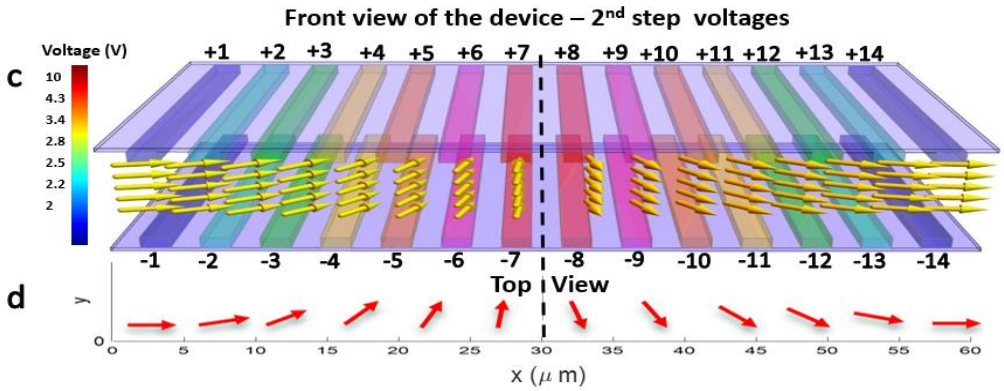

Figure 2.4 The front view of the device over one pitch with color coded electrodes indicating the applied voltage levels. Schematic top view of the device.

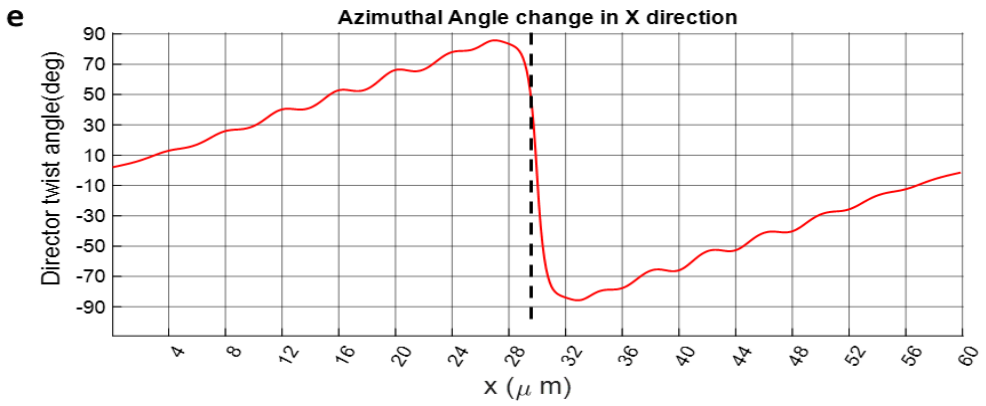

Figure 2.5 Azimuthal angle of the director over a single pitch.

As shown in figure 2.3, in the first step of the two-step process the director rotates in the opposite direction on either side of the dashed line. Figure. 2.4 displays the front view of the device with color coded electrodes corresponding to the voltage spectrum shown for a single pitch of the periodic structure in which the voltage on the electrodes is gradually lowered to provide the desired spiral structure. The electrode sign indicates the pre-tilt direction. Figure. 2.4 is the schematic top view of the director twist angle at a layer that is positioned midway through the cell thickness. Figure. 2.5 displays the azimuthal angle of the director axis showing a fairly linear change along the aperture of the cell which is required for efficient beam steering.

Figure 2.6 shows the applied RMS voltage to the PCEs for a sample of 14 electrodes. The plus and minus signs correspond electrodes on the top and bottom substrates, respectively. In the first step, as shown in figure 2.6, electrodes +1 to +7 and -8 to -14 have 10 V RMS while the rest of electrodes have zero volts. In the second step, the top and bottom electrodes have the same voltage applied. The magnitude of the voltage on each PCE corresponds to the desired rotational angle of the director.

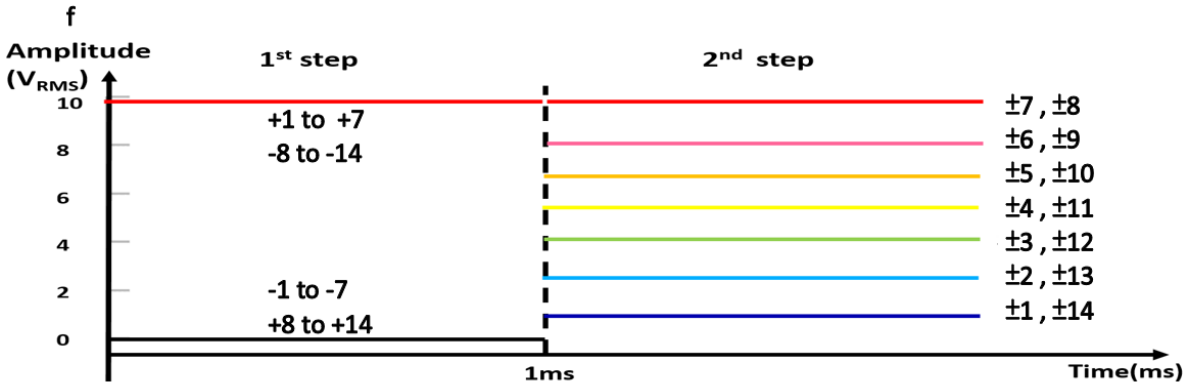

Figure 2.6 The RMS voltages applied to PCEs.

2.3 Modeling Methods

2.3.1 Director Modeling

This section represents the numerical calculation method used to optimize the device design to maximize the beam steering range and overall throughput efficiency.

An in-house program that uses a vector field method is used to model the LC director configuration as a 3D vector field over discretized grid points to precisely predict the final director configuration based on the initial parameters of pretilt alignment, applied voltage, and boundary conditions. The numerical relaxation method considers a generalized torque density on the director components nx, ny, and nz, as

$$[f_G]_{n_i} = -\frac{\delta f_G}{\delta n_i} = \frac{\partial f_G}{\partial n_i} - \sum_{j=x,y,z} \frac{d}{dj}\left[\frac{\partial f_G}{\partial\left(\frac{dn_i}{dj}\right)}\right] \quad i = x, y, z \tag{2.2}$$

Where fG is the Gibbs free energy density and -(δf_G)/(δn_i) is the functional Euler-Lagrange derivative of it. The Gibbs free energy density is composed of three energy terms,

$$\boldsymbol{f_G = f_{elastic} + f_{electric} + f_{surface\ anchoring}} \tag{2.3}$$

Which includes the Frank-Oseen equation formed by splay, twist and bend free energy densities as

$$f_{elastic} = \frac{1}{2}K_{11}(\nabla \cdot \vec{n})^2 + \frac{1}{2}K_{22}(\vec{n} \cdot \nabla \times \vec{n} + q_0)^2 + \frac{1}{2}K_{33}(\vec{n} \times \nabla \times \vec{n})^2 \tag{2.4}$$

The electric free energy is given by

$$\mathrm{f_{electric}} = \frac{1}{2}\vec{\mathrm{E}} \cdot \vec{\mathrm{D}} \tag{2.5}$$

More details on relaxation method is explained in the Appendix A, section A.2.

2.3.2 Efficiency calculation (FDTD)

we have used Finite Difference Time Domain (FDTD) calculation to predict the resultant diffracted light pattern from the PPD. FDTD is a precise numerical analysis method that uses grid-based differential approximations to solve the time-dependent Maxwell's equations in two or three dimensions. The electric and magnetic field vector components are repeatedly solved over a volume of space until a steady-state is reached. The near field data is then transformed to the far-field by the Kirchhoff integral theorem in order to do a beam steering efficiency analysis on the far field light pattern. A Gaussian beam with a beam waist that is much larger than the aperture size was chosen as the incident light to create a nearly top hat input beam.

We performed a reference calculation for an "ideal case" using a mathematically generated director profile of the ideal Pancharatnam-Berry geometry which undergoes a continuous π rotation in each cycle without any trapped wall or out of plane tilt. For each numerical case, a corresponding ideal calculation that employed similar specifications was used to normalize the peak intensity from which the related device efficiency was found.

2.4 Electrostatic Potential and Director Simulation

The director profile is simulated by a 2-dimensional LC model using vector field method. Solving the Euler-Lagrange derivative of Frank-Oseen free energy density, the director orientation is relaxed at each sampling point taking into account the initial voltage on the system, elastic free energy, electric free energy density and viscous torque on every local point.

Upon applying a voltage on the driving electrodes (PCE's), fringing fields form at the edges of electrodes due to the voltage difference between PCEs and common electrode. Consequently, the LC director at the locations near the edge of electrodes go under an in-plane rotation by the dielectric torque between LC and the electric field. This is one of the main mechanisms that switch the LC director. The other one is the elastic torque between LC molecules which tends to make the director field uniform. Figure 2.7 shows the calculated equipotential lines in the regions between the substrates. As seen, there is high in-plane potential difference at the edges of electrodes while there is not such a potential difference at the center of electrodes or the center of the gap. Also, the electric field lines are drawn perpendicular to the equipotential lines to show the in-plane component of electric field resulted from FFS structure .

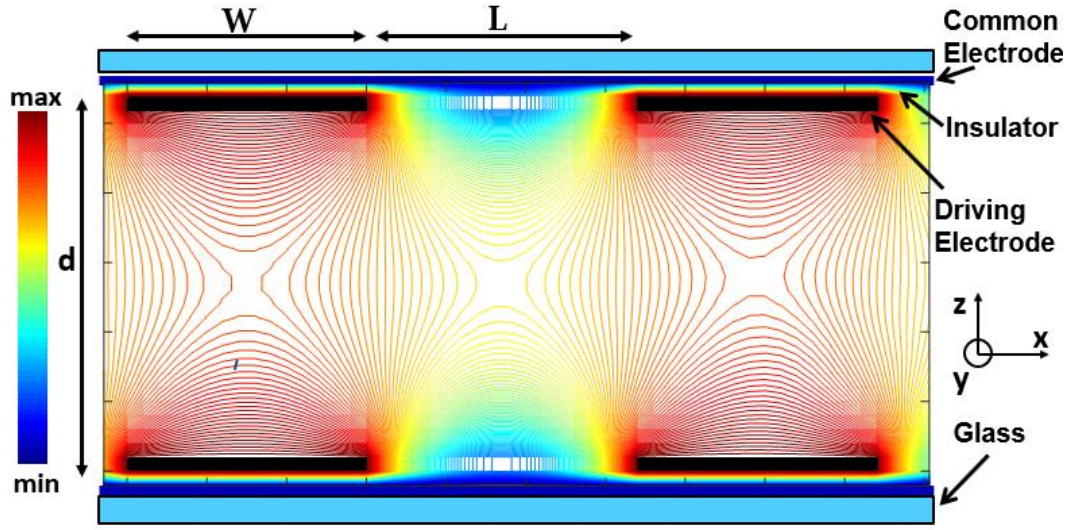

Figure2.7 Calculated electrostatic potential (i.e. equipotential lines) in the cell. The electric field is stronger near edges of electrodes and weaker in the center of electrodes and gaps.

In order to form a PPD structure within the LC molecules, we must control both the twist direction and magnitude. Using the "two-step voltage method", we define regions with a desired twist direction depending on if we activate the top or bottom electrodes first. We control the local magnitude of the twist by applying different voltages on PCEs. The combination of these tools enables us to create the PPD structure.

Figure 2.8.a shows top view of the device (PCEs) with a voltage gradient on a linear array of PCEs (Detail of the calculation method is described in chapter 3 and Appendix A). The width of each electrode is 2 μm which equals the gap width between electrodes. Figure 2.8.b shows a top view of the director field at a location midway between the two substrates for the case of the voltages applied in figure 2.8.a and an infinite anchoring energy on both surfaces. This example shows the basic device principle in operation whereby the in-plane director profile can be controlled by the PCEs. Fig 2.8.c shows the azimuthal rotation angle of the director field shown in figure 2.8.b The phase retardation as a function of coordinate x follows figure 2.8.c because of the linear dependency $\Gamma=2\beta(x)$.

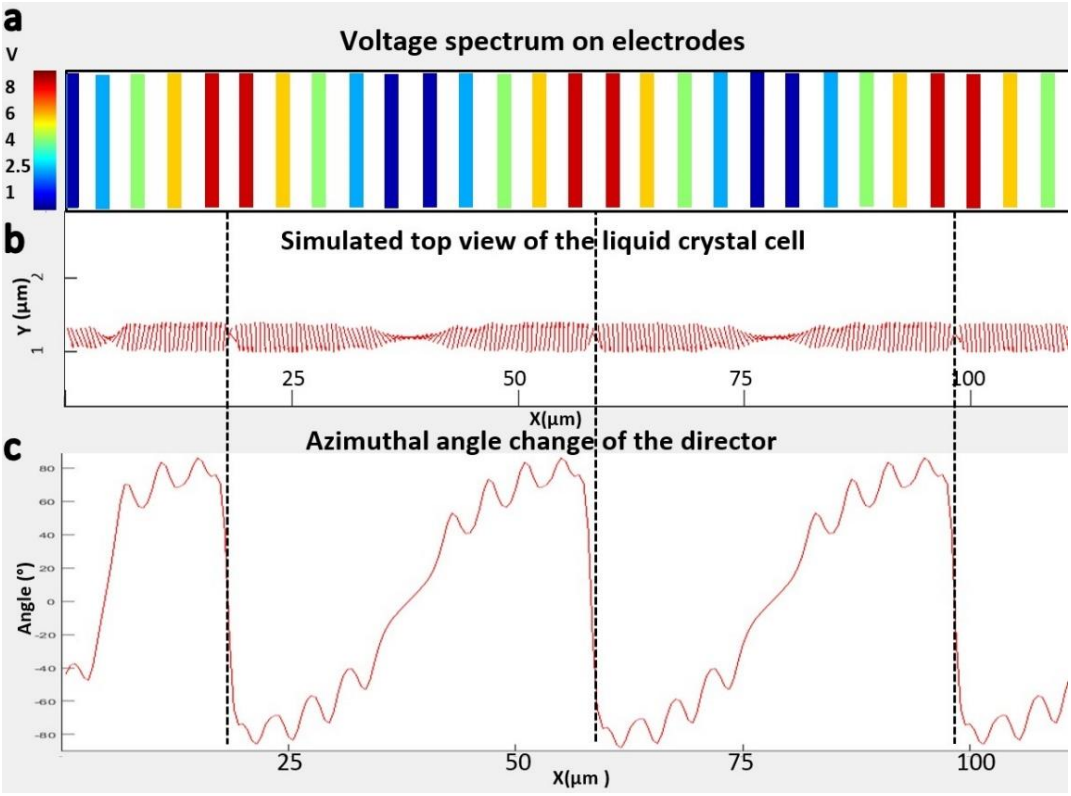

Figure. 2.8 a) Top view of the cell showing position of the electrodes with the voltage spectrum b) Top-view of director profile at the middle layer. c) Azimuthal angular rotation of the director field. Dashed lines show the locations of discontinuities.

The voltages have been applied to provide 3 cycles of a 180 degree azimuthal angle change of the director. As seen, the director rotation angle follows a fairly linear slope in the azimuthal angle across the cell with an average variation of around 10 °. Since these variations are within 10% change of a full π rotation of the director, their total effect would be to produce a rather small phase ripple of about 2 π /10 radians. The effects of these small nonlinearities will be significantly decreased by the optimization methods discussed in the chapter 3.

2.5 Issue with "Trapped Wall" in the structure

In addition to electrically adjusting the value of β(x) in a uniform way, the second objective is to minimize throughput efficiency losses resulting from defects in the structure of the cycloidal pattern. At the boundary between oppositely twisted director profiles, there is an abrupt change in the director angle from +90 to -90 degrees. This is a discontinuity in the angular profile introduced by the geometry of the device, which we call a 'trapped wall'. The director in this wall region is trapped between two neighbors with oppositely twisted director profiles and undergoes a tight 180 degree rotation in orientation. The formation of the trapped wall in topologically inevitable based on our proposed structure since there has to be two oppositely sense of rotations in the vicinity of each other in each period. Another way to think about this is that if for some reason, we could get rid of this discontinuity region, the director will not come back to where it was first started when the voltages on the electrodes are off again. Light deflected from this region will not be directed to the correct angle and will cause a lowering of the device efficiency. However, if the trapped wall width can be made substantially smaller than the wavelength of light, then its optical effect can be minimized so that the apparent rotation of the director profile over most of the aperture becomes quasi-continuous with the same rotational sense. Any light scattered from a trapped wall will lower the devices optical efficiency by an amount:

$$\eta_{TW} = \left(1 - \frac{\Lambda_{TW}}{\Lambda}\right)^2 \tag{2.7}$$

Where ΛTW is the total width of the trapped walls and Λ is the total width between defects . The high efficiency of this device is obtained by squeezing this wall, due to the

torque exerted by the two highest voltage electrodes, to an extent where its optical effect is made to be very small.

2.6 Uniformity of the desired director profile

One particular difficulty of FFS devices for beam steering is getting the LC director to rotate monotonically across the aperture (i.e. along the x-axis) due to the presence of the periodic fringing fields above the edges of electrodes. Above the center of an electrode or gap where there is no in-plane field the LC director will still rotate as a result of elastic torque between neighboring LC molecules, but the amount of rotation will be less than on top of an electrode edge. The uniformity of the director rotation angle will be related to the width of the electrodes and the gap between them with smaller widths yielding a more uniform angle . However, optical patterning of features less than 1 micron is difficult. As explained, the effective width of a gap is smaller than the effective width of an electrode. So, by taking the value L, larger than W, we can take this effect into account. With these considerations, we have considered an example design where the electrode width is 1 micron and the gap between electrodes is 2 microns.

With the considered 3μm center to center electrode spacing in this example, the minimum periodicity is over 5 electrodes and gaps which is 15μm. Correspondingly, the steering angle for 1.5 μm wavelength light is $\theta=\pm\sin^{-1}(\lambda/\Lambda) = \pm 5.7°$ and for visible light with 0.6 μm wavelength is 2.3°. Similarly, larger pitches controlled with more number of electrodes would result in lower deflection angle with no practical limitation.

We have also investigated the significant effects of the azimuthal anchoring energy on the director uniformity. We modeled the effect of both an infinite and weak (10^{-5} J/m^2)

azimuthal anchoring energy on the values of the azimuthal angle of the director over the center of the electrode (ϕ_me) , the center of the gap (ϕ_mg), and over the edge of the electrode(ϕ_ee) while the thickness of the device was fixed at 3.1 microns. We found that for the large anchoring energy the values were: ϕ_me=49°; ϕ_mg =54°;ϕ_ee=88°; while for the lower anchoring energy, the values were ϕ_me=72°; ϕ_mg =74°;ϕ_ee=90°. This shows the degree to which a lower anchoring energy provides a more uniform in-plane azimuthal twist angle of the director.

For a PPD, it is desirable that the director field has the same orientation through the thickness of the cell. Furthermore, the director should be perpendicular to the z-axis everywhere so that the condition of the device being a half wave retarder is fulfilled at all points across the aperture. To test the performance of simulated FFS-PPD device, we can consider the light transmission through the PPD that is between a crossed polarizer and analyzer. If the director is in a plane normal to z-axis yet uniformly rotated by an angle α along z-axis, we expect that the light transmission will be zero for all wavelengths of light if the polarizer is also rotated by the same angle α. Also, we want to check if a PPD is a half-wave retarder for any in-plane rotation angle. This condition will be met if the light transmission is maximized and the same for any voltage for the case when the polarizer is at 45 ° to the extinction angle. Figure. 2.9 shows graph of normalized intensity as function of the angle of the polarizer relative to rubbing direction of the cell at two locations of center of the electrode and close to edge of an electrode where the torque is maximum. This is shown for red light (620nm), green light (550nm) and blue light (460nm) wavelengths for an applied voltage of 10 volts that gives a director rotation

of 90°. When the polarizers are set to the minimum transmission level, the light transmission is close to zero for all wavelengths. Also, the maximum light intensity is achieved for the polarizer angle of 45° from the extinction angle. This demonstrates that the device is acting as a half wave plate whose optic axis is rotated to 90°.

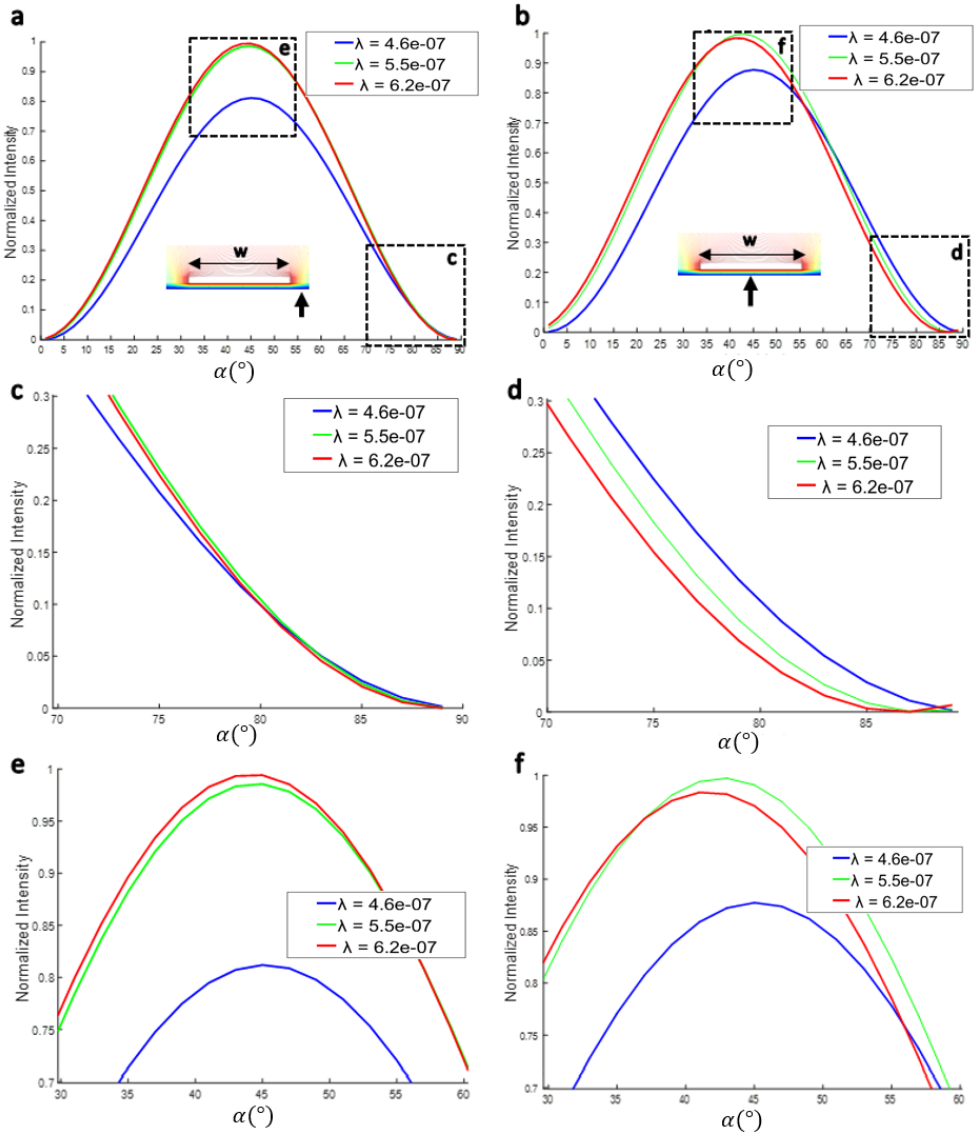

Figure. 2.9 Plots of Normalized Intensity as function of the rotational angle of the crossed polarizers α relative to rubbing direction of the cell for RGB light a,c,e) at the edge of an electrode (black arrow) and b,d,f) at the middle of an electrode (black arrow).

Figure 2.10 shows a graph of the extinction angle vs. applied voltage for 620 nm and 460nm light. That the extinction angle for these different wavelengths occurs at the same angle, for a given voltage, indicates that the director profile along Z direction is effectively uniform (not twisted which would cause the extinction angle to be wavelength dependent). Figure. 2.11 shows phase retardation of a PCE as a function of the applied voltage which controls the director rotation angle. It is seen that the retardation is constant over the required voltage range, which indicates the device can maintain the required half-wave retardation for any rotation angle. These data verify that the modeled device, based on our tunable PPD concept, is capable of providing the desired Pancharatnam beam steering device structure.

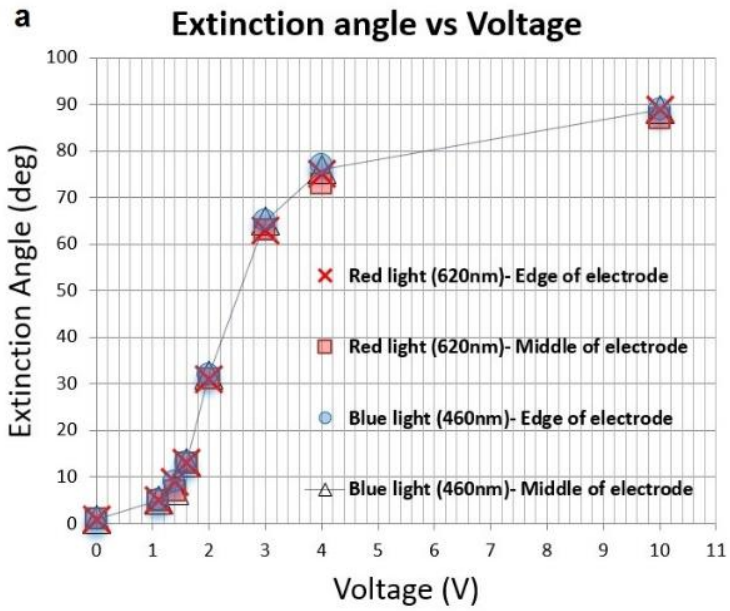

Figure. 2.10 Extinction angle vs. applied voltage for red (620nm) and blue light (460nm) at both the edge and middle of the electrodes

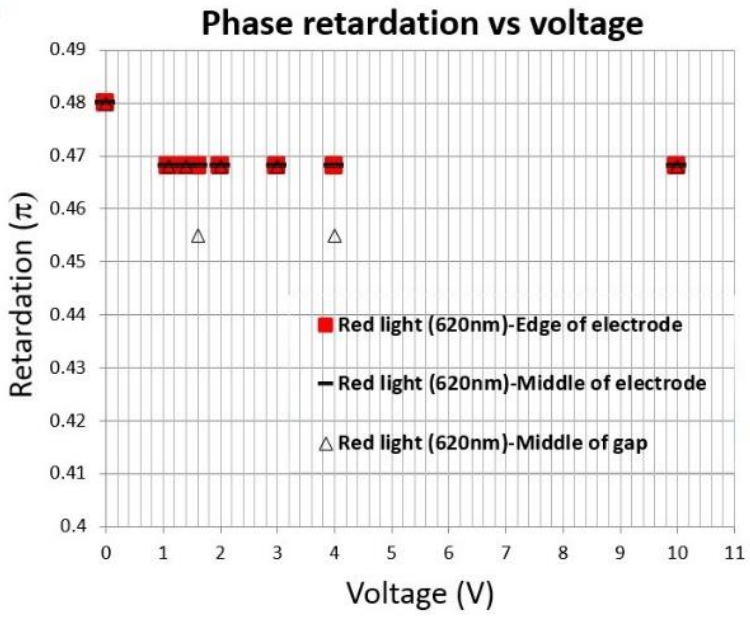

Figure. 2.11 The phase retardation vs voltage for red and blue light at the locations as indicated.

2.7 Design Goals

In this section, we discuss the importance of having a narrow wall as well as having a uniform cycloidal structure for obtaining a high efficiency. From Eq., we see it is desirable to have the wall as small as possible so that the ratio of trapped wall width to total pitch is low. We describe ways to confine the trapped wall to a gap in between neighboring PCEs. Then by choosing the gap width as small as possible to fabricate we can minimize the width of the trapped wall within the physical parameters of the device. An ideal LC director has an azimuthal angle which varies linearly along the x-axis but is uniform along the z-axis. In practice, however, the layers closer to the substrates

experience a greater effect from the anchoring energy and the spatially varying fringe field than layers in the center of the cell. Hence, the uniformity along z-axis, as well as along the x-axis, will be affected by the anchoring energy, cell thickness and electrode spacing parameters. Detailed determination of this dependency will be discussed in chapter 3. Ultimately, all these parameters must be optimized to achieve a high beam steering efficiency. Therefore, it is useful to first review the theoretical limitations of a PPD device, taking into account the trapped wall width, cell thickness and wavelength.

2.8 Optical Power Efficiency

To separate the effect of the trapped wall from other non-ideal aspects of the desired director profile, an ideal PPD structure with director profile

$$n_{x,y,z} = cos\left(\frac{\pi x}{\Lambda}\right)\hat{x} + sin\left(\frac{\pi x}{\Lambda}\right)\hat{y} \tag{2.8}$$

Was considered, where n is the unit vector of the director, Λ is the pitch and x is the coordinate value along the aperture. A trapped wall of width of K was created by imposing n(x)=n(y)=0 and n(z)=1 at the intervals of x=(2j+1)Λ/2 ±k/2 where j=0,1,2,… for an electrode width k. For example, a PPD structure with Λ=15.6 μm was considered with 3 different wall widths of k=0.5, 1 and 2 μm. The birefringence of the material was selected to be Δn=0.2 where efficiency was calculated as a function of wavelength. In each case, the thickness of the cell was set to meet the half-wave retardation condition for that specific wavelength of $\lambda = 600\ nm$ (i.e. d= $\lambda/\Delta n$ = 2.75 μm) . The far field intensity was then calculated by FDTD method for each case separately. For instance, figure 2.12 shows the total intensity of diffracted light for a PPD structure with different wall sizes for a wavelength of λ=0.5 μm. The deflection angle is θ=sin-1(λ/Λ)=sin-

1(0.5/15.62)=1.83 °. The efficiency was then estimated by taking the ratio of the peak intensity relative to the ideal case of Pancharatnam shape where there is no discontinuity on the director angle. Table 2.1 gives the efficiencies calculated in this way for wall width and wavelengths of interest. As the wavelength of the light increases relative to the size of the wall, a higher efficiency is expected since scattering from the wall will be reduced.

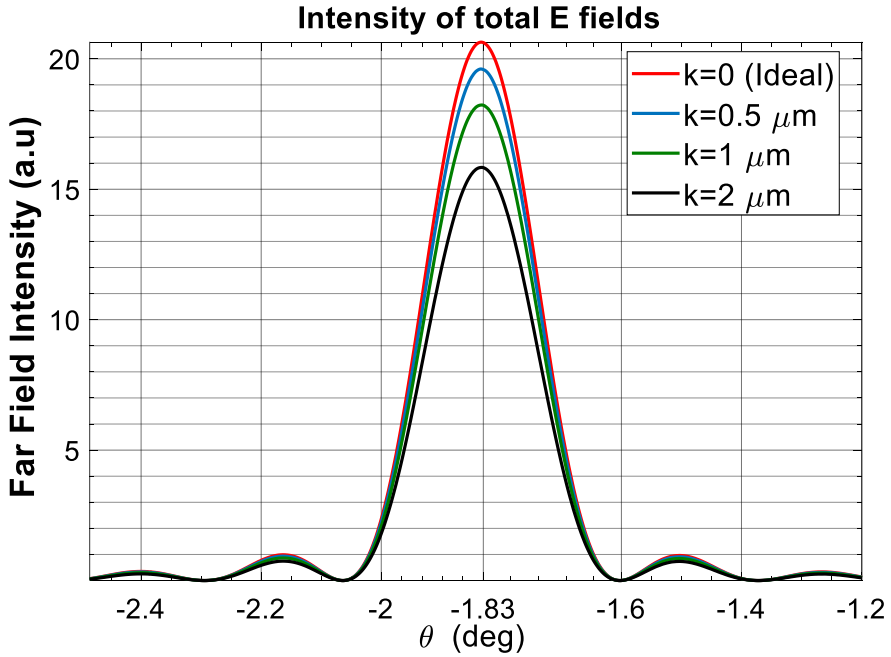

Figure 2.12 Far field intensity of the deflected light for different values of k.

Wall size	λ=0.5 μm	λ=1 μm	λ=1.5 μm
0.5 μm	94.5%	95.7%	96.4%
1 μm	87.4%	89.6%	91.3%
1.5 μm	76.4%	76.6%	78.6%

Table 2.1. Calculated efficinecies as a function of wavelength and wall size

Our data shows that there is fairly a linear relationship between the electrode width k and the beam steering efficiency. So, when k is between 0 and 0.5, the efficiency is lying between these two cases. Since an out of plane wall was manually inserted in the director field of an ideal structure, a sudden change in the index of refraction arose in that method. Therefore, we expect a slight improvement in efficiency calculations when we use the calculated director profile in the next section as this sudden change would turn into a gradual one. Although the approximated efficiencies shown above give us an overview about the practical limits of such a device, we will perform a more accurate calculation later in chapter 3 by using calculated director profile as an input for FDTD method.

CHAPTER 3 - EFFICIENCY OPTIMIZATION OF THE PPD DEVICE

3.1 DEVICE OPTIMIZATION PARAMETERS

In this chapter, we explain the numerical calculation method used to optimize the design, analyze the behavior of the trapped wall, and find possible ways to minimize the wall width. The size and shape of the trapped wall depends on several factors such as LC material, cell thickness, PCE sizes, anchoring energy and voltages. We classify these factors as material factors, such as parameters of the liquid crystal, namely elastic constants, dielectric anisotropy, and birefringence and design factors such as geometry of the cell, cell thickness, spacing size of the electrode structure, and anchoring energy of the alignment layer. MLC-6608 LC material properties were used for both modeling and experiment unless otherwise stated. The material properties are as listed: ne=1.5586, no=1.4756, Δn=0.0803, $\Delta\epsilon$=-4.2, at 20°C, K1=16.7 pN and K3=18.1 pN and clearing point is 90 C.

In considering the above parameters, the narrowing of the electrode and gap width may reduce the effective size of the trapped wall, but this result may be affected by the thickness of the cell. On the other hand, there are some limitations to many of these factors. For instance, available technology limits fabrication of sub-micron electrode spacing and assembly. Similarly, liquid crystal parameters are limited based on the availability of the material. The following simulation is an attempt to keep these limitations into account to allow the results of this study to be applied to devices. Considering the above limitations, we studied the effect of design parameters on the deviation of the actual director profile from the desired uniform in plane rotation with no

z-axis dependence and on the structure of the trapped wall. For each case considered, the final efficiency with the specified conditions is calculated.

3.1.1 Electrode/Gap Spacing Optimization

Considering the effect of the cell thickness on the pattern spacing ratio, we looked at the azimuthal angle difference between the edge of an electrode and the center of an electrode or gap as a function of z. The azimuthal anchoring energy of the surface layer in this example is considered to be infinitely large. For a strong azimuthal anchoring energy, we expect a strong tendency for the director to remain unchanged on the layers close to the surface over the center of the electrodes and at the center of the gap where the electric field effect is weak.

To examine the above different pattern spacing (i.e. different values of W and L) was modeled for a fixed cell thickness of d=3.6 μm. Figure 3.2 summarizes the results where ϕme, ϕmg & ϕee are the azimuthal angles right above the surface at the center of an electrode, center of a gap and edge of an electrode, respectively. ϕave is the average azimuthal angle at z=d/2 in the center of the bulk. Layers close to the surfaces experience more deviation since they are closer to the fringe fields while layers at the center of the cell have a more uniform angle along the aperture as the fringe field effects get averaged out in the center. Therefore, ϕ_{ave} is only several degrees different than its maximum at the surfaces. Figure 3.1 shows the azimuthal angle of the director along the aperture for W=1.5 μm, L=2.5 μm (a) and W=L=2 μm (b) over two PCEs several z-axis locations where the layers distances are shown relative to the bottom substrate. In this example, all electrodes are activated with an applied 10V RMS signal and the cell

thickness is d=3.6 µm, which would ideally yield a constant director angle along the x and z axes. As shown, the director is fully rotated to the maximum angle (90°) at locations corresponding to the edge of an electrode, but has less rotational angle at the center of an electrode or gap, especially for z values closer to the surfaces. The amplitude between the layers relates to the uniformity in the cell and depends on the pattern spacing relative to the cell thickness. With the help of arrows indicating the difference between twist angles in different locations in the cell, it is clear that for the case L>W, the cell is more uniform among all layers in both the x and z directions.

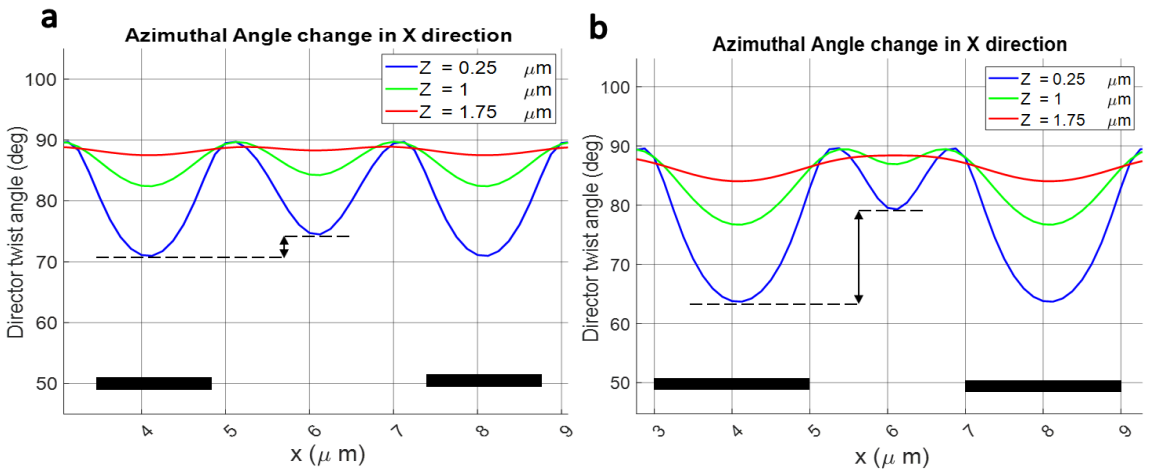

Figure 3.1 a) Azimuthal angle change vs aperture for a device with w=1.5 µm, L=2.5 µm b) Azimuthal angle change vs aperture for a device with w=2 µm, L=2 µm.

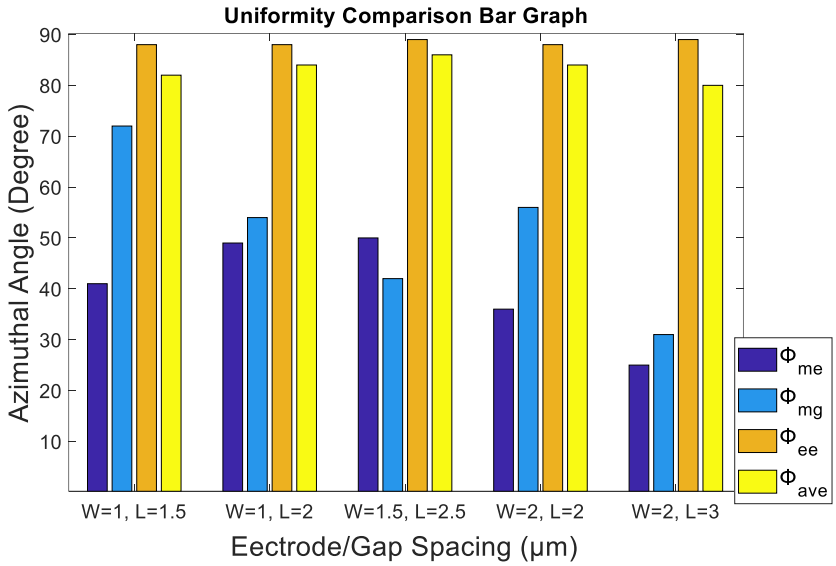

Figure 3.2 Bar graph of the azimuthal angle vs electrode/gap spacing with strong anchoring energy of $w_a=10^{(-4)}$ J/m^2 at different locations of middle of an electrode (dark blue), middle of a gap (light blue), edge of an electrodes (orange) and average value of a layer located at the middle of cell thickness (yellow).

The bar graph in figure 3.2, shows that for smaller values of W, the angle difference, ϕee - ϕme, is smaller resulting in a more uniform twist along x. Also, when L is slightly larger than w, the values of ϕme and ϕmg are closer together. This is because the maximum torque from the fringe field is not exactly at the edge of an electrode, but rather slightly toward the gap. This makes the effective width of the gap smaller. By making the value L larger than W, we can compensate for this difference. For example, from the data shown in the above the graph, two sets of W=1μm, L=2μm and W=1.5μm, and L=2.5 μm have the closest values of ϕmg and ϕme while the average of these two are closer to the ϕee value. Therefore, they have the least variation at different locations along x.

3.1.2 Modeling of Starting Point Device

With considerations of the previous section, the starting point for device optimization modeling is a device with W=1.5 μm and L=2.5 μm gaps. MLC-6608 LC material which we used in the modeling. A relatively strong anchoring energy of wa=wp=10-4 j/m2 was considered for the alignment layer. Device thickness was set to be 3.6 μm, which makes the device a half-wave retarder for λ=602nm. The rubbing alignment of the director angle in the proposed device is +ϵ ° on one surface and – ϵ ° on the other in relation to a defined axis of symmetry which is perpendicular to the strip of electrodes. This boundary condition sets an intrinsic bias for the sign of the angle and hence the direction, i.e. clockwise or counterclockwise, it will rotate when an electric field is applied (as described in Section). A device with eight electrodes was considered in the modeling. The simulated aperture starts from the center of 1st electrode and ends at the center of 8th electrode, which therefore contains 7 periodic PCEs. Considering W=1.5 μm and L=2.5 μm, the total aperture width is then 7*Λpce=7*(1.5+2.5)=28 μm. In this case, we used a so-called Normal Voltage Method (NVM) where both common electrodes are held at 0V and in the first step, and non-zero voltages are only applied to the electrodes.

Since the fringe fields are only generated at the edges of electrodes, the narrowest width occurs if the wall is trapped between the right edge of electrode 8 and left edge of electrode 9, which is within a gap. If the field is not strong enough at those locations, the director transition from -90 ° to +90 ° tends to widen in order to minimize the elastic

energy cost of this tight transition. In a 2nd step, a gradual voltage profile was applied to the PCEs as represented in Table 3.1 with both common plates held at 0 V, in order to achieve a cycloidal rotation of the director profile. Figure 3.3 shows a simulated side view of the director profile along the middle four PCEs (numbers 3 to 6). Figure 3.4 & 3.5 show azimuthal angle (i.e. calculated from x direction) and polar angle (i.e. calculated from z direction) versus x-axis for several layers along the z-axis, respectively.

PCE number	±1	±2	±3	±4	±5	±6	±7	±8
Voltage(V)	1.1	2	3	10	10	3	2	1.1

Table 3.1 2nd step voltage profile of PCEs

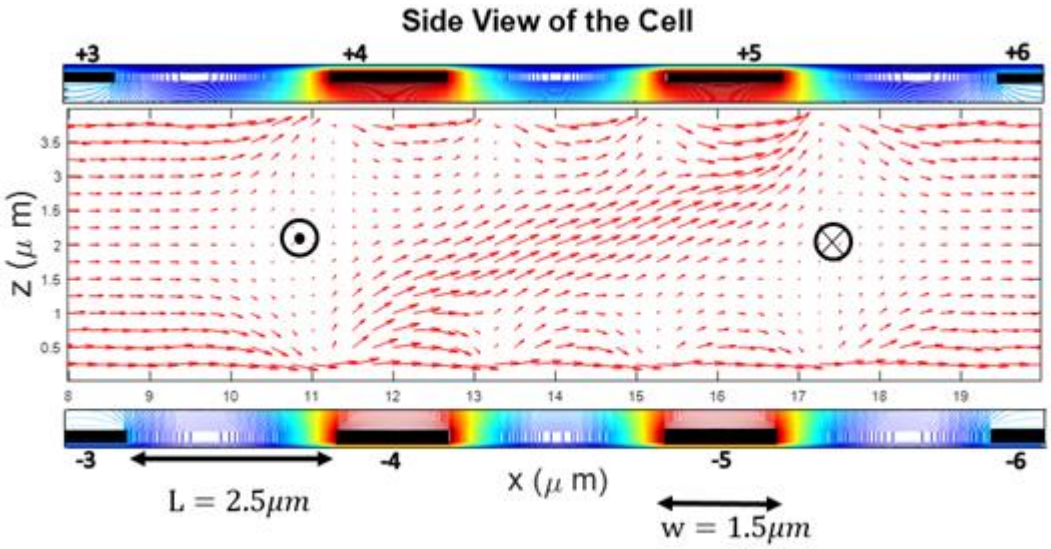

Figure 3.3 Side view of the director field simulated with the normal voltage method over the middle four electrodes. The electromagnetic potential is shown from minimum (blue) to maximum (red).

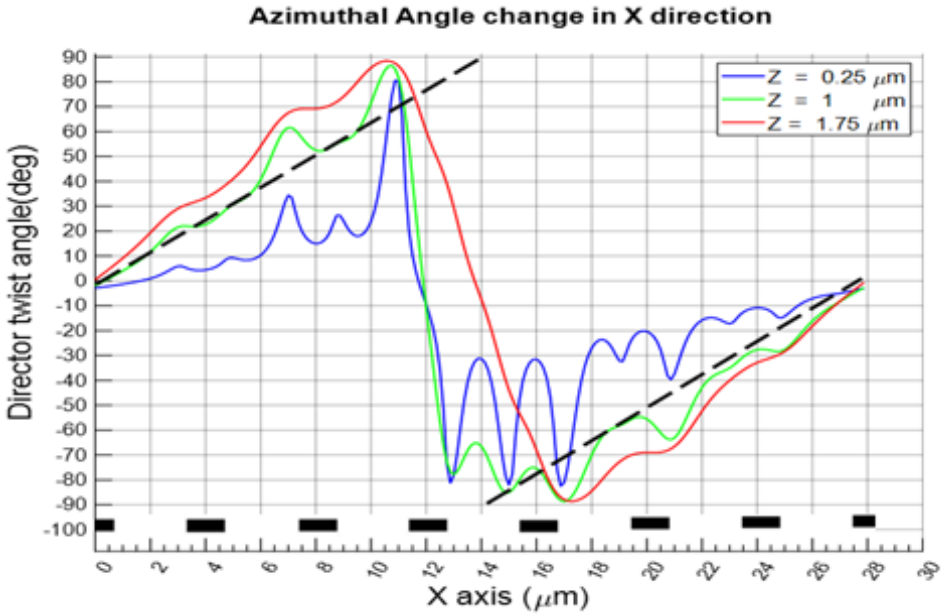

Figure 3.4 Azimuthal angle change of the director along the X-axis with the normal voltage method. Ideal director angle is shown in dashed line.

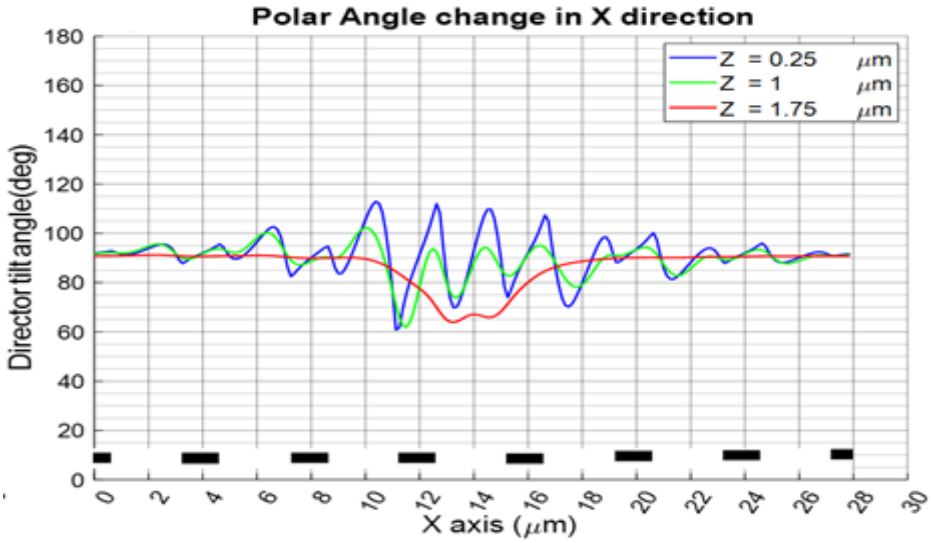

Figure 3.5 Polar angle change of the director along the aperture. Electrodes along the aperture are shown as black grid lines for each graph.

As shown in the Fig 3.4 the director on the left side of PCE-4 is approximately oriented along the +y direction and it undergoes a 180 ° azimuthal rotation that will end up pointing in -y direction at the right of PCE-6. The transition, as shown, is not within the x-y plane, but instead the director tilts out of plane during the π rotation. Another possibility for this rotation is that the director stays in the x-y plane and has a pure twist transition. However, the vertical splay configuration is preferable because it can have a lower elastic energy density and therefore potentially be squeezed to a smaller width. Furthermore, we find the wall is not uniform along the z direction, and in this example is not trapped in the gap between two electrodes as desired. This problem is addressed in the following section. Another useful piece of information we can extract from Fig. 3.4 is that different layers along the z-axis have different twist angles. While the layer at the center has an almost linear change in azimuthal angle, the layer very close to the surface is mostly wiggling around the rubbing direction angle. This effect can be expected since there is a strong in-plane field at the center of the bulk, whereas near the surface the effect of the anchoring energy is strong and the in-plane field varies along the x-axis (see Figure 3.3). To address this uniformity issue, a weak surface anchoring energy alignment will also be considered in the following sections.

3.1.3 Voltage Method

In the previous sections, voltages were only applied to the PCEs while common electrodes on both substrates were held at 0 V. In figure 2.7, with the normal voltage method, we see the density of the equipotential lines for such a condition is very low at

the center of an electrode and at the center of a gap in the middle of the bulk, meaning that there is a weak electric field at those locations. In this section, we describe an Inverted Voltage Method (IVM) to introduce a strong vertical electric field that causes the negative LC to stay more in the plane of the cell, making the director profile closer to the ideal form introduced earlier. Interestingly, the strong field at the middle of the electrodes will squeeze the trapped walls to be confined within a gap between two neighboring edges of PCEs with the highest voltage. Both effects are desired for a higher efficiency. Figure. 3.7 demonstrates the equipotential field graph with the inverted voltage method applied to the device. With the IVM, common electrode on one surface is at the maximum voltage and the corresponding electrodes to that plate are activated by the voltage difference to that maximum amount. In comparison to figure 2.7, the higher density of lines along the vertical dashed line in figure 3.7, suggests a stronger electric field compared to the same area in figure 2.7.

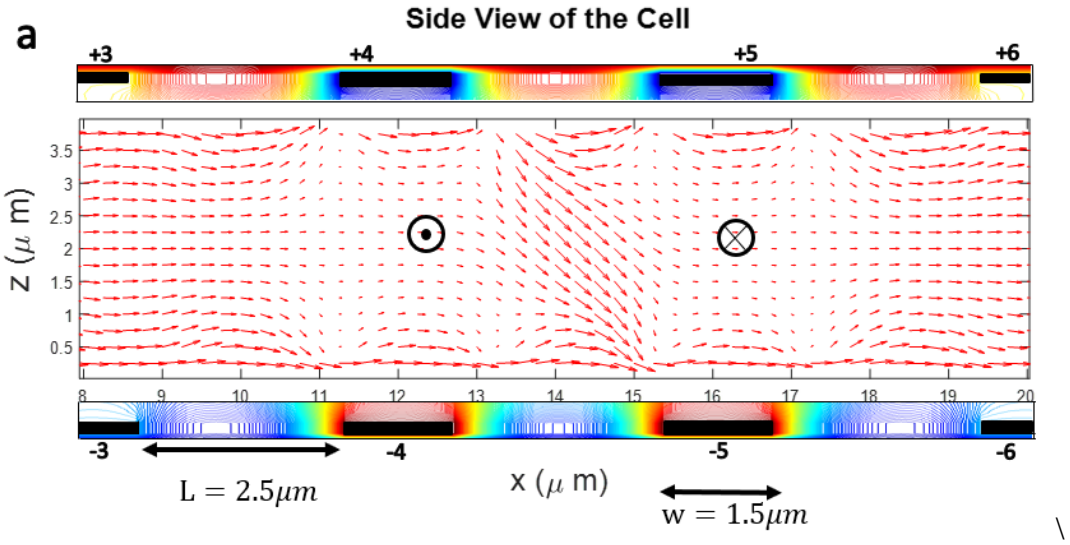

Figure. 3.6 Side view of the director field simulated with IVM over the middle four PCEs

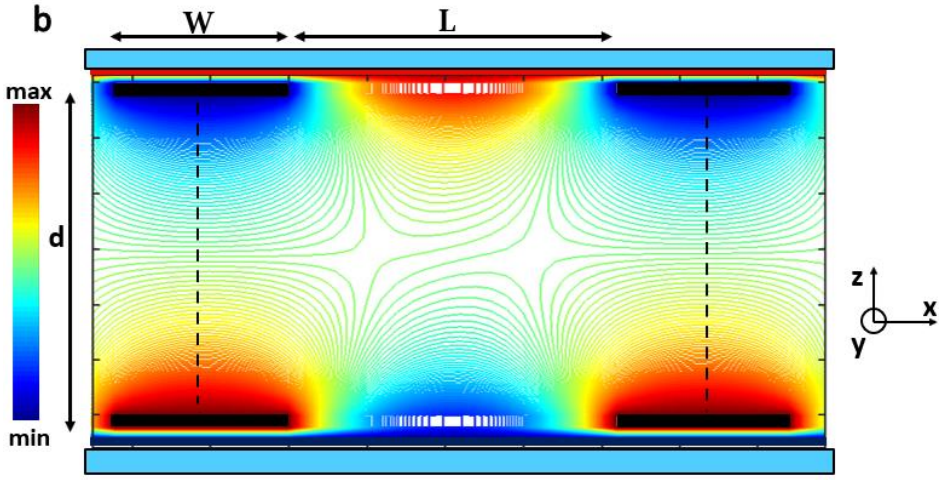

Figure. 3.7 The electrostatic potential around the electrodes in the cell using IVM, change from minimum (blue) to maximum (red).Dashed lines indicating the vertical component of the electric field

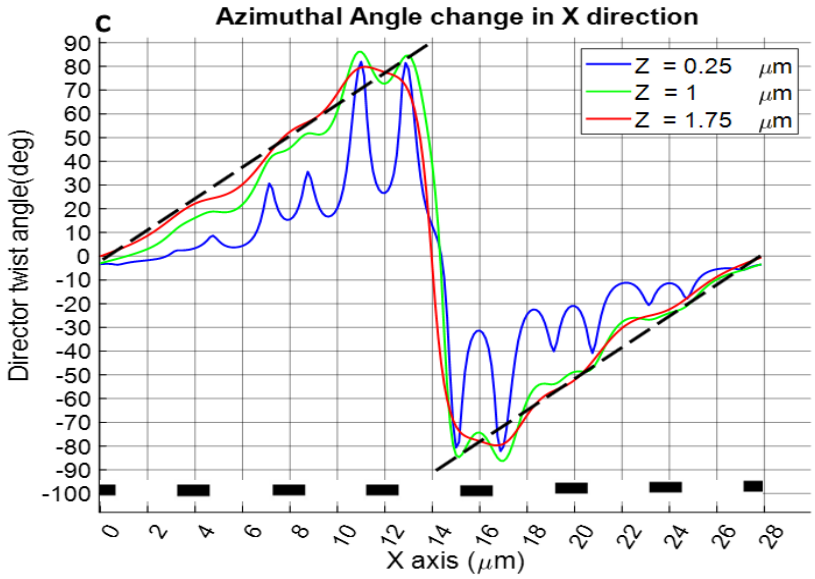

*Figure. 3.*8 Azimuthal angle change of the director along the aperture. Ideal director angle is shown in dashed black line.

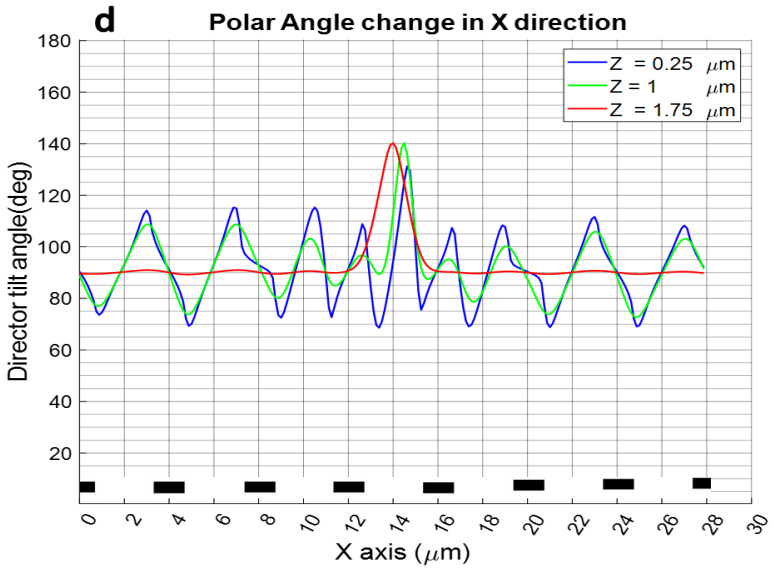

Figure. 3.9 Polar angle change of the director along the aperture

Using this IVM, the cycloidal pattern for a PPD was reached in a similar way to that explained in Section 3.1.2 However, as figure 3.6 and 3.8 show, the wall is confined to within a gap in the entire bulk in this case. The exact wall size was measured for the middle layer along the z-axis from Fig. 3.9 to be the same as the width of the gap (L=2.5 μm), and for the layer that is distanced 1 μm above the surface it was found to be k=1.5 μm . This means that most of the layers have even less wall width than a gap which is favorable for a high efficiency.

3.1.4 Anchoring Energy

Another important parameter for the uniformity of the twist angle along both the x and z axes is the anchoring energy. Figure. 3.4 and 3.8 show that the twist angle in a layer close to the surface is different from that in the middle of the bulk except for locations near the edges of electrodes where the fringe-field is strongest. In other words, the director has a maximum twist at the edges of electrodes but has much lower twist

everywhere else. Secondly, going along the z-axis, the director experiences a gradual twist to its maximum amount at the center and a gradual opposite twist back to the rubbing direction. We found that the stronger the anchoring energy, the more tendency for the director to stay in the rubbing direction in locations where the electric field is not sufficiently high. Azimuthal anchoring strength is determined by wa in Rapini–Papoular equation and having an infinite value means the easy axis of the LC director on each substrate is fixed regardless of the magnitude of an applied field. Therefore, to achieve a more uniform twist angle of the director profile along both directions, a lower anchoring energy for the surface alignment is favorable.

For the purpose of uniformity, a modification has made to the modeling algorithm to consider a lower azimuthal anchoring energy of wa=10-5 J/m2. Figure. 3.10 shows that in this case, even the layer 0.25 μm above the surface is now following the linear profile along the aperture more closely than the case with strong anchoring energy. Comparing the red curves from figure 3.11 with figure 3.8 reveals that the layer at the center of bulk also has a more uniform linear angular twist along the aperture. Therefore, the uniformity along both directions has been improved by lowering the azimuthal anchoring energy. The case of a lower polar anchoring energy (wp) was also considered, however, no significant difference was observed. This can be explained by the tendency of the director to stay in the x-y plane due to the vertical component of the electric field. Our findings here coincide with those of Kim et. al. from a report that shows the effect of polar anchoring strength in an FFS cell with negative LC material is negligible [83] . To further verify the effect of a lower azimuthal anchoring energy on the uniformity, data in

the bar graph of Figure 3.2 was repeated for the case of lower w_a with the results shown in figure 3.13.

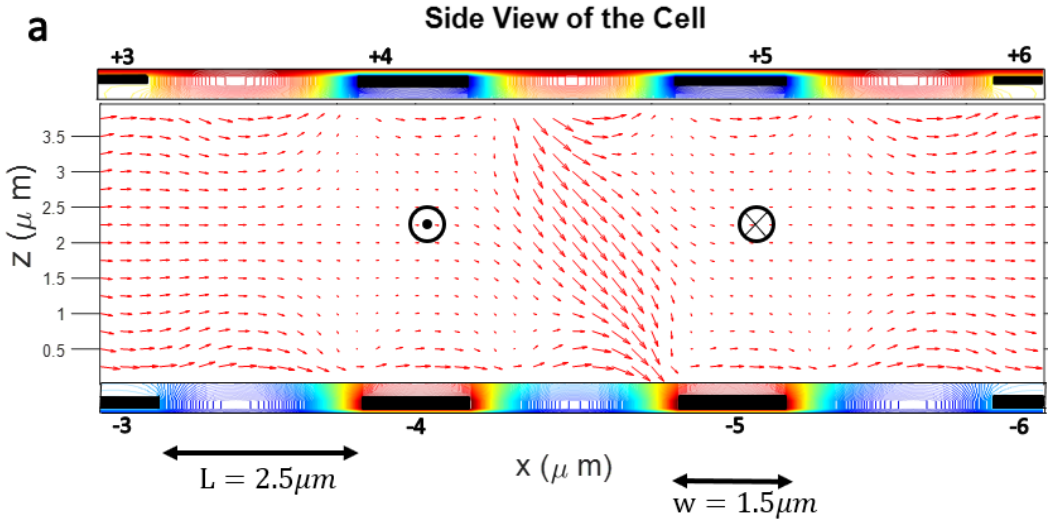

Figure 3.10 Side view of the director field using IVM and low anchoring strength (wa=10-5 J/m2) over the middle four PCEs

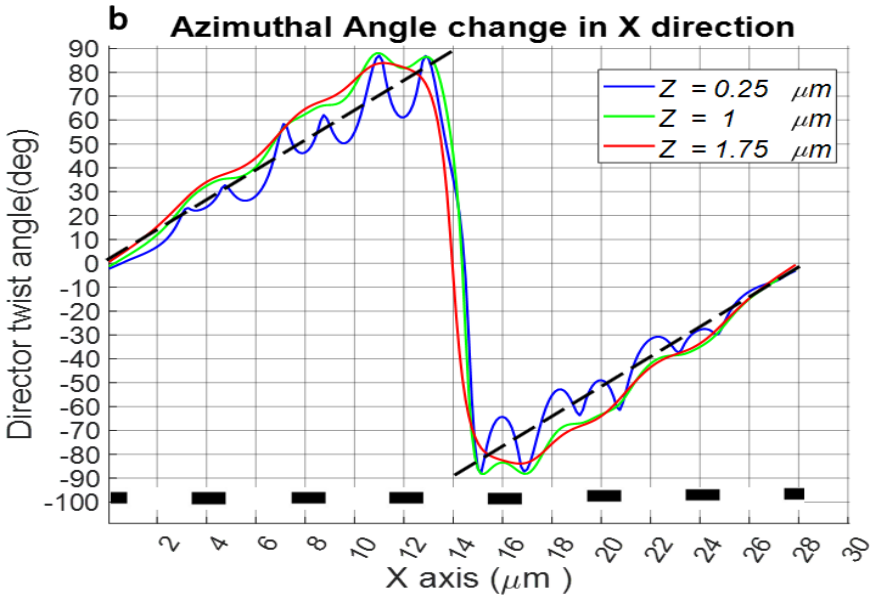

Figure 3.11 Azimuthal angle change of the director along the aperture. Ideal director angle is shown in dashed black line.

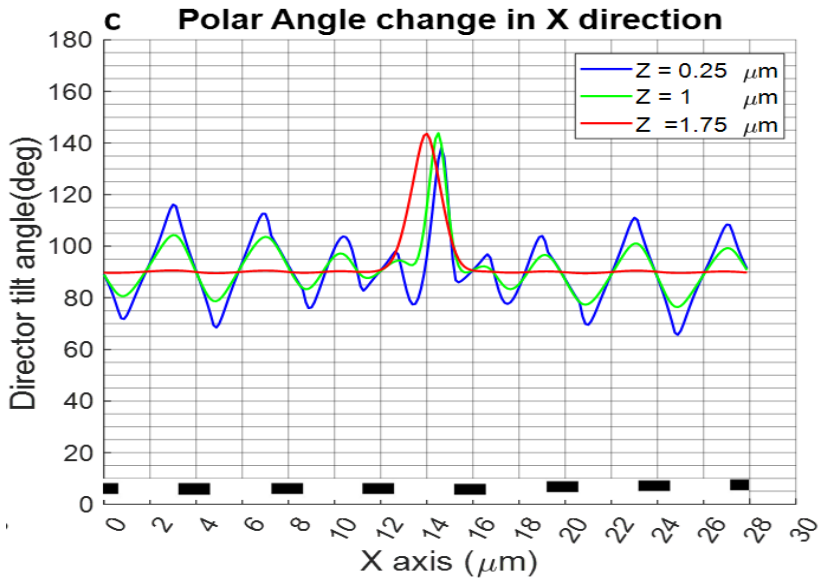

Figure 3.12 Polar angle change of the director along the aperture.

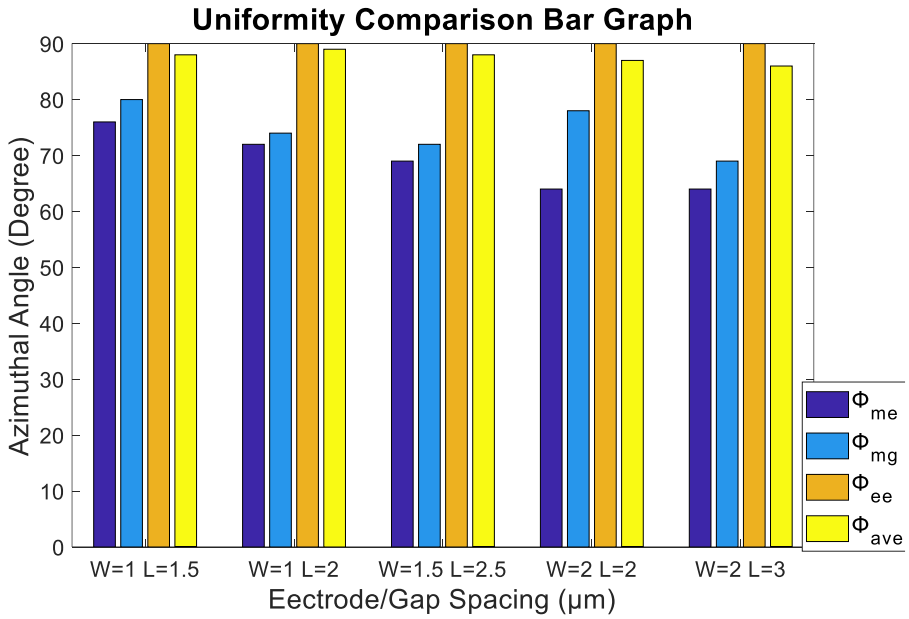

Figure 3.13 Bar graph of the azimuthal angle vs. electrode/gap spacing with weak anchoring energy wa=10-5 J/m2 at different locations, including: the middle of an electrode (dark blue), middle of a gap (light blue), edge of an electrode (orange) and average value of a layer located at the middle of the cell thickness (yellow).

As shown, the angle difference ϕ_{ee}-ϕ_{me} and ϕ_{ee}-ϕ_{mg} is much lower in all cases indicating more uniformity along the x-axis. Moreover, the difference between ϕme and ϕ_{mg} (shown by dark blue and light blue bars) is significantly reduced. Again, we can see that closer values of ϕ_{me} and ϕ_{mg} for the cases where (W=1μm, L=2μm) and (W=1.5μm, L = 2.5 μm). The result in Figure 3.13 brings the conclusion that for a uniformly twisted director profile, a low anchoring energy alignment layer is crucial.

3.1.5 The Effect of Cell Thickness

For a PPD, it is desirable for the director field to have a twist angle independent of the z direction. Moreover, the twist angle about the z axis as a function of x is desired to be a linear function of x. For the latter , a thicker cell is preferred [19]. However, if the cell thickness is much greater than the gap width, the trapped wall width may increase because the electric field strength in the bulk decreases as the cell thickness increases. Therefore, there is a tradeoff in setting the thickness of the cell (d) relative to the electrode and gap spacing (W+L).

A detailed study was performed on different values of W, L and d. It was found that the ratio R= (W+L)/d may affect the type of trapped wall as it affects the electric field density inside the bulk. Although other factors such as elastic constants and voltages play a role on defining the type and width of the wall, we tried to find the effect of R while keeping the elastic constants fixed at K1=16.7 pN , K2=7 pN and K3=18.1 pN. As shown in Figure 3.14 , different electrode and gap sizes with periodicities of Λ=2, 3, 4

and 6 μm were modeled with different cell thicknesses so that cases with R>1, R=1 and R<1 could be compared.

There are two main classifications for the wall structure observed. One is called type A which is characterized by a transition along two (or more) electrodes plus the gaps in between. Figure 3.3 shows an example of this type. The width of the wall is defined as the transition of the azimuthal twist angle from near +90 degrees to near -90 degrees from the azimuthal angle graph (Figure 3.4). As seen in figure 3.3 for this example, a type A wall occurs over two electrodes and their gap. This is a relatively wide length compared to one pitch and therefore will impact the final efficiency significantly.

A second type of the wall, type B, is defined by having the wall transition confined within a single gap. For instance, the wall in Figure 3.9 and 3.10 is a type B wall. This type is desired as it has a much lower effect on the beam steering efficiency. Another characteristic of the wall is the maximum tilt angle in the z direction measured from the x-y surface that the director will reach during the transition. For example, the maximum tilt angle in figure 3.5 with a type A wall is about 25 degrees whereas in figure 3.12 for a type B it is about 55 degrees. The higher tilt angle in the wall area is also desirable since the out of plane tilt of the director can potentially help the wall to be squeezed more than for just an in-plane transition.

Figure 3.14 shows a bar graph of maximum tilt angle for different electrode and gap spacing and different values of d. The red bars show cases with a type A wall whereas the green bars show the cases with the preferable type B walls. Figure 3.14 reveals that R=1 is the threshold where the type B and type A walls are distinguished. For

all cases with R<1, a type A wall is energetically favorable for the cell. However, for efficiency consideration, a type B wall with higher polar angle is favorable because it allows for a narrower transition. Therefore, it can be inferred from 3.15 that the thickness should be set based on a W+L value so that R=>1. On the other hand, when d is smaller than L, a type B wall with lower polar tilt angle is observed.

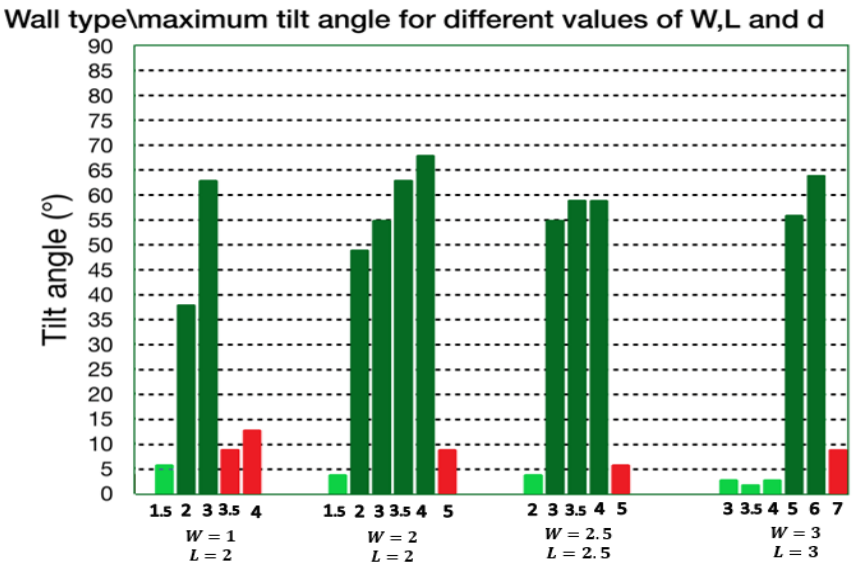

Figure 3.14 Bar graph of the maximum tilt angle for different values of W,L, and d (all in μm). The d values are indicated under each bar.

3.1.6 Lower Limit of the Pitch

In this section, we consider the minimum pitch size required for a PPD structure for the proposed device design. Director modeling similar to the above sections was done for different number of electrodes over one pitch. Figure 3.15.a shows a cycloidal pattern over 5 periodic PCEs while figure 3.15.b shows one along 3 periodic PCEs. For the latter case, the in-plane rotation angle does not show the desired "saw tooth" profile. Therefore, at least 5 electrodes and gaps are required to make one pitch of the cycloidal pattern.

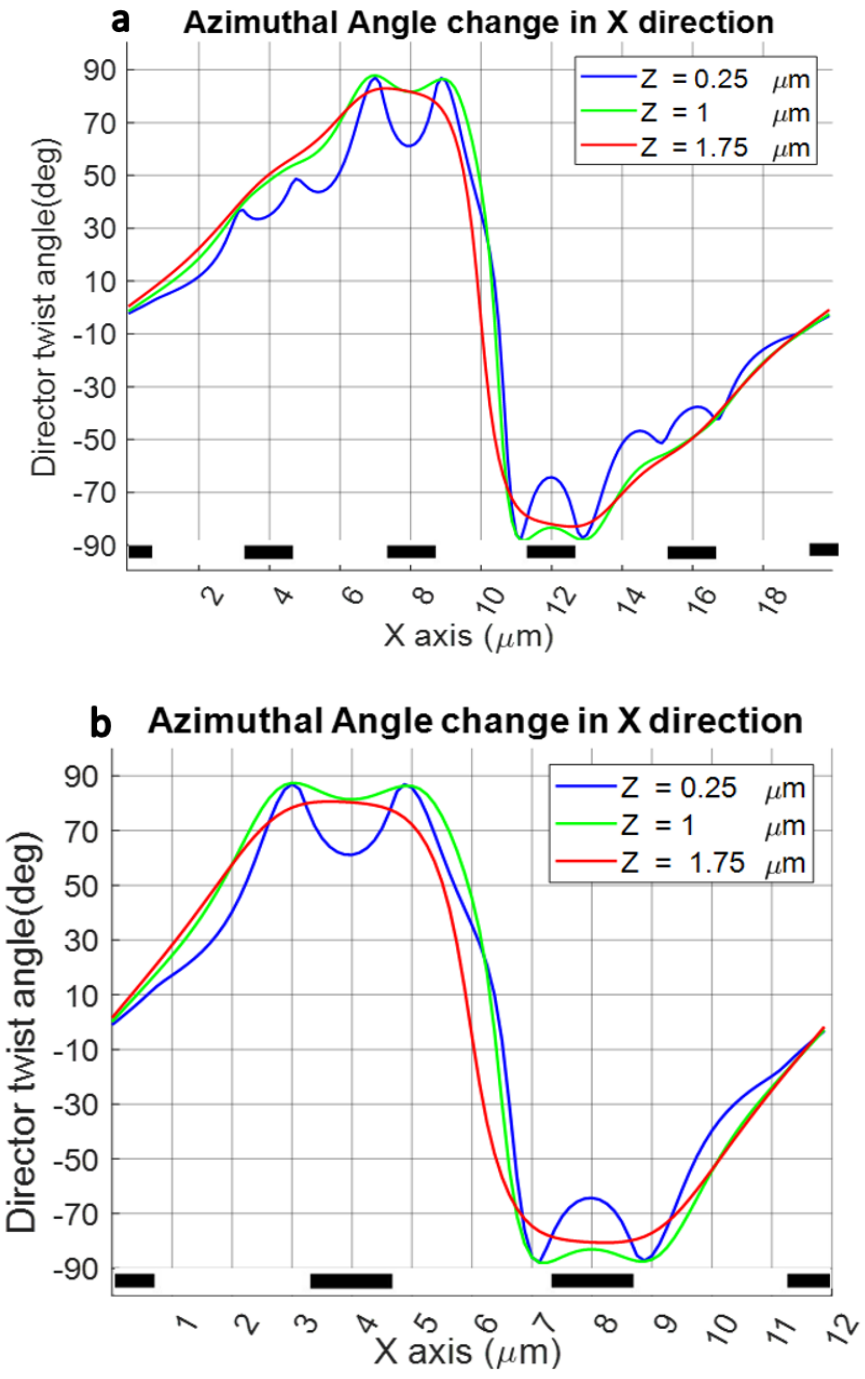

Figure 3.15 a) Azimuthal angle over one pitch with a) 5 and b) 3 PCE grating period

Theoretically, however, (i.e without considering fabrication limits) we can shorten the pitch of each period in the range of a few microns. But, we should consider that the shorter the pitch is, the larger the ratio of the trapped wall region to pitch will be as discussed in chapter 1 which will significantly reduce the high efficiency we are aiming to reach. We also found that the limit of the trapped wall is related to the cell thickness since the electric field is weak at the center of the cell as shown earlier.

3.2 OPTICAL POWER EFFICIENCY OF THE OPTIMIZED DEVICE

Based on the FDTD method explained in Section 2.3.2, efficiency was calculated for the different optimization cases of Section 3, for 3 pitch lengths of $\Lambda 1$=60 μm, $\Lambda 2$=28 μm and $\Lambda 3$=20 μm. Three aperture sizes of A1=240 μm, A2=112 μm and A3=80 μm were chosen to included four pitches for each case. The cell thickness was set to d=3.6 μm and the MLC6608 material characteristics were also used. The substrate was set to glass with ng=1.5.

For FDTD parameters, the wavelength of λ=602 nm for which the cell is a half-wave retarder and 30 grid points per wavelength was used. The far field intensity was distanced at 1 m from the cell and a Gaussian light with a full width at half maximum (FWHM) of 2,500 μm that is much larger than the aperture was set to approximate a top-hat beam in order to ensure that the aperture is uniformly illuminated. Figure 3.16 shows the point spread function (PSF) for a case with Λ= 28 μm. Figure 3.17 shows the z-component of electric filed. Looking more closely at the Ez plot, one can acquire meaningful qualitative data to understand the changes in the light wave as it passes through the cell. For example, the constructive interference of light waves shows a non-

tilted input wavefront at the bottom of the plot and the deflection of the output light wavefront at the top of the plot (as highlighted by the yellow lines). Additionally, Huygens wavelets at the location of trap walls caused by the abrupt change in the index of refraction are also visible.

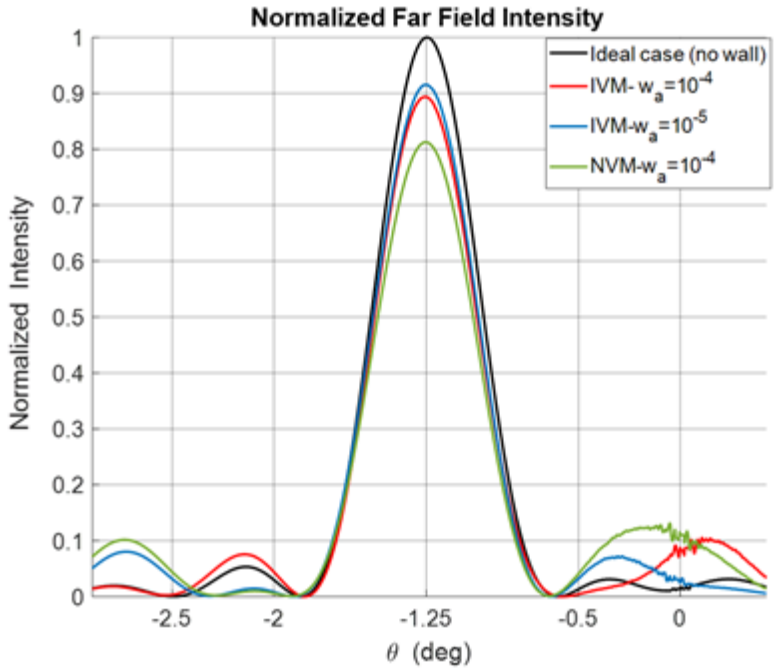

Figure 3.16 Far field intensity of the deflected light for three cases of NVM and IVM with both strong and weak anchoring energies compared to an ideal case.

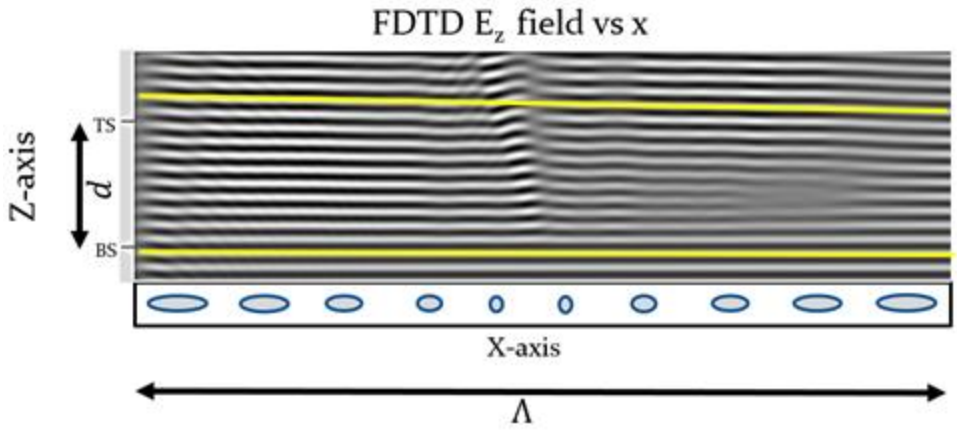

Figure 3.17 The z-component of the electric field for one pitch along the x-axis. Bottom substrate (BS) and top substrate (TS) are marked along the z-axis. Schematic side view of the cell is shown along the aperture. Yellow lines highlight the light beam at input (straight line) and at output (tilted toward θ).

Table 3.2 summarizes the calculated efficiencies for three cases using the IVM method with infinite and weak (wa=10-5 J/m2) anchoring energies (AE) and the NVM method with infinite anchoring energy. The efficiencies are obtained from the peak of the far field intensity. As expected, the efficiency increases as we switch from the normal voltage method to inverted method and it even further increases with a weak anchoring energy.

Pitch size	Deflection Angle (°)	NVM Strong W_a	IVM Strong W_a	IVM Weak W_a
$\Lambda_1 = 60\ \mu m$	0.6	92.3%	94.7%	98.8%
$\Lambda_1 = 28\ \mu m$	1.2	81.4%	89.2%	91.7%
$\Lambda_1 = 20\ \mu m$	1.7	67.5%	78.2%	84.5%

Table 3.2 Summary of beam steering efficiency calculation

CHAPTER 4 - FABRICAITON PROCESS AND EXPERIMENTAL RESULT

4.1 DEVICE GEOMETRY

In this chapter, we will introduce the design of the mask used to fabricate the test device and will explain the fabrication process, characterization method as well as the experimental data derived from the test device. We will also elaborate how the test device data meets the requirements of a high efficiency device

4.1.1 Electrode Design and Device (Mask) Symmetry

Design of the device consists two layer of conductive ITO layer on top of each other. The bottom layer provides a uniform conductive area over the entire area of which the beam would pass through. The top layer, includes strips of electrodes of width (W) separated by gaps of width (L), as shown previously. The mask is made up of an active area consisting of interdigitated electrode pattern at the center of the cell while the rest of the cell area is accommodating ITO pattern that connect the active area to the ledge of the cell (figure 4.1). When assembled, the active area on both substrates would be placed on top of each other with the connections symmetrically distributed around the active area all over to the ledges. Therefore, high precision aligning of the substrates is needed to place micron-size electrodes on top of each other.

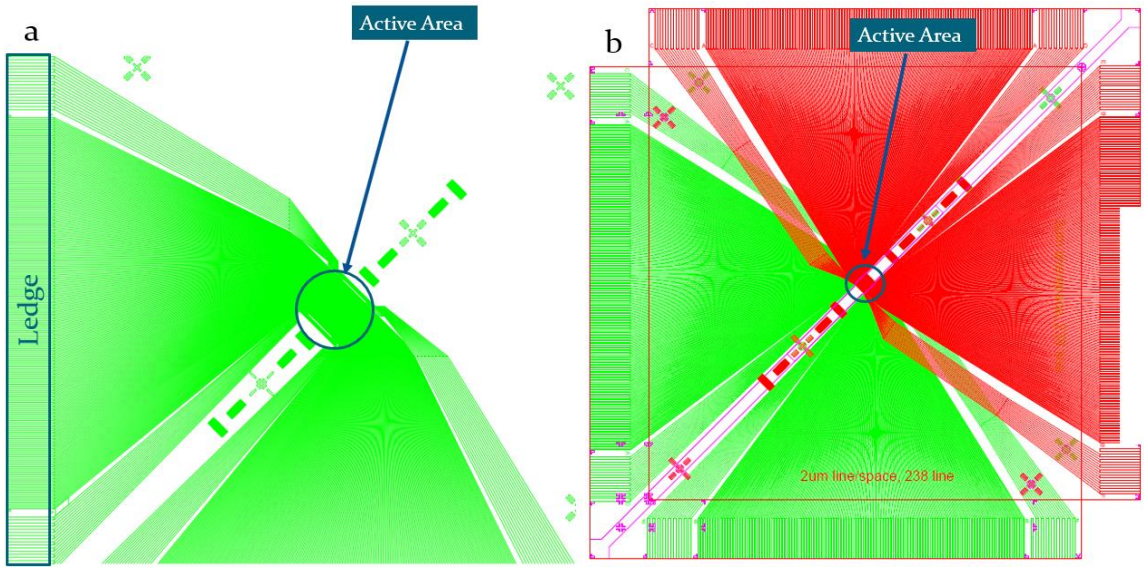

Figure 4.1 Overall mask design of top ITO layer a) substrate 1 (green) b) both substrates assembled on top of each other (green and red)

The active area consists of 238 electrodes and gaps. Considering W=L=2 μm, it can potentially cover about 1mm laser beam. However, driving these many electrodes individually at the same time requires a very complex electronic system. To limit the complexity of driving electronics, there are also two test areas each has a group of 16 electrodes positioned on either side of the active area in order to test the basic performance of the device and check the fundamental requirements. Figure. 4.2 shows a schematic view of the mask zoomed in around the test area.

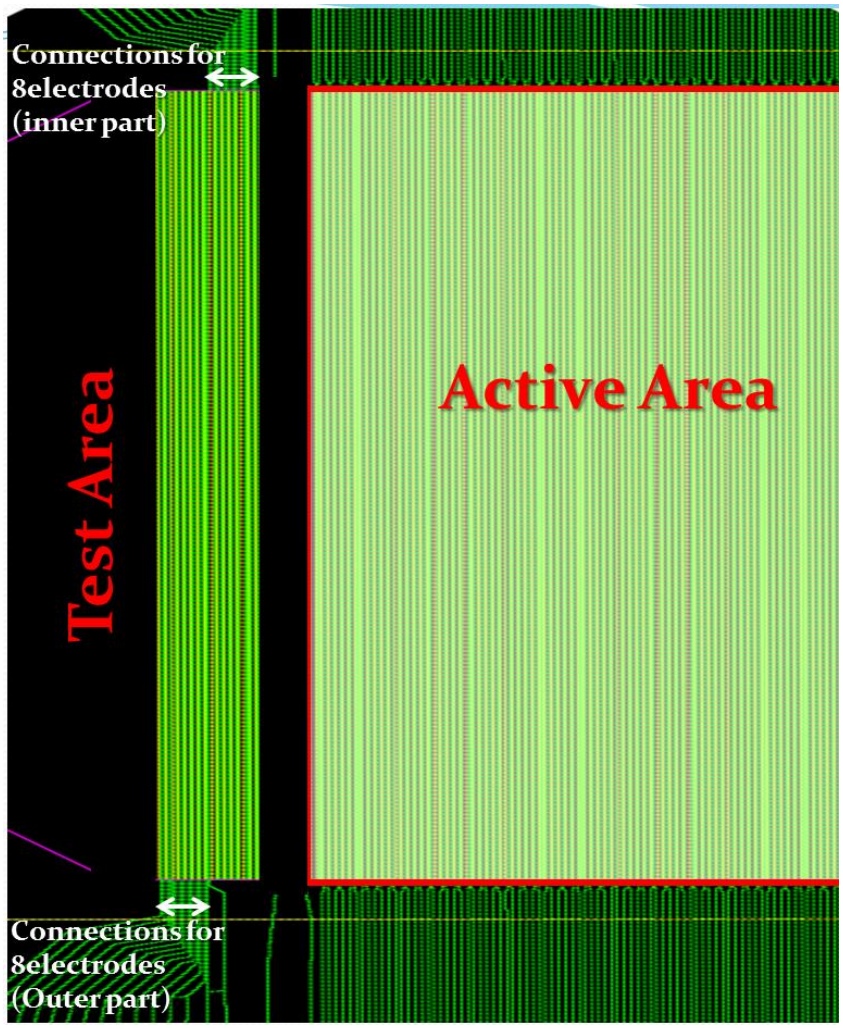

Figure 4.2 Schematic view of zoomed in active area of the mask design

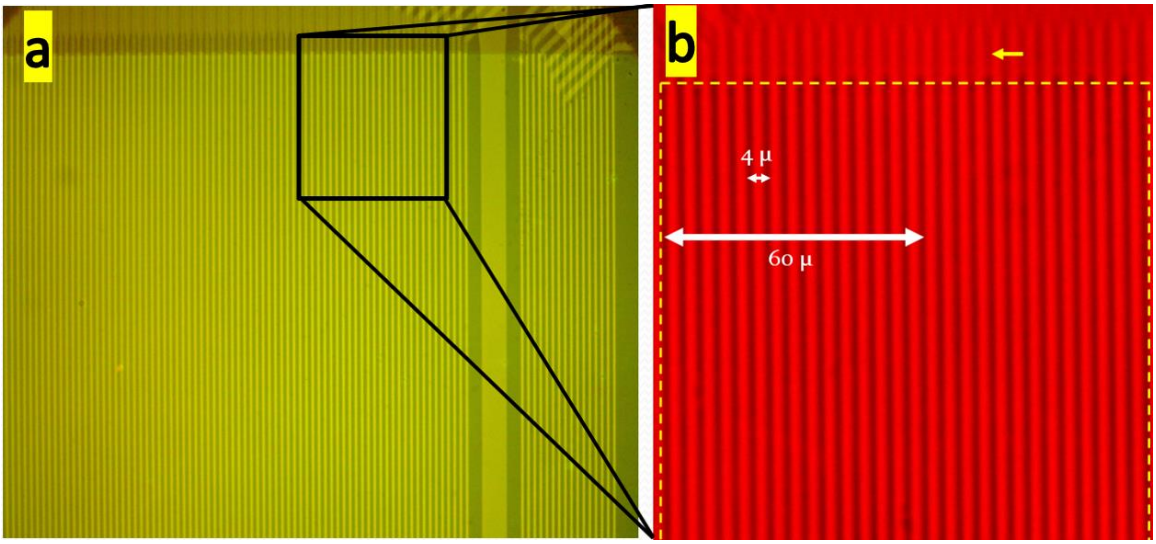

Figure 4.3 (a) Overall view of the active area under a microscope in a reflective light mode including long strips of electrodes on top of each other (brighter lines are ITO electrodes). (b) A magnified picture of the area (with red color filter) under a microscope in transmitted light mode with crossed polarizers (dark lines are ITO electrodes indicated by a yellow arrow).

4.1.2 Pre-Tilt Alignment

To define a pre-tilt angle, Polyimide PI-2170 material was used for its stability and its simple fabrication process. Then, the cells were rubbed with a proper fiber block at 3 ° angle with respect to a line perpendicular to the electrode lines. Since a negative LC material is used, the director will tend to align perpendicular to the fringe field upon applying voltage. Therefore, the pre-alignment angle was set to a few degrees (3 degrees in this case) from a reference line that is perpendicular to electrode strips.

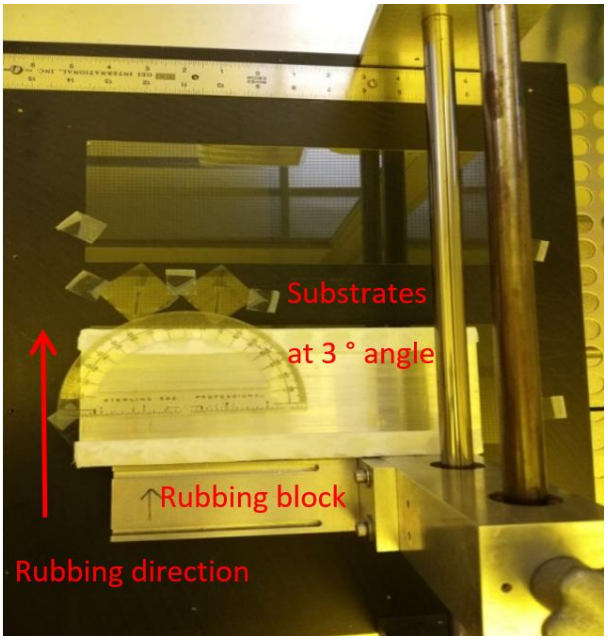

Figure 4.4 Pre-Alignment Station

Considering the mirror effect from assembly of plates on top of each other, both plates are initially rubbed in same direction so that when assembled they will have opposite directions with respect to each other.

4.2 FABRICATION PROCESS

The fabrication method for the tunable PPD employs a standard photolithography process similar to that used in the display industry. A test device was made out of two glass substrates. Using a vacuum sputter coater, each substrate is coated with conductive layer of Indium Tin Oxide (ITO) layer, a thin insulator layer of Silicon Dioxide (SiO2) with around 160 nm in thickness, and a second layer of ITO (~40-50 nm). The first layer of ITO provides a plain conductive area underneath of the 2nd layer of ITO with patterned

electrodes. After patterning ITO layers, the alignment layer of Polyimide SE2170 was spin coated at 1500 RPM for 90 seconds (i.e. thickness of around 50 nm) followed by 5 minutes of soft bake at 90°C and 1 hour hard bake at 200°C. While the first ITO layer provided a conductive common plate, the second ITO layer was patterned with 1.5 μm electrode lines and 2.5 μm gaps in between. The Polyimide (PI) alignment layer is then spun coated on each plate, cured and rubbed at +3 degrees from a symmetry axis perpendicular to the electrode lines. The next step is then spraying 3.6 μm fiber spacer and assemble of two substrates. Perhaps, the most difficult part of the fabrication was aligning the electrodes of two substrates relative to each other in the assembly process. The top and bottom plate alignment required high precision to place one exactly on top of the other while overlapping the electrodes. Our modeling verified that even a small misalignment would result in a significant performance degradation. This is consistent with the conclusion that S.T.Wu et.al reported on a FFS-based cell with similar configuration [84, 85]. A detailed explanation of each step described above is represented in Appendix .

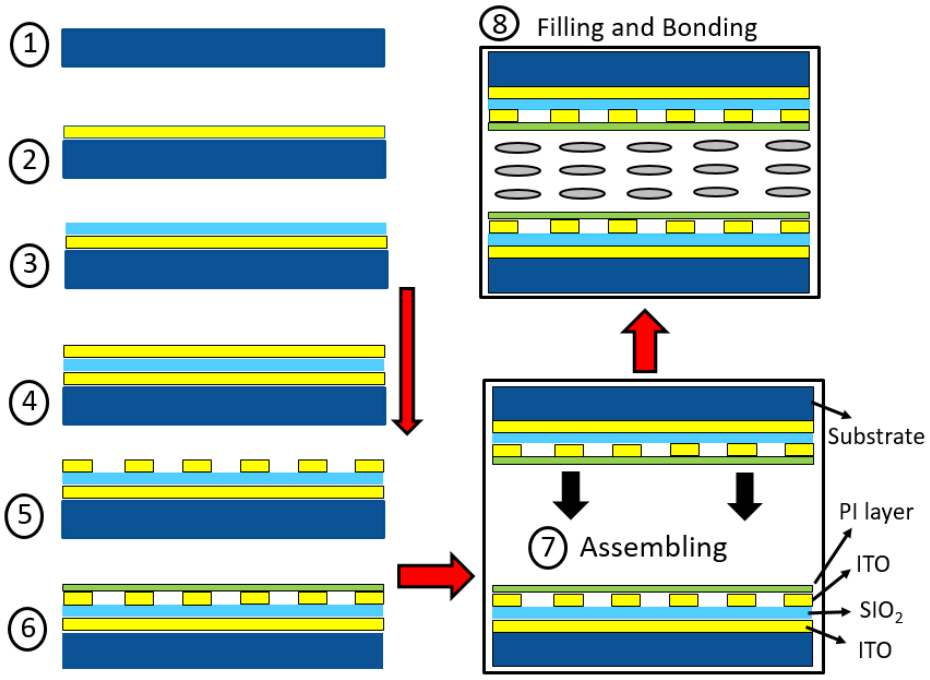

Figure 4.5 Schematic of the fabrication process steps.

Therefore, the substrates were carefully assembled with sub-micron accuracy to precisely line up the electrodes of the two substrates.

The liquid crystal material MLC-6608 was used to fill the space between the two substrates. The thickness of the cell is 3.6 μm, which makes it a half-wave retarder for 602nm light. Finally, a connection to the ground plate was made at the ledge of the cell (Figure 4.6) and the electrodes were connected to flex cable using a flex cable bonding machine.

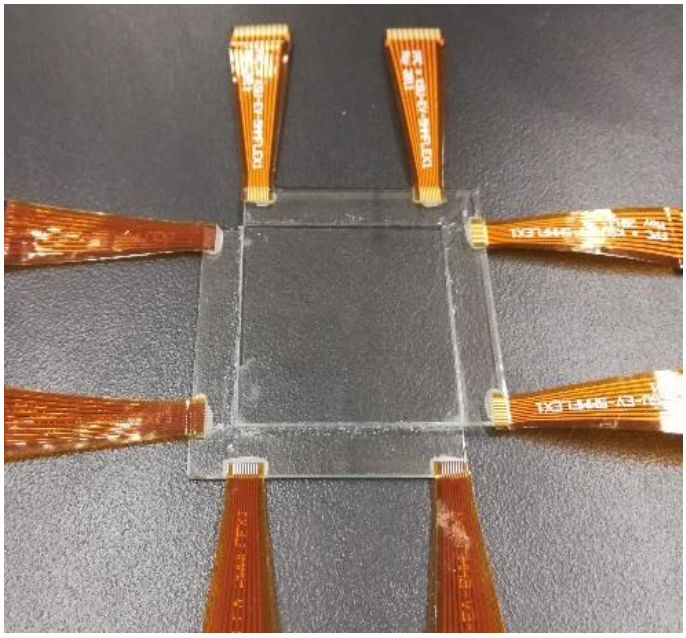

Figure 4.6 The final appearance of the assembled device with flex bonds connected to the ledges.

4.3 CHARACTERIZATION METHOD

To make our definition clear, 0 ° is defined to be the bisector of the two rub directions . we define clockwise rotation (CW) as negative rotation and counter clockwise rotation (CCW) rotation as positive rotation. Based on this definition and rubbing direction used, we can refer to the plate with positive pretilt as “P Surface” and the one with negative pretilt as “N surface”. Also, due to the fact that both plates were initially rubbed with same angle and then the top surface direction was mirrored when assembled on top of the other plate, the surface facing up which is closer to polarizer have always positive pretilt (P surface) while the surface facing down which is closer to

analyzer has always negative pretilt (N surface). In addition to that the initial position of Polarizer is at 0 ° and analyzer at 90 °. We refer to this position as “0 state”.

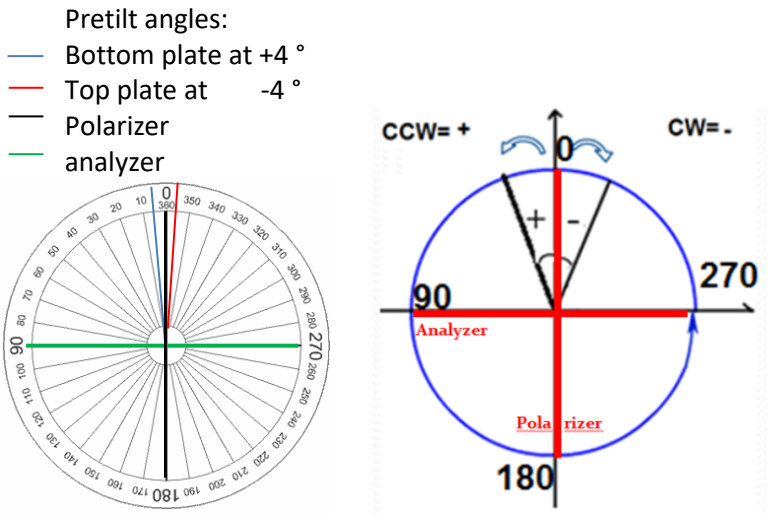

Figure 4.7 Pretilt angles with respect to the position of polarizer and analyzer

4.4 TEST DEVICE DATA

4.4.1 Director’s Rotational Angle Verification Test

As a test of the basic device operation, we demonstrated that we could produce a 180 degrees rotation of the director with a relatively small trapped wall width by controlling all 8 PCEs. We refer to the 8 PCEs on the negative/positive surface as ∓1 to ∓8, respectively. Using the two voltage method, in the first step we applied 10 V to electrodes +1 to +4 and electrodes -5 to -8. As second step, we set voltages on electrodes ∓ 1, ∓8 to 0 V, and electrodes ∓2, ∓7 were set to 1.8 V. Electrodes ∓3, ∓6 were set to 3V and electrodes ∓4, ∓5 to 10V to achieve an optimized cycloidal pattern. Figure. 4.8 shows a sequence of microscope pictures taken of the test device between crossed

polarizers to quantify the rotation of the director in the plane of the cell. Each picture in the sequence was taken with the crossed polarizers rotated to the angle shown in the upper left corner. To help finding the electrode locations, a subplot with reflective light (yellowish color) is indicated on the right side of each picture. The black horizontal stripe in each picture indicates locations where there is no change in the polarization state of light. This occurs where the director is aligned with either the polarizer or analyzer, or where the director is nearly along the normal to the cell surface. The pictures in Fig. 4.8 show the locations of the electrodes. From the picture labeled '40°', we see there is a black strip over electrodes 3 and 6, and a narrower one right in between electrodes 4 and 5. This indicates that the directors over electrodes 3 and 6 are at 40 degrees or 130 degrees. By observing the sequence of pictures, we ascertain that the orientation of the director over these two electrodes differs by 90 degrees. So we can label the orientation of the director over electrode 3 to be 40 degrees, and over electrode 6 to be 130 degrees. The thin stripe between electrodes 4 and 5, that is visible for each polarizer angle locates the trapped wall where the director is aligned nearly perpendicular to the plane of the device. The total width of the electrode structure shown in Fig. 4.8 is 28 μm, which includes several electrodes and gaps.

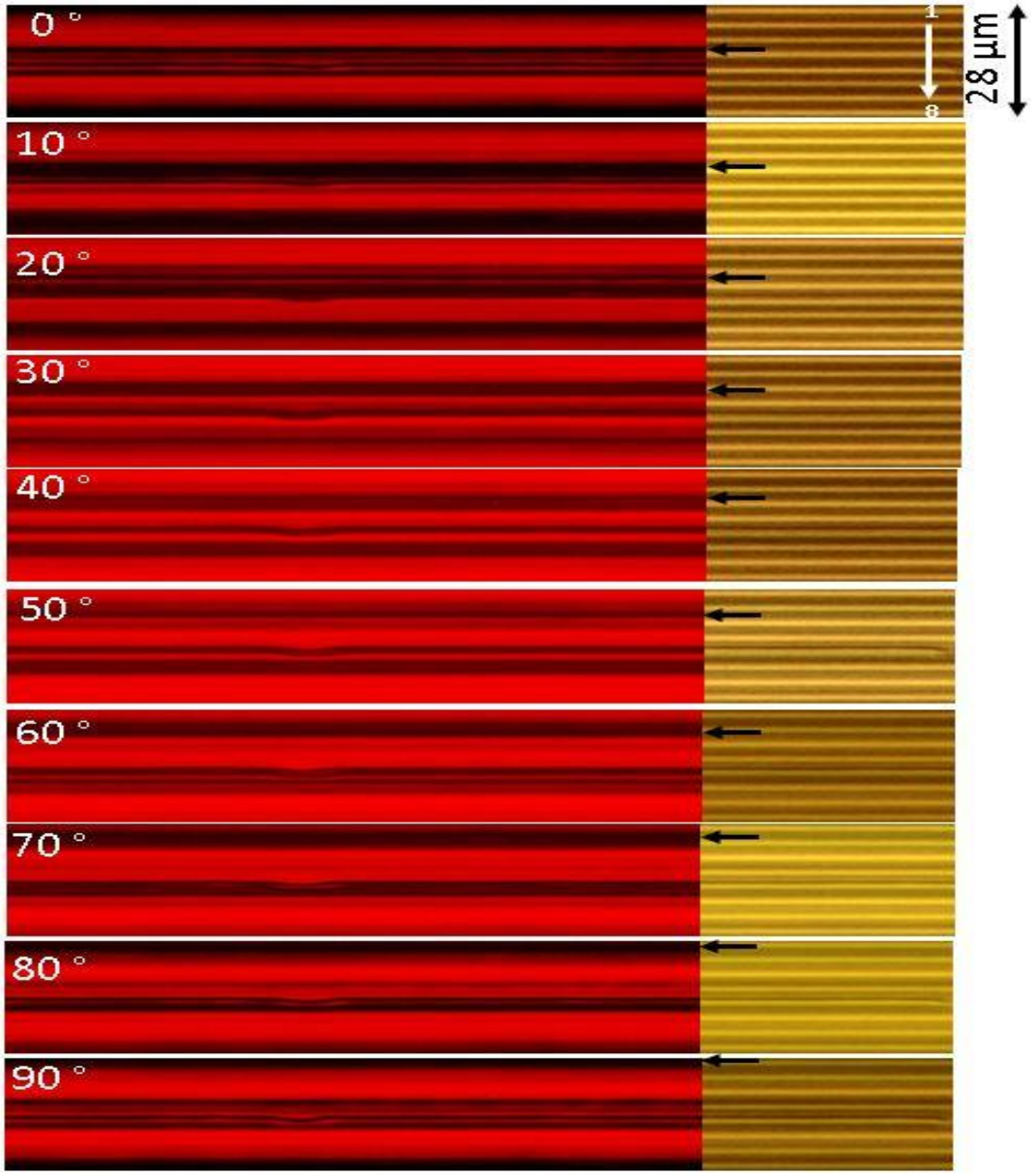

Fig 4.8 – Polarized Optical Microscopy (POM) pictures of the cycloidal pattern controlled by 8 electrodes that are numbered 1 to 8 from top to bottom (shown and numbered by white arrow). This contains a 7 grating period that creates 28 µm pitch for different rotational angle of polarizers. Reflective light mode pictures of the PCEs are shown on right side of each case.

4.4.2 Extinction Angle Along the Aperture

Figure 4.9 shows the extinction angle along the x-axis for a half-pitch of $\Lambda/2=14$ μm. Also, a comparison with simulation results from Section 2D verifies the functionality of the device. The calculated data in figure 4.9 are derived from the red curve (i.e. middle layer along the z-axis) of figure 3.11 for half of the pitch over the first 4 PCEs. With this data we have shown that we can make an array of PCEs and control the sign and magnitude of the director in each one.

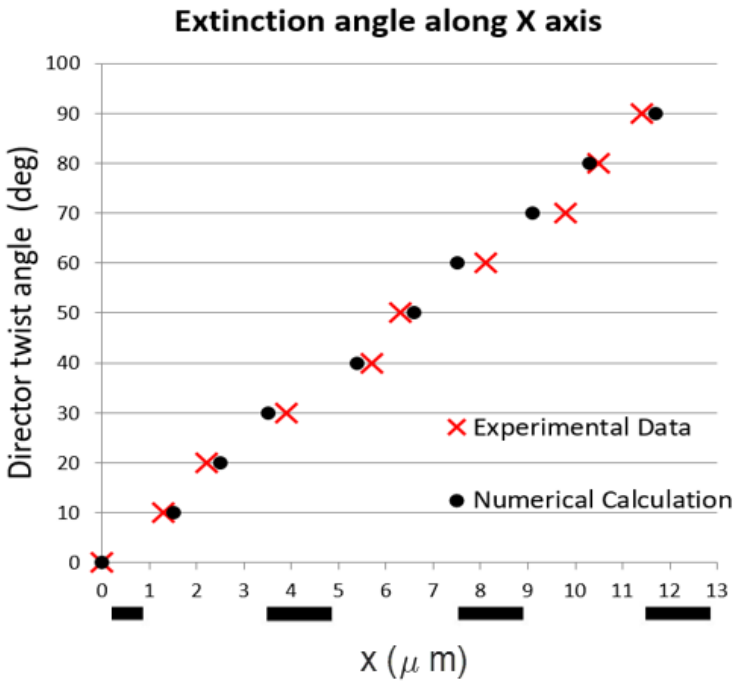

Figure 4.9 Graph of the extinction angle that shows the twist angle of the director along the x-axis for a half pitch.

4.4.3 Half-Wave Retarder Condition Along the Aperture

For the proposed FFS-PPD device to deflect light with high efficiency, the director needs to rotate linearly about the z-axis across the aperture. Figure. 4.9 shows

that this is indeed accomplished. But, we also need the device to be a half-wave retarder at each location in the aperture. To check to see if this second condition is met, we illuminate the device with circularly polarized light and measure the intensity of transmitted light using an analyzer that passes the same handedness of circularly polarized light. If the device is everywhere a half-wave retarder, the transmission through this set-up should be zero. And if the analyzer is changed to pass the opposite handedness of circularly polarized light, the transmission should be high and constant over the aperture. The latter is confirmed in Fig. 4.10

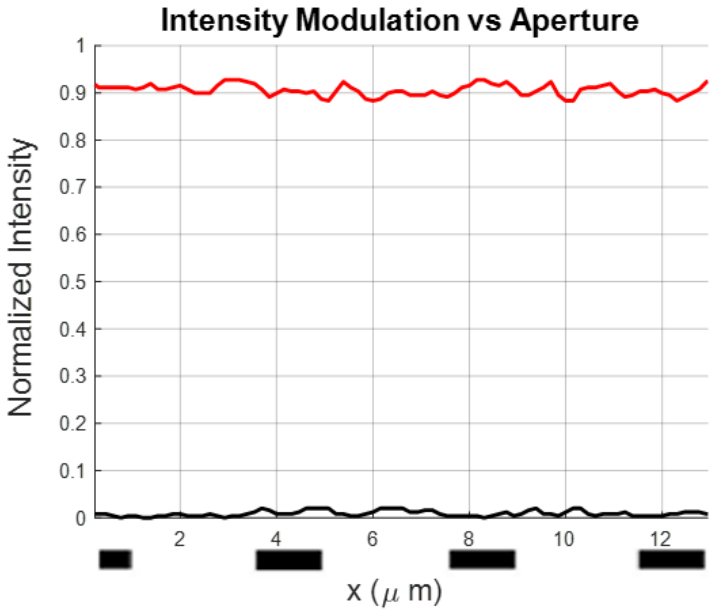

Figure 4.10 Normalized intensity of the transmitted circularly polarized light over one full pitch. Black lines show strip of electrodes corresponding to each graph

The data in this section confirm that the device meets the fundamental requirements for PPD beam steering with high steering efficiency. However, a device needs to be operated with several hundred electrodes to be able to cover a few millimeters of clear

aperture and to reduce the diffraction of light through a very small aperture. This will be the subject of a future paper. Although the final performance of the beam steering needs direct measurement from a large-aperture operating device, the preliminary test shown here proves the concept of the performance and brings confidence for a future large-aperture PPD.

CHAPTER 5 – ACHROMATIC LIMITS OF PANCHARATNAM PHASE LENS

5.1 INTRODUCTION

A particularly interesting application for PPDs is an optical lens made by modulating the Pancharatnam phase to provide an appropriate profile across an aperture. [32, 86-92]

A PPD lens is accomplished by fabricating a half-wave retarder that has its optics axis in the plane of the film while the azimuthal angle (β) ,is spatially varied along the radial direction forming concentric rings of constant β. The phase gained by circularly polarized light exiting a PPD is related to the angle β between the optic axis of the half-wave retarder with respect to a fixed lab axis by $\Gamma=2\beta$. A Pancharatnam lens can be fabricated by meeting the condition $\Gamma = \pi r^2/\lambda f$, which defines a parabolic phase profile for a lens with radius r (meter) and focal length f (meter) at a designed wavelength λ (meter). Combing these relations, the focal length of a PDD lens is given by:

$$\frac{1}{D} = f = \frac{\pi r^2}{2\lambda\beta(r)} \tag{5.1}$$

Where D is the power (diopter) of the lens and β (r) is the azimuthal angle (radian) defined above, along a lens radius of length r A lens fabricated in this way can changes its sign (e.g. from a 'positive' lens to a 'negative' lens) when the handedness of the input circularly polarized light is changed. Lens made with this method have many positive characteristics. They require a device thickness of only a few microns and this thickness is independent of aperture size. Additionally, they employ simple fabrication processes which can be easily extended to mass production. [93-95]

5.2 CHROMATICITY ISSUE OF PPL

Although Pancharatnam Phase devices introduce many unique advantages such as discussed in the previous sections, they are wavelength sensitive. While of exceptionally high efficiency when used with monochromatic light, there are two issues with polychromatic light. One is that a PPD device is designed to be a half-wave retarder for maximum efficiency at a particular wavelength, and the other is that the focal length of a PPD lens is wavelength dependent. (Equation 5.1)

The first issue, with the device not being a half-wave retarder for wavelengths other than that of the design wavelength, increases the intensity of light "leakage" that is not steered or focused by the PPD device and that exits with the same handedness of circular polarization as the input value. This problem has been addressed by utilizing a dual twist design [93, 96] . Also, the non-deflected light for lenses with f/# > f/2, the percentage of leakage light is small and can be blocked with a circular polarizer that has the opposite handedness as the input light. [27]

While viable solutions exist to solve or mitigate the chromaticity effects from the issue described above, the second issue of a wavelength-dependent focal length as given by Equation 5.1 is more problematic and is linked to the fundamental concept of the lens.

If a PPD lens is designed to have a focal length f_g for green light, then the focal length when illuminated with blue or red light is given by:

$$\boldsymbol{f_b} = \boldsymbol{f_g} * \left(\frac{\boldsymbol{\lambda_g}}{\boldsymbol{\lambda_b}}\right) \tag{5.2}$$

$$\boldsymbol{f_r} = \boldsymbol{f_g} * \left(\frac{\boldsymbol{\lambda_g}}{\boldsymbol{\lambda_r}}\right) \tag{5.3}$$

One way to conceptualize the effect of wavelength is to consider the spot size on the focal plane for the design wavelength (showing by line in Figure 5.1). For this simple example, the effect of diffraction is neglected. Consider that the focal distance of a PPD lens for green light is designed to be fg, and that we would like to know the spot size of light obtained for different wavelengths on the plane that is at a distance fg from the lens. If a diameter (L) is chosen for the lens, then the spot size on the plane at a distance fg from the lens can be calculated.

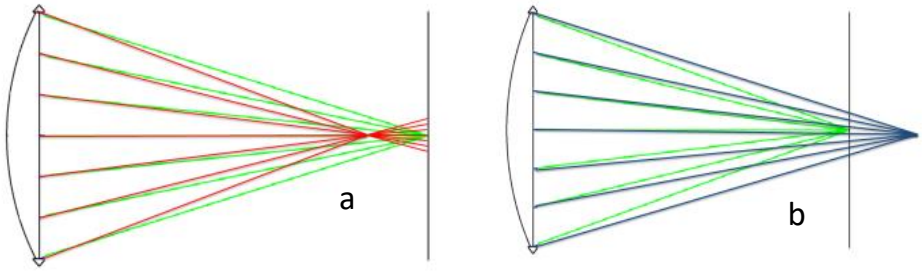

Figure 5.1. Schematic representation of the wavelength dependence of the focal length. a) green and red light focal lengths b) green and blue light focal lengths.

Figure 5.1 shows that red and blue light will focus at different points than the green light that the lens is designed for. It can be seen that the diameter of the wave-front at the distance fg from the lens is Sb for blue light and Sr for red light:

$$\boldsymbol{S_b = L * \frac{f_b - f_g}{f_b}} \tag{5.4}$$

$$\boldsymbol{S_r = L * \frac{f_r - f_g}{f_r}} \tag{5.5}$$

Using equation 5.2 (5.3),equation 5.4 (5.5) can be rewritten as:

$$\boldsymbol{S_b = L * \frac{\lambda_g - \lambda_b}{\lambda_g}} \tag{5.6}$$

$$\boldsymbol{S_r = L * \frac{\lambda_g - \lambda_r}{\lambda_r}} \quad (5.7)$$

These spot sizes are interestingly independent of the value of fg, but very dependent on the diameter of the lens as well as the difference between the design wavelength and the measurement wavelength

While Equations 5.2 and 5.3 as well as 5.6 and 5.7 demonstrate the basic problem when considering use of a PPD lens with a polychromatic source, it is expected that there are applications, possibly where the power and aperture of the PPD lens is small, that the chromatic effect may be acceptable.

The goal here is to provide insight into what the limits of the PDD lens power and aperture are for applications involving the human eye, and for camera type applications

5.3MODELING THE PROPAGATION OF LIGHT

Related to human perception, the optical system was modeled as shown in figure 5.2. In the test system the retina is modeled as a flat plane 20mm behind the eye. The eye is modeled as a 50 diopters lens with a parabolic phase profile and a 3mm aperture that will provide a diffraction limited spot on the retina for an object located at infinity. The PPD device is assumed to meet the condition provided in equation 5.1 which yields a parabolic phase profile. The spatial variation of the azimuthal angle of the optic axis ($\beta(r)$) is chosen to provide a power (Dg) of 0, 0.25, 0.5, 1.5, 2 , 4 and 10 diopters for λg which corresponds to green light. It is noted that the power will change for red and blue wavelengths such that $D_b = \frac{\lambda_b}{\lambda_g}$ Dg for blue light and $D_r = \frac{\lambda_r}{\lambda_g}$ Dg for red light.

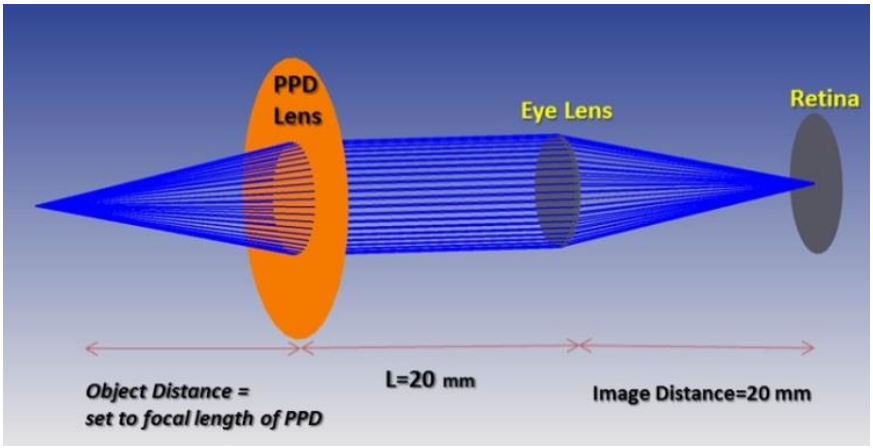

Figure 5.2 Schematic representation of the modeled system

In the case of green light, a point source on the image plane is expected to yield a diffraction limited spot on the image plane. Red and blue wavelengths are expected to yield a larger spot size since the focal length is wavelength dependent.

The spot size calculation utilizes scalar diffraction theory [15, 97-99] which is expressed by:

$$\boldsymbol{U'_{\mathrm{n}}(x,y) = \frac{z}{j\lambda}\frac{\int\int U_{\mathrm{n}}(\xi,\eta)(e^{jkr_{12}})}{r_{12}^2}\, d\xi d\eta} \tag{5.8}$$

In equation 5.8, λ represents the wavelength of incident light, z is the distance between the source plane and observation plane, r is the distance between a point (ξ , η) on the source plane and a point (x , y) on observation plane $r = \sqrt{z^2 + (x-\xi)^2 + (y-\eta)^2}$ and k is the wave number. In equation 5.8, Un is the complex electric field amplitude exits component “n” and Un' is the field from component “n” projection onto the entrance plane of component “n+1”. The output field U_{n+1} from component “n+1”, determined by $U_{n+1} = U'_n . e^{i\Gamma_{n+1}}$is the value of the input field (Un) to component “n+1” with the added spatially dependent phase term $\Gamma_{n+1}(\xi, n)$. This derivation is repeated until the scalar

amplitude of the field on the image plane is known. Finally, the light intensity at the image plane (point spread function PSF) is determined (Figure 5.3). The Modulation Transfer Function (MTF) can be then calculated by taking the Fourier transform of PSF (Figure 5.4). The calculation of equation 5.8 is done using a discrete Fourier transform method.

5.4 EVALUATION OF THE REQUIRED OPTICAL POWER BASED ON MTF

Using the above method to simulate the PSF and MTF, Figure 5.3 shows a representative result for the case of Dg=2 diopters for the λg = 540 nm; λb=460 nm, and λr =620nm in which case the distance of the image plane is fixed at the focal length for 540 nm light. . The results are shown in normalized curves due to the fact that the output of the calculation depends on the user defined input that can be adjusted arbitrarily.

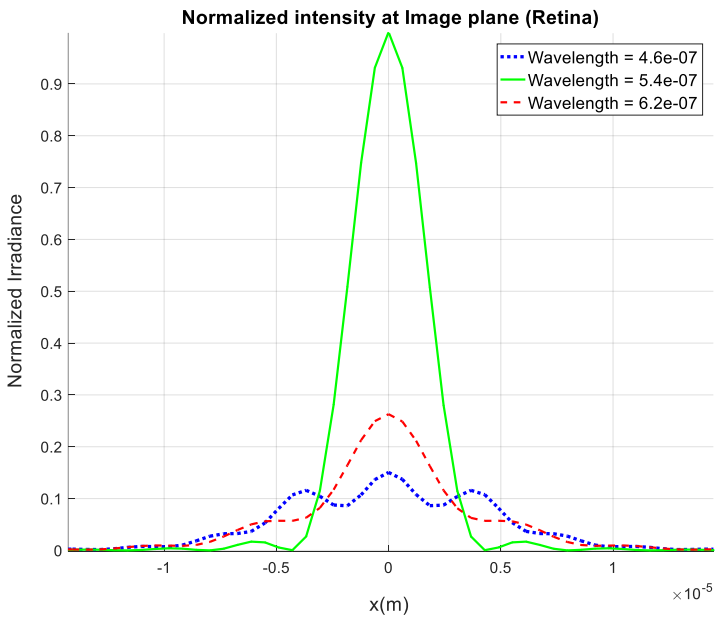

Figure 5.3 Normalized PSF for a 2D PPD devices at λb=460nm, λg= 540nm and λr =610 nm.

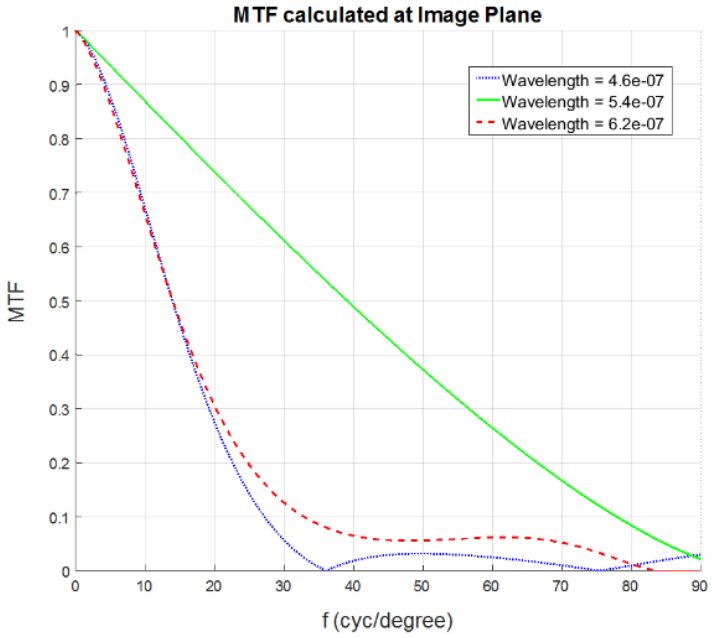

*Figure 5.*4 Normalized MTF for a 2D PPD devices at λb=460nm, λg= 540nm and λr =610 nm.

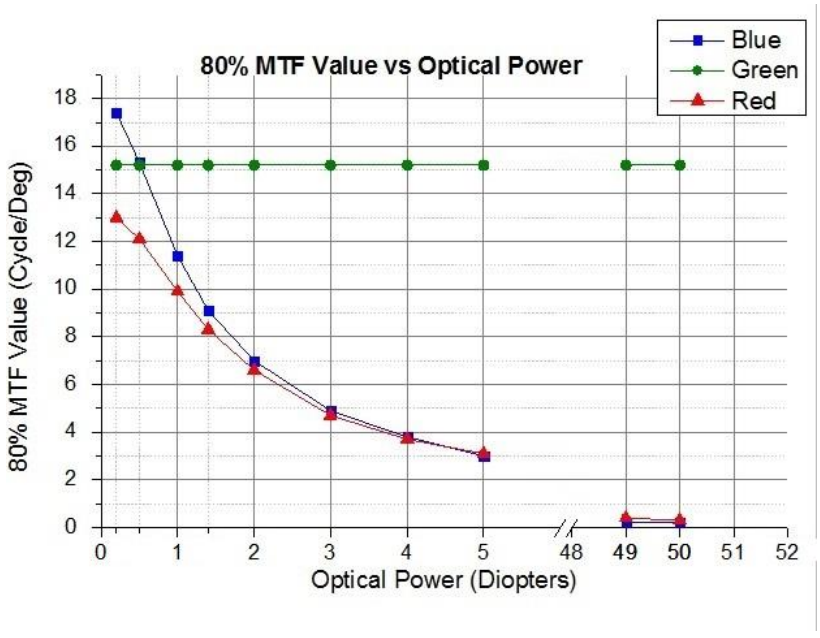

Figure 5.5 Graph of cycles/degree corresponding to an MTF value of 0.8 vs PPD lens power.

Note that a break is placed between 6 and 48 D on the x-axis for visualization purposes

Figure 5.5 summarizes the results of the calculations for other values of Dg, by plotting the cycle/degree value corresponding to an MTF value of 0.8.

It is reported that the resolution limit of the human eye is between 6 and 10 cycles/degree [100]. it can be inferred from figure 5.5 that PPD lens powers of less than 2 diopters have the potential for providing a level of image degradation that is not observable by the human eye. For a more intuitive interpretation of these numerical results, it is helpful to consider the case of white light comprised of three wavelengths across the visible spectrum: λ_b, λ_g and λ_r. For a particular PPD lens, the wavelengths will be focused at distances: fb, fg, and f_r, correspond to lens powers of 1/f_b (=D_b) ; 1/f_g (=D_g); and 1/f_r (=D_r). For lenses used in a human visual system, it is generally assumed that changes in lens power below value of DD_{max}=0.25 diopter are insignificant. Therefore, if the power of the PPD lens changes by less than DD_{max}, it will not be observable by the human eye. Explicitly, if:

$$D_g - D_b \leq DD_{max} \tag{5.9}$$

$$D_r - D_b \leq DD_{max} \tag{5.10}$$

Then the spectral components of the white light will appear in focus to the eye. Plugging Equation 2 (3) -- into Equation 9 (10) -- and solving for Dg yields:

$$D_g = \frac{DD_{max}}{1-\frac{\lambda_b}{\lambda_g}} \tag{5.11}$$

$$D_g = \frac{DD_{max}}{1-\frac{\lambda_r}{\lambda_g}} \tag{5.12}$$

Therefore, for given values of wavelength ratios and DD_{max} = 0.25, the limit on Dg for achromatic perception can be determined by using the smaller value from equation 5.12 and 5.13.

As a specific example consider that the wavelength for λb, λg and λr are as used in figures 5.3 and 5.4, and say that DDMax is 0.25 diopter. In this case λ_b/λ_g = 0.85 and λ_r/λ_g =1.15, and when both are plugged into equation 5.12, gives a maximum power of the lens for the design wavelength (λg) of 1.68 diopters.

To implement this lens, the spatial variation of the azimuthal angle of the optic axis (β(r)) is given by equation 1 in which the power of the lens can be related to the focal length as a function of wavelength, azimuthal angle (β) and radius (r).

As another example, the spot size for λ_r is considered when λ_g is in focus and compared to the model explained above. For this numerical evaluation, a glass lens paired with the PPD lens is considered. Therefore, when considering equation 5.4 and 5.5 as a predictor of the spot size, the focal length considered must be the effective focal length of the PPD lens and the glass lens ($1/f_E$ =1/f_PPD +1/f_ec) where f_E is the effective focal length, f_PPD is the PPD lens focal length and f_ecis the focal length of the glass lens considered that could be the eye lens or camera lens depend on the system. By plugging the calculated f_g into equation 5.2, the spot size for light of a wavelength different than the design wavelength can be obtained.

For the case above, it is found that the spot size for the red wavelength considered, is 17.3 μm. When this spot size and effective focal length are considered the

predicted 50% MTF is 10.3 (line pair)/(deg). The value predicted from the simple formulation, only differs slightly from the prediction of the model presented in figure 5.3. This result shows that the wavelength dependence of the focal length of a PPD lens is not significant as long as the power of the lens is less than 1.5-2 diopters. We have shown both by analytic and numerical calculations that the performance of PPD lens is suitable for use in applications with the human eye. Of course, this is only a guideline, with the actual value being dependent on user perception.

5.5 EFFECT OF POLYCHROMATIC LIGHT ON A PPD LENS

The use of a PPD lens with a camera is similar to use with the human eye but introduces variables such as adjustable aperture, varying pixel size, and varying lens quality. To keep the analysis general and applicable to a wide variety of camera systems, the approach taken here is to consider the effect on the depth of field (DOF) of the camera system. If a camera is focused at infinity and a PPD lens with a focal length of fg is placed in front of it, a green object at a distance fg from the PPD lens will appear in focus. However, for blue or red light the object distance to achieve sharp focus would be fb or fr respectively due to the wavelength dependence of the PPD lens focal length. If a white object was placed at distance fg, It would appear acceptably in focus if the DOF of the camera system is greater than the difference between fr and fb. This condition can be written explicitly as:

$$DOF@f_g > f_b - f_r = \frac{\frac{\lambda_g}{\lambda_b} - \frac{\lambda_g}{\lambda_r}}{D_g} \tag{5.13}$$

5.6 FABRICATION PROCESS

In this section we describe the fabrication process of Pancharatnam Phase Lens (PPL) shown in chapter 5. The fabrication was mostly based on experimental studies done by K.Gao [101]. The process consists of two main steps of photoalignment and polymerization. A comprehensive study by Wang and McGinty [102] has explored important factors to the photoalignment process such as humidity of the environment during the spin-coating process of Brillinat Yellow (BY) and Nitrogen flow during RM polymerization. [101].

For the fabrication of the lens, we have used a holographic setup based on Mach-Zender interferometer to create desired optical pattern and record the wavefront pattern of a "template" lens (TL) as a physical element on the BY coated substrate. The holographic setup is used to record the wavefront pattern of a "template" lens (TL) as a physical element is based on the modified Mach-Zehnder interferometer. This employs the idea of interference of a phase modified beam using a physical element (i.e. template lens in our case) with a reference beam. The interferometer separates a beam into two arms and recombine them after each pass through a different path in order to make the interference pattern.

A 547 nm laser was used to create a 3mm beam. A 10x beam expander is then used to expand the beam to 30mm. A very important factor here is to make sure that the beam is coherent and will stay the same size after propagating a large distance. For this purpose, mirrors can help us to expand the optical path to test and align the beam size. Then, the beam is getting polarized by passing through a linear polarizer. An additional test is to make sure the beam remains unchanged in XZ coordinates relative to the optical table. Next, a beam splitter separates the beam into two arms. Each beam gets circularly polarized using a quarter wave plate (QWP) with one of them being focused by a template lens (TL) while the other arm is maintained as reference. Because of an additional reflection from the second beam splitter, the two beams exit the second beam splitter (BS2) are orthogonally circular polarized. Both beams combine again at the location of the PPD and results in an interference pattern that is linearly polarized with its polarization axis being a function of the radial distance from the center of the pattern. The azodye Brilliant Yellow, coated on a glass substrate is placed in the location of PPD in Figure 5.6a, as close as possible to the beam combiner (BS2). Figure 5.6c shows the interference pattern from the setup captured by a CCD placed at the location of PPD. Figure 5.6d is the image of the actual 1.4 diopters lens while using a green color filter at front of it.

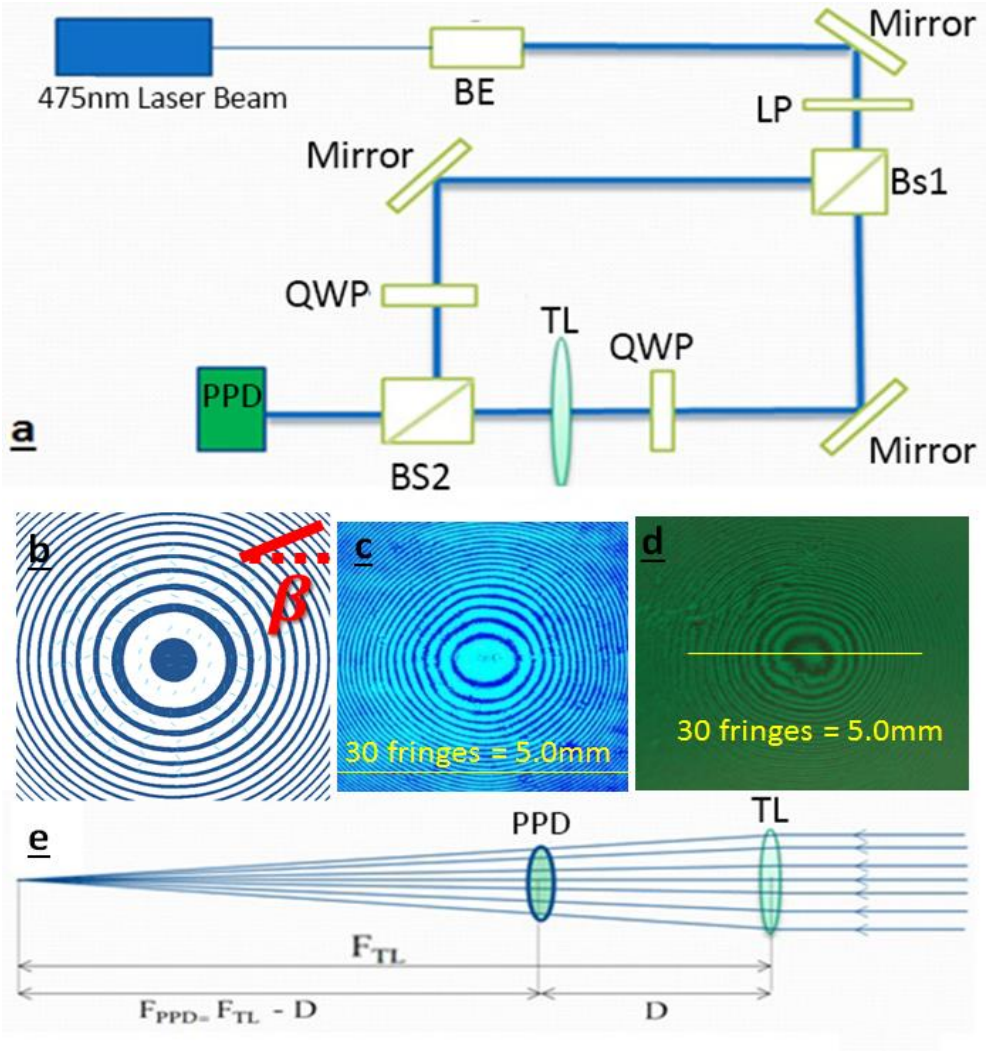

Figure 5.6 a) Shows the schematic of the interference hologram setup used to record the desired pattern on the substrate (PPD) where BE is beam expander, LP is linear polarizer, BS is beam splitter, QWP is quarter wave plate and TL is template lens.

b) shows the direction of polarization inside each circular ring and its radial dependence.

c) Interference pattern of the setup d) Picture of the actual 1.4 D lens, using the design wavelength color filter e) Schematic view of the template and the PPD lenses and their respective focal lengths

Knwoing the exposure wavelength λ_e and the design wavelength λ_d. the focal lens of the PPL can be calculated as:

$$f_{PPL} = f_d * \frac{\lambda_d}{\lambda_e} \quad (5.14)$$

The substrates is placed at the focal distance f_{PPL} from the template lens. The resulting aperture size was driven by the second beam splitter with 24mm*24mm width as:

$$d = \Delta * \frac{f_{PPL}}{f_t} \quad (5.15)$$

Where d is the lens diameter and Δ is the beam splitter size and f_t is the template lens's focal length.

As indicated in the figure 5.6 e, the designed focal length of the PPD will be shorter than the focal length of the template lens based on the distance of the two components so that $F_{PPD}=F_{TL} - D$ where FTL is the focal length of the template lens, FPPD is the focal lens of the PPD lens and D is the distance between the focal point of the template lens, and the PPD lens. During fabrication special care was taken to minimize this distance and keep the focal length of the PPD lens within 10% of the value of the template lens.

Prior to the sample preparation, the substrate was first cleaned and exposed to UV\ozone for 10 minutes. With ideally no break in between, the substrate was then coated with 1.5% BY dissolved in dimethylformamide (DMF) at 3000 rpm for 30s. 30 seconds of bake at 90C plate was followed to let the solution evaporate. A nitrogen flow was also used to control the humidity of the room and maintain it below 40% during the

coating process. The sample was then exposed for 10 minutes with a blue(λ=457nm) and the total power of the combined beam was 7 mW. It should be noted that the blue laser light used, would define the focal length of the PPD for blue wavelength of 475nm. The process is followed by a photo-polymerization of a reactive mesogen (RM). After the exposure, reactive mesogen (LC monomer), RM257 solution was spun coated at 200 rpm for 30s. Reactive mesogen (RM) solution contains 10% by weight RM dissolved in toluene plus photoinitiator irgacure with the amount of 5 % of RM weight. After spin coating the substrate is soft baked at 55 oC for 60 s and cured under nitrogen flow with 365 nm fluorescence UV light at an intensity of 3.5 mW/(cm^2) for 7 min. The RM coating step is repeated until the thickness of the film reached to half wavelength of the design wavelength (in this case, green wavelength).

5.7 CHARACTERIZATION RESULTS

As an example, If the power of the PPD lens is considered to be 1.4 diopters, then fb and fr are determined to be 0.84 m and 0.62 m respectively in order to allow all wavelengths to be in focus. This means that the DOF of the camera system at fg should be greater than 22 cm. To test this prediction experimentally, a 1.4D PPD lens was fabricated.

The setup used for evaluating the performance of the PPD lenses is shown in figure 5.7 . The lens evaluated was placed in front of a camera focused at infinity and the image quality was determined for varying object distance and F/#. Previously, it was

determined that the DOF of the camera system should be at least 22 cm to overcome the wavelength dependence of the PPD lens focal length.

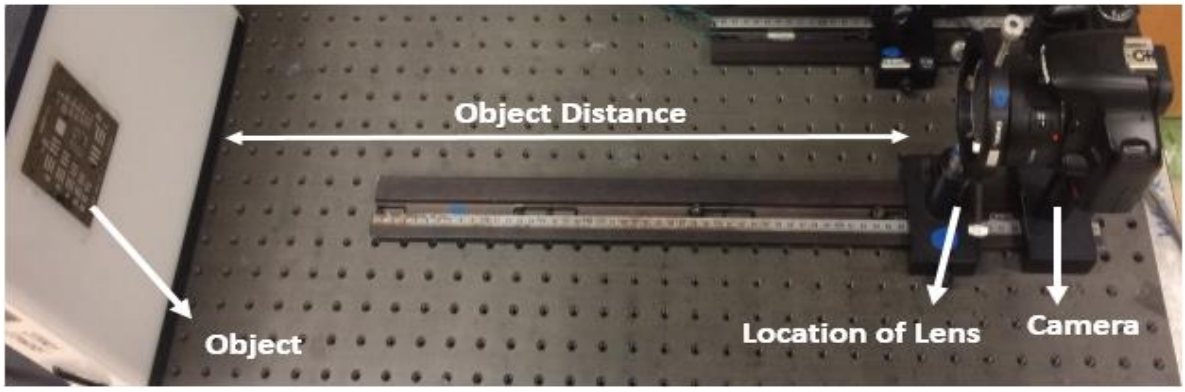

Figure 5.7 Shows an experimental set up to observe the effect of the DOF of the camera system to the detectability of chromatic problems with a 1.4 diopters PPD lens

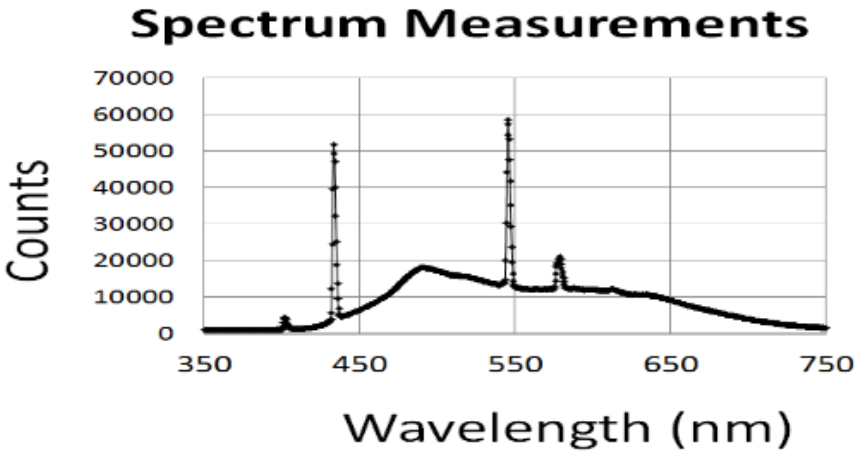

Figure5.8 The spectrum of the white light used in background .

Figure 5.9 shows a series of images taken with a 1.3D glass lens placed in front of the camera. The f-number was adjusted to be either f/4 or f/22 and the object distance that provided best focus was determined to be 82.5 cm. The object distance was changed from 74 to 96 cm to correspond to a DOF of 22 cm. Figure 5.9 shows that the DOF for f/22 appears to be at least 22 cm since the image remains focused as the object distance is changed. On the other hand images taken at f/4 are noticeably blurred over a 22 cm DOF.

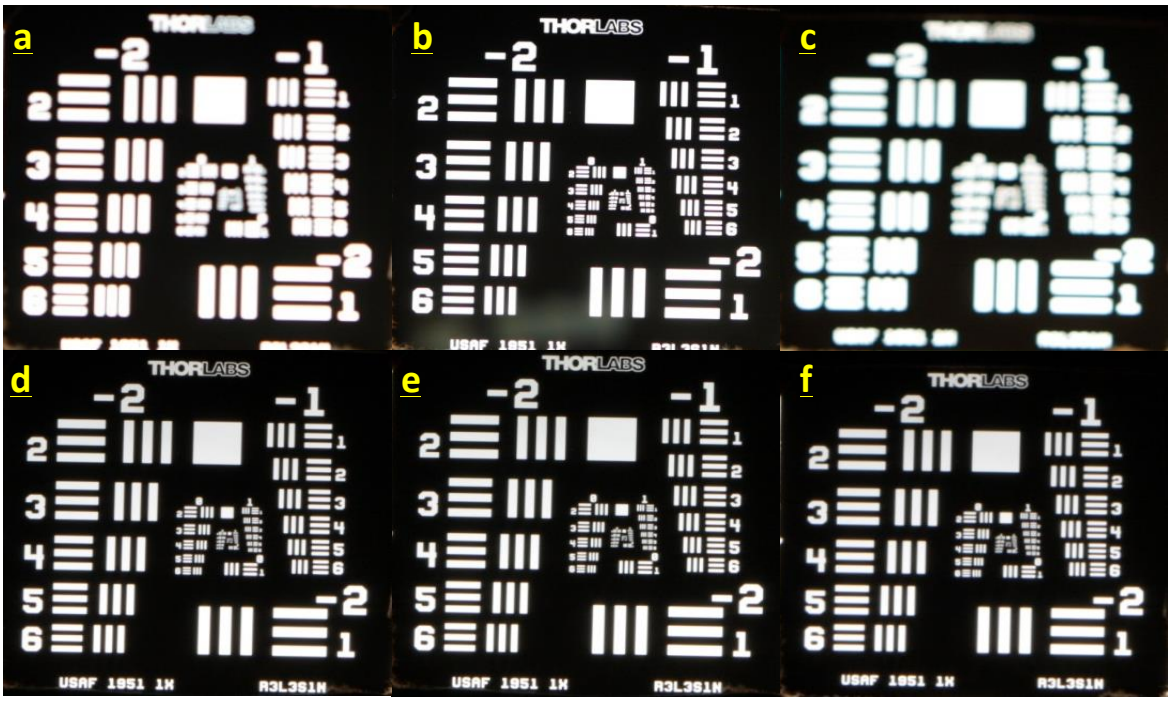

Figure 5.9 Pictures of images with a camera focused at infinity, and with a 1.3D glass lens. Figures (a) ,(b) and (c) are for the camera with f/4 setting, while figures (d), (e) and (f) are with f/22. (b)&(e) are with the object at the "best focus" distance of 82.5 cm. (a)&(d) are taken with the object at 74cm, while (c)&(f) are taken with the object at 96cm

Figure 5.10 and 5.11 show pictures taken at best focus for green light with the 1.3 D glass lens removed and the 1.4 D PPD lens put in place. Figure 5.10 shows PPD lens performance when the target was illuminated with white light. It can be seen in figure 5.10.d that some chromatic effects are seen when considering the f/22 image in the form of a blue shadow image. This is related to the first issue with the wavelength dependence of PPD lens that was discussed in the introduction, the effect of the device not being a half-wave retarder for blue light. This "leakage" light can be blocked by adding a second circular polarizer that has the opposite handedness of the input circular polarizer. Figures 5.10.b and 5.10.e show that including the 2nd polarizer noticeably reduce the chromatic effects. However, due to the smaller DOF the pictures images taken at f/4 still show some chromatic effects. For a more detailed analysis, figures 5.10.c and 5.10.f show the zoomed and cropped versions of the middle region from 5.10b and 5.10.e respectively. In order to examine this further, figure 5.11 shows a circular part of the resolution target with 2cm diameter that includes lines of group (-1) with elements 3-6 using blue(459nm), green(545nm) and red(610nm) color filters attached to the object which is placed at the best focus location for green light.

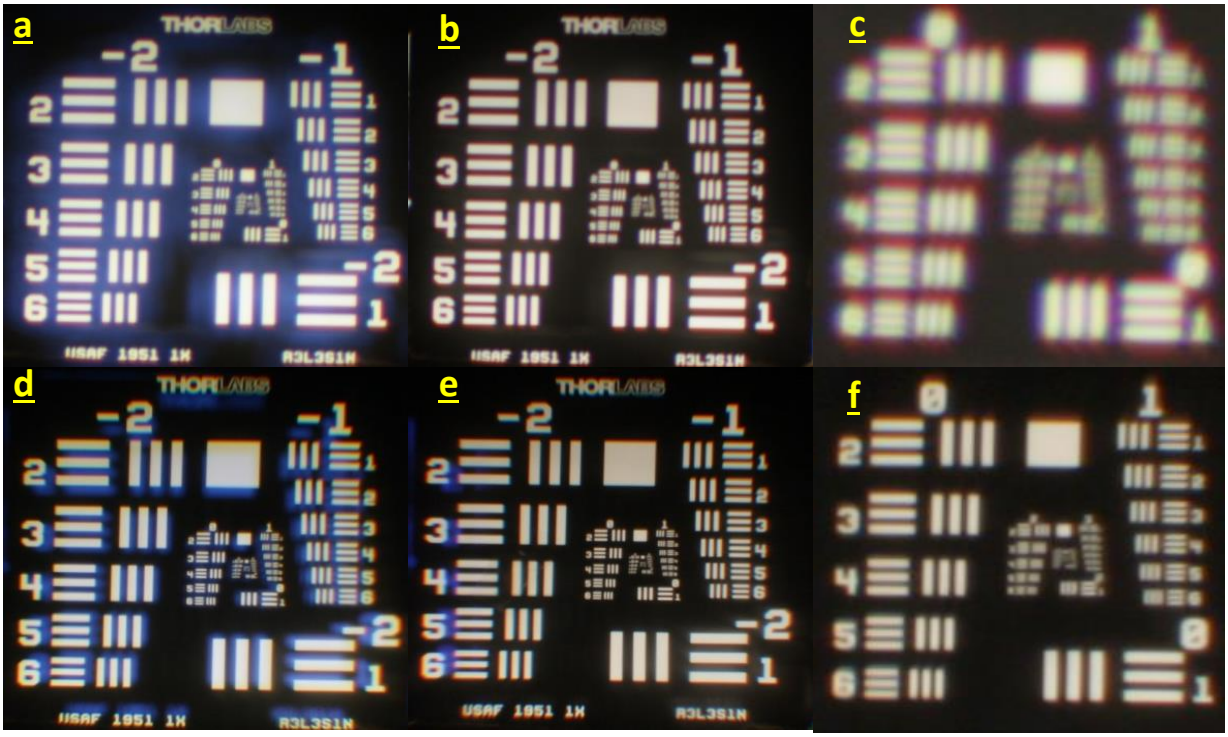

Figure 5.10 Pictures of image with PPD lens at the "best focus" distance of 71cm. (a)&(b) are taken with the camera setting of f/4, while (d)&(e) are taken with f/22, (a)&(d) are taken with a single circular polarizer, while (b)&(e) are taken with a circular polarizer on both sides of the PPD lens as explained in the text. (c) &(f) are just the middle region of the pictures (b)&(e), zoomed and cropped.

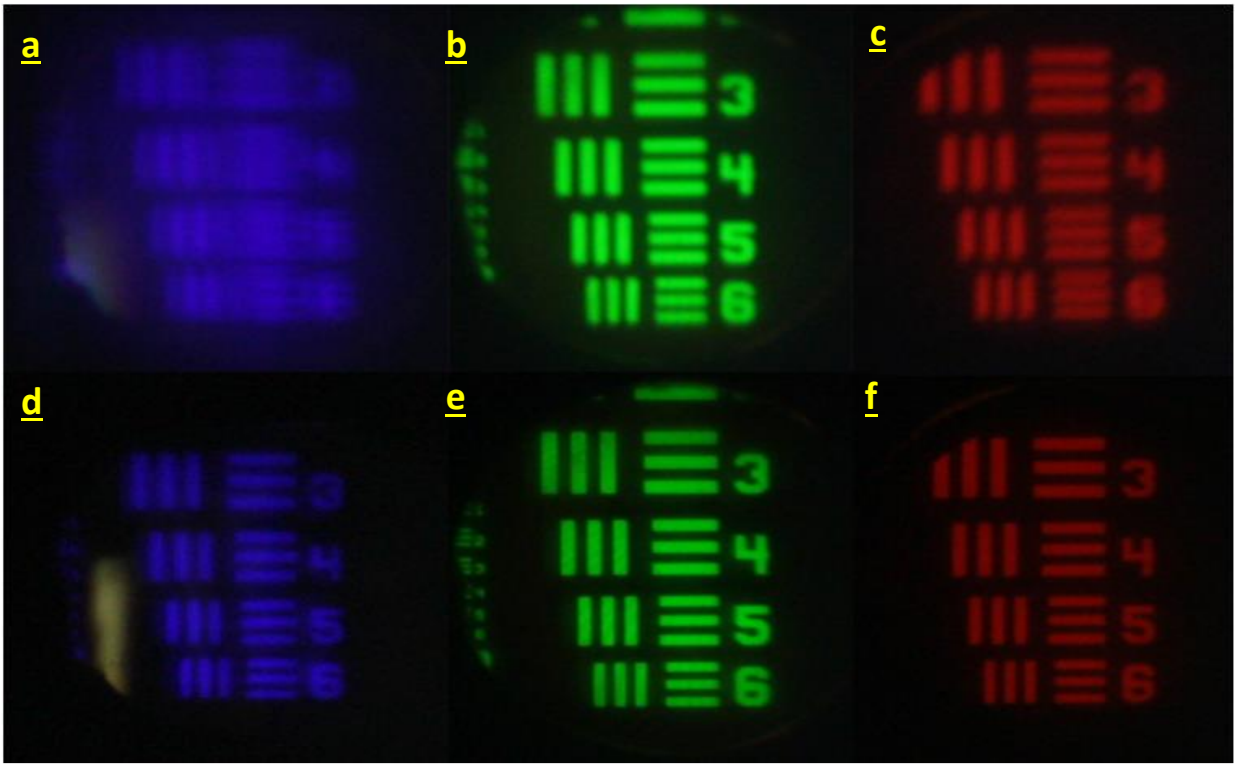

Figure 5.11 Pictures of the group (-1) elements using PPD lens with blue (left)(459nm), green (center)(545nm) and red (right) (610nm) color filters attached to the object and circular polarizer on both sides at the "best focus" distance of 71cm .(a),(b)&(c) are taken with f/4 and ¼ second exposure time while (d),(e)&(f) are taken with f/22 and 3 seconds exposure time.

5.8 MTF EVALUATION

As expected, the green light is fairly at focus for both f/4 and f/22 setting while the blue and red are not at focus for the case of f/4. These last two colors show large amount of haze when depth of field is small (f/4). However, in the case of illumination by blue and red light, the camera set at f/22 shows improved performance thanks to the large

DOF. This confirms that the DOF limit of Equation 5.13 can be used as a guideline to determine the limits of the PPD lens power and useable optical bandwidth.

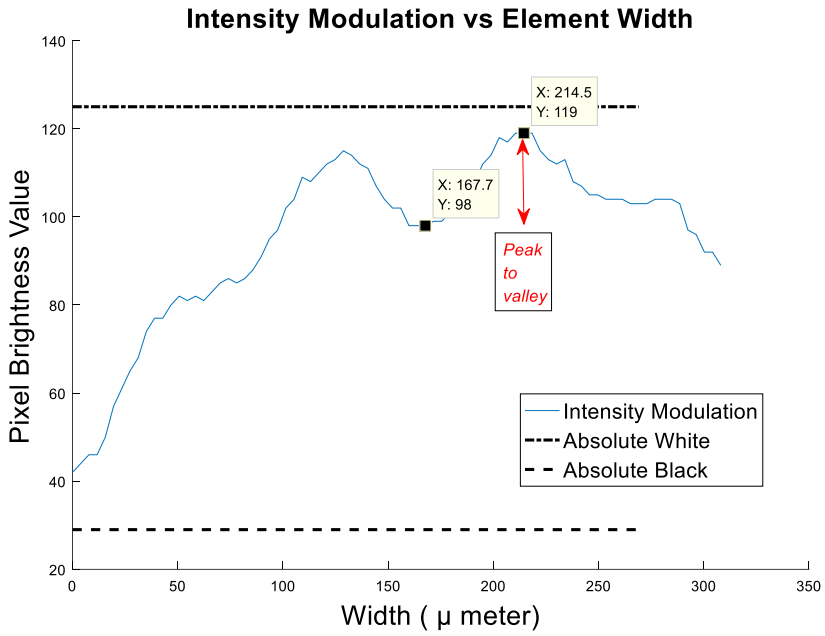

Figure 5.12 Intensity modulation of the element 3 of group (-1) in the figure 5.10.a for blue

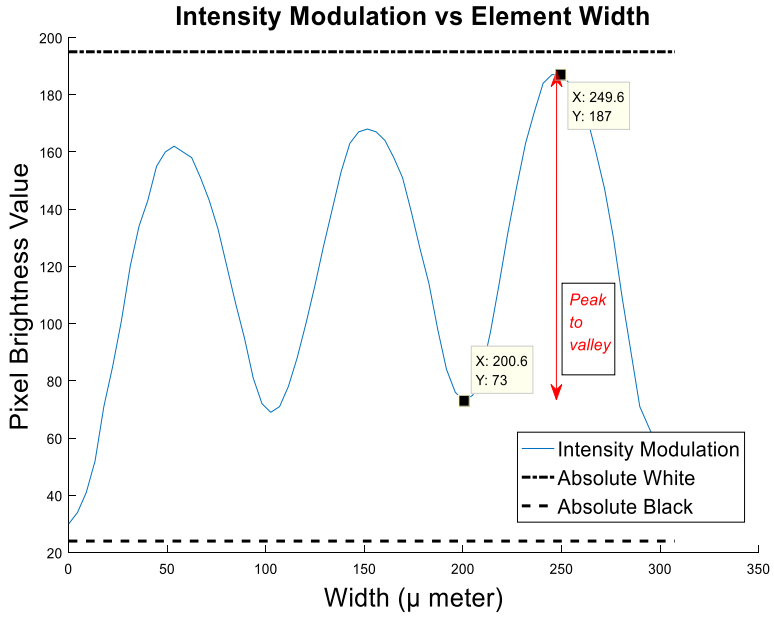

Figure 5.13 Intensity modulation of the element 3 of group (-1) in the figure 5.10.b for green

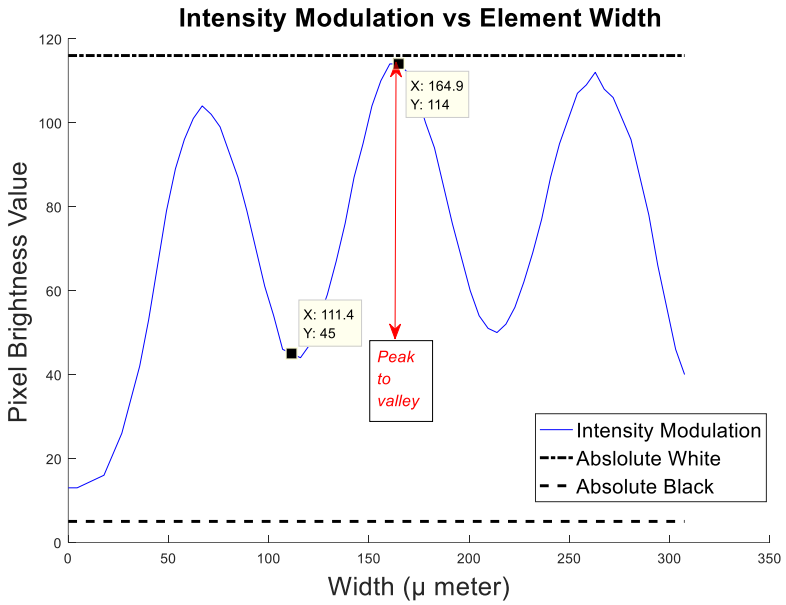

Figure 5.14 Intensity modulation of the element 3 of group (-1) in the figure 5.10.c for red

Knowing the pixel size of our camera and the USAF 1951 target resolution dimensions data, the magnification and corresponding spatial frequency value for each element of interest shown in the figure 5.11 was determined.

Using the modulation definition:

$$Modulation = (I\_\max - I\_\min)/(I\_\max + I\_\min) \tag{5.16}$$

where I_max& I_min are maximum and minimum m intensity near the bars respectively), the contrast from peak to valley difference was found as shown in figure 5.12 through 5.14. Then, the intensity is normalized to the absolute black and white values in the large areas nearby the group elements of interest. Next, the MTF values were determined for each element shown in figure 5.11. Figure 5.14 shows a sample of

the intensity modulation of the pixels from element 3 in the figure 5.11.c from which the MTF value was determined. In this particular case, the peak to valley amount was found 114-45=69 which resulted in contrast ratio of

(I_max-I_(min) / (I_max+I_min) = (114-45) / (114+45) = 0.434.

Then the contrast ratio was normalized with respect to the absolute values of the white and black (which was 116 & 9 respectively) pixels; the resulting MTF value for this example was determined to be 0.50. Using different color filters, this analysis was performed to the same element number for green (Figure 5.11.b) and blue light (Figure 5.11 a) and the resulted MTF values of 0.56 and 0.14 was found respectively (Figure 5.12 & 5.13). Furthermore, the results of the MTF of element 3 of Figure 5.11.c was compared with expectations from the "simple model" prediction of Equation 5.4 and 5.5 and from numerical calculations introduced in section 2A.

For the prediction of the "simple model", the value of L in Equation 5.4 (5.5) was determined to be 12.5 mm from the f/# of the camera setting (f/4) along with the 50 mm camera lens focal length. Using thin lens combination formula and the PPD lens design power of 1.4D, the spot size for the red light was found from equations 5.2 through 5.5 to be 0.097mm. This leads to an expected value of 5.1 lp/mm for a MTF value of 50%. For the prediction from a numerical calculation, the method described in section 2.A was used but with the "eye lens" replaced by the camera lens that has an aperture of 12.5 mm and a focal length of 50mm, and with the PPD lens having a power of 1.4D. In this way, the spatial frequency was determined to be 5.5lp/mm for a corresponding MTF of 50%

that agrees very closely with the “simple model” and validates the proposed design criteria.

The predictions from both approaches can be compared with the data shown in Figure 5.12 to 5.13, for the element group that has an MTF of 0.5 and a spatial frequency of 8.7 lp/mm. This comparison demonstrates that the proposed design criteria is quite useful.

CHAPTER 6 – PERFORMANCE EVALUATION OF A LIQUID CRYSTAL FRESNEL-SEGMENTED PHASE PROFILE LENS

6.1 INTRODUCTION

Human eye is a complex system capable of adopting to different environmental conditions as well as adjusting its lens to focus on different objects at different distances. In an ideal optical situation, all light rays coming from an object from which the eye is focused on, will experience same optical path difference (OPD) and will focus at a point on the retina. However, any deviation of wavefront from its ideal case could lead to optical aberrations. Various optical elements, such as optical lenses, are used to address these possible wavefront deviations by taking that effect into account and apply the same effect in reverse direction. Eyeglasses are a simple example of this.

Vergence angle is referred to the angle formed between the two eyes as gaze converges or diverges [ref to science direct]. Accordingly, Vergence distance is defined with respect to the gaze and is known as viewing distance (Figure 6.1). In everyday examples in real world, the vergence distance is coupled with the focal distance of the eye (also known as accommodation distance) which is dynamically changing for different objects. However, this could not be the case in some emerging applications such as head mounted displays (HMDs). Particularly, in virtual reality (VR) and augmented reality (AR) systems, these distances could be decoupled. In this case, accommodation distance is often fixed at the display location while the convergence distance is changing based on “apparent object” location. As a result, all objects at different locations looks focused despite our everyday

experience in real cases where everything pretty much looks blurry but the particular object that we are looking at. This issue is known as accommodation and convergence (AC) mismatch.

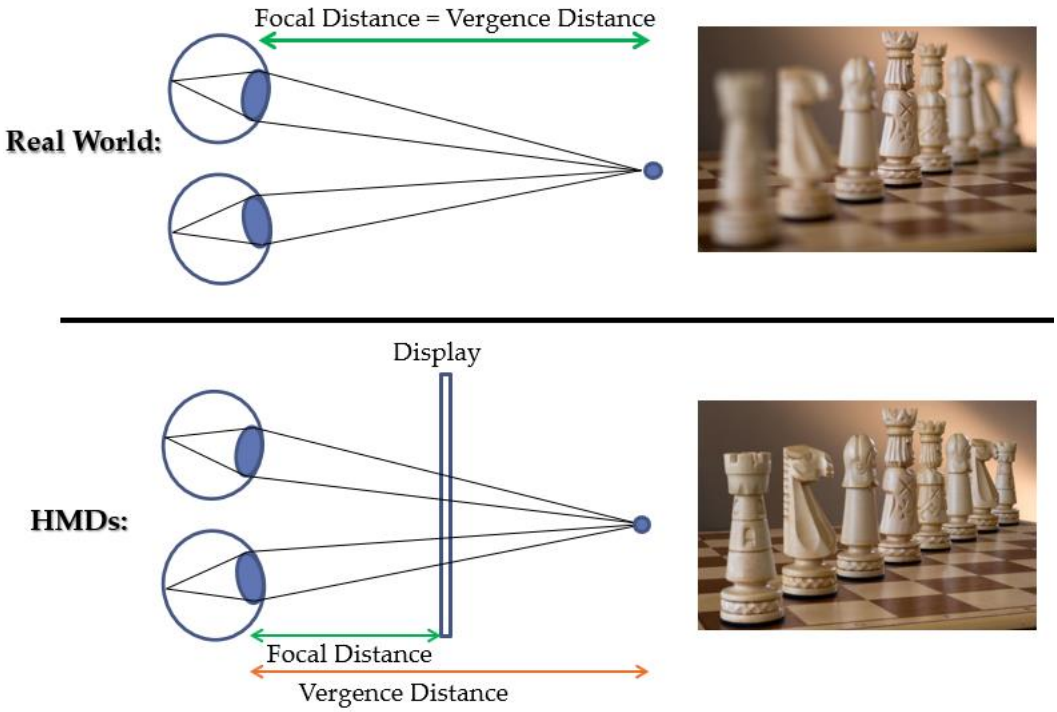

Figure 6.1 AC mismatch in HMDs vs real world comparison

Also, HMDs have additional feasibility requirements for their components due to their unique application. For example, these requirements impose some limitations in the optical components including lightweight, wide field of view, high image quality, adoptable depth of focus and fast response time. Mechanical objects, such as glass lenses, simply fail to meet one or more of these conditions. On the other hand, non-mechanical optical elements (e.g liquid crystal lens) can meet most of the above conditions with additional benefit of low operational voltage. Consequently, variant approaches such as

varifocal displays [103], multifocal displays (Volumetric displays) [104], light field displays [105] and holographic displays [106, 107] have been investigated to find a viable solution. Among these candidates, varifocal display which demands on adaptive optics to change focus so that it can track with the eye has attracted attentions. In a recent study, Kramida and Varshney explored advantages and disadvantages of each proposed solution [108]. The literature study concluded that eye-tracked varifocal optics with liquid crystal lenses have the highest potential for solving the AC problem.

Tunable liquid crystal lenses have been widely investigated in recent years [81]. Recently, Jamali.et.al [80, 106] demonstrated the significance of designing large aperture electronic lenses based on refractive Fresnel lens with Segmented Phase Profile (SPP) with excellent control over the phase profile of the light by using discrete ring electrode design. In addition to being eclectically switchable between different optical powers, the design allows for thin, fast and powerful liquid crystal device with low operational voltage. The goal is to create a parabolic spatial variation in the phase so that the transmitted light converges to the focal point defined by the optical power. The work represent design, fabrication and characterization of LC SPP lens of 20 mm in diameter and optical swing range of 0 to 1.5 D. A hybrid system was also proposed to further increase the optical power to about 2.5 D. As a continuation of that work, we will further investigate the lens performance by analyzing point spread function (PSF) and modulation transfer function (MTF). We will discuss a more careful characterization of SPP lens that had been designed for 10 mm radius with 4.5 Fresnel segments and we plan to stack 2 lenses in order to reduce the effect of viewing angle. We use test data derived

from a sample fabricated lens to measure PSF and MTF in order to quantify the lens performance. The results will be then compared with regards to simulated diffraction limit performance.

6.2 DESIGN SPECIFICATIONS

SPP lenses are a specific implementation of a GRIN (Gradient in the Index of refraction) lens [Hecht]. To make a spherical lens, the index must vary parabolically as a function of radial position:

$$n(r) = n_{center} - \frac{r^2}{2fd} \tag{6.1}$$

Where n(r) is the index at a radius, r, from the center, n_{center} is the index at the center of the lens, f is the focal length of the lens, and d is the thickness of the lens. Considering the Optical Path Difference (OPD) between two rays, one passing through the center and the other passing through the edge at radius r, as $OPD = \Delta n * d$, where $\Delta n = n(r_{center}) - n(r_{edge})$, the above equation could be reformed as:

$$OPD = \Delta n\, d = \frac{r^2}{2f} \tag{6.2}$$

or in terms of optical power, as:

$$D = \frac{1}{f} = \frac{2\,\Delta n\, d}{r^2} \tag{6.3}$$

The maximum power of a liquid crystal lens is then determined based on the maximum birefringence of the liquid crystal (Δn), cell gap (d), and radius (r). A quick estimate of the power of a lens with a 1cm radius, 10 um cell gap, and a birefringence of 0.2, we find

only a power of 0.04 diopters. To raise the power, we must either decrease the radius, increase the thickness, increase the birefringence, add Fresnel segments, or stack multiple lenses. Since larger area and thinner cell is desired for high field of view and fast response time respectively, adding more Fresnel segments are considered. Also the effective usable birefringence cannot be increased significantly with commercially available materials. So, we add Fresnel segments, where N_S is the number of segments. Then:

$$D = \frac{1}{f} = \frac{2\,\Delta n\, d\, N_S}{r^2} \tag{6.4}$$

Where OPD = N_W* λ, N_W is the number of waves change in optical path across the reset and λ is the wavelength. In the aforementioned work, it's shown that if the Fresnel segments are larger than 1mm, any diffraction will be less than 1 arcmin which is near the limit of detection of the human eye (based on green light at λ = 543.5nm). Considering that N_W is an integer number (i.e. there are integer number of waves at each reset), we'll get:

$$D = \frac{1}{f} = \frac{2\,N_L\,N_S\,N_W\,\lambda}{r^2} \tag{6.5}$$

Where N_L is the number of lens cells in the stack (in this case N_L=2), N_S is the number of Fresnel segments, and N_W is the number of waves change in optical path across each Fresnel reset.

Liquid crystal BDH 18349 with a birefringence of about 0.27 has been used. Due to switching limitation, we can approximately estimate that the effective birefringence would be ~80% of total value (i.e. $\Delta n \approx 0.216$). Knowing that OPD = $\Delta n\, d = N_w\, \lambda$, we

can see that for N_W values of 2, 3, and 5 waves, the corresponding cell gaps are roughly 5 um, 7.5 um, and 12.5um respectively. By adjusting the voltage applied, we can tune the lenses to the integer number of waves. Using the above equation, we can estimate the total lens power will be ±0.20, ±0.29, ±0.49 diopters for the respective cell gaps. If the cell gaps are not exactly the same, the final numbers could vary slightly.

6.3 CHARACTERIZATION METHOD

6.3.1 Voltage profile Tuning

To find the voltage profile, the first step is measuring transmission vs voltage (T-V) curve for a cell that is sandwiched between crossed polarizers at an 45 degree angle. From the T-V curve, the retardation vs voltage is then derived. Then, we calculate the desired phase on each bus line. The ITO is patterned such that each Fresnel zone has 64 rings. The area of each ring is the same, forcing the radial dimension of each ring to shrink parabolically as the distance from the center increases. This imposes our parabolic phase profile if we force the retardation to vary linearly across the rings:

$$\Gamma_n = \Gamma_0 - \Gamma_R F_n \tag{6.6}$$

where Γ_n is the retardation at the nth ring from the center (start counting from zero), Γ_0 is the retardation of the innermost ring of each Fresnel zone, Γ_R is the change in retardation across each Fresnel reset (if measured in number of waves it's equivalent to N_W in equation 6.5), and F_n is the numerical fraction of the position of the nth ring within the zone. Detailed explanation of the design and how the bus lines are connected to ITO rings are explained in [ref:afsoon dissretation].

In the second step, to account for real-world variables such as internal resitances,… a compensator cell is used while stacked with the lens cell with the rubbing direction perpendicular to that of the lens. While viewing through crossed polarizers in a microscope, when both cells have the same value of retardation the image should appear dark because the retardation of one cell will cancel the retardation of the other. The estimated voltages of a particular lens from the first step is then applied to the cell. The compensator is derived with a proper voltage equal to the bus line that we desire to tune. The compensator in this step acts as a simple electronically controlled birefringence (ECB) cell. The rings that correspond to that particular bus line should be appeared dark under cross polarized microscope. The voltage could be adjusted for each bus line to make sure the corresponding rings appear dark.

Finally, the cell is tuned using 'macro' image to see the whole phase profile in the third step. Using green light at 543 nm, we place the lens cell between parallel polarizers oriented parallel to the rubbing direction of the lens. We use a DSLR camera with a 100mm macro lens focused on the cell to take a photograph. As shown in figure 6.2, four dark rings are distinguished in each zone representing the number of retardation waves for this particular lens. Having two lenes in stack with 4.5 zones that each contains 4 waves, the estimated power of ~0.4D is calculated based on equation 6.5.

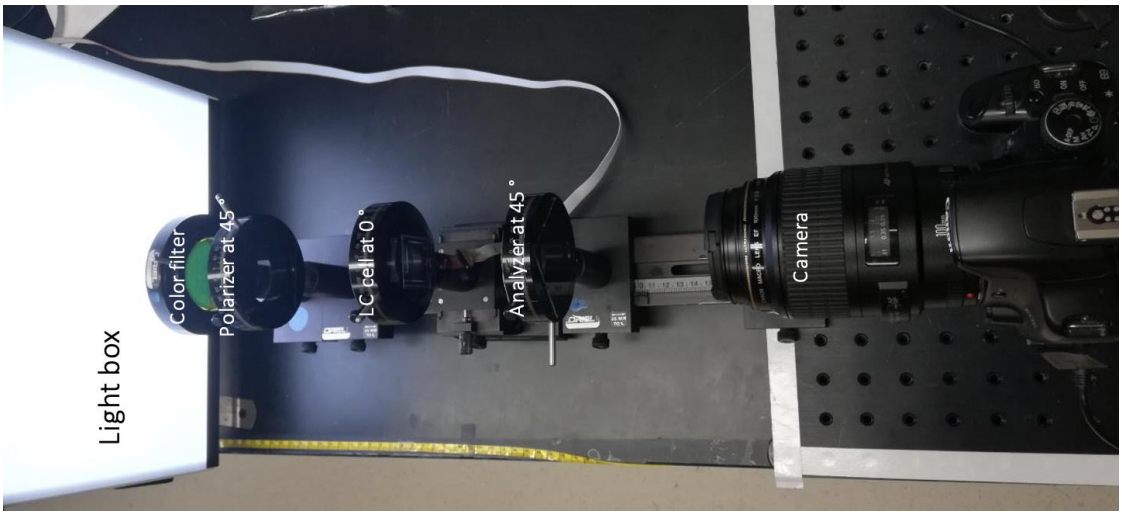

Figure 6.2 setup for phase profile measurement

Then, intensity of cross-section of the phase profile is calculated from the picture and is compared to the ideal curve. Figure 6.3 shows a sample of phase profile for a chromatic light with 4 waves in each zone.

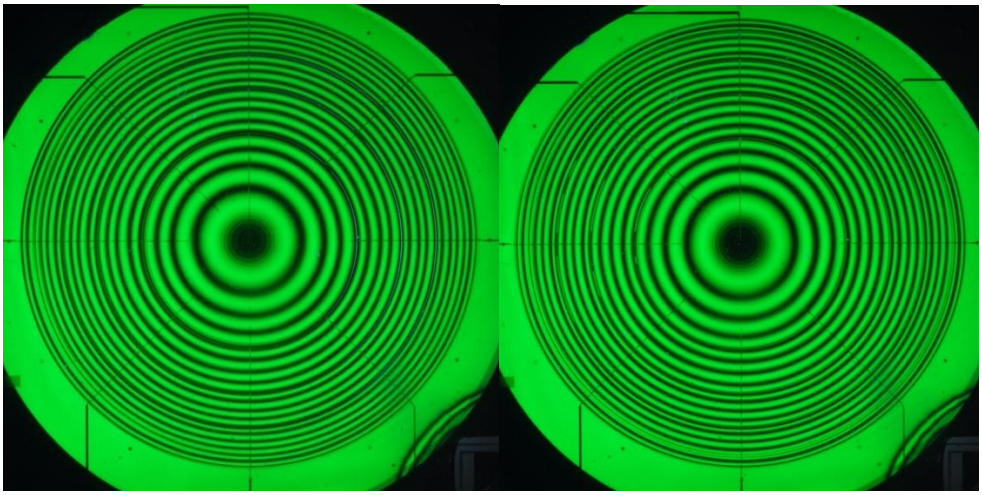

Figure 6.3 Left: positive phase profile . Right: Negative phase profile.

The ideal intensity curve is simulated knowing the supposed phase retardation over the entire cell width. For each pixel of the image, the retardation is calculated based on the

coordination of the pixel (i.e. its relative position to the center), the number of retardation in each zone as well as number of resets. From the retardation matrix, the intensity profile is calculated considering parallel polarizers:

$$I(x) = 1 - \sin\left(2\pi * \frac{\Gamma}{2}\right)^2 \tag{6.7}$$

Figure 6.4 shows sample of ideal phase profiles for both positive (converging) profile and negative (diverging) lens from which the intensity modulation was acquired. The phase profiles shows 4.5 reset along the aperture and 4 waves retardation amplitude.

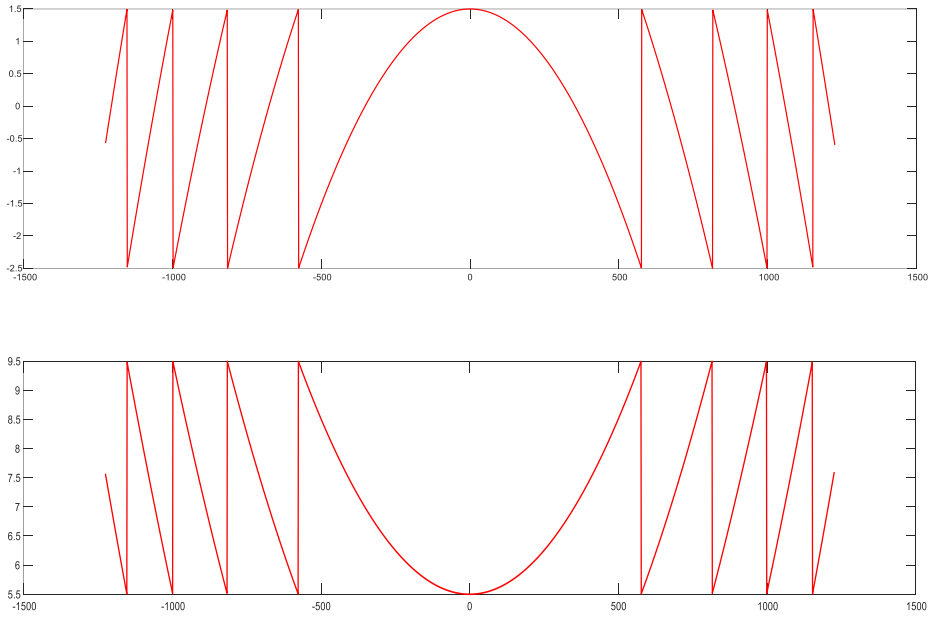

Figure 6.4 Top: Ideal positive phase profile . Bottom: Ideal negative phase profile

Figure 6.5 shows the intensity of the light derived from both experimental picture and the simulation method. Blue lines are the data derived from figure 6.3 and the red lines are ideal intensity data derived from simulated phase profiles in graph 6.4.

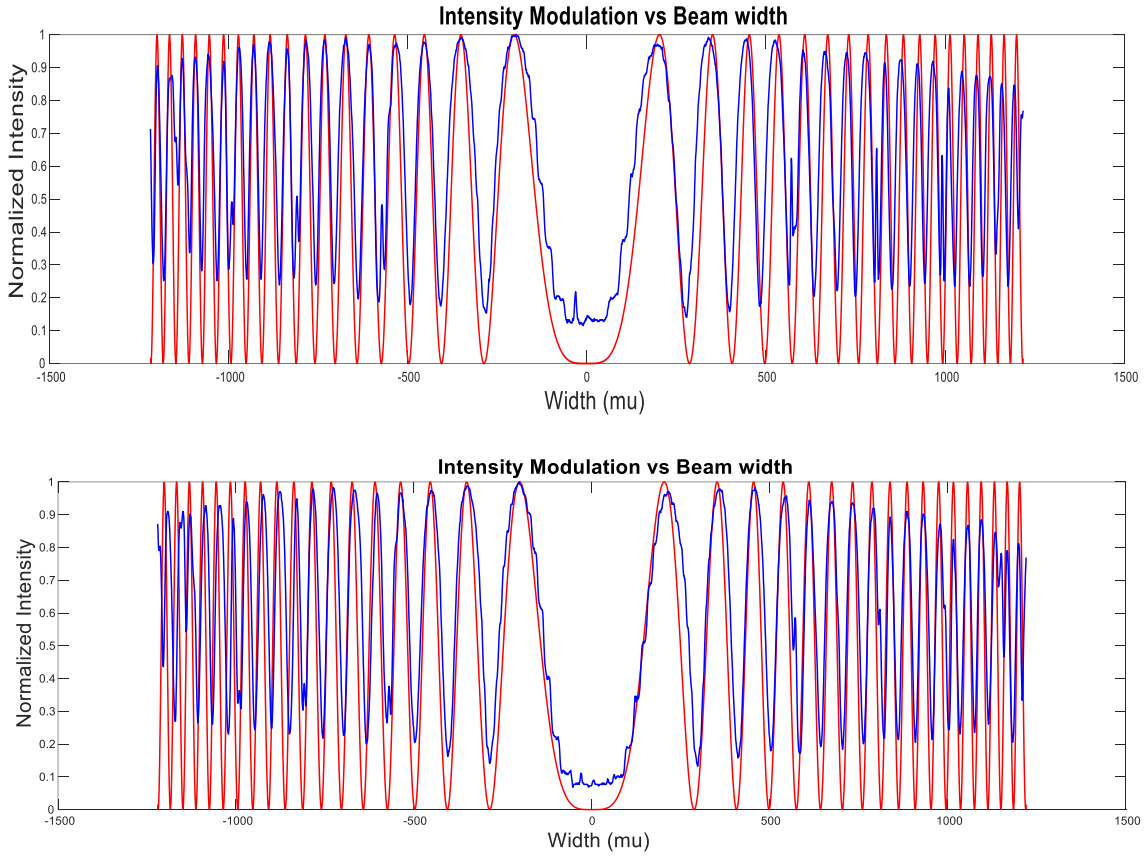

Figure 6.5 Top. Intensity data for positive phase profile of the lens corresponding to figure 6.3 (left) and 6.4 (top). Bottom. Intensity data for negative phase profile of the lens corresponding to figure 6.3 (right) and 6.4 (bottom).

6.3.2 PSF measurement

The point spread function of each cell as well as the stacked lenses was measured using the setup shown in Figure 6.6. A green laser (0.543μm) light shines the light into a beam

expander. The light will then become polarized and the intensity will be attenuated using a ND filter. At about 1.5m distant, a 5mm aperture cut the light and 1 diopter lens is used to shorten the measurement distances. When LC is off with no voltage, the point spread function was measured for reference. Then PSF from center and edges of the lens was measured using both positive and negative voltage profiles.

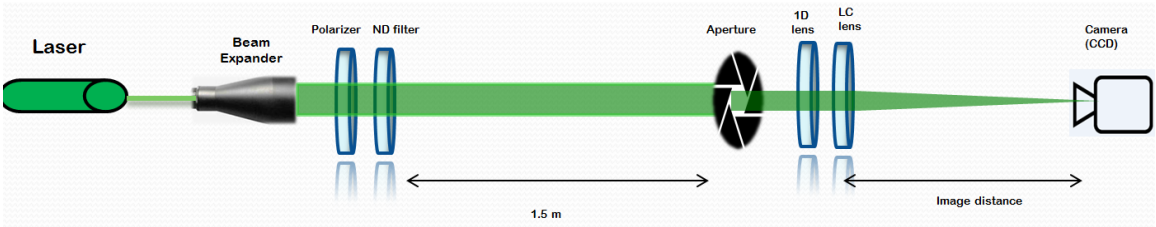

Figure 6.6 PSF measurement setup

The following graph [Hetch] shows airy pattern resulted from Fraunhofer diffraction at a circular aperture where the location of the first minimum is determined as:

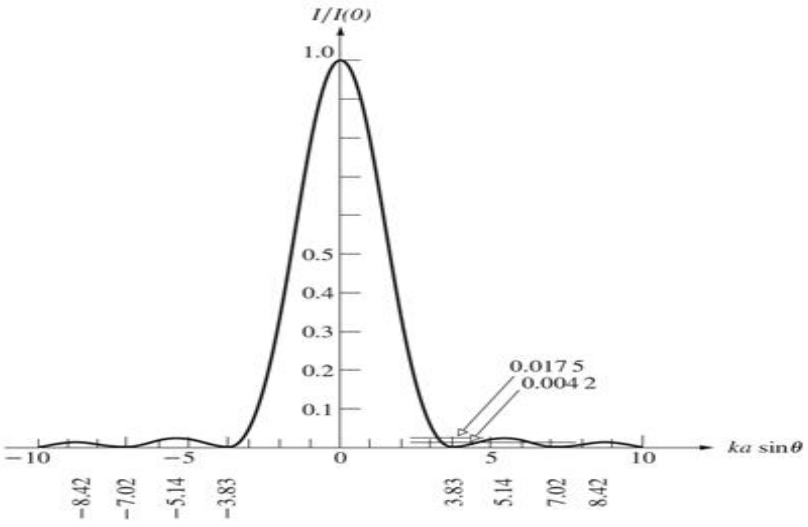

Figure 6.7 Fraunhofer diffraction limit (Airy pattern) resulted from a circular aperture.

$$x = 1.22\, f\, \frac{\lambda}{D} \tag{6.8}$$

When LC lens is off, we only have glass lens and a D=5 mm aperture. The focal plane for our glass lens has found to be 101cm which corresponds to about 0.99D. The LC lens power was also adjusted to have 0.49D for this measurement. Since we have a combination of two lenses in this case, we use thin lens approximation to find the "back focal length" which is defined to be the distance between the 2nd lens (LC lens in our case) to the focal plane (camera's sensor location) :

$$f_{bl} = \frac{f_2 * (d - f_1)}{d - (f_1 + f_2)} \tag{6.9}$$

Where d=7cm is the distance between the lenses. For the negative power lens, $f_{bfl\ is:}$

$$f_{bl} = \frac{-2 * (0.07 - 1.01)}{0.07 - (1.01 + (-2))} = 1.773\ m \tag{6.10}$$

And for the positive lens, it becomes:

$$f_{bl} = \frac{2 * (0.07 - 1.01)}{0.07 - (1.01 + (2))} = 0.639\ m \tag{6.11}$$

The theoretical location of the first minimum of airy pattern is then calculated as:

$$x_{theoretical} = 1.22 * \frac{1773mm * 0.000543\ mm}{5mm} = 235\ \mu m \tag{6.12}$$

And

$$x_{theoretical} = 1.22 * \frac{639mm * 0.000543\ mm}{5mm} = 85\ \mu m \tag{6.13}$$

For the negative and positive powers, respectively.

Pictures were taken from the above optical setup for each case of negative and positive lens powers. The images were then imported to Matlab to calculate the pixel by pixel intensity variations along a line that passes through the center of the PSF spot. One important factor is to adjust exposure setting of the camera to make sure the image intensity is not saturated in any pixel of the image so that we can normalize the intensity to the maximum value.

Also, PSF function of an "ideal" lens setup was calculated in a way similar to the modeling method described in section 5.3 using the glass lens power and the LC lens power. Figure 6.8 shows both the experimental intensity of the focused light beam (blue curve) passing through the center of the lens and the diffraction limited PSF found by simulation (dashed black curve) for both negative and positive phase profiles.

Both graphs shows an excellent overlap of the experimental data over the simulation curve. The sources of error for measured data could be any small deviation of aperture size from the expected value, voltage profile of the lens, not having a perfectly collimated light or finding the exact distance where the image is at its best focus.

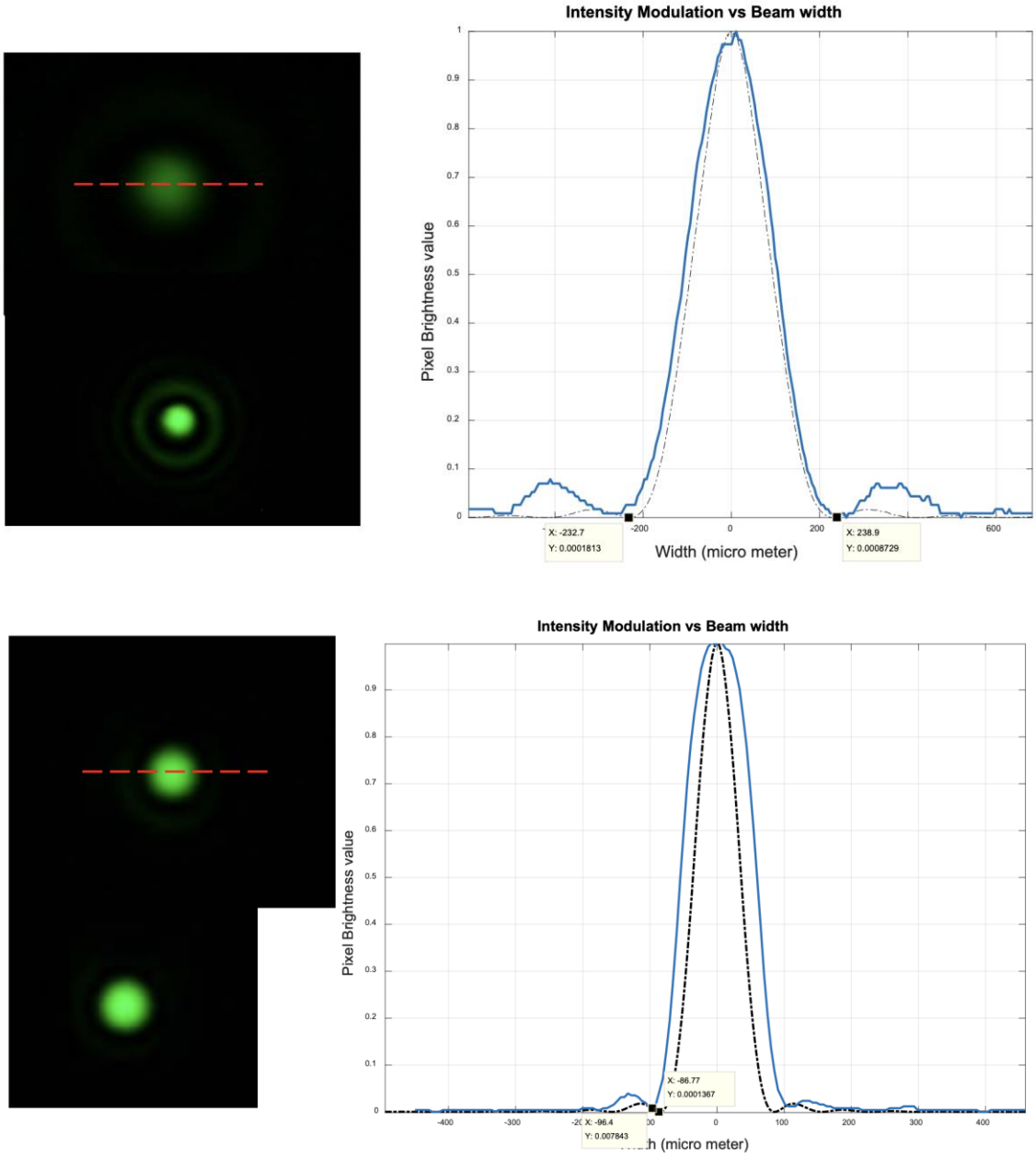

Figure 6.8 Top: PSF function of the negative lens calculated from the picture shown on the left side compared to theoretical limits. Bottom: PSF function of the positive lens corresponds to the picture shown on the left side. Dashed red line shows the path along which the intensity graph was determined.

Similarly, the PSF was measured and compared for the beam that pass through the most outer edge of the lens (i.e. the beam is tangential to the outer ring of the lens). As described in [afsoon 110issertation], following shape is expected for the PSF in this case. Figure 6.9 shows the graphs of PSF for both negative and positive lens powers,

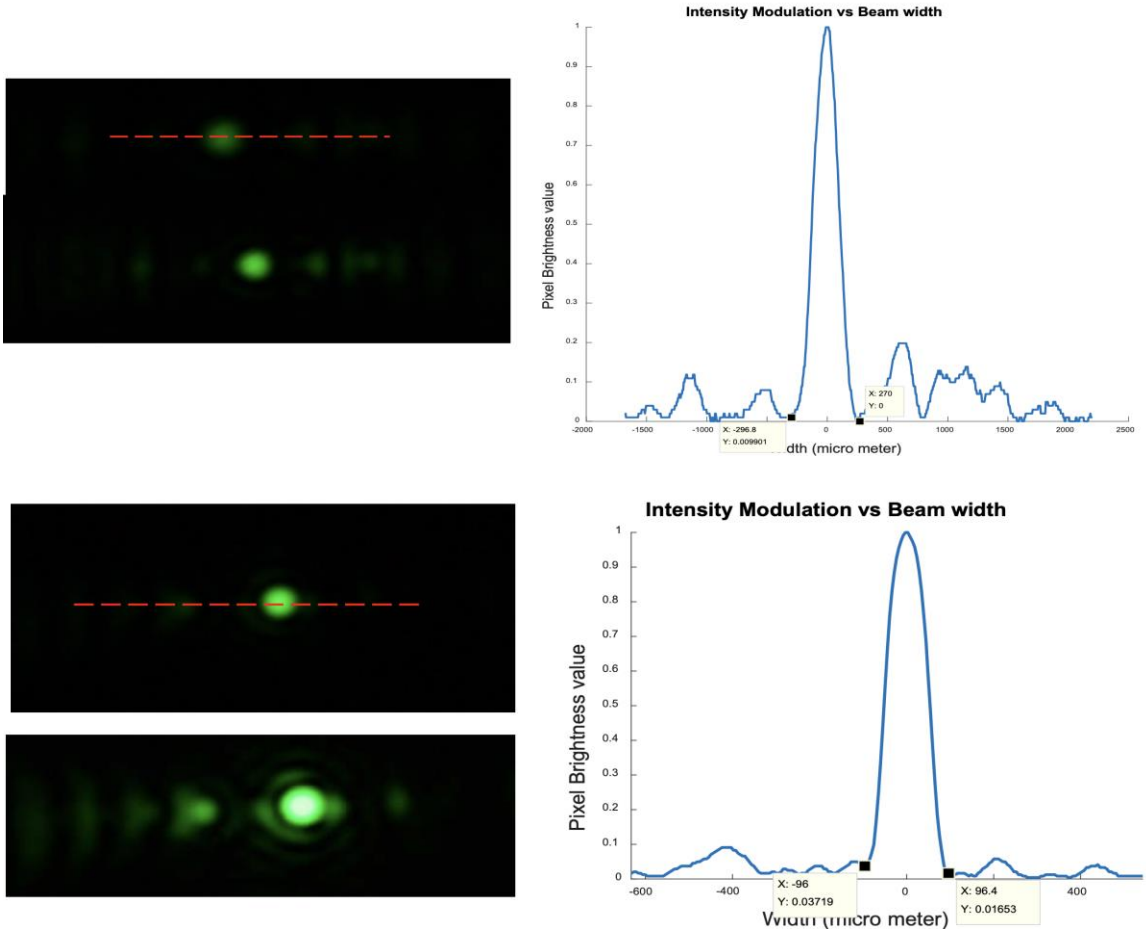

Figure 6.9 Top: PSF function for the edge of the negative lens. Bottom: PSF function for the edge of the positive lens Again the PSF images corresponding to each case is shown on the left side. Dashed red line shows the path along which the intensity graph was determined. For each of the above cases, a saturated brighter version of the PSF image is also shown for better illustration of the PSF shape.

6.3.3 MTF measurement

In order to analyze the optical performance of the LC lenses, we've calculated MTF function for both center and edge of a 0.4D lens which is practically consist a pair of LC cells. The test was done for both on-axis and off-axis incoming light at different angles. 1951 USAF resolution target with known data was used as the reference object. We have used Canon 450D camera to take the pictures.

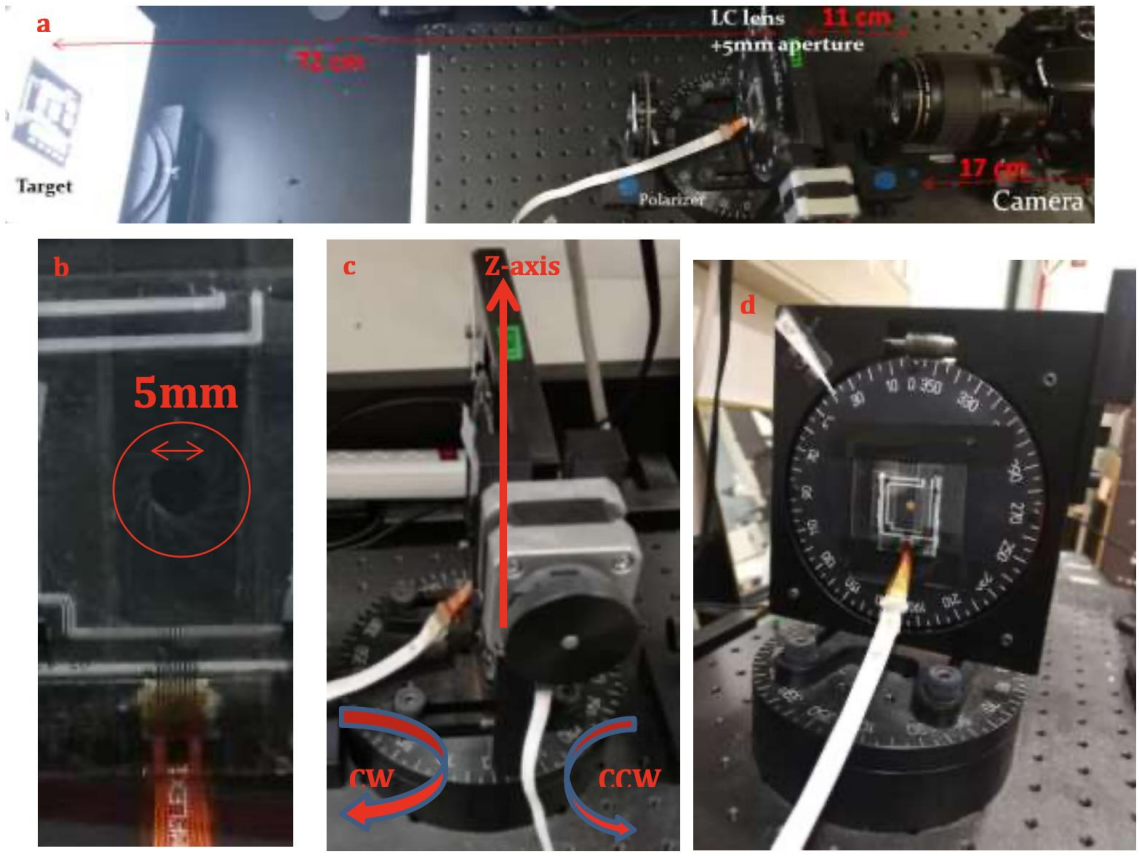

Figure 6.10 a) optical setup b) LC lens and 5 mm aperture mounted on rotation mount c&d) rotational mount

Since we know the spatial frequency data for each element of the target, we've chose element 6 from group 0. The corresponding spatial frequency was found to be 1.78 lp/mm according to the data table of the 1951 USAF target.

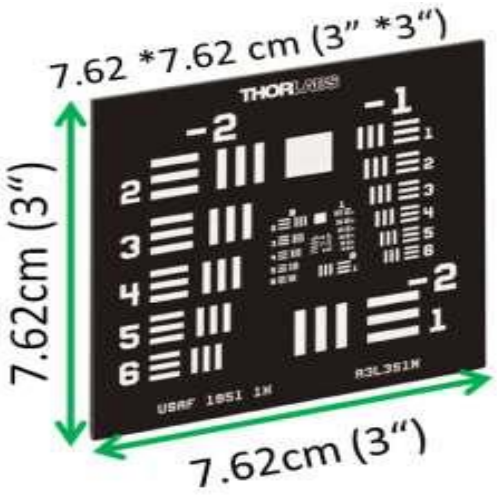

Figure 6.11 1951 USAF resolution target dimension

In order to convert that data to lp/degree, we need to use the distance from the target to the lens. Since the camera lens is made up of a complex lens system, an approximation was made for the distance from target to the camera lens to be (d=90cm).

Therefore, we can estimate the spatial frequency of the image as :

$$f_{\frac{lp}{deg}} = f_{\frac{lp}{mm}} * d * \frac{\pi}{180} = 1.78 \frac{lp}{mm} * 900\ mm * \frac{\pi}{180} \cong 28 \frac{lp}{deg} \qquad (6.14)$$

This value is close to the resolution of the human eye which is about 30 lp/degree .

As explained in section 5.8, contrast ratio is synonymous with modulation transfer function, and is most commonly defined as:

$$contrast\ ratio = Modulation\ Transfer\ Function = \frac{I_{\max} - I_{\min}}{I_{\max} + I_{\min}} \qquad (6.15)$$

Here I_{max} and I_{min} are the maximum and minimum intensity curve in the image respectively. In order to take the pictures, Camera was first focused at the target with no voltage on LC lens (off). Then , LC lens was turned on with positive power (i.e. the total power of the system has then changed). Then, Camera was then adjusted to focus again at the target with LC lens on. Data was taken for center of the cell at positive power for different angles. Then, the pictures were imported into Matlab in order to measure the intensity modulation of the picture of the bars. Intensity values were taken from Green channel of the RGB image data.

Knowing the corresponding spatial frequency of the target, a plot of intensity modulation vs pixels over a line that crosses the bars (red line shown in Figure 6.12) was derived from which we can estimate the MTF value from the equation 6.15. Figure 6.12 shows the image and the intensity plot for element 6 –group 0 for the case where the LC lens is off with no voltage.

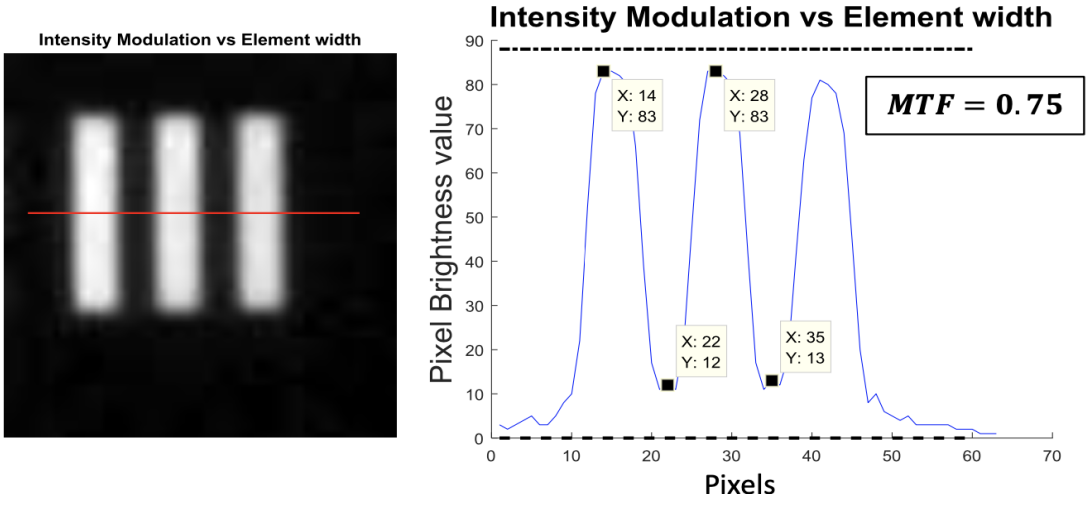

Figure 6.12 Image of the bars from group 0 – element 6 of the resolution target with LC lens in off status and the corresponding intensity modulation graph

according to the equation 6.15, an MTF value of 0.75 was estimated using $I_{\max}$ = 83 and I_{min} = 12 from plot in figure 6.12.

This value, that is shown with blue plus sign in figure 6.13, is very close to the simulation result of the diffraction limited value, calculated for an Ideal lens system. Simulation was made using the numerical Matlab algorithm based on Rayleigh-Sommerfeld scalar diffraction theory that is previously described in section 5.3. When LC lens is off, data points found from our calculation and the simulation of the ideal case match pretty exactly which validates our experimental approach.

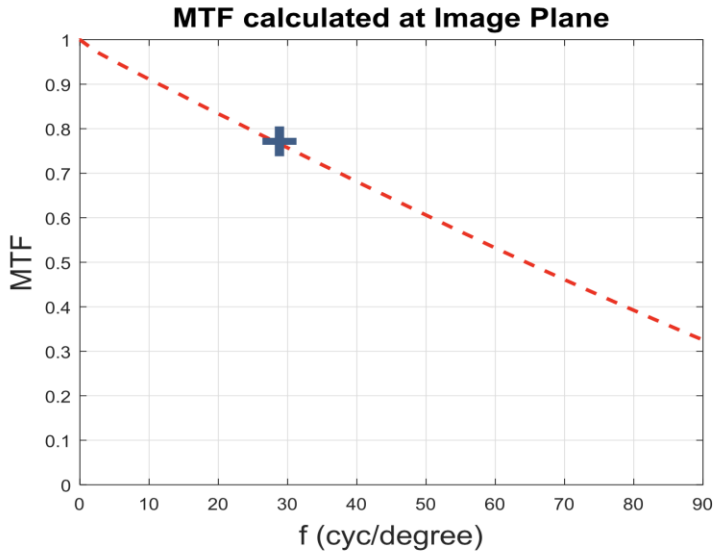

Figure 6.13 simulation result for MTF of a diffraction limited system with similar specifications of our experimental setup

Also, Figure 6.14 shows sample of the image plus the data derived from it at 10 degree angle of clockwise rotation (CW) for the center with calculated MTF value of 0.7 and edge of the positive lens with calculated MTF values of 0.46 and 0.60, respectively. Note

that for the edge of the lens, both vertical and horizontal intensity modulation was calculated because the lens rings are not symmetric at that area.

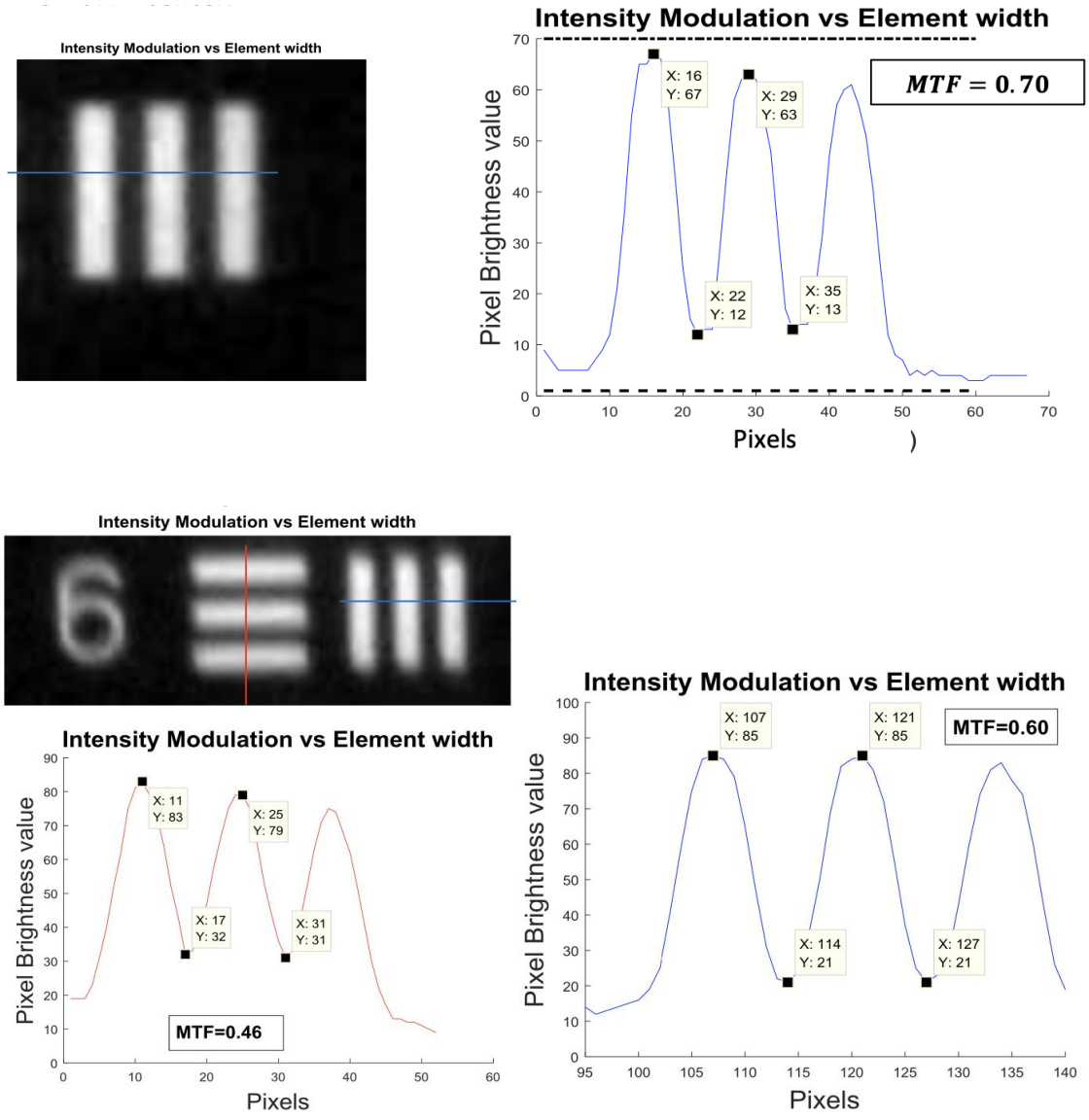

Figure 6.14 Image of the bars from group 0 – element 6 of the resolution target with LC lens on positive power. Top: corresponding intensity modulation graph MTF for 10 degrees clockwise rotation of the lens at the central part of the lens. Bottom: 10 degrees

clockwise rotation at the most outer edge of the lens. Red and blue curves correspond to vertical and horizontal directions, respectively.

Similar calculation was repeated with LC lens on for both center and edge of the lens for different angles of 0 °, 5 °,10 °,15 °and 20 ° and both clockwise and counterclockwise rotational directions of the stage. Additionaly, group 0 – element 3 of the resolution target was also analyzed whose spatial frequency was determined to be ~20 lp/deg, similar to equation 6.14.

These calculation is summarized in Figure 6.15 and Figure 6.16 for the center and most outer edge of the lens, respectively.

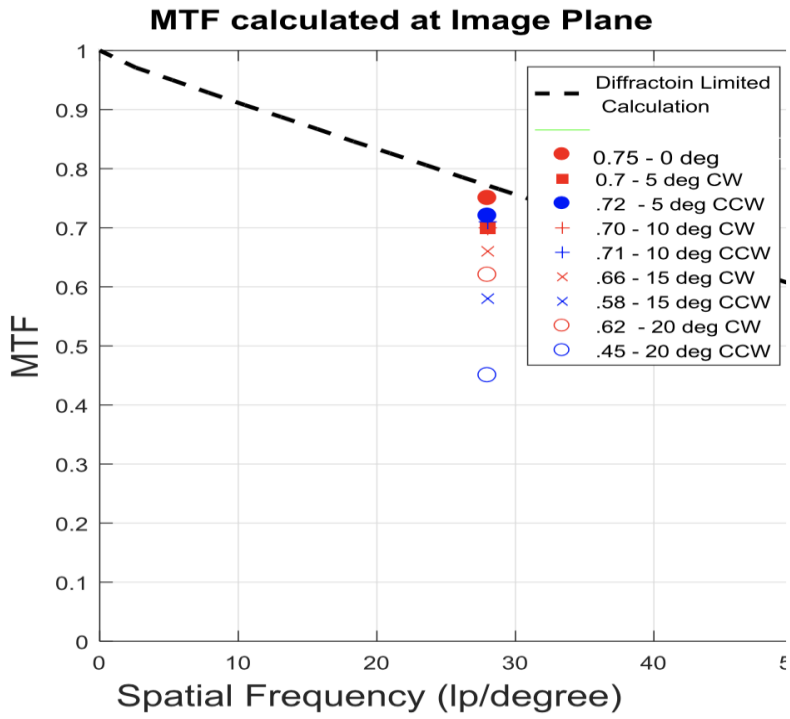

Figure 6.15 summary of calculated MTF values at different angles and different rotational senses of CW and CCW for center of the lens. Dashed black line is the calculated MTF for an ideal lens system with similar specifications.

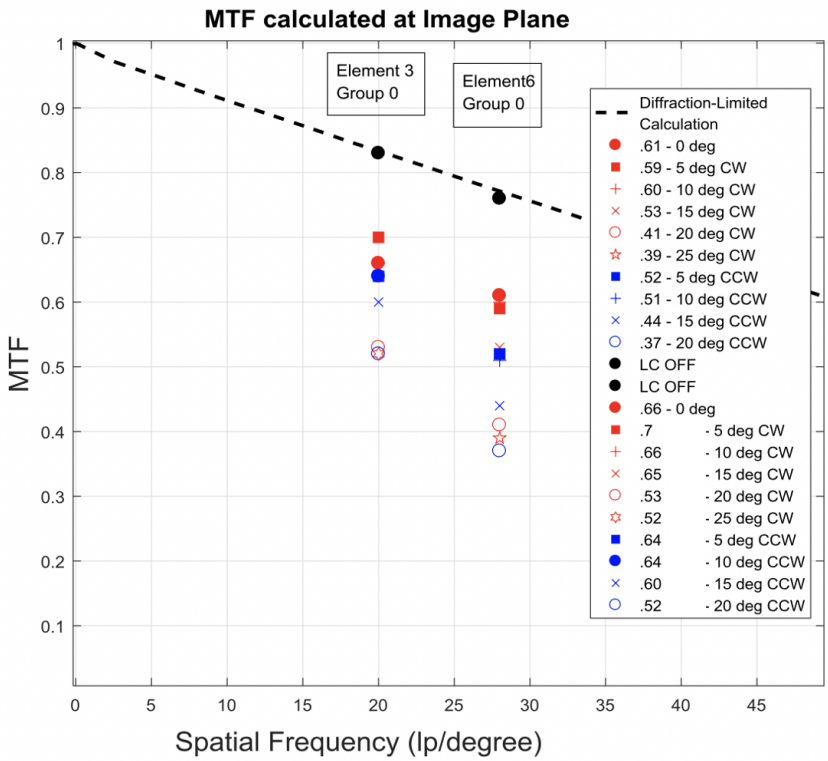

Figure 6.16 summary of calculated MTF for most edge of the lens elements of 3 and 6 from group 0 of the resolution target.

As expected for the element 3, we see MTF s have higher values than element 6 yet it still has approximately similar drop over 20 °angular rotation in which case, MTF starts from 0.65 and drops to 0.64, 0.60 and 0.52 for 10, 15 and 20 °angles.

It is worth to mention that part of MTF drop is due to the diffraction of the light from periodic rings and gaps over which the LC has different index of refractions. Nevertheless, it's a different source of diffraction which could be significantly addressed as shown in [79].

CHAPTER 7 – CONCLUSION AND FUTURE WORK

7.1 CONCLUSION

In this dissertation, we have introduced a novel approach to build a fast switching, tunable beam steering device based on Pancharatnam phase. Chapter 2 elaborates the concept and working principle of the device. We deliberately engineered the device so that an in-plane rotation of the LC director along the aperture is achievable by implementing fringe-field switching and using negative LC material. The basic idea is using an array of PCEs to control the in-plane twist of the director field at every location along the aperture (x direction). The modeling methods explained in this chapter, enabled us to derive the director profile of a customized configuration with different initial parameters and voltage input. Initial modeling has shown a promising result where we have enough control over the twist angle and uniformity of the twist. Based on the required uniformity of the director profile for a high efficiency output, design goals were determined as a guide to reach to a desired result. It also reviews one of the main limitations on efficiency loss due to the presence of so called “trapped walls” at certain locations where the director undergoes a tight 180 deg rotation. The formation of a defect is inevitable based on the proposed structure since there has to be two oppositely sense of rotations in the vicinity of each other in each period. As an early prediction, table 1 shows the calculated efficiency of a configuration with perfectly uniform director profile but with an inserted trapped wall of an arbitrary size compared to a defect free structure.

Chapter 3 reviews the detail of the optimization process based on the design goals that was derived in chapter 2. Initial parameters including both material related, and geometrical specifications were changed one by one and the effect of each parameter was studies separately. Step by step optimization shows how to reach from starting point device to an upgraded structure with enhanced performance. Electrode spacing shows that narrower electrode and gap sizes are beneficial to a more uniform structure. Smaller gap sizes promote narrower trapped wall sizes as the wall can be confined within one gap. However, fabrication limitation set the lower limit for these sizes. Also, it is shown that slightly larger gap width results in a more uniform profile along the x direction than equal electrodes and gap widths. Through a careful analyzation of electrode/gap widths within the practical range, w=1.5 μm and L=2.5 μm were chosen for continuation of the development. It was shown that an inverted voltage method helps to create an additional vertical electric field component which causes the negative LC material to stay more in plane. The increased electric force along z direction also helps the trapped wall size to be further decreased between two neighbor edges which is why a trapped wall is formed withing a gap. Different surface anchoring energies were tried with modified simulation code showing that lower anchoring energy significantly helps the uniformity of the director profile in both XZ direction resulting in an increased output beam efficiency (Bar graph 3.14). The effect of cell thickness was also investigated. Cell thickness has to be carefully chosen within a range that is determined by electrode/gap periodicity. As a thumb rule, cell thickness could not be larger than one pitch and smaller than one gap's

width. More specifically, it has to be chosen within this interval with respect to the design wavelength for which it is a half-wave retarder.

Table 3.2 summarized beam steering efficiency for different cases and three different deflection angles assuming visible light of $\lambda = 620\ nm$ is used. One can easily find that for infrared wavelengths, larger deflection angles are associated with the same pitches. Optimized data predicts that the proposed apparatus is capable of achieving high efficiency. Although the effect of a trapped wall on efficiency is not negligible, we have shown that a high efficiency can be reached by optimizing the design parameters to minimize the width of the wall. Another key parameter to this device is response time. Although the response time depends on several factors such as cell gap, electrode spacing, rubbing angle, LC material; Lee et al. [50] showed that a response time of around 10 ms is expected for a FFS mode device with negative dielectric anisotropy and similar cell parameters to FFS-PPD device.

Chapter 4 shows the fabrication and characterization process. Test data shows that there is promising results regarding controlling director profile with high uniformity. Figure 4.9 shows excellence match between experimental data from a sample fabricated device with the modeling. This confirmed that we have enough control over fundamental factors of the device, such as the twist angle and maintaining a half-wave retarder over the entire aperture (Figure 4.10). The data in this section confirm that the device meets the fundamental requirements for PPD beam steering with high steering efficiency. However, a device needs to be operated with several hundred electrodes to be able to cover a few millimeters of clear aperture and to reduce the diffraction of light through a

very small aperture which could be the subject of a future work. The result proves the concept of the performance and clears the way for the subsequent device optimization effort to achieve a tunable Pancharatnam based tunable beam steering device relatively short term.

Chapter 5 has provided a guideline for the limits on PDD lens power and aperture under which it can be considered “achromatic” for applications involving the human eye or imaging with a camera . PPDs have many advantages such as high efficiency, large deflection angle, relatively large aperture, lightweight, low fabrication cost in mass production and most importantly electrically switchable that makes them an excellent candidate for many applications involving head mounted displays, AR, VR and 3D systems [109]. However, they have an inherent chromaticity issue that can potentially limit their application. One reason is that they are designed to be a half-wave retarder for a specific wavelength while the other reason is fundamentally associated with their principle due to the fact that the focal length of such a lens is inversely proportional to the designed wavelength. Although there are some viable solutions to address the former reason, the latter reason is more problematic. Figure 5.5 summarizes modeling results of MTF value for different optical powers that can be analyzed to judge its optical performance. While PPD lenses have a strong chromatic effect, acceptable performance can be obtained, for applications involving the eye, providing that the lens power is around 1.6 D. The proposed criteria have been both experimentally and analytically verified in the continue of this chapter. Finally, for imaging applications, we have found

some criteria for the DOF of the camera that allows acceptable performance for a given PPD lens power and an optical bandwidth range. And further considerations for camera involving applications are discussed.

chapter 6, was a continuation of a work that was done by previous students to further evaluate performance of a liquid crystal Fresnel SPP lens. Design specifications was briefly introduced at first. The fine voltage tuning process was then described in detail. After voltage profile was found, we used a camera to capture the real phase profile and fine tune the voltages in order to account for real world errors. This was done by mapping the experimental curve on top of a simulation curve that is calculated for an ideal case. Point Spread function was then found experimentally and was evaluated with the help of simulation. Consequently, MTF function was determined to better represent the performance of such a lens under optimized tuning. The future work to further optimize the optical response include adding a floating electrode layer to reduce the diffraction caused by index of refraction variations over the gaps, customize the design to accommodate larger area without sacrificing the response time and material investigation to allow higher yield rate in mass production.

7.2 FUTURE WORK

Electro-optical beam steering methods have come a long way over the past few decades. Most attempts were initially based on LC because of its high birefringent under low voltage. There are two fundamental ways to steer the light. One common way is to build an optical phased arrays (OPA) to create an optical path delay (OPD). OPD based devices

would result in a sawtooth shape phase profile that has a “reset” at each periodicity. The usual problem with this method is that these periodic resets reduce the useful aperture of the device and consequently, reduce the efficiency of the device significantly. On the other hand, directly creating a phase delay is another fundamental way that was first recognized by Pancharatnam in his 1955 paper [110]. Unlike the first method, there is potentially no reset required in this way since the phase is the same for 0 or any other multiple of 2π. Both methods are periodic but the latter one can be continuous by taking advantage of the phase property. This was discussed in detail in section 1.2. Although our approach of FFS-PPD was based on the second method (Pancharatnam phase), we have encountered a geometrically inevitable region so called “trapped wall” where the director has to ‘reset” its rotational angle. The impact of this wall on efficiency is similar as the phase resets. Therefore, we have reviewed possible ways to reduce the size of this wall as much as possible.

Over the course of this study, we have shown that several factors such as material properties, electrode and gap sizes, cell thickness, anchoring energy and voltage method have significant impact on the formation of this wall. For instance, by combination of a specific electrode and gap widths, low anchoring energy and inverse voltage method, we reached to a director profile where the trap wall was only as big as one gap width. This was assumed to be the lower limit of the trap wall size. However, there are some fabrication limits that defined the lower limit of the widths. One possibility is to further reduce the size of the electrode and gap by advancing fabrication methods. This way, the

size of the trapped wall will further reduced and the efficiency will be improved. Also, smaller cycloidal pitches will be achieved which corresponds to larger steering angles. Furthermore, if the trap wall is confined within an electrode width rather than a gap, it will have even lower size since the electrode has lower width than a gap in our design as it was shown to be more effective on uniformity. So making a trap wall to form within the edges of an electrode instead of a gap would immediately reduces the size of the wall by a factor of around 2.

Another interesting area is to investigate reflective type device based on this approach. All the materials and results represented here was considering a transmissive device. However, the same methodology can apply to the reflective type of device in which the thickness could potentially be half of the cell thickness in transmissive mode. The cell thickness in transmissive mode is limited by the birefringent of the LC material because the cell should meet the condition of being a half-wave retarder for a particular wavelength $\Delta n.d = \lambda/2$. The lower the cell thickness, the higher the birefringence should be. But the birefringence in negative LC material is usually much lower than the positive ones. Therefore, the cell thickness in transmissive mode is limited by LC material choice. Consequently, considering reflective mode device can be a possibility to further decrease the cell thickness.

Finally, we have considered one dimensional beam steering here by designing long narrow strips of electrodes. As a result, the cycloidal pattern is formed only along a line perpendicular to the electrode strips and the deflection angle also varies only in this direction. However, by considering small square shaped electrodes instead of long strips,

the pattern can be shaped in both axis of the planes that is parallel to substrate. This way, the deflection angle could also be either in X or Y direction or a combination of both. This introduces a series of new challenges to the design of the device such as complication in defining areas with particular twist preference in the first step of applying voltages which might need multi-domain pre-alignment, the positions of trapped walls in either direction, the uniformity of the layers closer to the substrates and most importantly aligning the micron size squares of electrodes precisely in both directions. Nevertheless, the proof of device concept shown here and confirming the adequate control over the key parameters of the design that are required for the performance of this device with both simulation and experimental results presented in this dissertation paves the way for 2D analysis of this device and open new doors to future investigation in this area.

.

APPENDIX A – MODELING APPROACH AND CODE DEVELOPMENT

In this Section, a detailed description of the modeling system is represented. The simulation represented in this dissertation benefits from various modeling theories and different programs. This includes calculating director configuration, obtain phase profile of exiting light based on that director configuration, simulate light propagation throughout the cell or a desired optical system, find diffraction pattern of the light at image plane as well as updating and customizing the tools to be able to perform these tasks. A review of each method is discussed here.

A.1 Updating Modeling Code and Programs

- Throughout this work, most of numerical calculations for light propagation methods and director relaxation were performed in Matlab. Although many of the required codes were written from scratch, some of the codes, were originally developed by previous students. But since the pre-existing codes still required flexibility to change the model parameters and conditions, line by line update was made which required a deep understanding of the codes. In some cases, additional steps had to be taken in order to make the previously developed tools into work. In particular, updating old Fortran based codes in a format that is usable in recent versions of Matlab software was a painstaking long process that required knowledge of both softwares as well as converting their format in order to be compatible with each other.
- V-COPA is a numerical GUI based program on Matlab with user friendly environment that was used for director relaxation and numerical modeling of the

Beam Steering device. Useful features of the program include LC director relaxation and visualization, dynamic modeling, polarized optical microscopy visualization and scalar integral method for optical simulation. The program uses some Fortran based codes inside the Matlab environment. Since the Fortran codes were originally developed more than a decade ago, they were based on older version of Fortran and Matlab software. As the software have undergone dramatical changes during this time, the codes were impractical to use with the current versions of those software. Additionally, Fortran is no longer available and Matlab uses a differnet method in which old Fortran codes are compiled into a so called “mex” file. However, the compiler itself is a third party program and had been changed in many ways during these years. Therefore, a significant update was needed to be able to use the codes again. These changes are described in the following. Also, an example to use the updated V-VCOPA program is shown later in this appendix.

- As mentionded, the Matlab versions later than 2016, call Fortran subroutine using compliled MEX files. To update and create these mex files a comination of compatible compilers are needed to run and cross talk at the same time. An example of these three compatible software is Matlab 2016b, Intel Parallel Studio XE 2015 Cluster Edition and Microsoft Visual Studio 2013. However, each of these softwares update their version each year and the compatibility of new versions should be checked based on latest versions. Also, the order of installment is important in this case. First, install Matlab. Then, Microsoft visual Studio needs

to be installed making sure that C++ and Fortran boxes are checked during the installment. And the compiler has to be installed in the last step. Upon completion of the compiler installation, it will automatically integrate into Visual Studio. If there is any change and modification in the installation of any of these three, uninstall everything and repeat these steps from beginning.

- (Please see: https://www.mathworks.com/help/matlab/fortran-mx-matrix-library.html)
- Once the softwares are running and cross-talking, MEX files should be created in order to call to call a Fortran subroutine in MATLAB.
- Here are the Steps to create Mex files:
    - Create Source File
    - Create Gateway Routine
    - Declare mex function Arguments
    - Declare Functions and Local Variables
    - Verify MEX File Input and Output Arguments (Optional)
    - Computational Routine
    - Declare Variables for Computational Routine
    - Read Input Array
    - Prepare Output Data
    - Perform Calculation
    - Copy Results to Output Argument
    - Build the MEX file in Matlab

- Test the file
- Call the function in Matlab just like a normal Matlab function (make sure mex file is placed in the same folder)

A.2 Director Relaxation Modeling

Director modeling represented earlier predicts the director angular change along the aperture as well as throughout the cell thickness. Assuming that the director remains unchanged along one of the in-plane coordinates (y-axis), a 2D modeling was used to calculate the director relaxation due to the inserted electric field. To calculate the equilibrium (or dynamic) state of director configuration in a confined geometry, free energy must be minimized.. The Frank-Oseen free energy density equation describes the energy density related to elastic forces for a nematic liquid crystal :

$$f_{el}=1/2*(\ \mathrm{K}_{11}(\nabla.\vec{n})^2+\mathrm{K}_{22}(\vec{n}.\nabla\times\vec{n}+q_0)^2+\mathrm{K}_{33}(\vec{n}\times\nabla\times\vec{n})^2\ ) \qquad (A.1)$$

where $K11$, $K22$ and $K33$ are splay, twist and bend elastic constants respectively and q_0 is determined by the chiral property of twist deformation.

On the other hand, the liquid crystal director interacts with an applied electric field in a way to either align parallel (if $\Delta\varepsilon > 0$) or perpendicular (if $\Delta\varepsilon < 0$) to the electric field depends on the sign of the dielectric anisotropy $\Delta\epsilon = \epsilon_{\parallel} - \epsilon_{\perp}$. The electric free energy at constant voltage is given by:

$$f_E=-1/2\ E.D=-\ ½\ E.[\varepsilon_0\varepsilon_{\perp}E+\varepsilon_0\Delta\varepsilon(E.\vec{n})\vec{n}] \qquad (A.2)$$

Or:

$$f_E = -½\ \varepsilon_0 \varepsilon_\perp E^2 - ½\ \ \varepsilon_0 \Delta\varepsilon E_i E_j n_i n_j \qquad i,j=x,y,z \tag{A.3}$$

Gibbs free energy (fG) is the sum of elastic free energy and electric free energy. Taking functional Euler-Lagrange derivative of the Gibbs free energy density would give generalized torque density:

$$[f_G]_{ni} = -\frac{\partial f_G}{\partial n_i} \tag{A.4}$$

$$[f_G]_{ni} = = \frac{\partial f_G}{\partial n_i} - \sum_{j=x,y,x} \frac{d}{dj}\left[\frac{\partial f_G}{\partial(\frac{dn_i}{dj})}\right] \quad i = x, y, z \tag{A.5}$$

Then, the equation A.4 is balanced to viscous torque density as shown in equation (A.6) to find the update formula for the director.

$$\gamma \frac{\Delta n_i}{\Delta t} = [f_G]_{n_I} \tag{A.6}$$

$$\Delta n_i = \frac{\Delta t}{\Delta \gamma} [f_G]_{n_i} \tag{A.7}$$

$$n_i^{new} - n_i^{old} = \frac{\Delta t}{\Delta \gamma}\ [f_G]_{n_I} \tag{A.8}$$

Where γ is the viscosity coefficient. The above equation can be used is updated at each iteration of the simulation and is renormalize back to unit length as follow:

$$\frac{n_i}{\sqrt{n_x^2 + n_y^2 + n_z^2}} \qquad i = x, y, z \tag{A.9}$$

Under a given voltage profile, the electric field is calculated and then the steps to calculate the equilibrium state of the director is taken.

At each iteration, the director is updated by equation (A.8) and then normalize it again using equation (A.9). Next the new value of voltage at current grid point is calculated.

Next, we update the time forward ($+\Delta t$) and next iteration starts over. Using the above formulation, a repeating loop so called successive displacement was used to calculate the updated formula. This loop continues until a relaxed state where the difference between the update n+1 and n cycles falls below an arbitrarily set value.

A.3 Implementation in Matlab Based GUI

- Here is an example of implementing the above formulation into Matlab. As explained earlier, V-COPA is a GUI based Matlab tool that provides a user friendly environment to define the many cell parameters instead of directly changing them in the code which would have been a confusing and time consuming task. V-COPA v3.3 was first updated on Dec 2016 by updating Fortran based codes, defining compatible gateways and compiling new MEX files as well as adding new features to the program such adding FFS mode simulation capability by designing a new voltage plane near to the electrodes, reconstituting pre-alignment definition on the electrode strips and modifying the program to be able to account for adjustable finite anchoring energy. The main windows of the program includes some main buttons that will be described as follows:
- Device Setting: this button would direct us to a new windows where we can adjust basic material properties such as liquid crystal elastic constants, dielectric anisotropy, refractive indexes of the cell (e.g. glass or air) as well as some design

parameters such as cell thickness, surface alignment number of electrodes and gaps, and their spacing widths. (Figure A.1)

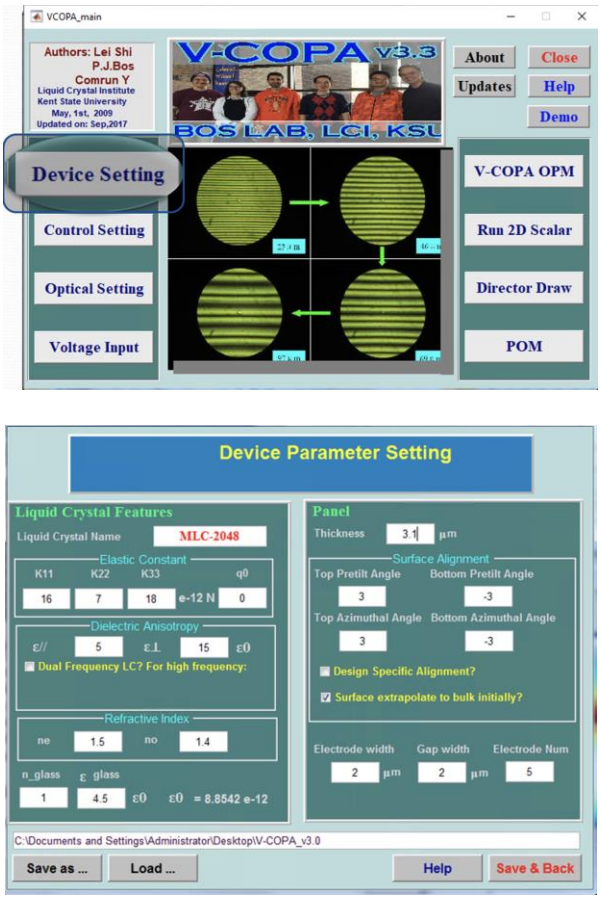

Figure A.1 VCOPA software-Device setting

- Control Settings: provides ability to adjust simulation parameters such as grid spacing, calculation method (which was fixed based on the method explained in the previous section), boundary conditions (e.g. periodic vs continuous), overall array dimensions and director relaxation parameters including number of relaxation loops, relaxation speed and convergence tolerance (i.e. the minimum value under which the director is considered as being “relaxed”). (Figure A.2)

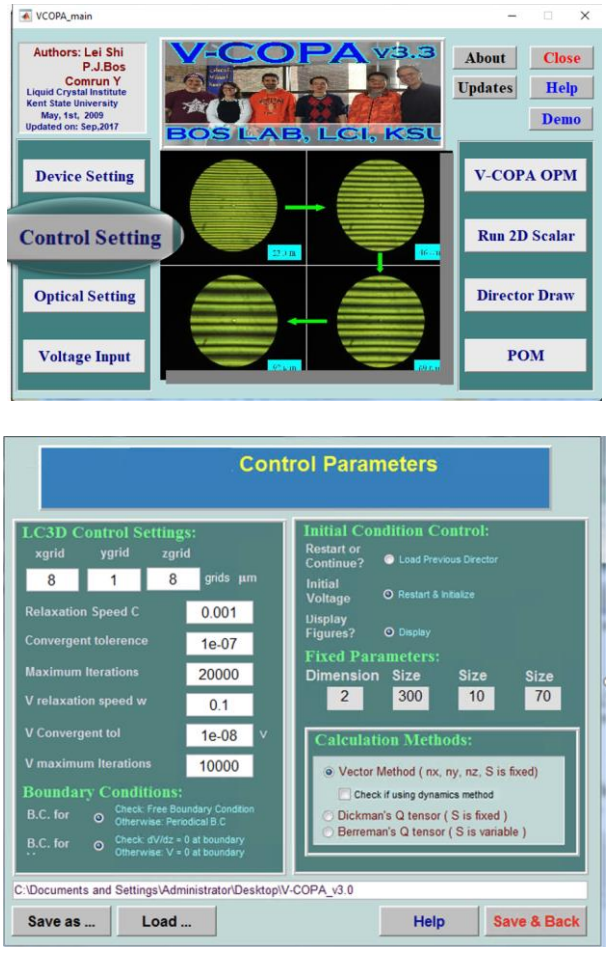

Figure A.2 VCOPA software-Control setting

- Optical Settings: brings the post-relaxation related parameters for optical purposes such as light information and FDTD parameters. FDTD calculations in this dissertation were performed separately which was described in chapter. Section.-. (Figure A.3)

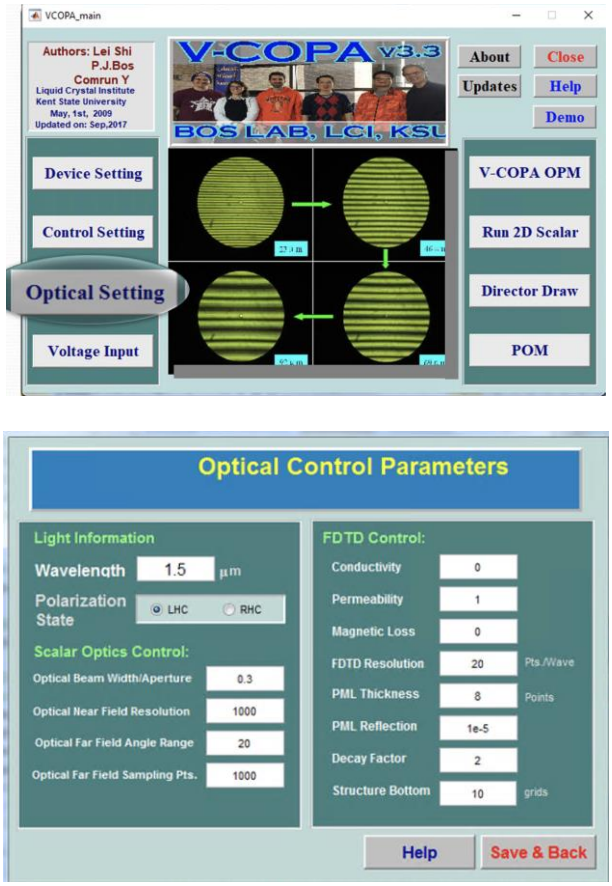

Figure A.3 VCOPA software-Optical setting

- Voltage Input: enable us to define specifics of voltage application including voltage profile method, initializing voltage on each electrode and defining a FFS mode inside the cell and a voltage pattern drawing option that helps to visualize and double check the voltage definition.

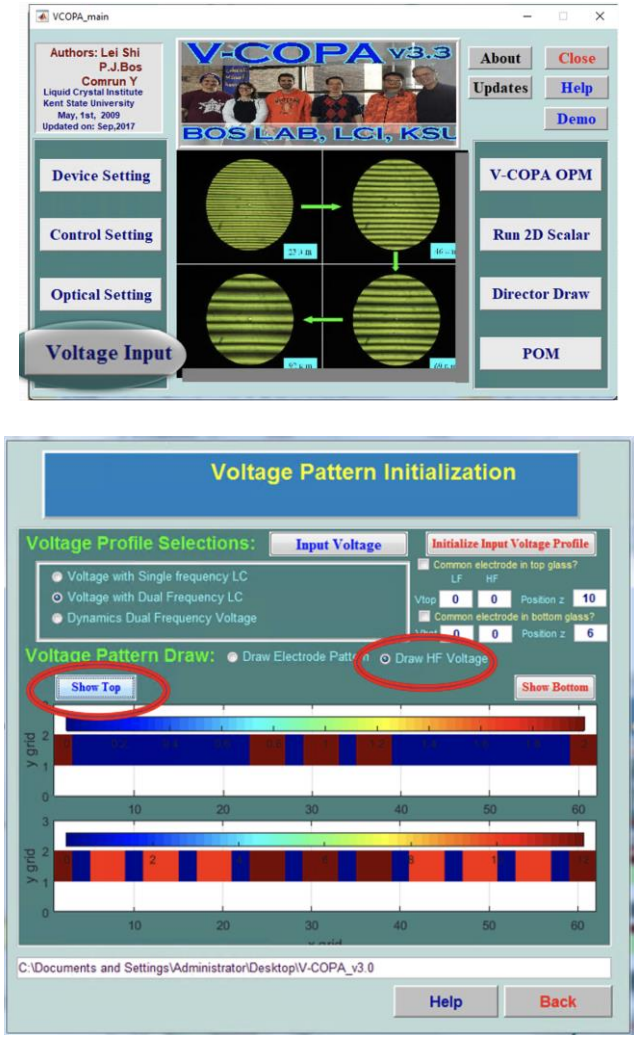

Figure A.4 VCOPA software-Voltage Input

- After setting all the necessary parameters required for the simulation, the OPM button performs the calculation and the results will be graphed after it finishes.

In the following example, we will demonstrate an application of the two-step voltage method to find director profile in a device similar to what we have shown in the context. In this example, we use inverse voltage method and weak anchoring energies of $W_a = 10^{-5} j/m^2$ and $W_p = 3 * 10^{-4} j/m^2$ for azimuthal and polar surface anchoring,

respectively. We start to input the initial device parameters using MLC-6608 material specifications :

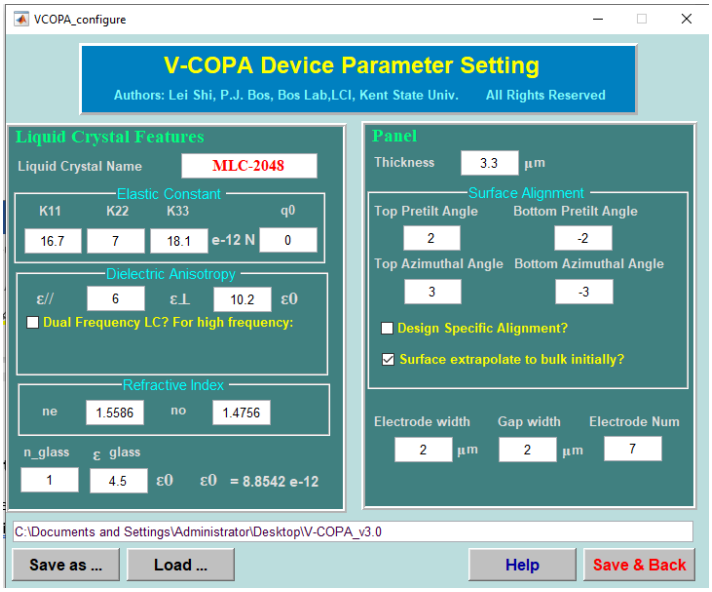

Figure A.5 VCOPA software-Device Parameter Setting values for MLC-6608

Note that having "surface extrapolate to bulk initially" option marked, the surface pre-twist and pre-tilt alignment would determine the LC director orientation at the off state just as a real case. If multi-domain pre-alignment is needed, the option design specific alignment could be marked in which case a new window would pop up that will let the user to define pretilt and pre-twist over each individual electrode or gap.

Next, we input grid spacing per micron and process parameters such as relaxation speed, convergent tolerance, maximum iterations before showing the result, relaxation speed and convergence tolerance as well as boundary conditions in the control setting:

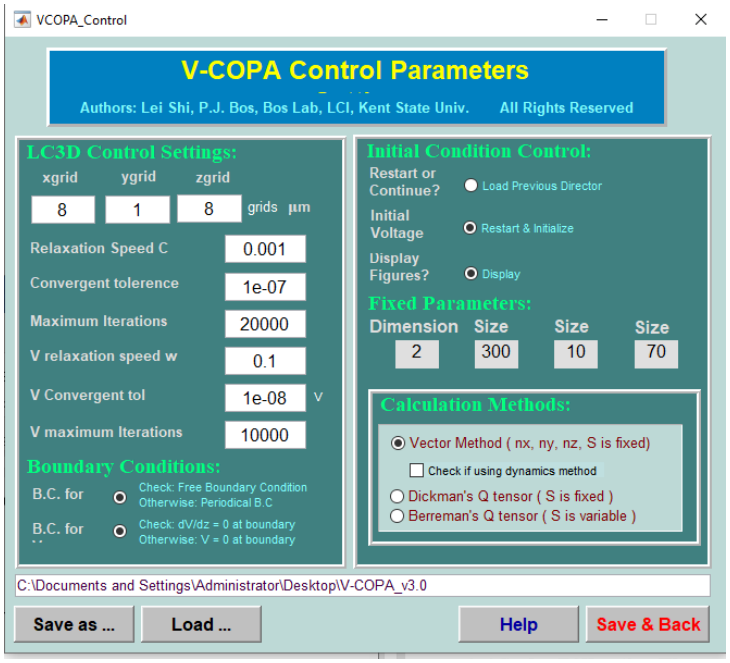

Figure A.6 VCOPA software-Control parameters

Since we are not using optical simulation at this point with this program, we leave that parameters unchanged. Then, we can define voltage input by choosing “voltage with single frequency” in the “voltage input” option in the program:

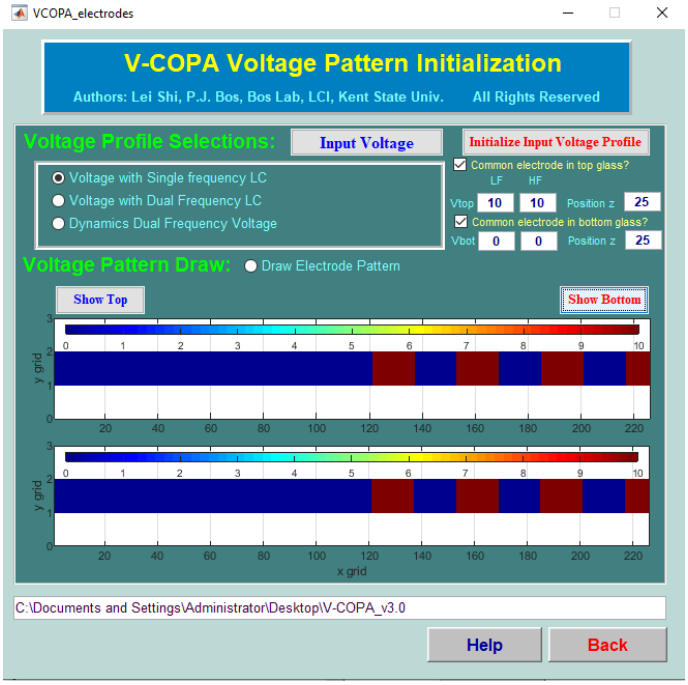

Figure A.7 VCOPA software-Voltage Pattern Initialization

Also, note that both common electrodes are marked which would enable the first ITO layer in FFS-PPD design. As discussed earlier, in the inverse voltage method, we put top common electrode as maximum voltage (10V in this case) and the bottom common electrode at 0. Position layer is determined based on grid spacing in Z direction and cell thickness. Since, we would like to have the common electrode as close as possible to the driving electrodes, we multiply the cell thickness to the grid spacing and round the number to the nearest integer value less than or equal to that amount. This would mean that the insulator layer is only one grid spacing thick (0.125 μm in this case) which is around the real case value.

In the first step, using the "input voltage" option shown in the above picture, we set all first four electrode (i.e. ±1 to ±4) voltages to 0, resulting in activation of first four top

electrodes because of their relative voltage difference of 10V to the corresponding common electrode layer, and set all last four electrode (i.e. ± 5 to ±8) voltages to 10 V, resulting in activation of last four bottom electrodes due their relative voltage difference to the bottom common electrode.

After setting all the required parameters explained here, we click on "V-Copa OPM" button on the main program interface and the calculation starts. The following result was found for the first step voltage profile.

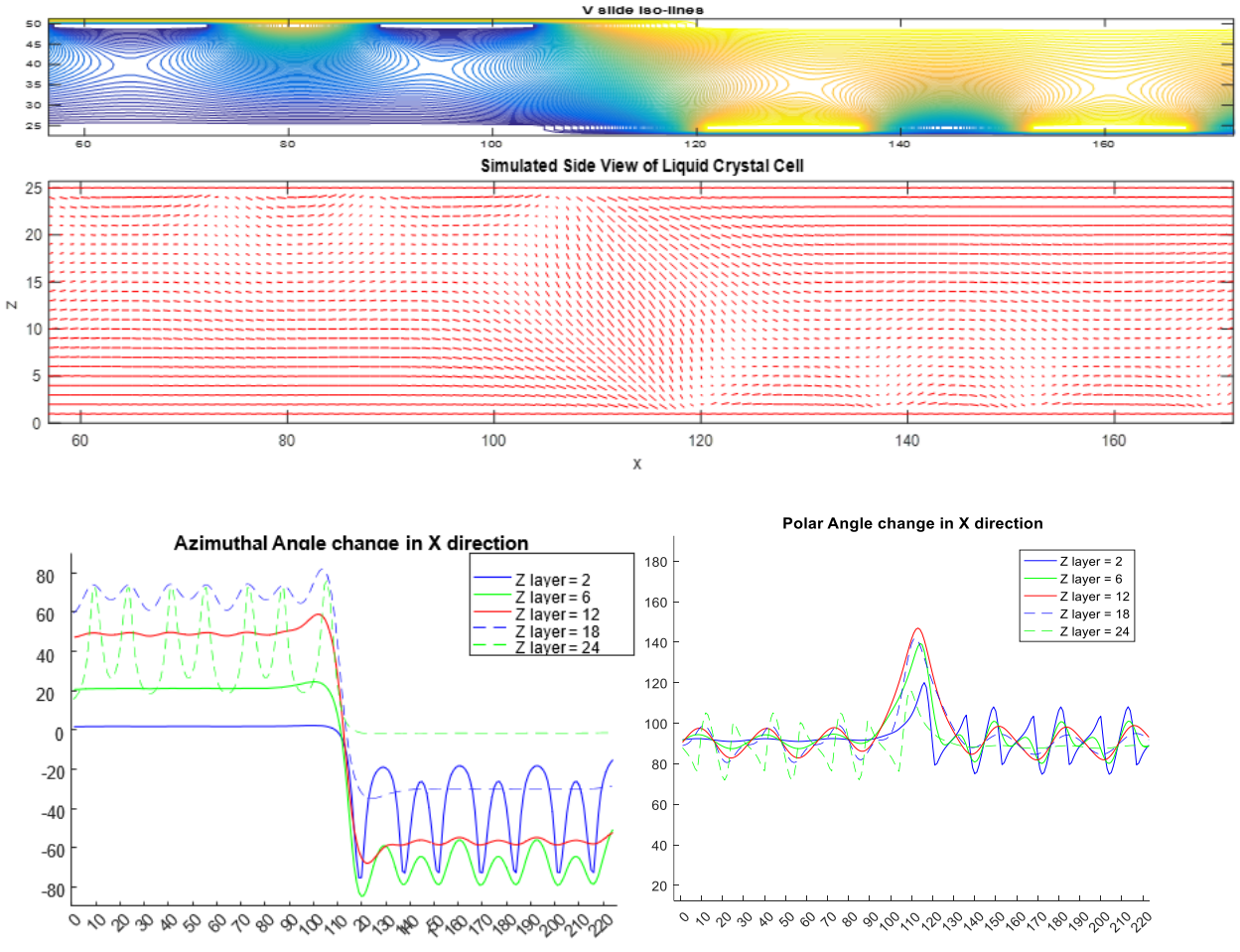

Figure A.8 Result graphs (i.e. voltage profile, director profile, azimuthal angle and polar angle graphs) derived after 1st step voltage.

As seen the director is t wisting in the opposite directions on each side of the cell depend on what electrodes on which side are activated. The director profile shows that the layers toward the side that is not activated, remains mostly unchanged. Though, even small tendency (e.g. solid blue line with a few degrees of twist) to the desired direction is enough for our purpose at this step. Azimuthal graph indicates that there are two oppositely twisted sides with layers closer to the activated side, having more twist angle. Next, we only change the voltage profile to the values that are desired for second voltage step which activates all electrodes of the cell. Similarly, we click on "V-Copa OPM" button on the main program interface to start the calculation with all the other parameters unchanged.

The result of the 2nd step calculation are shown in the following.

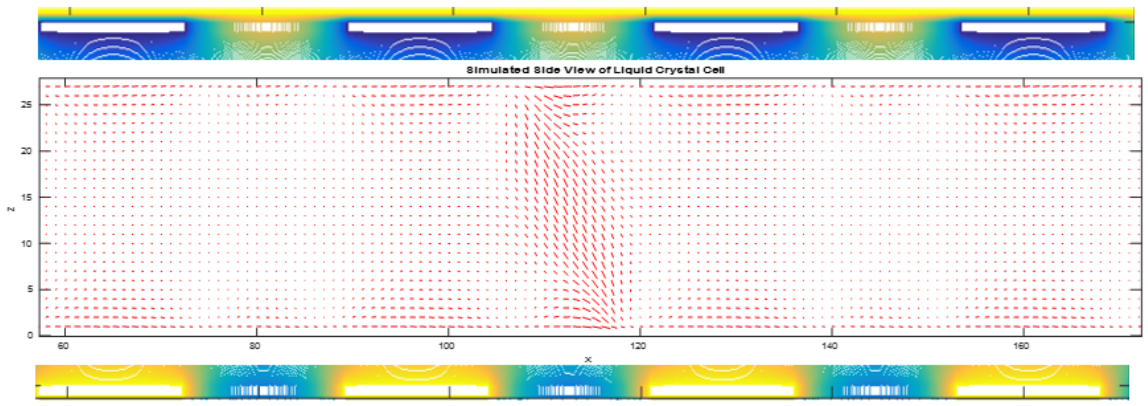

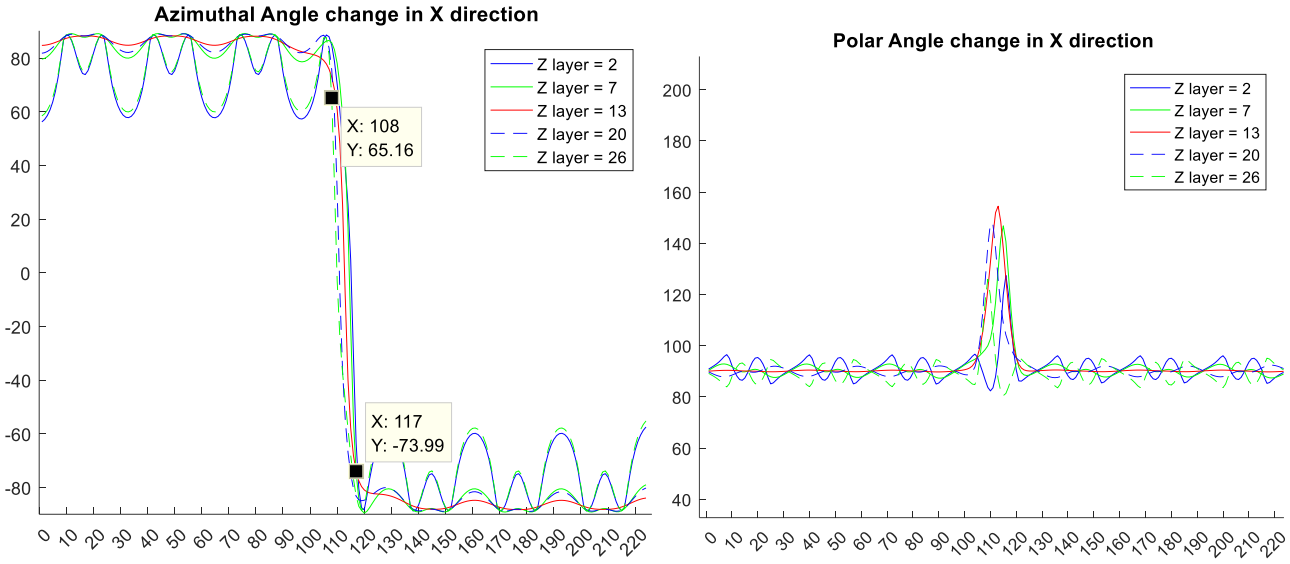

Figure A.9 Result graphs (i.e. voltage profile, director profile, azimuthal angle and polar angle graphs) derived after 2nd step voltage.

As expected, the director is mostly pointing either in or out of the plane almost everywhere in the cell except between the gaps right in the middle of the cell where the trapped wall is shaped and director goes under a tight 180 degrees rotation. In the former case the director is mostly shown as points whereas in the latter case, the director is seen to have more like line shape due to its XZ components as it turns around. For a more clear representation, the graph is zoomed in to only show the four electrodes area in the center of the cell.

Also, graphs of azimuthal angle and polar angle vs X direction, confirm that there are two sides (left vs right) within the cell with oppositely twisted angles where the layer midway through the cell thickness has the most twist angle average and the most uniformity in the

twist (red curve in the figure A.9). However, polar angle graph shows that the director is mostly stayed in the XY plane as desired except at the location of the trapped wall.

A.4 Scalar Diffraction Theory Computation

The goal of this section is to describe the evolution of an optical field as it propagates from point source to focal plane. The phenomenon of diffraction underlies the behavior of propagating waves. Diffraction is the bending and spreading of waves, when its lateral extent is confined for example around an obstacle. The effect of diffraction is more apparent when the confinement size is in the scale of wavelength of light. Diffraction is used in many optical applications for example; diffraction of x-ray is used to make image of small structure such as DNA and diffraction is also used for astronomical imaging. The propagation behavior of an optical wave is fundamentally governed by Maxwell's equations. In most cases, electric field $\boldsymbol{E}(Ex,Ey,Ez)$ and magnetic field $\boldsymbol{H}(Hx\ ,\ Hy\ ,\ Hz\ )$ are coupled. There is also coupling between the individual components of the electric field, as well as between the magnetic components. However, in the case that a wave that is propagating in a linear dielectric medium (i.e. field quantities from separate sources can be summed), isotropic (independent of the wave polarization), homogenous (permittivity of the medium is independent of position), nondispersive (permittivity is independent of wavelength) and nonmagnetic (magnetic permeability is equal to the vacuum permeability), Maxwell's vector expressions become decoupled, and the behavior of each component of the electric or magnetic fields can be expressed independently from other components [97]. Propagation behavior of light under this

condition is scalar diffraction. Propagation in free-space is one example of scalar diffraction. One can characterize a linear, isotropic and homogeneous system with a single impulse response. A point source at origin of an input plane is considered. This point source produces some field and amplitude on output plane distance z away from the input plane. The output field and amplitude h(x, y) is called impulse response. For an arbitrary coherent input light, we can obtain the output field and amplitude $u2(x, y)$ by taking impulse response h(x, y) and convolve it with its input field $u1(x, y)$. In order to understand how the point source propagates and gives impulse response, we need to understand the propagation. Although based on Huygens-Fresnel principle we can guess that h(x, y) must be spherical waves, mathematical proof of impulse response is provided in the following.

A propagating optical wave in any media follows Maxwell's equation:

$$\Delta \times E = -\frac{\delta B}{\delta t} \tag{A.10}$$

$$\Delta \times H = \frac{\delta B}{\delta t} + J \tag{A.11}$$

$$\Delta . D = \rho \tag{A.12}$$

$$\Delta . B = 0 \tag{A.13}$$

Where J is the total electric current density an ρ is the totatal electric charge density. The relation between the displacement field (***D***) and the electric field (***E***) as well as the magnetic flux density (***B***) and magnetic field strength (***H***) is described by constitutive relations which are :

$$D = \epsilon E \tag{A.14}$$

$$B = \mu H \tag{A.15}$$

where Ɛ is permittivity and μ is permeability of the material. In free space the total electric current density ($\boldsymbol{J}$) and the total electric charge density (ρ) are zero and permittivity (Ɛ) and permeability (μ) are scalar constants. Therefore the Maxwell's equations in free space using constitutive relations are

$$\Delta \times E = -\mu \frac{\delta H}{\delta t} \tag{A.16}$$

$$\Delta \times H = \epsilon \frac{\delta E}{\delta t} \tag{A.17}$$

$$\Delta . E = 0 \tag{A.18}$$

$$\Delta . B = 0 \tag{A.19}$$

Considering the harmonic electric and magnetic field solutions:

$$\boldsymbol{E}(x, y, z; t) = \boldsymbol{E_0}(x, y, z)e^{-jwt} \tag{A.20}$$

$$\boldsymbol{H}(x, y, z; t) = \boldsymbol{H_0}(x, y, z)e^{-jwt} \tag{A.21}$$

The Maxwell's equations becomes:

$$\Delta \times E_0 = j\omega\mu H \tag{A.22}$$

$$\Delta \times H_0 = -j\omega\epsilon E_0 \tag{A.23}$$

$$\Delta . E_0 = 0 \tag{A.24}$$

$$\Delta . B_0 = 0 \tag{A.25}$$

Performing the operations would gives us:

$$\nabla^2 \boldsymbol{E_0} = -\omega^2 \mu \varepsilon \boldsymbol{E_0} \tag{A.26}$$

Which is known as the wave equation. Solving this equation in spherical coordinates, one can find the impulse response (hz (x, y)) of the radiating source located at the origin of an input plane, at a distance z from the output plane

$$\mathrm{h_z}(x, y) = e^{ikr} \tag{A.27}$$

where $\mathrm{r} = \sqrt{\mathrm{x}^2 + y^2 + z^2}$ is the distance between a point on the output plane to the origin of input plane. In the above equation z, the distance between input and output planes, is the system parameter and x and y are the variables of the system. For a coherent light, convolving the input field with the impulse response gives the output field.

$$u_2(x, y) = u_1(x, y) * \mathrm{h}_z(\mathrm{x}, y) \tag{A.28}$$

This is a convolution called Rayleigh-Sommerfield diffraction integral. To have general form of the integral, one can consider the monochromatic radiating point source located at (ξ, η) on the input plane with input field distribution of $u1(\xi,\eta)$ (Figure A.10), the field distribution in the output plane $u2(x,y)$ with distance z away from the input plane can be obtained with Rayleigh-Sommerfield diffraction integral as shown in equation (A.42)

$$u_2(x, y) = \frac{z}{j\lambda} \int \int u_1(\xi, \eta) \left(\frac{e^{ikr}}{r^2}\right) d\xi \, d\eta \tag{A.29}$$

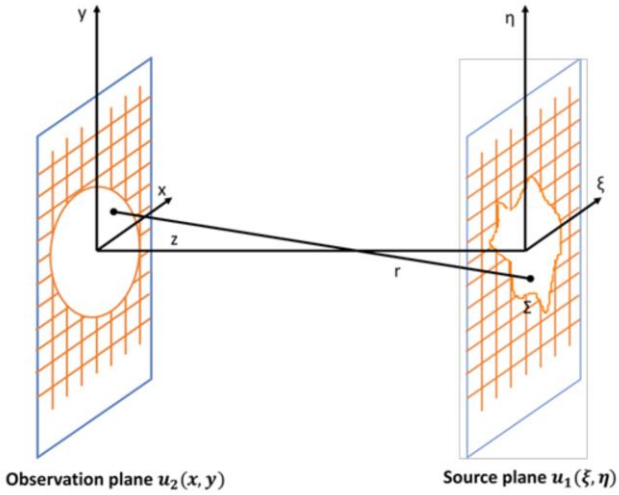

Figure A-10 coordinate system of Rayleigh-Sommerfeld Diffraction theory.

Here Σ shows the illumination aperture. λ is the wavelength of light, k is the wave number, z is the distance between the source plane and observation plane, and r is the distance between the source point (ξ , η) on the source plane and a point (x , y) on observation plane ($\mathrm{r} = \sqrt{\mathrm{x}^2 + y^2 + z^2}$) The Rayleigh-Sommerfeld diffraction formula is the most accurate solution for the precise scalar diffraction calculation and propagation of light in an isotropic, homogenous and linear medium that is well founded when the aperture size is much greater than the wavelength of light [97]. As discussed earlier equation consists of two main terms: the field term ($U1(\xi, \eta)$) and the Rayleigh-Sommerfeld impulse response $\mathrm{h_z}(x, y) = \frac{1}{j\lambda}\frac{e^{ikr}}{r}$ multiply by obliquity factor ($\chi = z/r$) which forces propagation to be in z direction. The term $\frac{e^{ikr}}{r}$ express Fresnel-Huygen's principle that each point in the aperture acts as a source of spherical waves that combine to give the diffraction pattern. Besides some specific situations, it is not feasible to analytically solve the Rayleigh- Sommerfeld diffraction formula. Under

specific criteria, Fresnel and Fraunhofer approximation of Rayleigh-Sommerfeld integral are used to compute the light diffraction. If the area of the aperture is smaller than the separation between the two planes ($(x-\xi)^2 \ll z^2 \; and \; (y-\eta)^2 \ll z^2$) the Fresnel impulse response or the Fresnel point spread function is obtained after some trivial mathematical steps.

$$h_F(x,y) = \frac{1}{j\lambda}\frac{e^{jkz}}{z} e^{\frac{jk}{2z}(x^2+y^2)} \tag{A.30}$$

The propagating wave shown is parabolic rather than spherical in the case of Rayleigh-Sommerfeld equation. Fraunhofer approximation is an approximation to Fresnel impulse response. In this approximation the separation between the two planes are far such that the parabolic waves become plane waves. Although Fresnel and Fraunhofer approximations are very useful in certain regimes, a more specific approach to numerically solve the Rayleigh Sommerfeld equation with least approximations is taken here.

A number of algorithms are suggested in the literature to numerically solve the Rayleigh-Sommerfeld integral, mainly based on the two methods of Angular Spectrum (AS) and Direct Integration (DI). For the purpose of our study, we utilize the DI approach, the approach calculates Rayleigh-Sommerfeld integrals in the spatial domain using numerical integration. In this procedure, an integration is considered as a linear convolution and can be computed by virtue of Fast Fourier Transform (FFT) and the Inverse Fourier Transform (IFFT). A nice presentation of computing the diffraction integral by means of linear convolution and FFT was provided by Voelz[97]. Our numerical modeling of the light propagation based on DI Rayleigh-Sommerfeld is built on the Voelz strategy.

According to the DI method, the superposition integral shown in equation () can be expressed as a convolution integral:

$$u_2(x,y) = \int\int u_1(\xi,\eta)\, h(x-\xi, y-\eta)\, d\xi\, d\eta \tag{A.31}$$

Taking the Fourier transform of both sides of equation () and using the convolution theorem (Fourier transform of a convolution is the simple multiplication of Fourier transforms.), one can re-write equation () as follow:

$$u_2(x,y) = F^{-1}\{F\{u_1(x,y)\}\,.\,F\{h(x,y)\}\} \tag{A.31}$$

or

$$u_2(x,y) = F^{-1}\{F\{u_1(x,y)\}\,.\,H(f_X,f_Y)\} \tag{A.32}$$

where $H(fX\ ,\ fY\ )$ is the Rayleigh-Sommerfeld transfer function given by:

$$H(f_X,f_Y) = \exp\left(jkz\sqrt{1-(\lambda f_X)^2-(\lambda f_Y)^2}\right) \tag{A.33}$$

Where the condition $\sqrt{(f_X)^2+(f_Y)^2} < \frac{1}{\lambda}$ must be always satisfied.

In our numerical model, a radiating point source is considered. The light propagates through different optical elements in the system. At the plane of each element, the phase profile of that element is taken into account and is added to the light phase. Then the Rayleigh-Sommerfeld transfer function conveys the light from one optical element to the other. Lastly, the light intensity at the focal plane (point spread function, PSF) is determined. The Modulation Transfer Function (MTF) can be then calculated by taking the Fourier transform of PSF. More specifically, the outcoming field of mth optical element is determined by the input complex field amplitude ($u_{in}{}^m$) together with the phase associated with that optical element (φ^m)

$$u_{out}^{m} = u_{in}^{m} \cdot e^{i\phi^{m}} \tag{A.34}$$

The Fourier transform of the complex field amplitude at exit plane of optical element m is then calculated.

$$U_m = F\{u_{out}^{m}\} \tag{A.35}$$

The field of optical element m is carried to the next optical element of the system (m + 1) using the Rayleigh-Sommerfeld Optical Transfer Function (OTF) which is the Fourier transform of the Rayleigh-Sommerfeld impulse response in the spatial domain

$$H_m(f_u, f_v) = F\left\{\mathrm{e}^{\left(jkz\sqrt{1-(\lambda f_u)^2-(\lambda f_v)^2}\right)}\right\} \tag{A.36}$$

Or equivalently:

$$u_f = F^{-1}\{U_m(F_u, F_v) \cdot H_m(f_u, f_v)\} \tag{A.37}$$

where u_f denotes the final field at observation plane. The PSF is the incoherent impulse response ($|h(x,y)|^2$) which can consequently be determined at the observation plane. In order to evaluate the imaging performance of the optical system of interest, one can calculate the modulus of OTF which is known as the Modulation Transfer Function (MTF) and is given by:

$MTF = |\mathrm{H_f}(\mathrm{F_u}, \mathrm{F_v})|_{\mathrm{norm}}$

A.5 Expanded Scalar Diffraction Simulation

- One of the challenges in Fourier transform theory is to maintain enough sampling point to model the diffraction as light propagates in the system. The array size and point spacing will change as beam propagates while the total number of array points stays constant. If the array width is much larger at beam waist compare to the waist size, there would be relatively few points across the beam waist. This would lead to smaller array size far from the waist with large number of pints across the beam size. On the opposite hand, if the array size is too small at the waist, the array size will grow large far from the waist, leaving few sample points to show the beam. Therefore, there is a tradeoff between good sampling of the beam at different locations of the beam.

For an example, in chapter . section. , we encountered multi components case where the size of the first optical component (PPD lens) was considerably larger than the size of the second optical component (eye lens). Therefore, only a fraction of the output beam from the PPD lens will shine on the eye lens which would not provide enough sampling points for a desired resolution on the image plane (retina). In order to overcome this issue without losing data points, we have used interpolation technique to fill in missing data points for the part of the beam that is outside the eye lens diameter. Interpolation is a useful technique to add new sampling data points within a range of a set of existing data. For this hybrid system of lenses, we have taken central part of the output beam from PPD lens equal to the eye lens diameter and then interpolated that part to bring it back to the original data size required for a desired resolution.

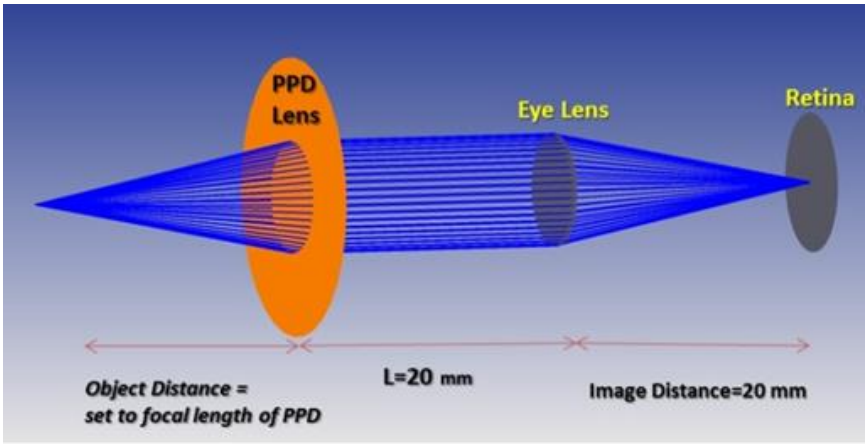

Figure A.11 Multi lens system example from chapter 5.

This process can potentially be repeated from element to element until the final image is acquired. The output field ($U_{(n+1)}$) from component "n+1", determined by $u_{n+1} = U_{n'}.e^{i(\Gamma_{n+1})}$ is the value of the input field (U_n) to component "n+1" with the added spatially dependent phase term $\Gamma_{(n+1)}(\xi,n)$ which comes from the effect of that particular component (whether it's a lens,grating,…) . This derivation is repeated until the scalar amplitude of the field on the image plane is known. Finally, the light intensity at the image plane (point spread function PSF) is determined and the Modulation Transfer Function (MTF) can be then calculated by taking the Fourier transform of PSF.

A.6 Optical System Modeling in Zemax

In this section, we will review an example of modeling an optical system in Zemax based on Physical Optics Propagation (POP) and provide some tips to help avoid the possible mistakes which could cause confusion if not known. POP is a powerful tool in the Zemax which can be used to analyze the diffraction of the beam through a custom optical

device. Based on the Zemax User Manual, we can see that it has all the correct formulation in order to perform a real diffraction calculation. Performing this real diffraction calculation is the main characteristic of the POP tab that distinguishes it from other analytical tabs such as PSF, Beam analyzer, layout … that are mostly based on ray tracing approach. Nevertheless, It might not be very straightforward to get to use this powerful tool because of it's tricky features. So In this section, an experience with the POP calculation in Zemax is shared through the following given examples. We will also review How to use POP to analyze diffracted optics, finding deflection of the diffracted beam from optical axis, importing desired phase profile into Zemax and defining a custom grid lens, analyzing position of the beams through POPD operand in merit function editor, analyzing intensity distribution of the diffracted beam using pop calculation and comparing pop calculation results with analytical and theoretical results. Our goal is to analyze the effects of our designed lens with importing it's phase profile into Zemax.

- As a basic example, let’s look at the deflection of the beam passing through a blazed grating with the following properties:
- 33 blazed in a 1-mm aperture (i.e. a=with of each blaze=30 micron and
-

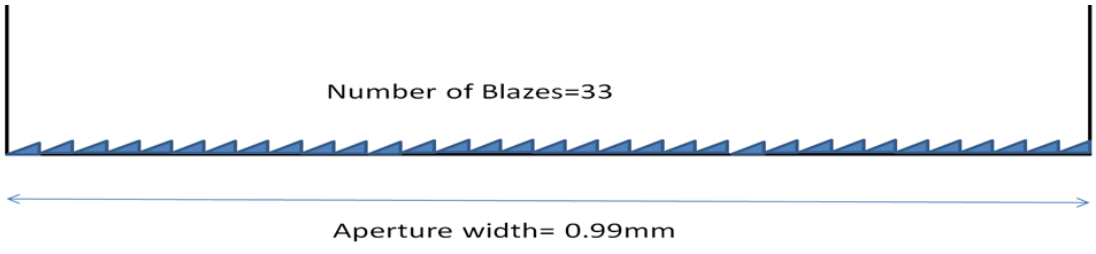

Figure A.12 Blazed grating example

- The following system was defined in Zemax:

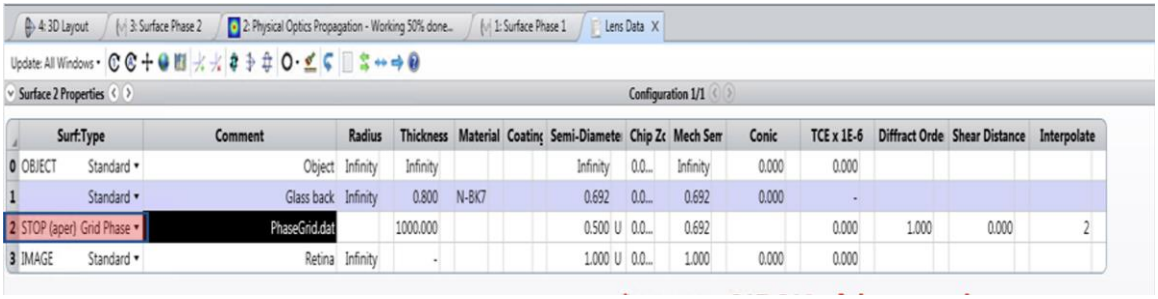

Figure A.13 Zemax screenshot of inputs

- with Surface 2 being defined as “Grid Phase” type. It would be the surface on which we import our phase profile and it would play the role of assumed physical element.
- We calculated the phase profil in Matlab and then exported in .dat format. We can then import that file into the Zemax following the steps as shown with a cursor in Figure A.14

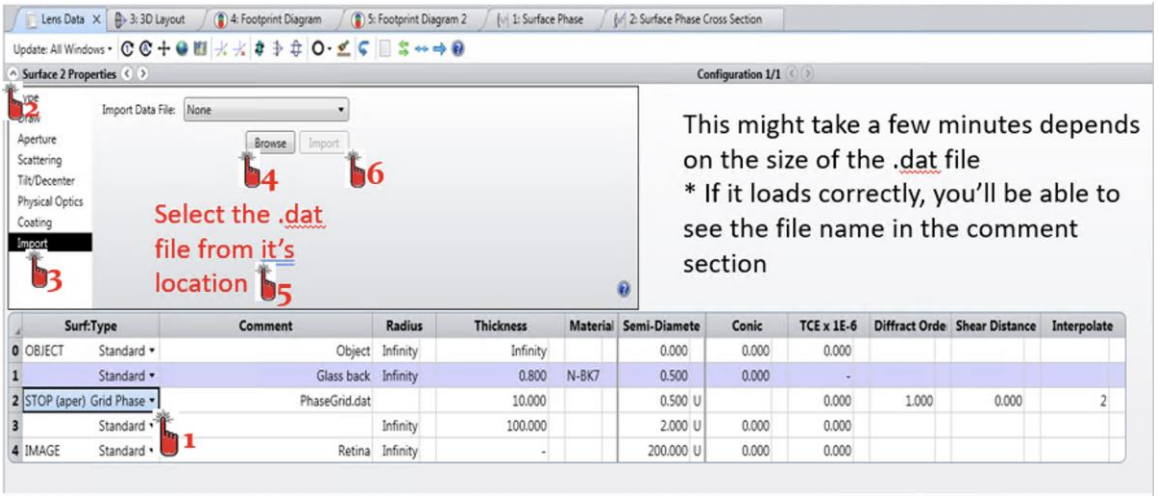

Figure A.14 Zemax screenshot of inputs

- We can also double check that the phase profile matches our desired one.

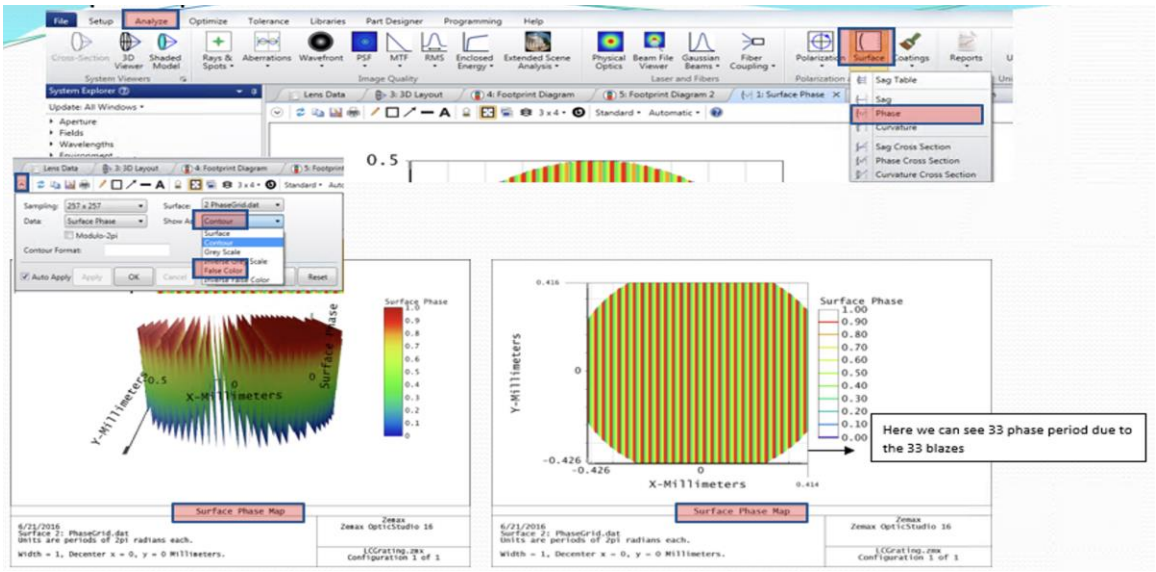

Figure A.15 Zemax phase profile

- Now, if we run POP calculation and look at the graph, we'll get:

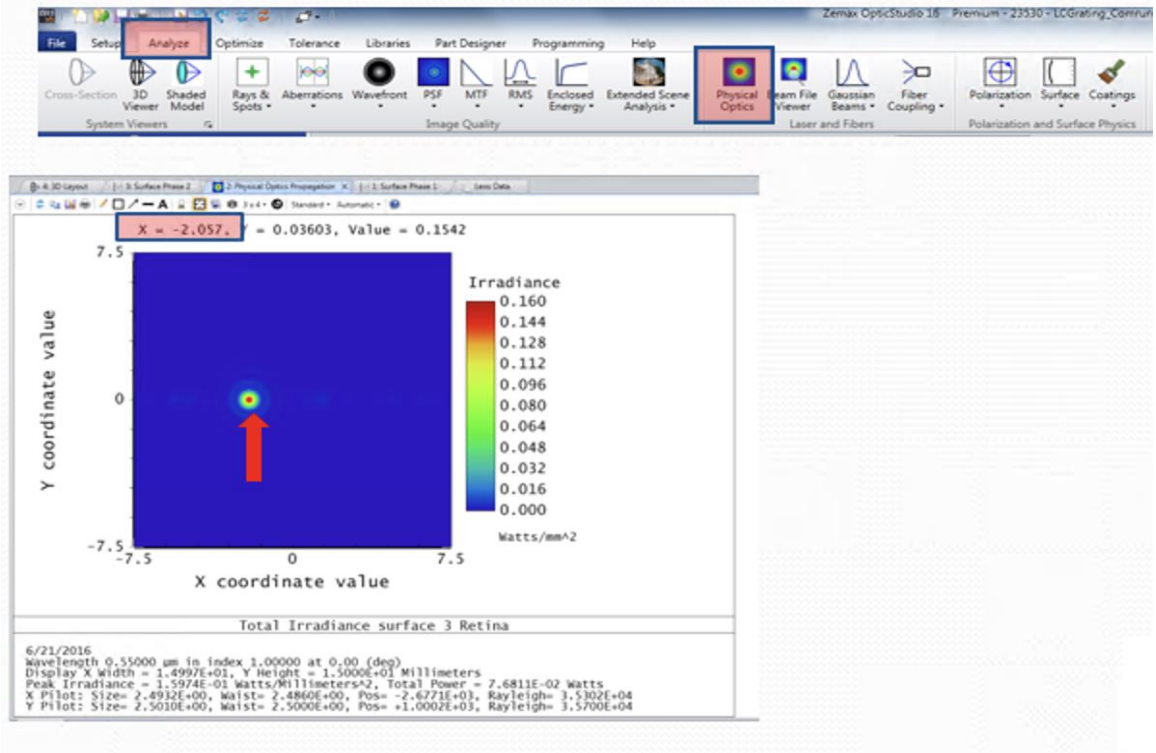

-

Figure A.16 Zemax POP calculation

-

- Which based on the given coordinates and knowing the image distance, the deflection angle is calculated as :

$$\theta = sine^{-1}\left(\frac{x}{z}\right) = 0.12\,^{\circ} \tag{A.38}$$

However, analytically, for $\lambda = 0.55\ \mu m$ light we expected a deflection angle of:

$$sin\theta = \frac{m\lambda}{a} \rightarrow \theta = 1.1\,^{\circ} \tag{A.39}$$

The confusion here arises from the fact that direct measurement of POP results doesn't match our analytical expectation even for a simple example. After a careful investigation into this matter, it turned out that the Zemax POP tab is doing its calculation centered on the chief ray, therefore the location derived by the POP window is the coordinates of the chief ray. The chief ray is defined to be the ray from an off-axis point in the object passing through the center of the aperture stop and crosses the optical axis at the locations of the pupils. The deflection angle of the chief ray as well as the deflection angle of the beam with respect to the original coordinates can be found in merit function tab withing the POP section. Based on the Zemax manual, operand 11 gives the XYZ coordinates of the center of the beam array on the end surface and operand 21 gives the XY coordinates of the centroid of the intensity distribution in local coordinates relative to the center of the beam.

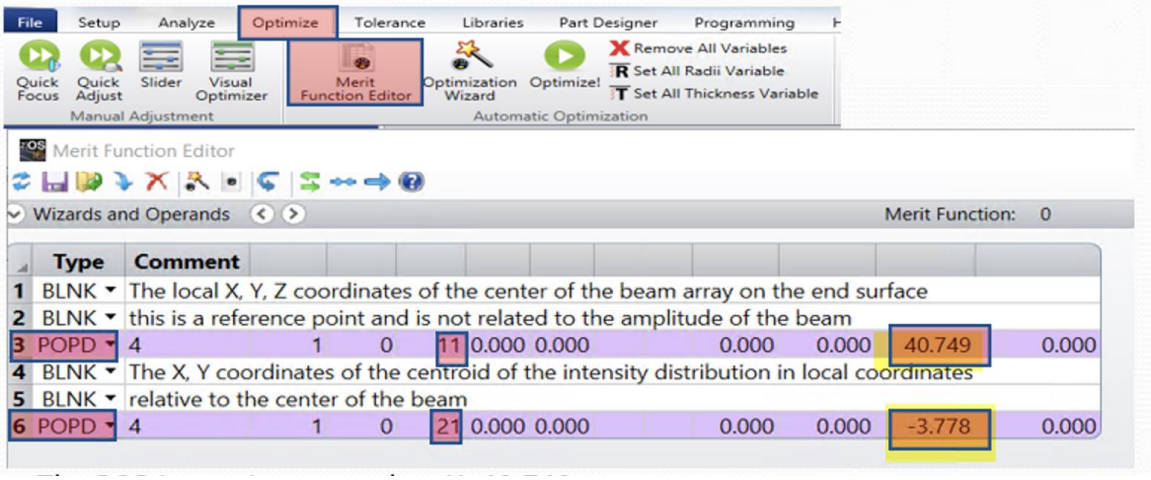

Figure A.17 Zemax Merit function

In the above example, if we sum up the results of this two operands and repeat the deflection angle calculation we will get 1.1 degree which matches to our expectation.

A second example of the Zemax system is related to parabolic phase profile. In this attempt, we are interested in finding the intensity distribution of the beam passing through a surface with a parabolic phase profile, using POP calculation.

Using the same procedure, we would import our desired phase profile which is created with Matlab. This time we want to confirm the diffracted pattern of the beam at image distance by analyzing our calculation result for the radius of the first disk in Airy pattern with the POP calculation. Knowing that when the image plane placed in the focal point, we can relate the radius of first Air y disk (first minimum) created by the diffraction to the F# of the lens, we put the image plane in the approximate range of the focal length . Similar to the previous example, we define the following optical system:

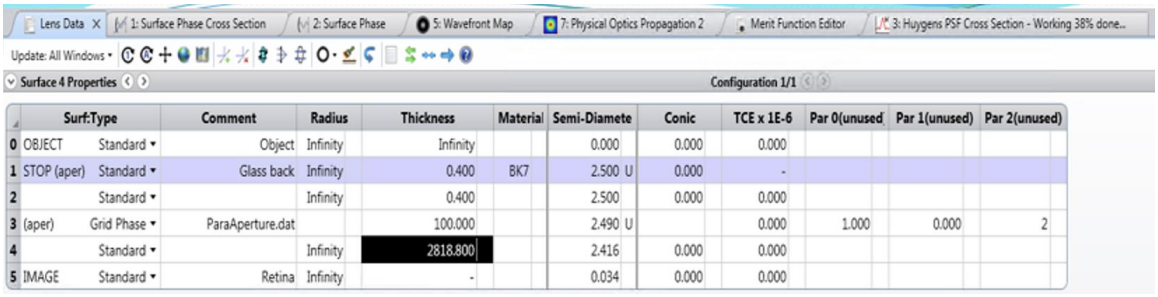

	Surf:Type		Comment	Radius	Thickness	Material	Semi-Diamete		Conic	TCE x 1E-6	Par 0(unused	Par 1(unused)	Par 2(unused)
0	OBJECT	Standard	Object	Infinity	Infinity		0.000		0.000	0.000			
1	STOP (aper)	Standard	Glass back	Infinity	0.400	BK7	2.500	U	0.000	-			
2		Standard		Infinity	0.400		2.500		0.000	0.000			
3	(aper)	Grid Phase	ParaAperture.dat		100.000		2.490	U		0.000	1.000	0.000	2
4		Standard		Infinity	2818.800		2.416		0.000	0.000			
5	IMAGE	Standard	Retina	Infinity	-		0.034		0.000	0.000			

Figure A.18 Zemax Input table

This time the surface 3 is the one we use to import the phase profile. First, we need to make sure that the lens surface is shined uniformly with the initial beam defined for the pop that is the waist size of the initial Gaussian beam should be large enough proportional to our aperture size. When we look at the lens surface through POP, we should see homogenous Irradiance across the aperture. This can be achieved inside POP menu by choosing the desired surface as “end surface”

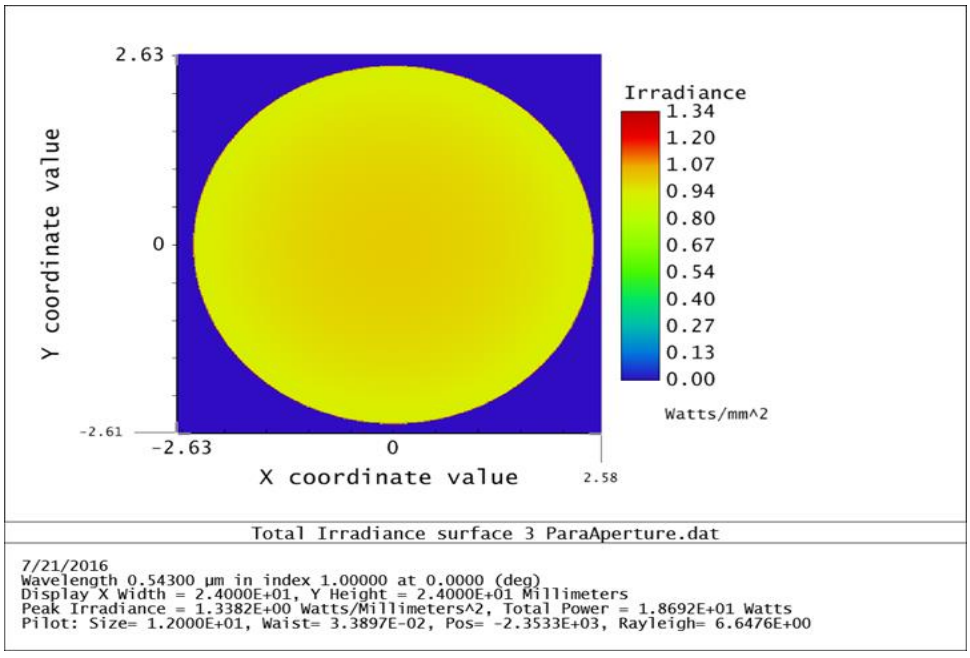

Figure A.19 Zemax – total irradiance on surface 3

After running the calculation, we can change the end surface to image plane to get the result graph. Then placing the cursor at the first minimum location, we can read the data from the graph as shown:

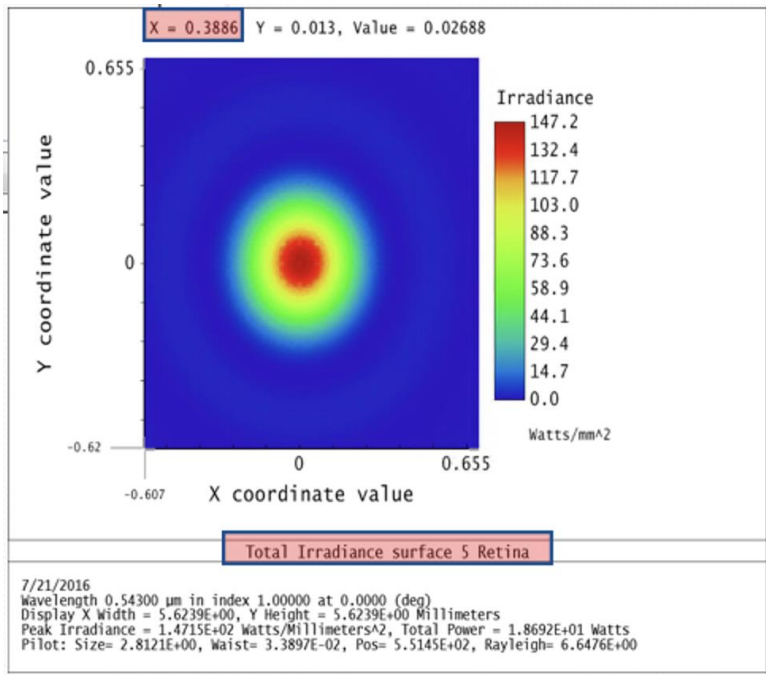

Figure A.20 Zemax – total irradiance on surface 5

This result is compatible with other analytical methods in Zemax such as “FFT cross section” and “Huygens cross section” both of which can be found under analyze menu.

As a real world example, we have also tried to obtain the point spread function of a light beam that passes through a Fresnel SPP lens which is discussed in chapter 6. Jamali et.al [79] showed both on-axis and off-axis performance of SPP lens as well as the effect of Fresnel phase segments on the shape of PSF. The results from modeling and experimental tests is shown in figure 2-15 and 3-15 of her dissertation, respectively. However, the modeling was exclusively done with

Matlab. Our goal in this example is to double check the aforementioned results and confirm the general shape of a beam passing through center and edge of a SPP lens.

For this purpose, an ideal phase profile of a Fresnel phase grid was mathematically created and imported in Zemax similar to the steps shown in previous example. Figure below shows the phase profile corresponding to the center of such a lens, PSF result obtained from POP calculation as well the the similar result corresponding to the edge of a Fresnel lens with sawtooth shape phase profile.

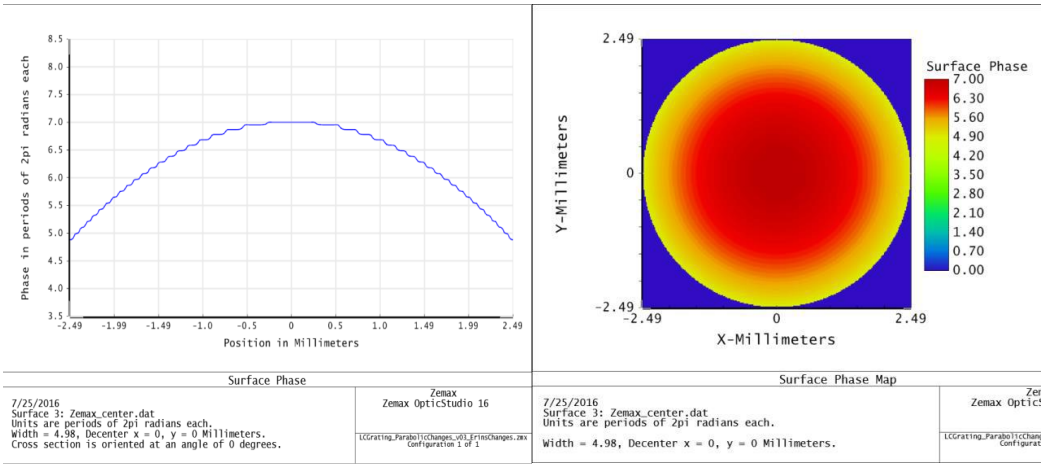

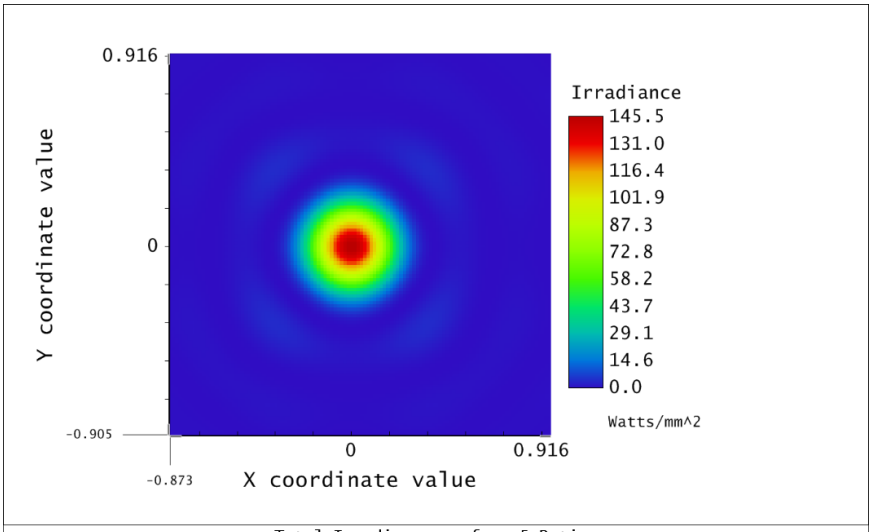

Total Irradiance surface 5 Retina

7/25/2016
Wavelength 0.54300 µm in index 1.00000 at 0.0000 (deg)
Display X Width = 3.2520E+01, Y Height = 3.2520E+01 Millimeters
Peak Irradiance = 1.4553E+02 Watts/Millimeters^2, Total Power = 1.8591E+01 Watts
Pilot: Size= 4.0830E-01, Waist= 4.8484E-02, Pos= 1.1372E+02, Rayleigh= 1.3600E+01

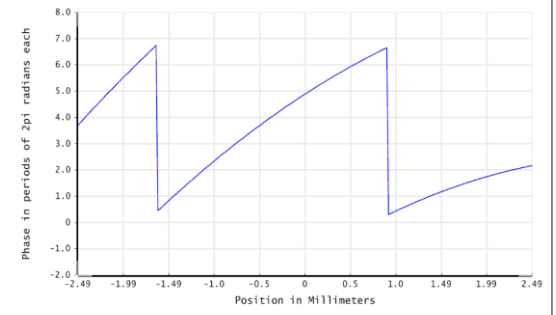

Surface Phase

7/27/2016
Surface 3: FresnelEdgeZEMAX.dat
Units are periods of 2pi radians each.
Width = 4.98, Decenter x = 0, y = 0 Millimeters.
Cross section is oriented at an angle of 0 degrees.

Zemax
Zemax OpticStudio 16

LCGrating_ParabolicChanges_v03_ErinsChanges.zmx
Configuration 1 of 1

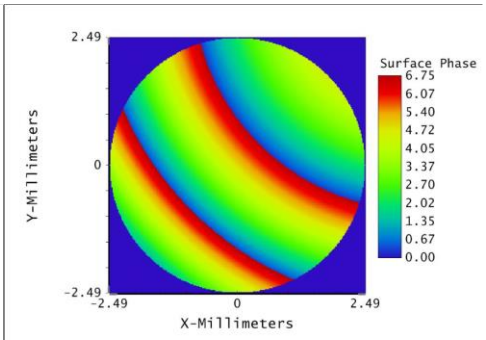

Surface Phase Map

7/27/2016
Surface 3: FresnelEdgeZEMAX.dat
Units are periods of 2pi radians each.

Width = 4.98, Decenter x = 0, y = 0 Millimeters.

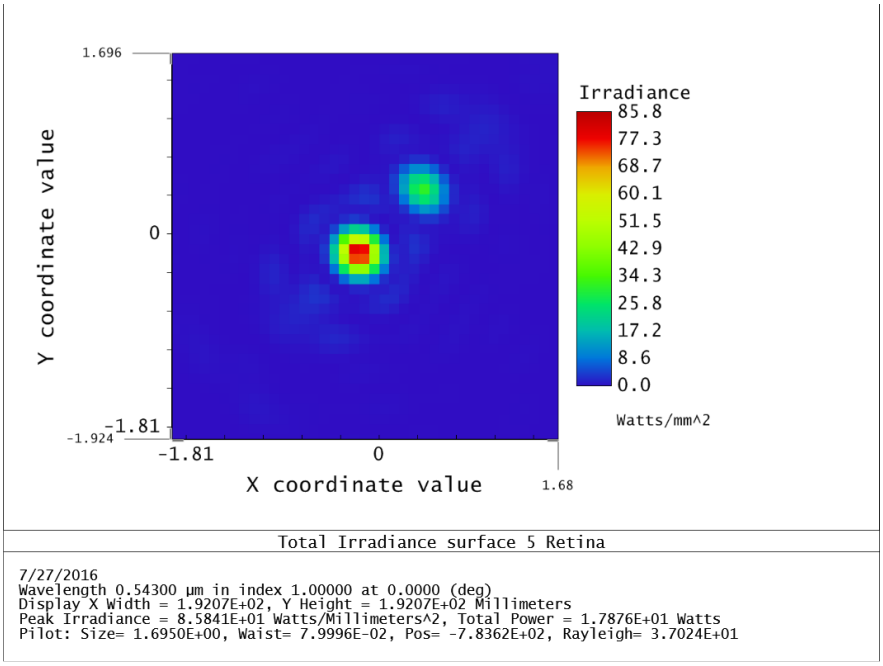

Figure A.18 Zemax – POP result , phase profile and PSF

These results confirms our expectations from PSF of a light beam passing through a Fresnel SPP lens that is discussed in [79]. The above experience is explained in more detail through a tutorial video called “Zemax Tutorial -Physical Optics Propagation POP analysis” available on www.youtube.com [111].

A.7 MATLAB Code

The following code (please find Vcopa.POM.m and GetI.m in the attached folder to this dissertation) was used to find the plots shown in figure 2.9. using Jone’s calculus we were able to follow the polarization state of the light beams as they pass through the optical

system and the liquid crystal layers. The plots are showing the intensity of the light as a function of rotation angle of the polarizers.

```
%-------------------------------------------------------------------------
---%
%     Liquid Crystal Polarization Grating Simulation Matlab-version
%
%-------------------------------------------------------------------------
---%

clc
format long
%--------------PART I. Load device and control parameters--------------
----

%--------------------Liquid Crystal parameters-------------------------
----
load opticscontrol
load VCOPA_opmdata
tic;
nxx = nx;
nyy = ny;
nzz = nz;
clear nx ny nz
theta1 = asin(nzz);

% According to the sign of nx&ny, decide the phi1 direction
for countx = 1 : Numx+1
    for county = 1 : Numy+1
        for countz = 1 : Numz+1
            if nxx(countx,county,countz)<0
            phi1(countx,county,countz)=pi-
asin(nyy(countx,county,countz)/sqrt(nxx(countx,county,countz)^2+nyy(cou
ntx,county,countz)^2));

            elseif nxx(countx,county,countz)>=0 &&
nyy(countx,county,countz)<0

phi1(countx,county,countz)=2*pi+asin(nyy(countx,county,countz)/sqrt(nxx
(countx,county,countz)^2+nyy(countx,county,countz)^2));
            else

phi1(countx,county,countz)=asin(nyy(countx,county,countz)/sqrt(nxx(coun
tx,county,countz)^2+nyy(countx,county,countz)^2));
            end
        end
    end
end
VCOPAConfigureData = getappdata(0,'VCOPAConfigureData');
d=VCOPAConfigureData.thickness*1e-6;
```

```
randnumber=round(rand*1000);

lambda1=[0.46*1e-6 0.55*1e-6 0.62*1e-6 1*1e-6];
for oo=1:3
    lambda=lambda1(oo)

alpha1=1:2:90;
alpha1=flip(alpha1);
for o=1:45
alpha=alpha1(o);

% jones method
for ii=1:Numx+1
    for jj=1:Numy+1
        inputtheta = pi/2-theta1(ii,jj,1:Numz+1);
        inputgamma = phi1(ii,jj,1:Numz+1);
        I(ii,jj) =  GetI(inputtheta,inputgamma,d,lambda, alpha);
        end
end

legendInfo{oo} = ['Wavelength= ' num2str(lambda1(oo))];

I_bt=I(1,:);
I=I';
I_at=I(1,:);
IS(:,oo,o)=I_at;

end
%
figure(randnumber);
hold on
set(groot,'defaultAxesColorOrder',[0 0 1;0 1 0;1 0 0],...
      'defaultAxesLineStyleOrder','-|--|:')
  x_x=alpha1;
  y_y1=IS(61,oo,:);
  y_y=y_y1(:);
plot(x_x,y_y);
title([' Normalized Intensity vs rotational angle of polarizers']);
xlabel('alpha(deg) ');
ylabel('Normalized Intensity ');
set(gca,'XTick',0:5:90);
axis([0 90 0 1]);
hold off
legend(legendInfo)

end

function [ I ] = GetI( theta,gamma,d,lambda,alpha )
%GetI: Use Jones matrix to calculate and get the light intensity
%      pass through crossed polarizers and a liquid crystal model
%       ( Only consider normal incident )
%   [ I ] = GetI( theta,gamma,d,lambda )
```

```
%
%  in:  th = given theta profile along z axis at a point(x,y)
%       phi = given phi profile along z axis at a point(x,y)
%       d = given LC cell thickness
%       lambda = wavelength of light
% out:   I = Light Intensity after cross polarizers and LC cell
%
VCOPAConfigureData = getappdata(0,'VCOPAConfigureData');

no =VCOPAConfigureData.no;
ne =VCOPAConfigureData.ne;

              % Define the rotation angle of the crossed polarizer (in
degrees)
alpha=alpha*pi/180;

nn = length(theta);          %number of layers is Z
delz = d/(nn+1);             % thickness of each layer




Ein = [1;i];           %  circular light input
Px=[1 0;0 0];            %Polarizer jones matrix in x direction
R1=[cos(alpha) -sin(alpha); sin(alpha) cos(alpha)];    % left side
rotational matrix
R2=[cos(alpha) sin(alpha); -sin(alpha) cos(alpha)];     % right side
rotational matrix
P=R1*Px*R2;                % old x-polarizer rotated by alpha
Ein=P*Ein;              %apply the effect of polarizer

for ii = 1:nn
    beta = theta(ii);
    ne_eff = (ne*no)/(sqrt(no^2*sin(beta)^2+ne^2*cos(beta)^2));
    phi0 = 2*pi*delz*no/lambda;
    phie = 2*pi*delz*ne_eff/lambda;

    %jones matrix here is the result of Lc matrix sandwiched
    % between rotational matrix by angle of gamma which is defined as
    % azimuthal LC angle
    Jones = [ cos(gamma(ii))^2*exp(i*phie)+sin(gamma(ii))^2*exp(i*phi0)
sin(gamma(ii))*cos(gamma(ii))*(exp(i*phie)-exp(i*phi0))
              sin(gamma(ii))*cos(gamma(ii))*(exp(i*phie)-exp(i*phi0))
sin(gamma(ii))^2*exp(i*phie)+cos(gamma(ii))^2*exp(i*phi0)];

    E_middle = Jones*Ein;        %apply the jone matrix of the next
layer on input E-field
    Ein = E_middle;              % Take the output from layer ii as
input of the next layer
    Eout= E_middle;
```

```
end

Py=[0 0;0 1];        %Polarizer jones matrix in y direction (Analyzer)
A=R1*Py*R2;                % old y-analyzer rotated by the same alpha
angle
Eout=A*Eout;
I = Eout'*Eout;
```

APPENDIX B – PROCESS FOR RM STABILIZED CELLS AND CAVITIES

In this Appendix, details of the fabrication process of the THE-FFS-PPD including layer deposition, patterning, coating, rubbing and cell assembly are represented. The process is based on standard wet photolithography used in display industry. We did all of the fabrication steps excluding layer deposition in the clean room of Advanced Materials and Liquid Crystal Institute (AM-LCI).

B.1 Scribing

- Using Villa Precision, Inc (VPI-GS210) automated glass scriber machine, the 14” by 16” sheet of ITO coated glass is scribed into 4” by 4” pieces.

Figure B.1 Villa Precision, Inc (VPI-GS210) automated glass scriber machine

B.2 Cleaning

- The glass substrates are next to be thoroughly cleaned. The substrates are first hit by Nitrogen spray gun to remove the tiny shred of glass produced by scribing. The substrates then sit in the ultrasonic machine that includes 10 ml of all-purpose Cavi-Clean liquid detergent diluted in 15 liter of DeIonized (DI) water at 65° C for about 15 minutes.

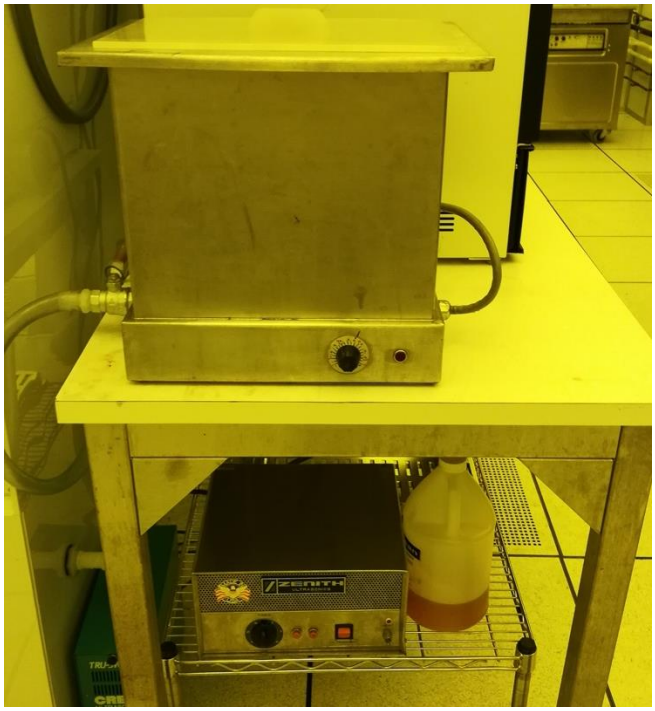

Figure B.2 ultrasonic machine in AMLCI cleanroom facility

- The substrates are then rinsed with DI water followed by an Isopropanol rinse. The former rinse is to remove the detergent from the surface while the latter rinse is to remove the water to avoid sticking components when dried.

- The batch of the substrates were dried afterwards at 90° C oven for 10 minutes. Prior to spin coating of photoresist material, an additional 10 minutes of bake at 200° C was used to make sure the surface is completely free of any humidity.

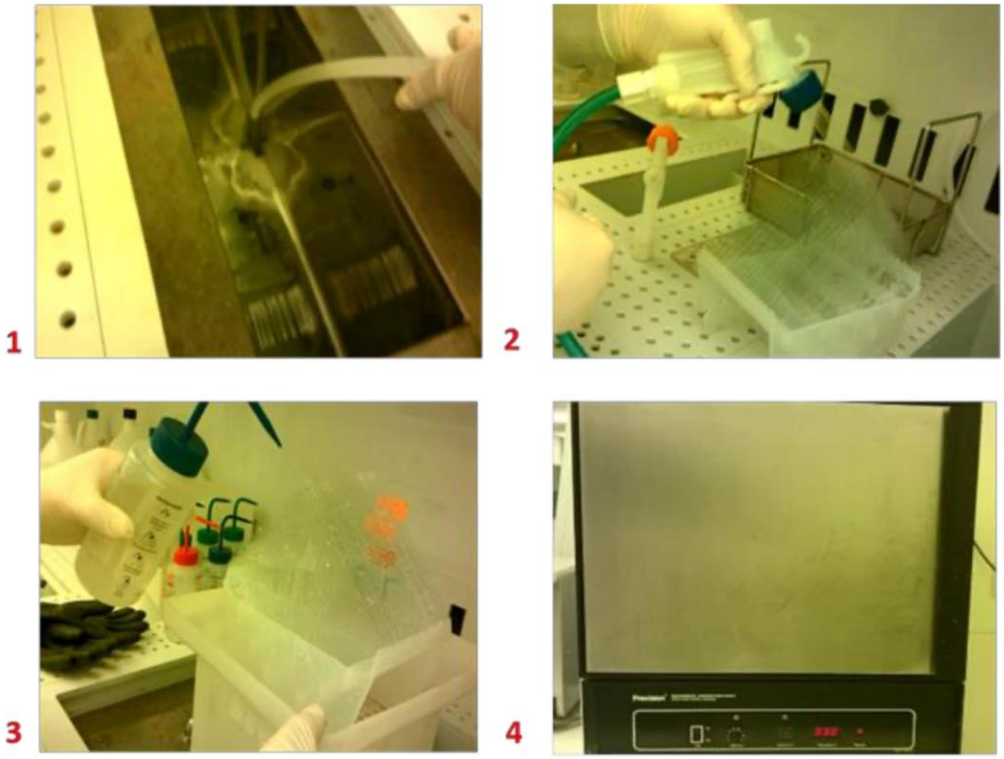

Figure B.3 glass cleaning steps

Figure B.4 Cleaning station

B.3 First ITO layer Patterning

- The substrate was then spun coated with photoresist-S1818 (diluted 1:3 with AZ EBR) at 1500 rpm for 30 s followed by 90s bake at 95° C hot plate to allow the solvent to evaporate.

Figure B.5 Spin coating station

- After the photoresist coating, certain areas of the substrate has to be exposed with UV light (350W at 365nm) for 5 seconds in order to be soluble in low PH

carboxylic acid. UV light breaks down the polymer chain of positive photoresist so that it will be soluble. A mask that covers desired pattern was brought into close contact with the substrate using Karl Suss mask aligner. At this step, the mask is covering uniform areas of ground plate at the 1st layer and there is no need for alignment since no prior pattern is present.

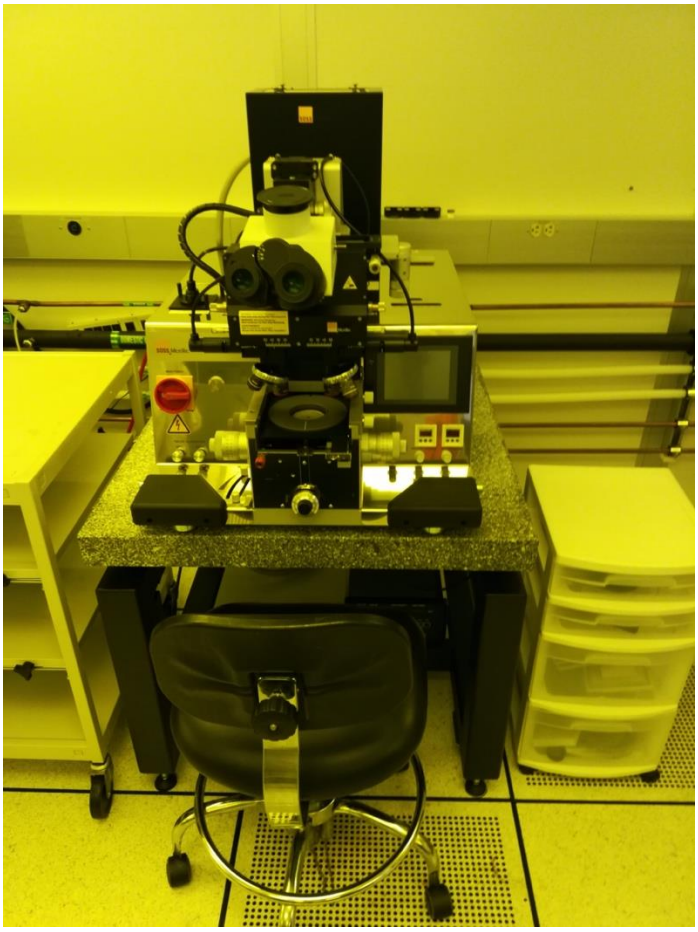

Figure B.6 Karl Suss mask aligner

- This step contains wet processing. After UV exposure, the exposed area will be removed by getting into contact with low PH carboxylic acid while non-exposed

areas of photoresist will not be affected. After 1 minute of dipping and shaking the plates in the solution, they are placed in DI water shortly before the next step.

- Next, Hydrochloric (HCL) solution (diluted 1:2 with DI water) is used to etch the ITO layer outside of the areas covered by the mask. Depend on the HCL concentration, this step can take a few minutes. Before the next step, the resistance of open areas are measured to make sure there is no conductive pieces left. Also, another quick rinse before the next step helps not to mix the different solutions.
- As the last step of wet processing, the photoresist on top of remained ITO areas are removed by the help of acetone. The plates are then going through another cleaning cycle as explained before.

B.4 SiO_2 + ITO layer deposition

- Next, a thin layer of SiO2 (~150 nm) is deposited on the substrate using vacuum magnetron sputtering machine by Material Research Cooperation (MRC) [ref]. The target material is sputtering using a combination of electromagnetic wave and plasma ionization process. Constant magnetic field orthogonal to the cathode electric field is generated by magnets positioned on the back of the magnetron cathode. Imposed magnetic field produced by magnetron sputter gun increases the path length of electron flow, enhancing the plasma ionization density near the target surface, resulting in higher sputtering rate. The process also include a plasma ionization created by using a heavy gas (i.e Argon for SiO2 deposition or mixture of Argon and Oxygen for ITO deposition) under high vacuum and high

electric field. Depend on the application, direct current (DC) or radio frequency (RF) power sources can be used. In DC sputtering, suitable for ITO layer deposition, target material is bombarded with ionized gas molecules until target molecues “sputtered” off into the plasma. On the other hand, in RF sputtering which works better with insulating layer (e.g SiO2), electric field is oscillating at radio frequencies which in turn propagates electromagnetic waves. Radiated waves with changing sing at driving frequency avoid charge-up effect which is advantageous for insulating material. The base pressuer in MRC is usually in the order of 10^{-6} torr. After a beam of high energy free electrons inside the plasma chamber bombards the surface of the cathode, the target material is “evaporated” and will be deposited on the anode surface (substrate).

B.5 2nd ITO layer patterning

- Starting from photoresits coating, 2nd ITO layer was patterned in a similar manner to the first layer.
- The main difference is that for the deposited ITO layer, a DI water diluted (1:3) acid was used to decrease the density. It usually takes less time to etch the deposited layer since it’s in the amorphous state. The etching time is variable depend on the solution density and being measured carefully after a few test trials. In test trial, different spots of the plate is etched with different timing and the resistance is being measured on each spot until a desired timing is found.

Following the similar steps as the first layer patterning, the remained photoresist is then removed by acetone and the substrates go through another cleaning cycle.

B.6 Rubbing, glue dispensing and scribing

- Next, the plates were spun coated with Polyimide PI 2170 material filtered with 1 mu filter at 1500 rmp for 30 seconds. The plates rest of 80C hot plate for 5 minutes to allow solvent evaporation. Then, they are baked at 210 C for 60 minutes.
- Then, the cells were rubbed with a properly weighted fiber block at 3 ° angle with 10 repetition with respect to a line perpendicular to the electrode lines. Since a negative LC material is used, the director will tend to align perpendicular to the fringe field upon applying voltage. Therefore, the pre-alignment angle was set to a few degrees (3 degrees in this case) from a reference line that is perpendicular to electrode strips. Considering the mirror effect from assembly of plates on top of each other, both plates are initially rubbed in same direction so that when assembled they will have opposite directions with respect to each other.

Figure B.7 Oven in AMLCI cleanroom facility

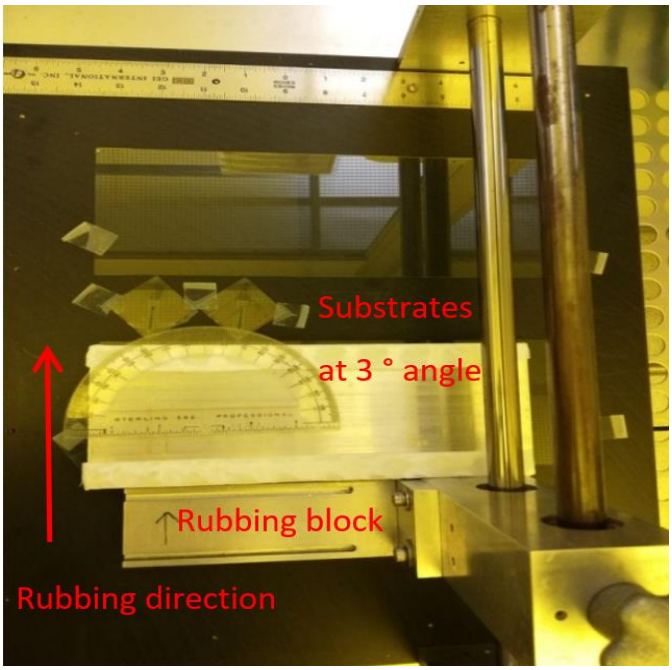

Figure B.8 Pre-alignment station in AMLCI cleanroom facility

- After rubbing, UV curable glue was dispensed on the substrates using programmable Asymtek XY dispenser machine. The speed can be adjusted to achieve a desirable line thickness.

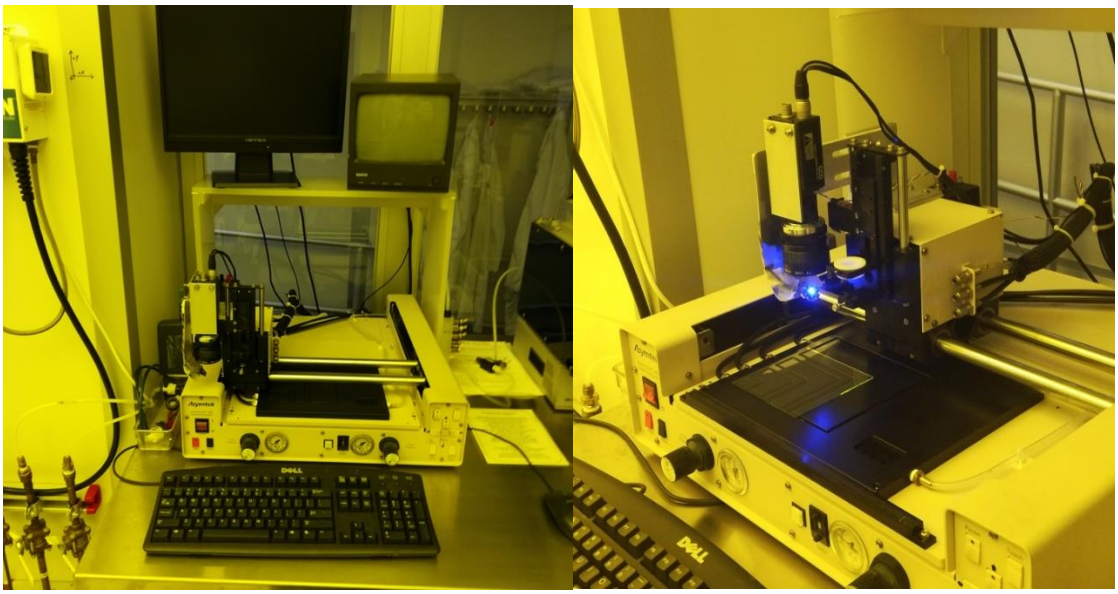

Figure B.9 Asymtek XY dispenser machine in AMLCI cleanroom facility

- Before assembly, the 4” * 4” substrates were scribed into 4 individual pieces with respect to the mask design considerations. Individual pieces allow for a more controlled assembly process. The individual pieces were designed completely symmetric, making no difference on which one places on top.

B.7 Cell assembly

- Next, 3.6 mu glass fiber spacers were sprayed on one substrate. Usually, one substrate were sprayed with spacers and the other one carried the glue.

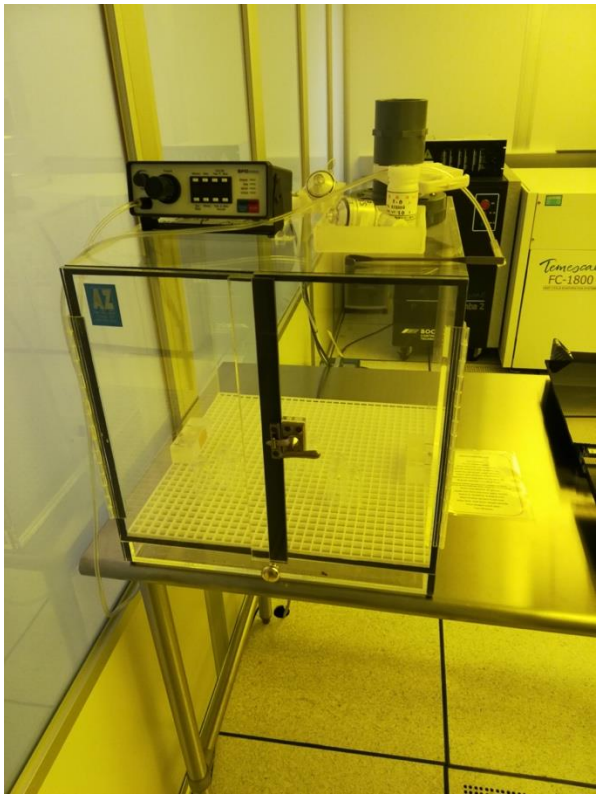

Figure B.10 Spacer dispensor

- As the most challenging part of the process, the cells are supposed to be assembled with sub micron precision. Therefore, any loose movement during the aligning process should be restricted. One important factor is controlling the amount of glue which affects the flexibility of the substrate movement with respect to each other. However, even small vibrations including building shakings that would not normally sensed can be enough to mess up the alignment. Therefore, it was found that the plates under vacuum would have more rigid situation that would provide enough stability for the process. Consequently, a mechanical stage was used to allow for vacuum while providing XYZ movement. A thin plastic wrap was put on top of vacuum stage to allow suction. inserting a

favorable uniform force on the top surface. The stage is then was set up under microscope lenses with reflection mode light. Another important factor is to maintain enough depth of focus (DOF) to be able to see both plates which are separated by more than an electrode width. On the other hand, higher magnification is preferred but there is an optical trade-off between depth of focus and magnification. To do so, a 20x lens under adjusted lighting was found to works best to balance the magnification and DOF. Digital zoom-in was then used to help reaching the required magnification. Since the active area is much smaller than the substrate dimensions, a small hole on the plastic wrap right on top of the active area prevents any blurring effect under microscope. After finding the right optical conditions, the position of the substrates were continuously adjusted until an ideal position is reached.

- 

- *Figure B.11* Cell assembly station under vacuum

-

- Once the alignment is correct, all or part of the glue were cured by UV light gun. Then the cell is patched to make sure the glue is UV cured all over the cell except an opening gate.

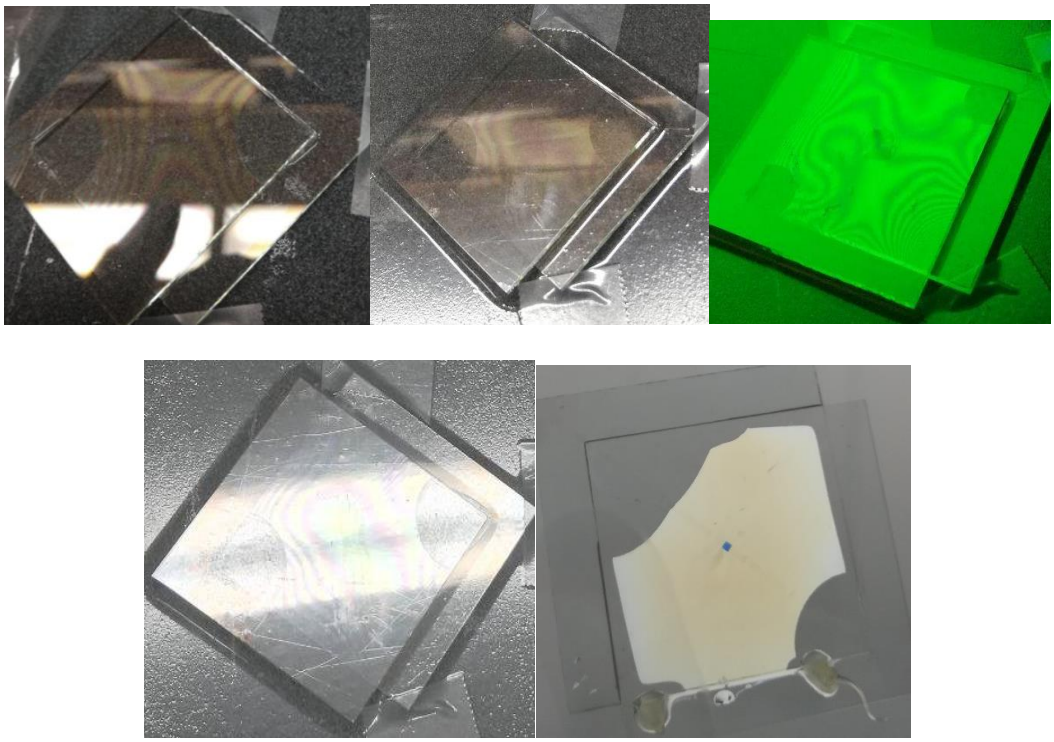

Figure B.12 Cell assembly at different steps

B.8 Filling, end sealing and bonding

- The cell was then filled under vacuum with MLC-6608 material with birefringence of 0.08.
- Next, the cell was put under 14 psi pressure in press machine and end sealed with UV cured glue. The ledge was also cleaned, and the extra PI material was removed on surface by plasma pen to prepare the ledges for bonding.

- Finally, the ledges were bonded using anisotropic conductive film (ACF) to create electrically conductive adhesive bonds. The cell is ready for testing at this setp.

- 

-

- *Figure B.13 a)* Liquid crystal material b) End seal press machine

-

- 

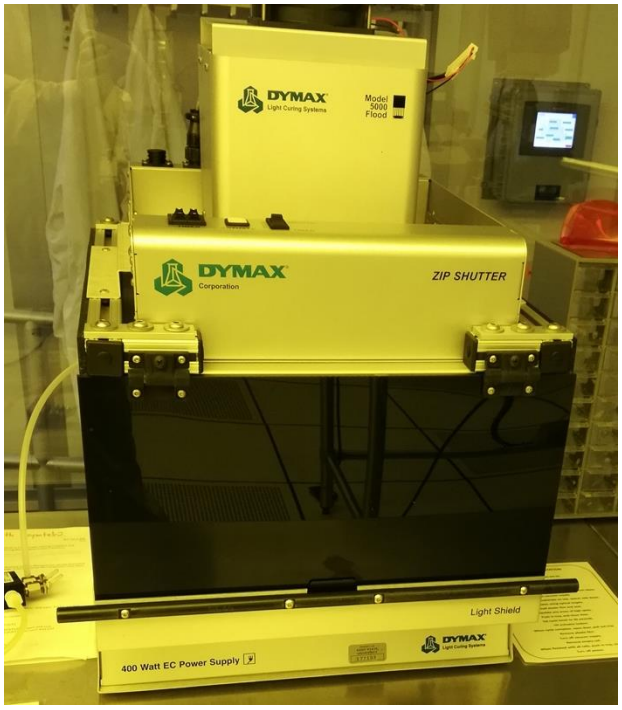

- *Figure B.14 a)* PlasmaPen machine b) DYMax UV light station

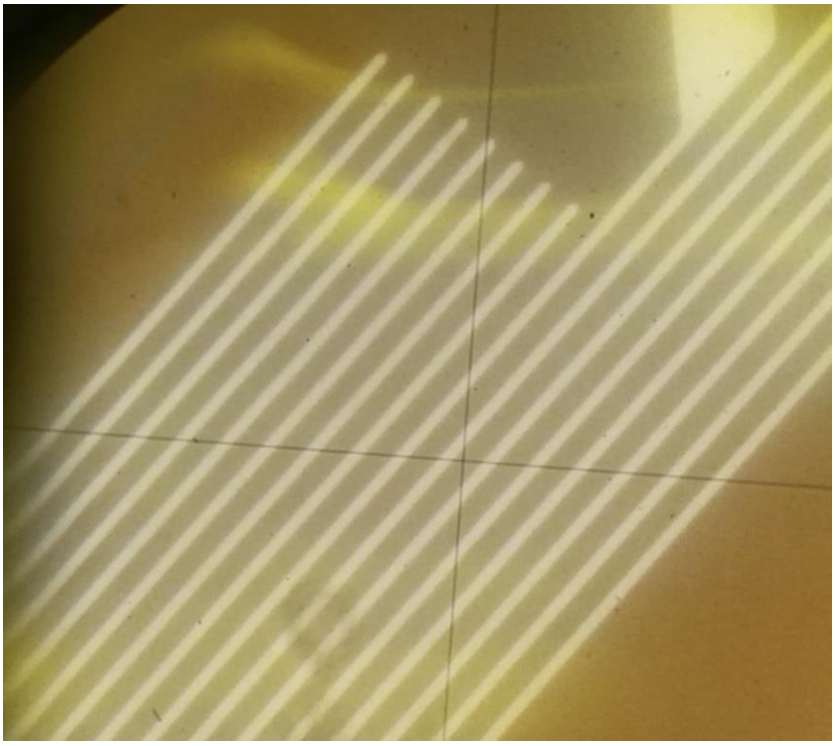

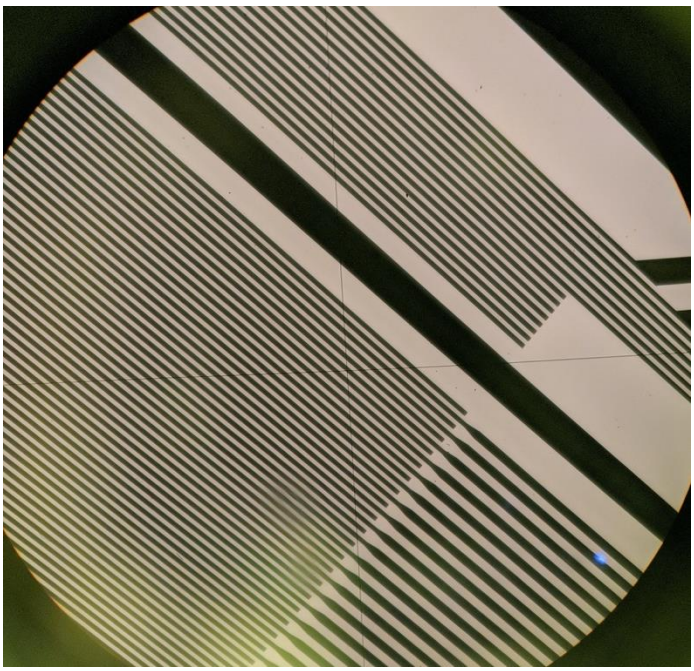

- *Figure B.15 a)* & b) etched ITO electrode lines under microscope

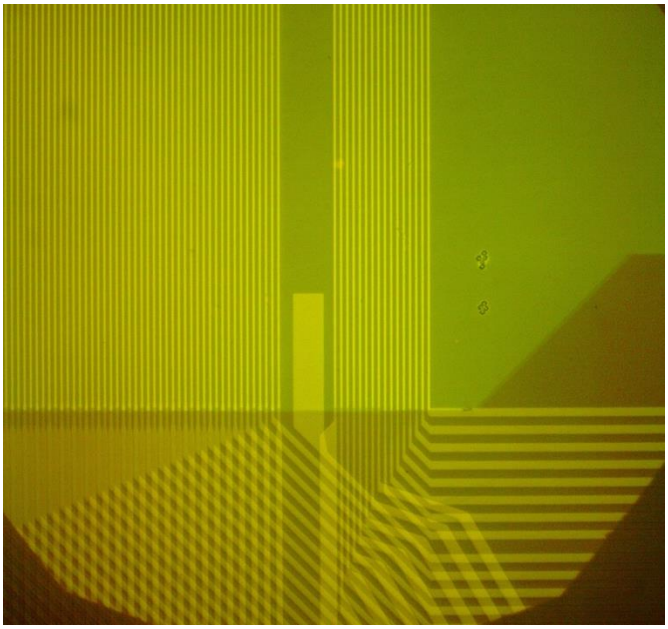

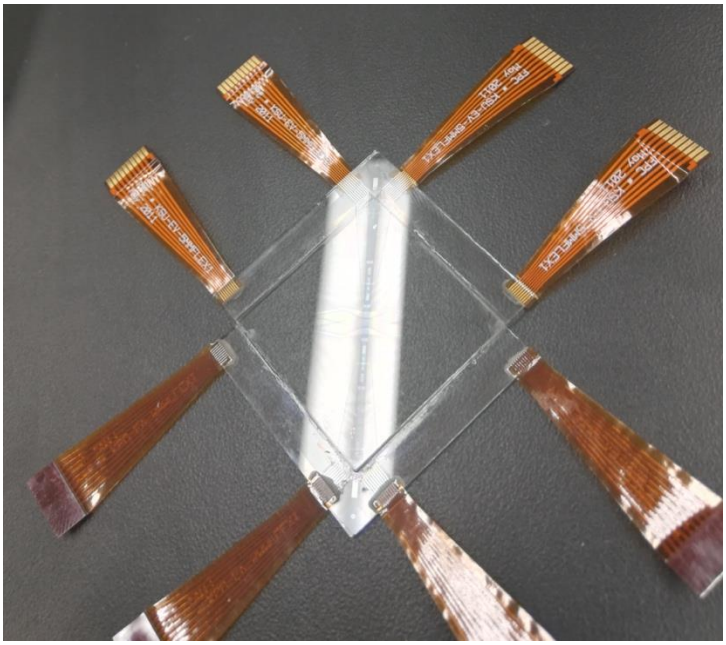

- *Figure B.16 a)* etched ITO electrode lines under microscope

  b) assembled cell final look

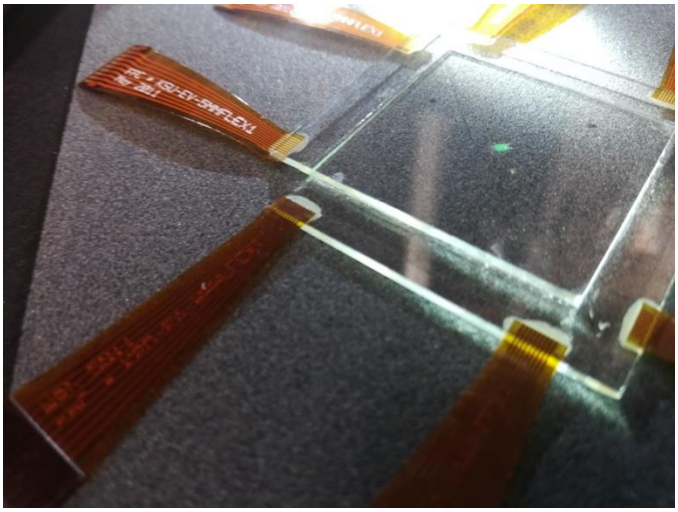

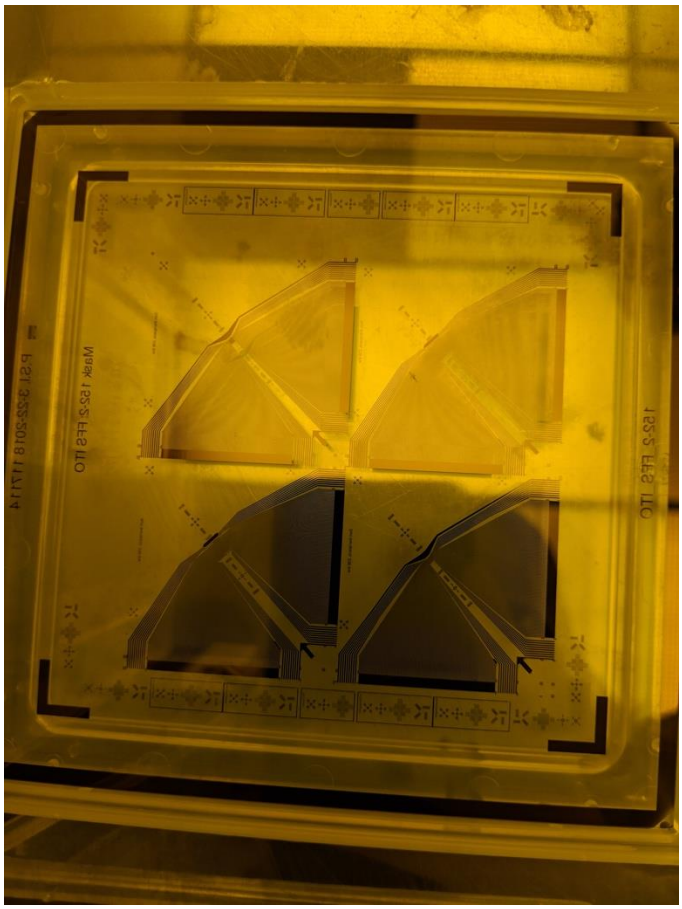

- *Figure B.17 a)* assembled cell final look

- *B)Mask used for ITO etching*

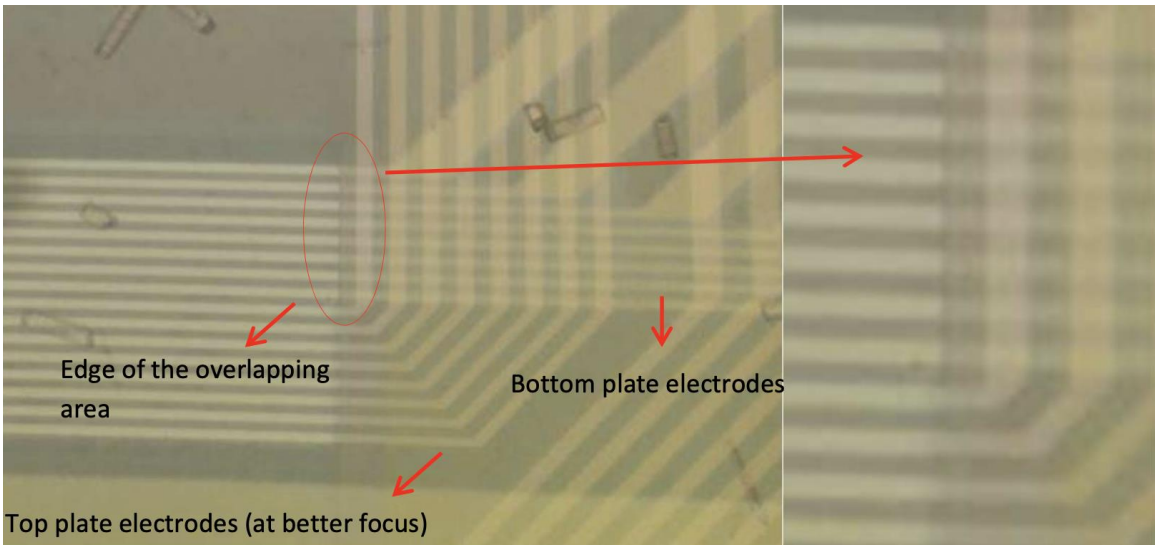

- *Figure B.18 Assembled* ITO lines from both plates under microscope

APPENDIX C – CHARACTERIZATION METHOD OF THE DEVICE

After completion of the fabrication process, making a connection to the ground plate (1st ITO layer) and connecting the flex bonding, the cell is being set up under microscope for evaluation tests. During this time, the connections are very sensitive to any unwanted voltage or electrical charges that can be accidentally carried to the electrodes. Even randomly touching the flex conductive parts can carry enough charge to cause damage to the electrodes specially where they get micron size narrow toward the active area. So, extra cautious should be taken to avoid any unexpected touch to conductive areas. The device should be fixed under microscope with crossed polarizers, ideally with a 4D adjustable stage (XYZ dimensions plus rotation) to allow the following tests. If the electrodes are etched neatly during the fabrication process, there should be no short between them and they can be individually activated. The following tests are the main verification tests to check the required criteria for a quality performance device.

C.1 Cell Assembly check

- The first criteria is to double check the alignment of substrates relative to each other to make sure that the patterns are right at top of each other. As mentioned in section 4.2, even a small misalignment with result in dramatic degradation of the cell performance. Therefore, it is vital that the electrodes are aligned with respect to each other with sub-micron precision. To check the alignment, we use reflection mode light of the microscope to see the reflection light from ITO electrodes. If perfectly aligned, the electrodes from bottom surface is covered by

top surface pattern so the best area to check this is right at the edges of active area where the top and bottom electrodes start to overlap. These locations are indicated with red arrows in figure below. the brighter lines are the ITO electrodes from top surface while the dimmer lines are from the bottom surface. These lines should be exactly matched in a line on both sides of the overlap area to make sure there is no offset on either side.

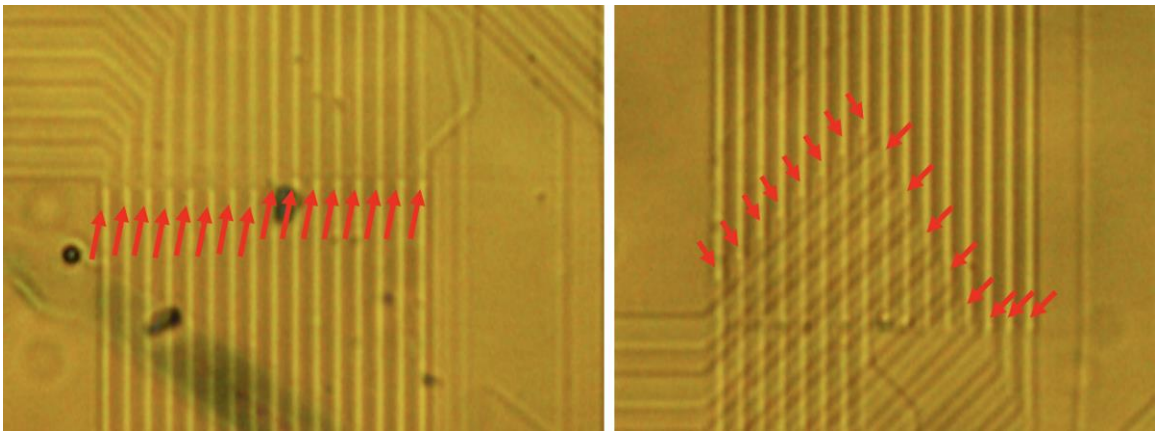

- *Figure C.1* Assembled etched ITO lines from both plates under microscope

C.2 Alignment check

- Next, we can check the surface pre-twist alignment on each surface, considering the definitions in section 4.3. Based on definitions given in section 4.3 (graph 4.7), we can refer to the plate with positive pretilt as “P Surface” and the one with negative pretilt as “N surface”. Due to the fact that both plates were initially rubbed with same angle and then the top surface direction was mirrored when assembled on top of the other plate, the surface facing up which is closer to

polarizer have always positive pretilt (P surface) while the surface facing down which is closer to analyzer has always negative pretilt (N surface). We refer to the initial position of polarizers (i.e. polarizer is at 0 ° and analyzer at 90) as “zero state”. The alignment check then is verified by slightly rotating polarizer and analyzer at a time in opposite direction. Rotating polarizer by +3 degree and analyzer by -3 degree should result in a darker state compared to the zero state.

-

C.2 Finding estimated director angle

After we confirmed the surface alignment by rotating polarizers, we can estimate the director angle from the following procedure.

To be able to track the director profile we rotate polarizer and analyzer separately by some angles until a dark state happens. When the area is at its darkest state, we know that the director falls in the direction of polarizer at the bottom surface and falls perpendicular to the analyzer direction at the top surface (exit surface) so that the light gets blocked. Data is represented as angle of rotation for both polarizer and analyzer. Therefore, we can expect for director angle at P surface to be :

$$\theta_0 = 0\,^\circ$$
$$\theta_P = \theta_{rotation}$$
$$n_{director} = \theta_P$$
$$\rightarrow \boldsymbol{n_P = n_{director\ at\ P\ surface} = \theta_{rotation\ of\ polarizer}}$$

And for analyzer’s angle :

$$\theta_0 = 90\,^\circ$$
$$\theta_A = \theta_{rotation} + \theta_0$$
$$n_{director} = \theta_A - 90^\circ$$
$$\rightarrow \boldsymbol{n_N = n_{director\ at\ N\ surface} = \theta_{rotation\ of\ analyzer}}$$

Where θ_0 is the initial angle of the polarizer/analyzer at zero state as defined.

Voltage	Estimated Director angle
10 V at 2nd step	n_P = -70 °, n_N = -62 °
8 V at 2nd step	n_P = -60 °, n_N = -60 °
6 V at 2nd step	n_P = -60 °, n_N = -58 °
4 V at 2nd step	n_P = -45 °, n_N = -38 °
3.5 V at 2nd step	n_P = - 40 °, n_N = -38 °
3 V at 2nd step	n_P = -30 °, n_N = -32 °
2.5 V at 2nd step	n_P = - 26°, n_N = -24 °
2 V at 2nd step	n_P = - 15°, n_N = -20 °

Table C.1 estimated director angle vs activation voltage

- Alternatively, we can keep the polarizers fixed and rotate the cell under the microscope to verify this.

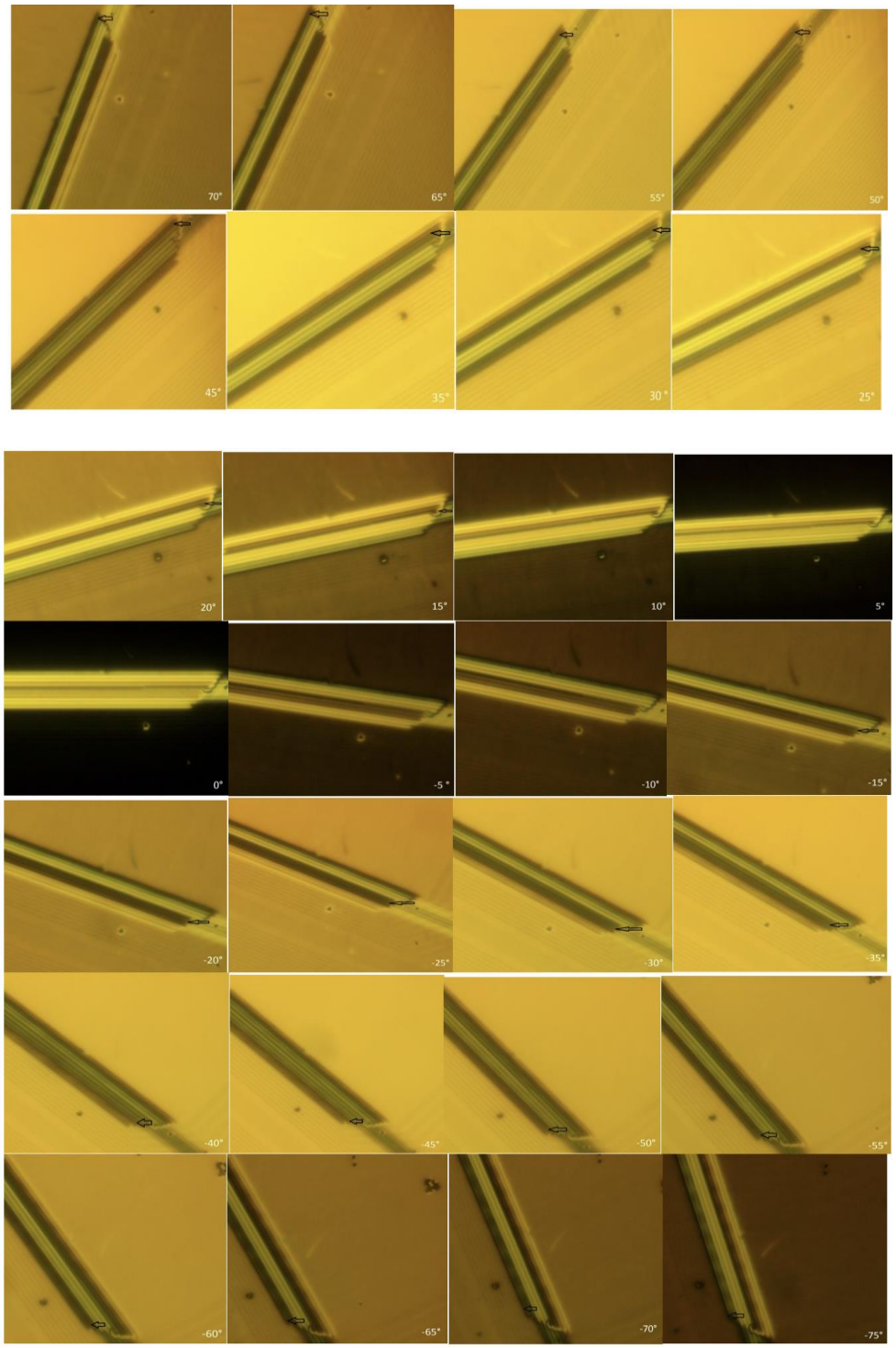

Figure C.2 Polarized optical microscope (POM) pictures of ITO test lines at different rotational angles under fixed polarizers

C.3 Extinction angle check

- In this test, the exposure was set to over-expose the cell so that we can find minimum for extinction angle Polarizers were rotated in steps of 5 ° in one direction to find the minimum. Then, we analyzed the pictures with Matlab to plot Intensity variation over the aperture along a line that is perpendicular to the electrodes. Some samples of these plots are shown here.

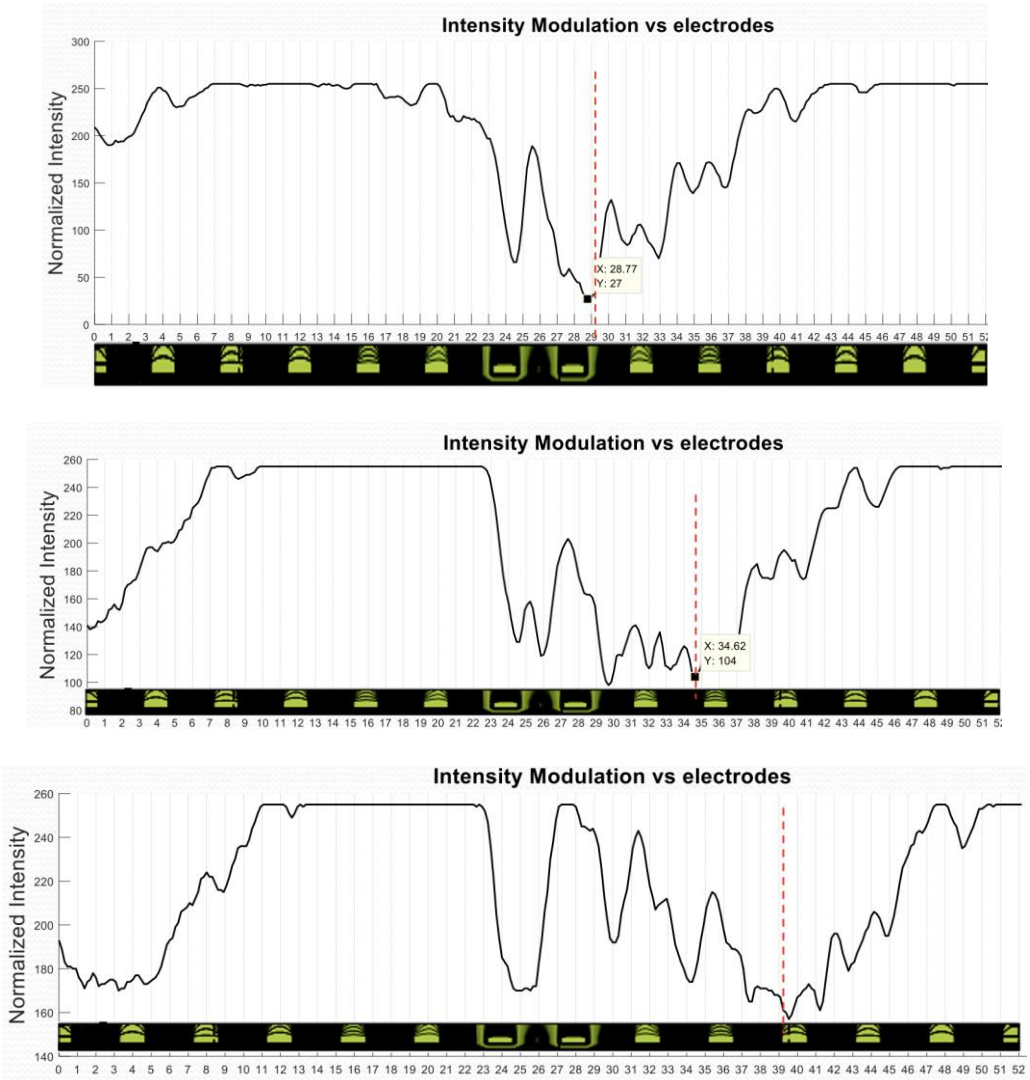

Figure C.3 Intensity modulation vs x-axis (aperture)

C.4 Uniformity test

Data shown in figure 4.10 verified the uniformity of the director by measuring S3 polarization factor. Polarizer was at 0 ° (y- axis) and analyzer was at 90 ° (x-axis) Quarter wave plates were calibrated separately to be exactly at the maximum transmission position (both angles was found very close to 45 ° and -45 °)

The graphs were normalized to the average value of maximum transmission.

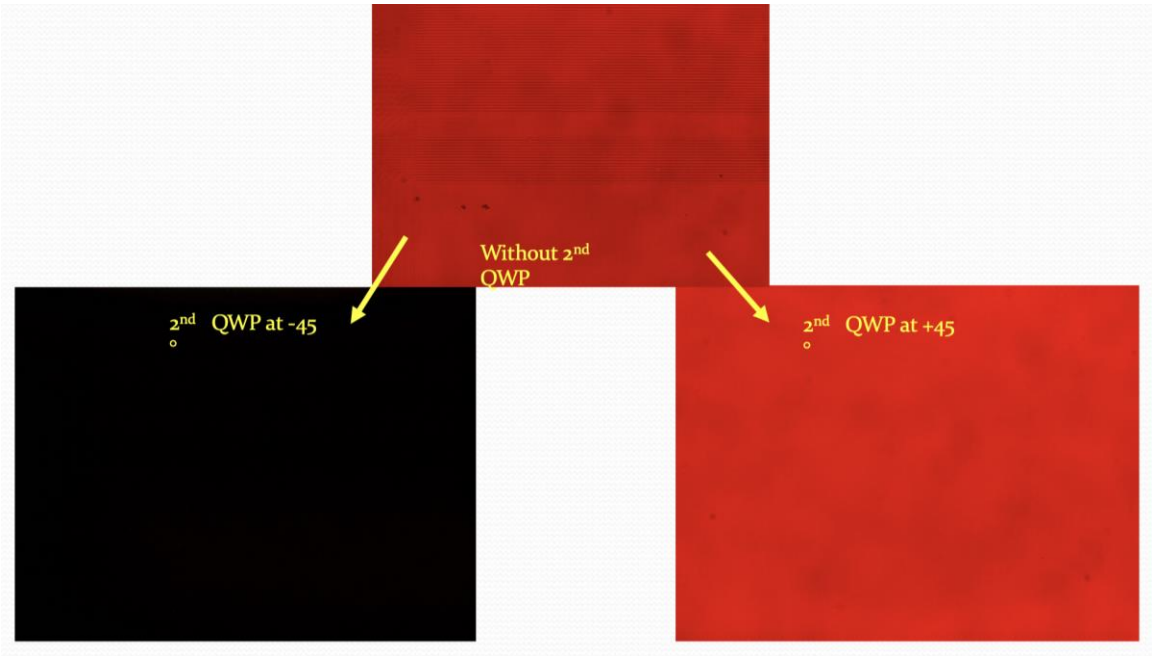

Figure C.4 test area sandwiched by Quarter Wave plates under maximum/minimum transmission

The intensity graph was then plotted along the aperture.

C.5 Transmission Intensity test

After finding optimized voltages via simulation, the director profile was used as an input to find the output intensity of a linearly polarized light (e.g. x-polarized) using jones method with the a similar code that was represented at A.7. The output light intensity was

then compared with experimental data with similar optical system. A total of 14 electrodes (i.e. 52 μm) were considered to make one pitch.

For the experimental part, it was found that the light source of the microscope has some polarization dependency. Therefore, the data was normalized based on the following procedure to eliminate this factor. At 10 degrees angle increments, the cell was placed under POM while the polarizers are crossed and was slightly rotated until maximum intensity occurs. The intensity is being dynamically measured with a compatible software of the camera. Then, a screen shot of the cell with spiral pattern was taken, and the intensity was averaged over all the pixels to determine the mean value. Here, a very careful consideration should be taken to make sure that the same area is being evaluated at each different angle. For consistency, a position of a fixed point (e.g. a spacer) can be regarded as reference. The experimental data for each angle was then normalized with respect to the mean value of the maximum intensity corresponding to that angle.

Plotting both modeling result and experimental data on the same graph, we will get the following graphs. Note that based on our earlier definition, given in chapter 4, the clockwise rotation (CW) is being considered negative and counter clockwise rotation (CCW) is being considered positive.

Below, some example graphs for rotational angles of the polarizers at 0,±10, ±20,…., ±80 degrees are shown. Though, polarizers remain crossed with respect to each other at all the times.

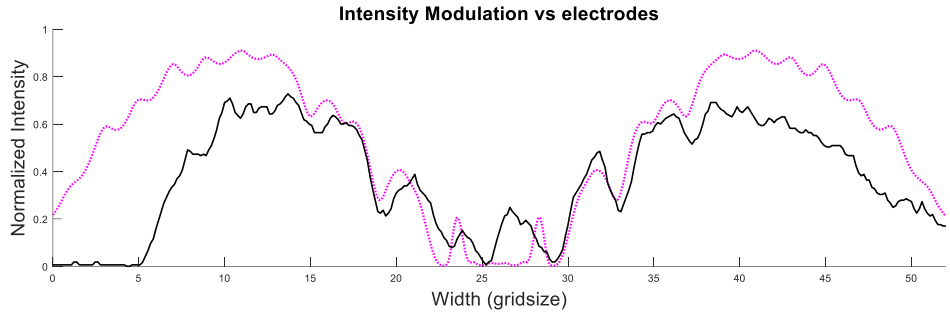

polarizers at 0 degree. Black/pink lines are experimental/simulation data respectively.

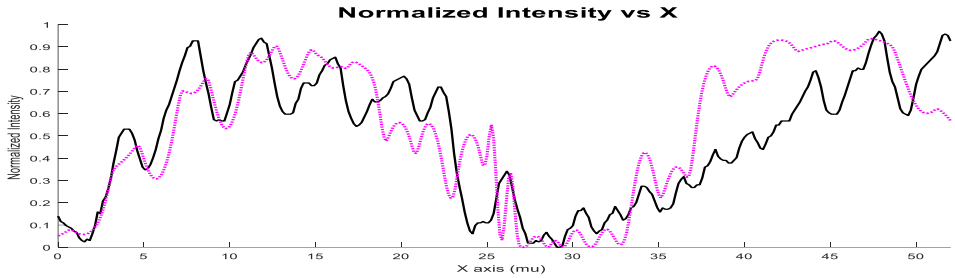

polarizers at +10 degree Black/pink lines are experimental/simulation data respectively.

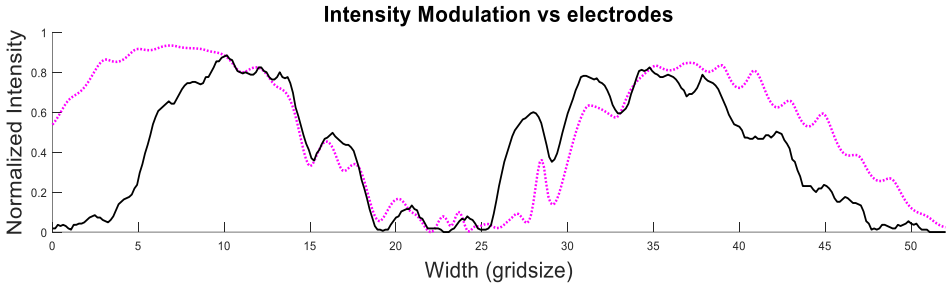

polarizers at -10 degree.Black/pink lines are experimental/simulation data respectively.

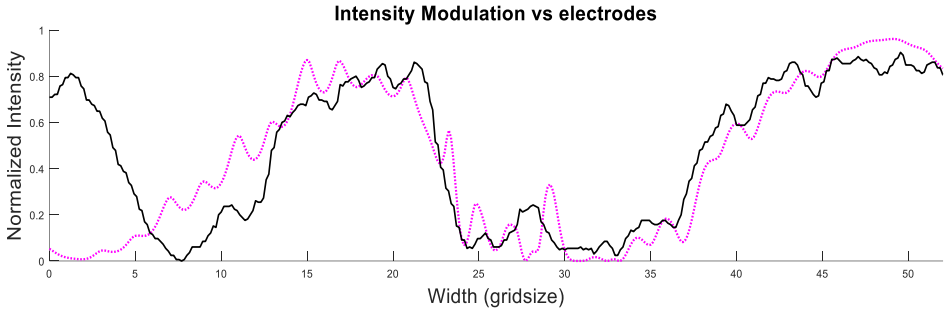

polarizers at +20 degree. Black/pink lines are experimental/simulation respectively.

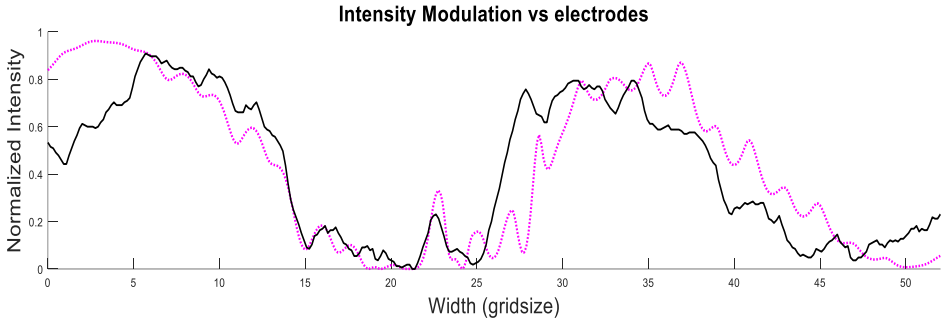

polarizers at -20 degree. Black/pink lines are experimental/simulation data respectively.

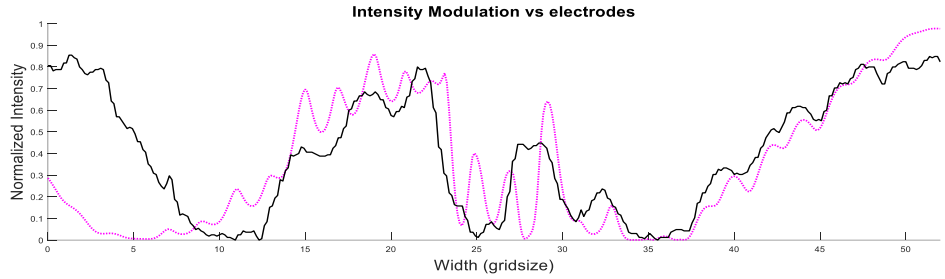

polarizers at +30 degree. Black/pink lines are experimental/simulation respectively.

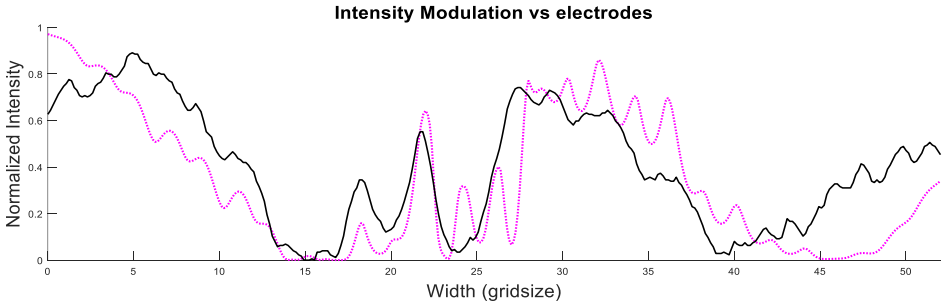

polarizers at -30 degree. Black/pink lines are experimental/simulation data respectively.

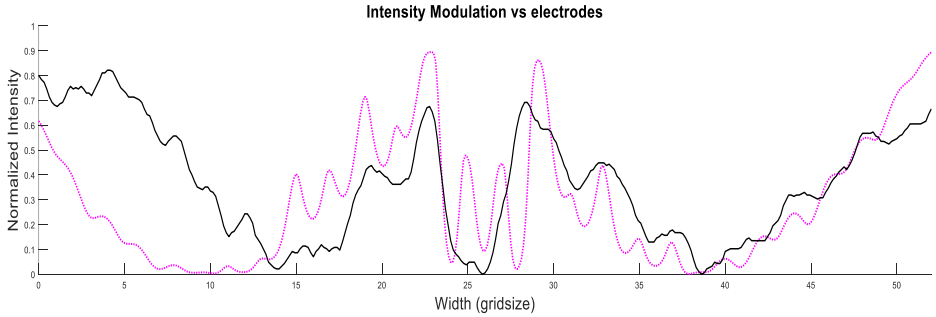

polarizers at +40 degree. Black/pink lines are experimental/simulation respectively.

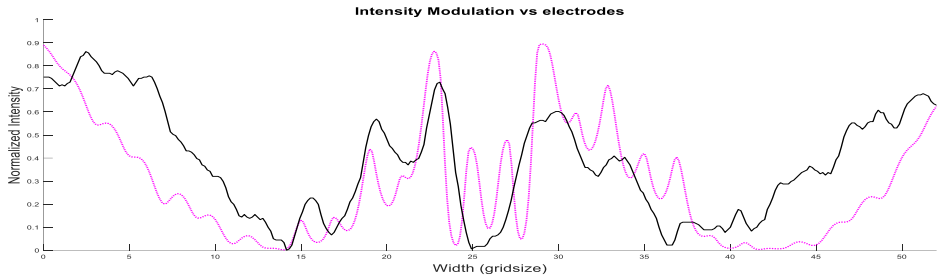

polarizers at -40 degree. Black/pink lines are experimental/simulation data respectively.

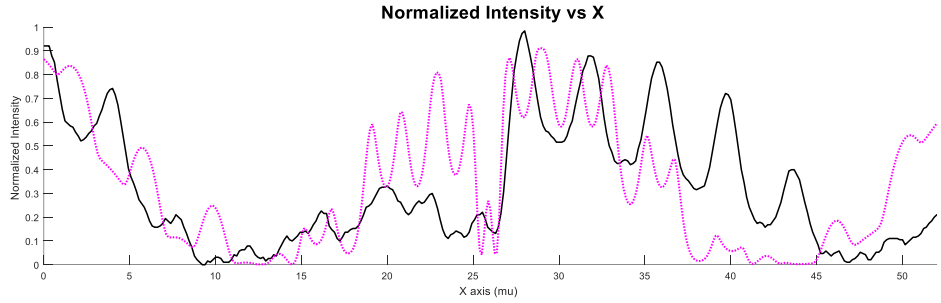

polarizers at +50 degree. Black/pink lines are experimental/simulation respectively.

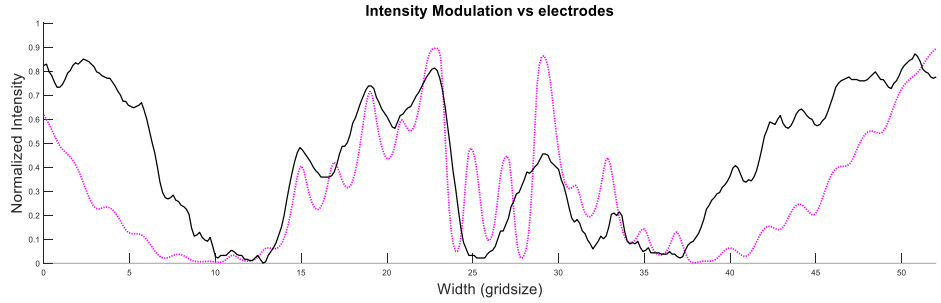

polarizers at -50 degree. Black/pink lines are experimental/simulation data respectively.

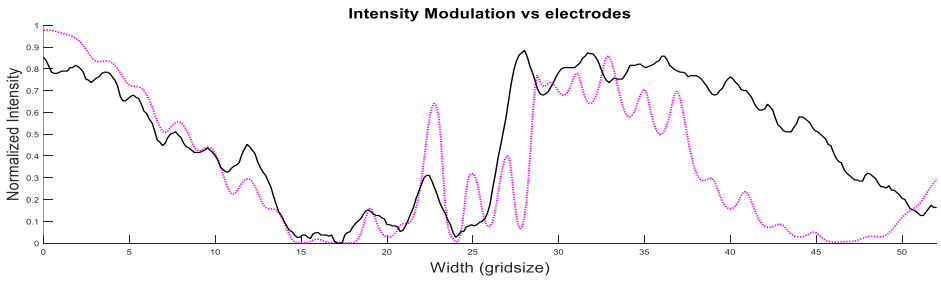

polarizers at +60 degree. Black/pink lines are experimental/simulation respectively.

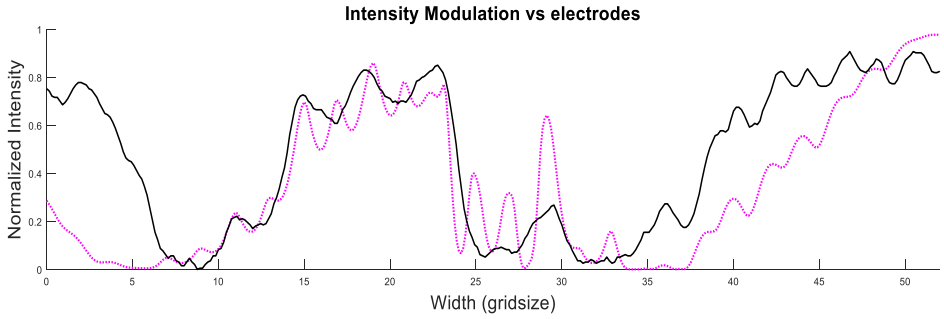

polarizers at -60 degree. Black/pink lines are experimental/simulation data respectively.

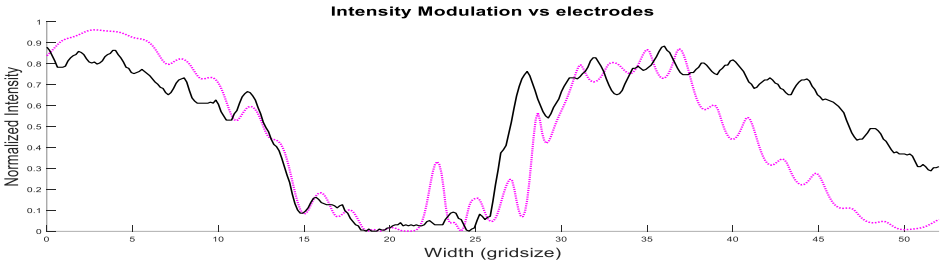

polarizers at +70 degree. Black/pink lines are experimental/simulation respectively.

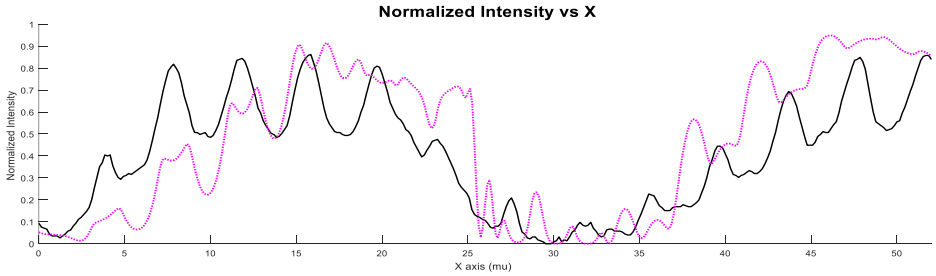

polarizers at -70 degree. Black/pink lines are experimental/simulation data respectively.

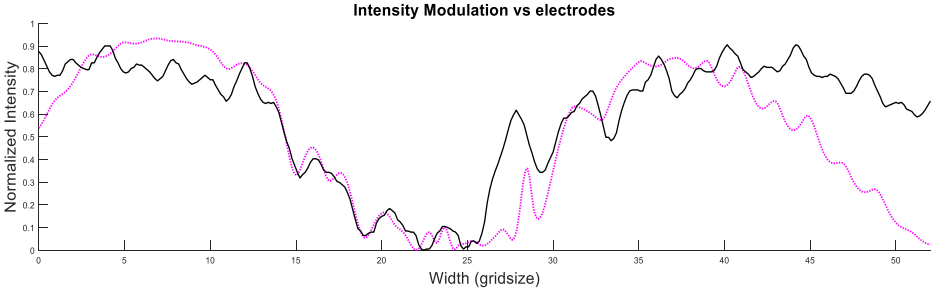

polarizers at +80 degree. Black/pink lines are experimental/simulation respectively.

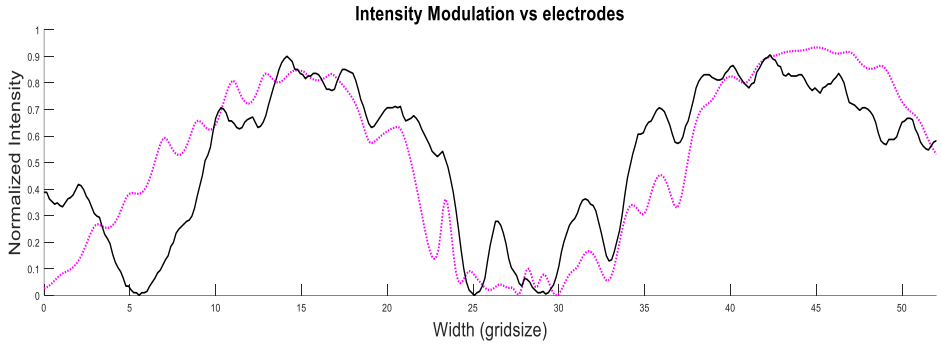

polarizers at -80 degree. Black/pink lines are experimental/simulation data respectively.

Figure C.5 Intensity modulation vs x-axis (aperture) for different angles of polarizers

Overall, the experimental curve seems to follow the simulation curve closely which is what it is expected to be based on the modeling of the director profile. This would further confirm the presence of the spiral pattern of the director as desired. However, some discrepancies are observable mainly around the edges. That can be explained due to the fact that the actual voltage on the active area could be different from what is applied on ledges because of the resistance associated with ITO layer. As the voltage approaches the Freedericksz thresholf voltage (~2.1 V_{rms} for MLC-6608) below which there would be no change on the director angle [reference to Deng-ke Yang book, P:224] , even a small amount of deviation can make noticeable difference on the amount of twist angle since the twist angle is more sensitive to the voltage around the threshold area. Therefore, a more careful optimization of the experimental data that take this effect into account, can make the curves even closer.

C.6 Multi step vs two-step voltage method

To get a more uniform wall, we can use multi-step voltage method instead of two-step. Similarly, we first activate two areas that are oppositely twisted without activating neighbor electrodes on the middle. Then, we try to activate the middle ones so that the zones will be right next to each other. This way, we get a more uniform wall along the neighbor electrodes.

The voltages was applied in this order:

V Steps	Electrode (+10 to +16)	Electrode (-10 to -16)	Electrode (-1 to -7)	Electrode (+1 to +7)	Electrodes (-8 & -9)	Electrode (+8 & +9)
1	8	0	0	0	0	0
2	8	8	0	0	0	0
3	3	3	8	0	0	0
4	3	3	8	8	0	0
5	3	3	8	8	8	
7	3	3	8	8	8	8
8	8	8	8	8	8	8

Table. C.2 Multi step voltage to activate the electrodes

At step 8 where all electrodes are activated with 8 V, we get a more uniform wall in between. Note that the picture is widened horizontally to better see the electrodes. So the aspect ratio in this picture is not 1:1. Also, for the simplicity to show the separated areas, polarizer and analyzer are not crossed in this picture.

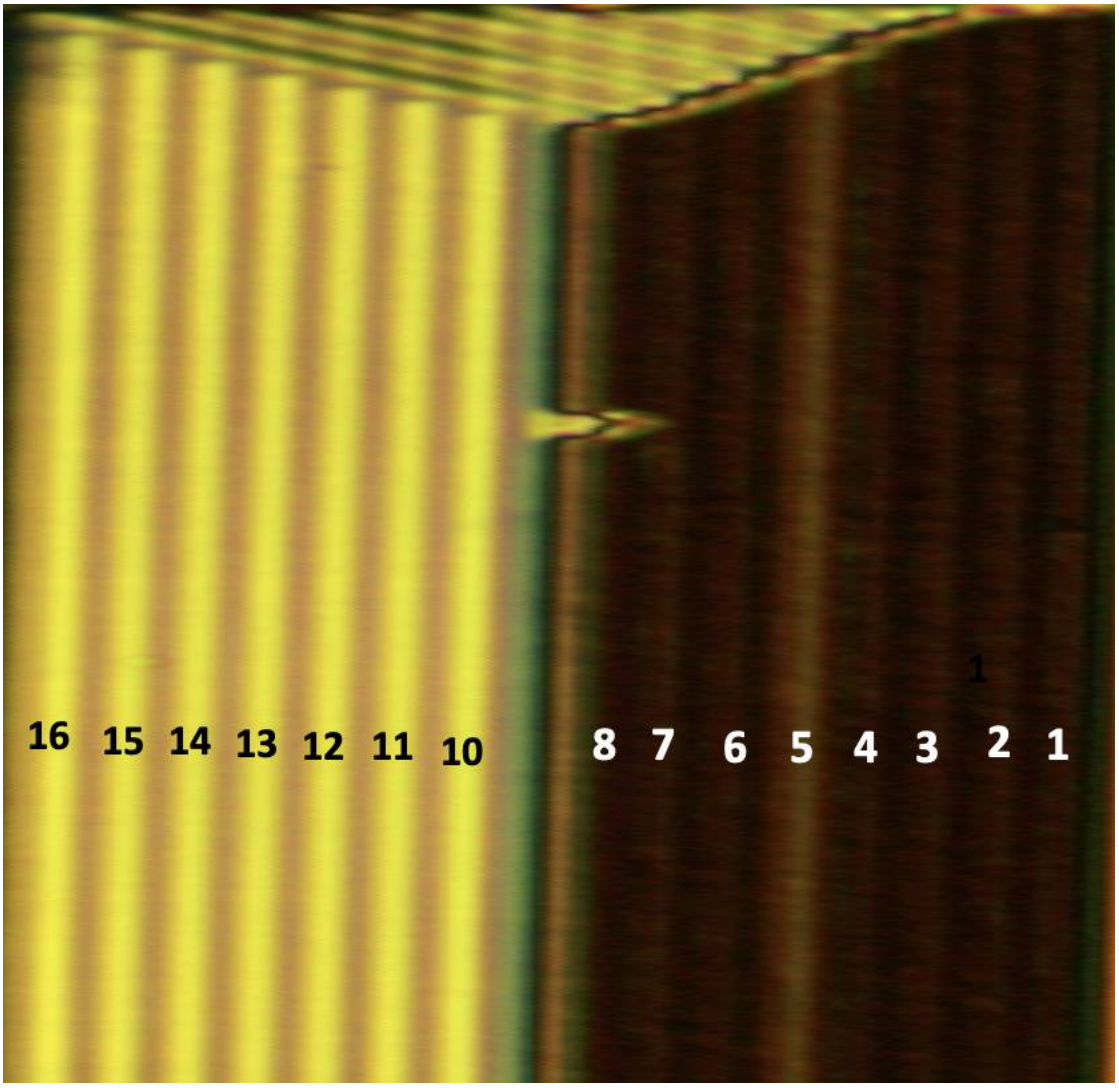

Figure C.6 oppositely twisted areas with the trapped wall in between after all PCEs are activated

And finally, after all electrodes are activated, the gradient voltages are set as :

Electrode	1	2	3	4	5	6	7	8	9 & 10	11	12	13	14	15	16
Voltage(V)	1.5	2	2.5	3	3.5	4.5	5	6	6	4.5	3.5	3	2.5	2	1.5

Table C.3 gradient voltage profile in the last step

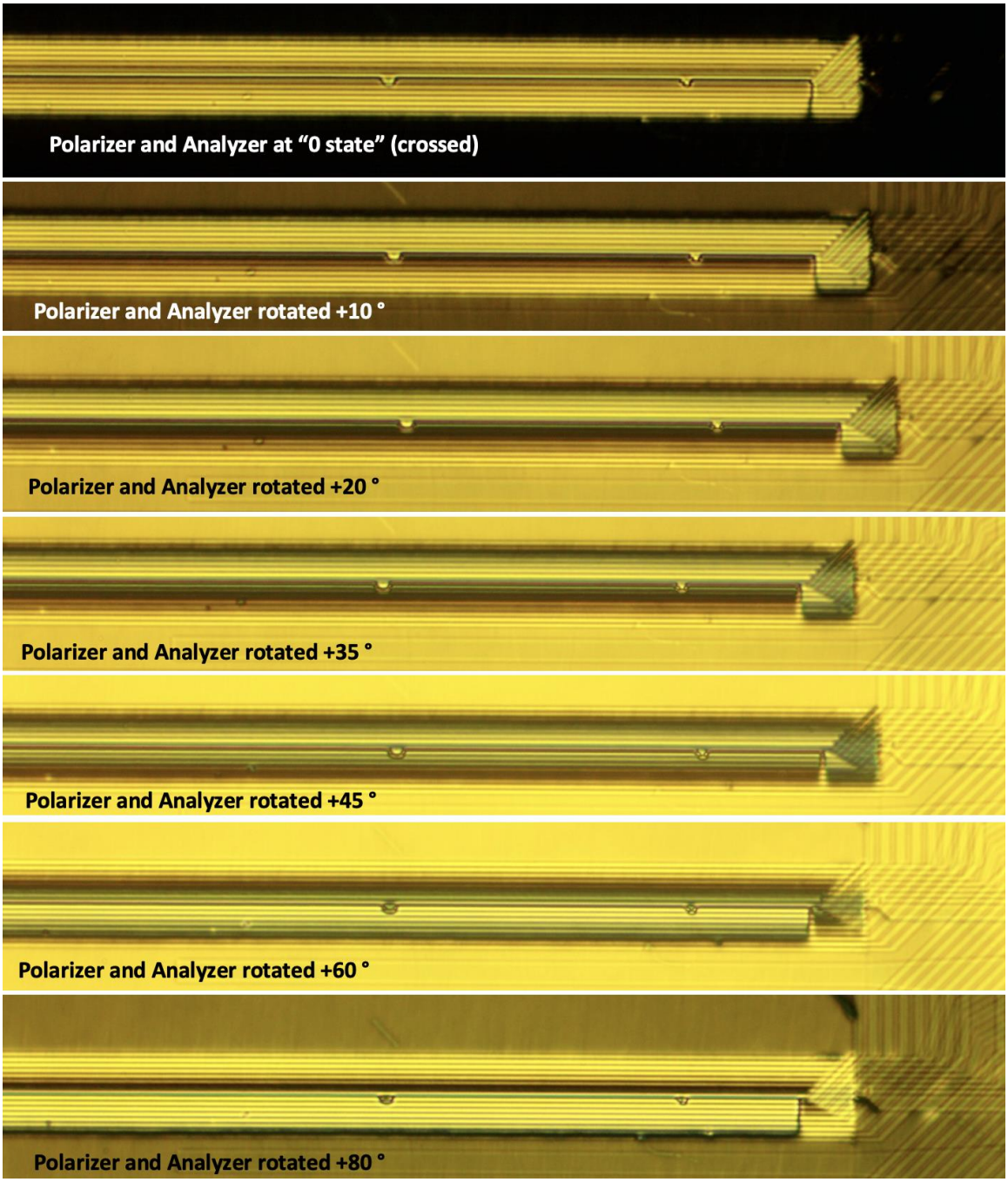

Figure C.7 Test area sandwiched by crossed polarizers at different angles relative to the cell

Again by rotating both polarizers, we can verify the spiral pattern. We can see that as the polarizers are rotating to more angles, the dark part in the spiral pattern move from the middle to the edge showing that the director has its highest angles at the middle and lowest angles at the edges.

APPENDIX D– CHARACTERIZATION OF SPP LENS

D.1 Finding and tuning the voltage profile for a lens

As discussed in chapter 6, the first step of SPP lens characterization is to find the voltage profile. This starts with measuring transmission vs voltage (T-V) curve for a cell that is placed at 45 degrees angle relative to crossed polarizers. Considering a sample cell of 7.7 um thick, using BDH 18349, the optical path length retardation vs voltage is determined by measuring the transmission vs voltage. This is done for both individual cells and some compensator cell that has the same thickness as the cell but without any pattern. Figure below shows a typical T-V curve for the aforementioned cell. All bus lines were driven at the same voltage in this case.

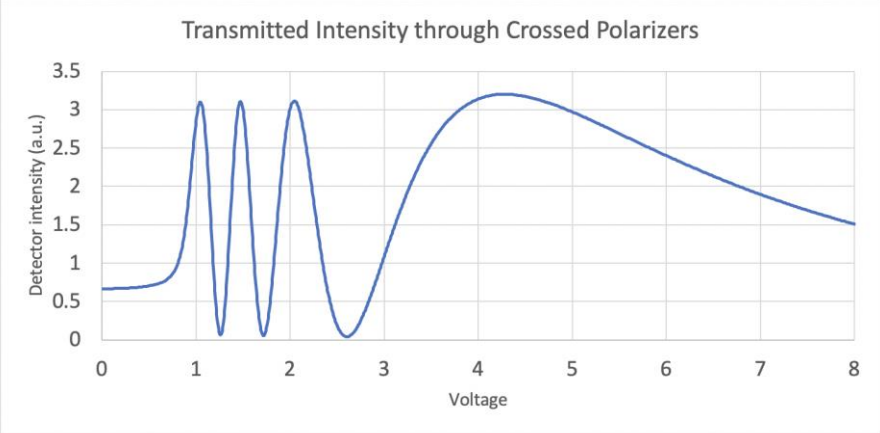

Figure D.1 Typical Transmission vs Voltage curve (for a 7.7 um thick cell).

-

Going from left to the right In Figure D.1, the maxima correspond to the half-integer number of waves of OPD whereas the minima correspond to the integer waves. Therefore, the data can be plotted on retardation curve :

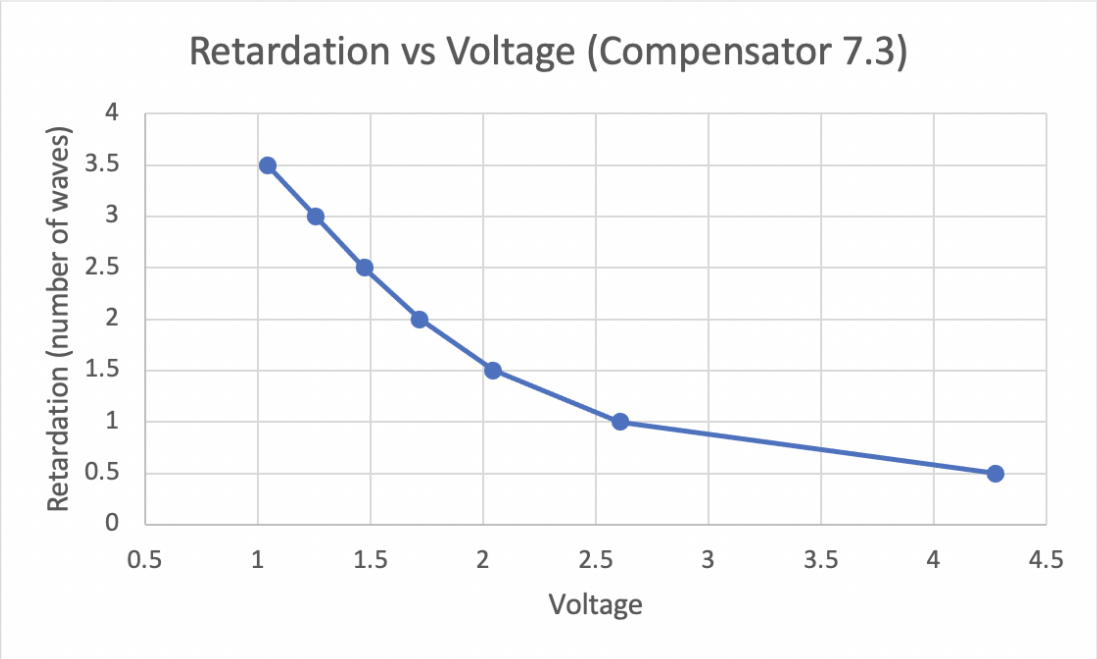

Figure D.2 Optical Path Retardation vs number of waves.

Based on this graph, we can now tune the lens voltages to achieve the desired phase profile on the lens. For example, for this cell thickness, we have three waves retardation at each reset. Therefore, the lens is tuned in the voltage range corresponding to 0.5 to 3.5 waves and achieve the 3-wave difference at each reset.

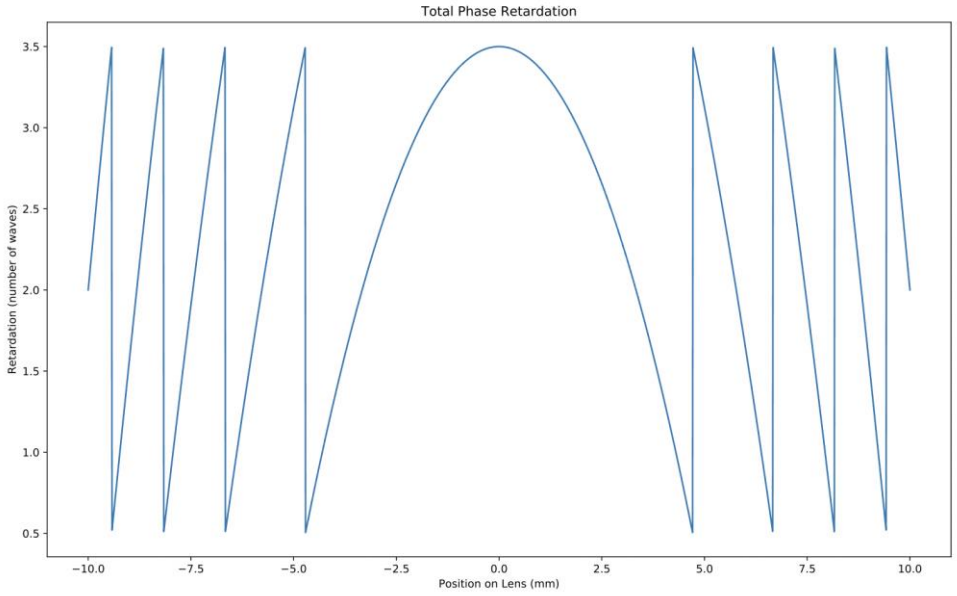

Figure D.3 Ideal Optical path retardation Profile for a positive lens.

The next step is to calculate the desired phase on each bus line. The cell design specifies 64 rings in each zone and the area of each ring is constant, hence, the radial dimension of each ring has to decreases parabolically with respect to the distance from the center of the lens to meet this condition. So, having the retardation to vary linearly across the rings, it imposes a parabolic phase profile :

$\Gamma_n = \Gamma_0 - \Gamma_R F_n$ (1)

where Γ_n is the retardation at the nth ring from the center (starting from zero), Γ_0 is the retardation of the innermost ring of each Fresnel zone, Γ_R is the change in retardation across each Fresnel reset (if measured in number of waves it's equivalent to NW in equation 5), and F_n is the numerical fraction of the position of the nth ring within the zone.

As the authors mentioned in [79], the eight bus lines are connected to the rings as shown in Table 1. The ring number corresponds to which ring in the sequence has the via to that particular bus, numbered starting at zero at the innermost ring of the zone and moving outward.

Bus number	1	2	3	4	5	6	7	8
Ring # at Via	0	10	20	30	40	48	56	63
Ring Fraction (F_n)	0	10/64	20/64	30/64	40/64	48/64	56/64	63/64

Table D.1 Location of each bus connection to the ITO rings.

Bus number	1	2	3	4	5	6	7	8
Desired OPD (Γ_n)	3.5	3.031	2.563	2.094	1.625	1.250	0.875	0.547

Table D.2 The "Desired OPD" is an example set of retardation values for each bus ring calculated for a positive lens with 3 waves at the reset and 3.5 waves at the center.

However, we must account for real-world variables, mostly the internal resistances of the bus lines and the rings themselves. The estimated voltages need to be fine-tuned to achieve a good phase profile. We accomplish this by using a 'compensator cell' that has a known retardation vs. voltage curve. The compensator cell acts as a simple ECB (electronically controlled birefringence) cell and is stacked on the lens cell with the rubbing direction perpendicular to that of the lens. While viewing through crossed polarizers in a microscope, when both cells have the same value of retardation the image should appear dark because the retardation of one cell will cancel the retardation of the other. We follow these steps:

1. Apply the estimated voltages on the lens to make the proper phase profile. This is acquired from the retardation vs. voltage curve measured for that particular cell.

2. Apply the proper voltage on the compensator corresponding to the bus we desire to tune. This is acquired from the retardation vs. voltage curve measured for that particular cell.

3. In the microscope, through crossed polarizers, find the rings that correspond to that bus and see if they appear dark.

4. Adjust the voltage on the lens bus to make those rings appear dark.

5. Repeat for all 8 bus lines. (going to both directions, for example: move from ring 8 to ring 1, then repeat the process backward)

Using the OPD in Table D.1, and the curve in Figure D.2, we can find the desired voltage on each bus line to create the proper lens phase.

Bus Line	Retardation (positive profile)	Compensator Volts	Retardation (negative profile)	Compensator Volts
1	0.5	4.57	3.500	1.05
2	0.969	2.85	3.031	1.27
3	1.438	2.21	2.563	1.49
4	1.906	1.85	2.094	1.73
5	2.375	1.58	1.625	2.04
6	2.750	1.40	1.250	2.43
7	3.125	1.23	0.875	3.20
8	3.453	1.08	0.547	4.39

Table D.3: An example of Retardation values and corresponding voltages for a 7.7 um thick compensator.

After the cell is tuned, we will take the ‘macro’ image to see the whole phase profile (figure 6.2) . Using green light at 551 nm, we place the lens cell between

parallel polarizers oriented parallel to the rubbing direction of the lens. We use a DSLR camera with a 100mm macro lens focused on the cell to take a photograph.

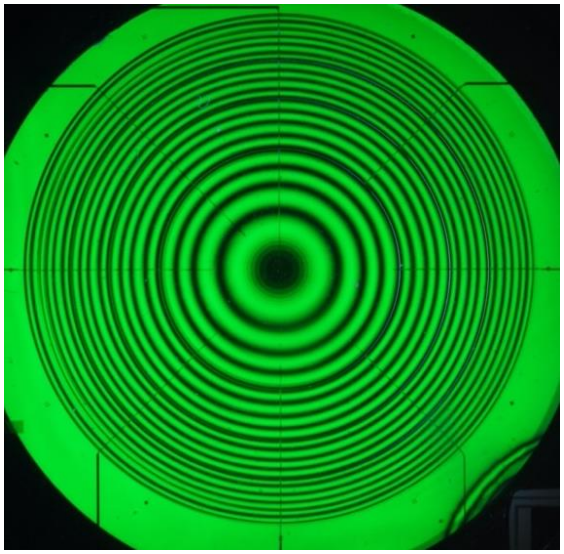

Figure D.4 Macro image of a lens with negative profile between parallel polarizers

The voltage profile is then being tweaked with the help of overlapping to an ideal curve shown in figure 6.5. From the intensity profile of the experimental picture on top of ideal curve, we can adjust the voltage profile as follows:

1- See the difference in peaks of experimental vs ideal curves

2- Find the corresponding bus line that controls that peak

3- Tweak the voltage on corresponding bus line and visually confirm the change

4- Take another picture of the phase profile

5- Import the picture in the PC with the code

6- Crop a very narrow slice of the image from the center (figure D.5)

7- Derive the intensity phase profile of experimental vs ideal again in Matlab

8- Repeat the steps if necessary

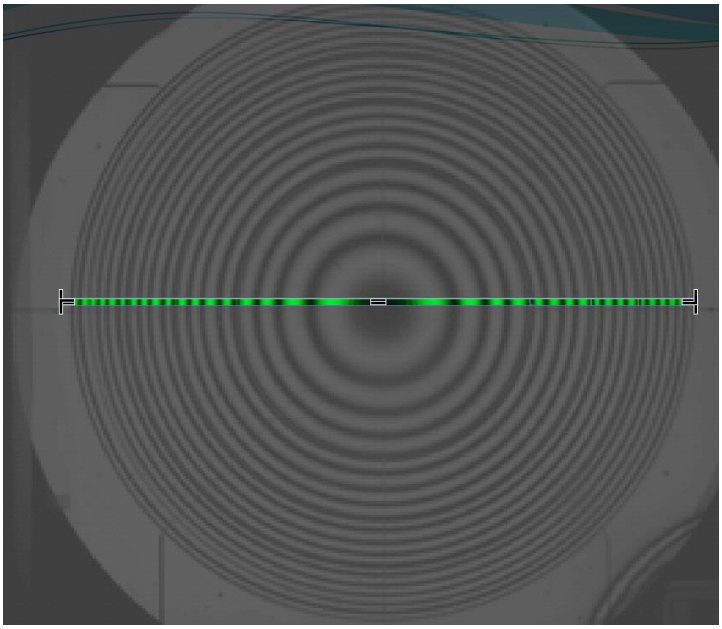

Figure D.5: a narrow slice of the phase profile close to the center is cropped in order to extract the intensity data

This is done for both positive and negative profiles.

The following graphs are the final voltage profile for a sample lens with ±0.19 D power , when adjusted following the above steps.

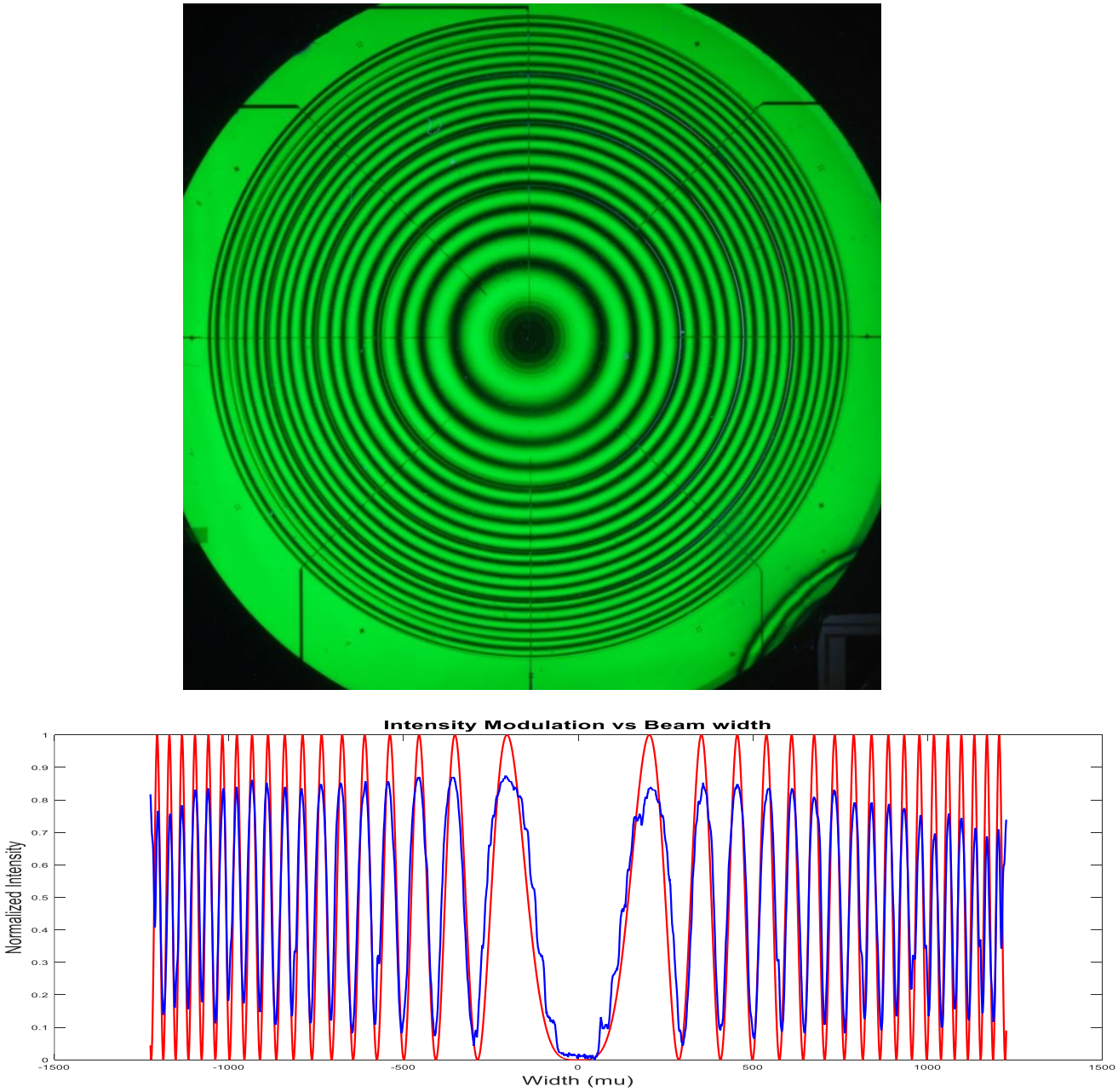

Figure D.6 Positive phase profile. Red line is ideal curve. Blue line is acquired from the experimental image

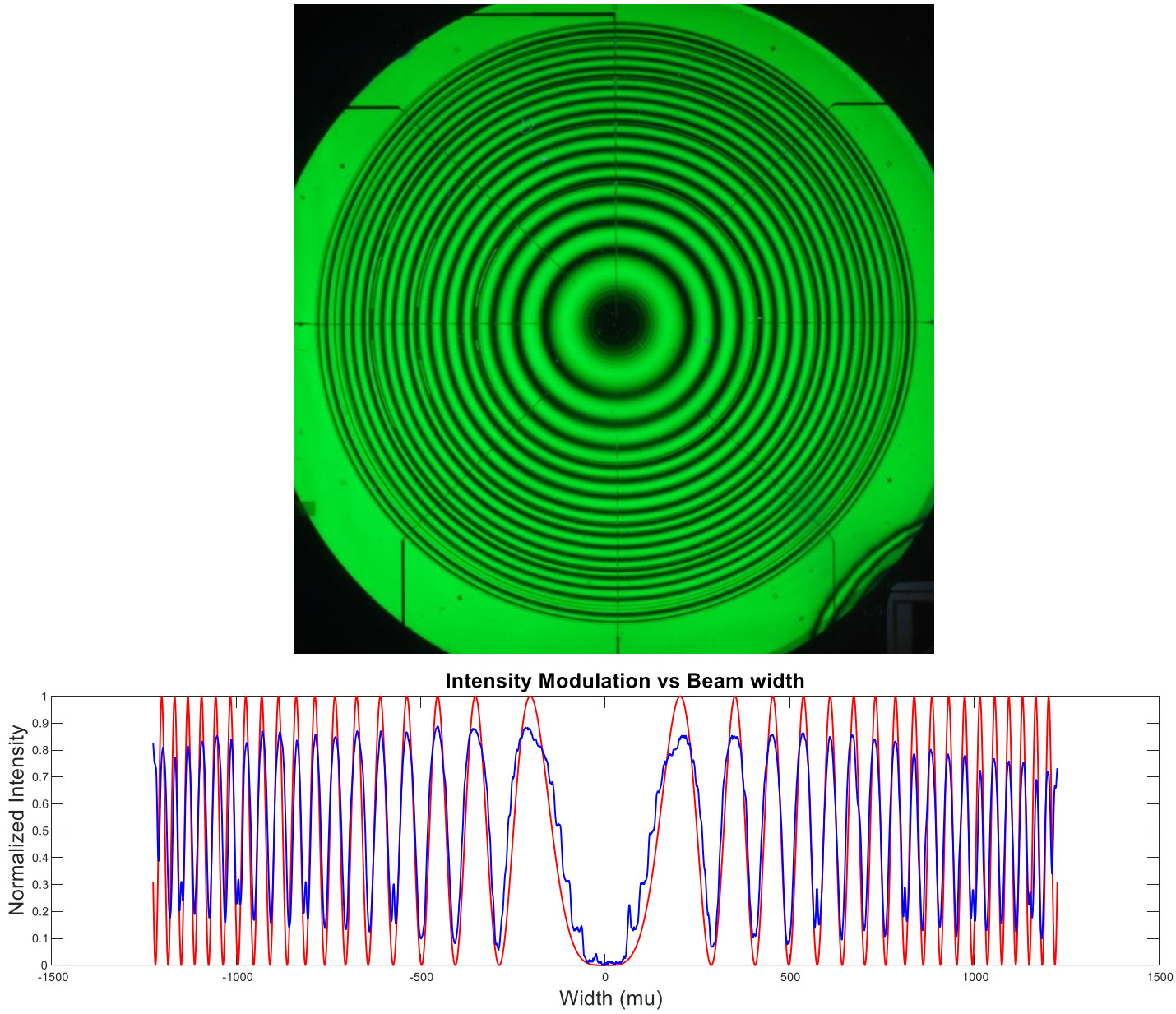

Figure D.7 Negative phase profile. Red/blue line is ideal/ experimental curves respectively.

REFERENCES

1. Collis, R.T.H., *Lidar.* Applied Optics, 1970. **9**(8): p. 1782-1788.
2. Hair, J.W., C.A. Hostetler, A.L. Cook, D.B. Harper, R.A. Ferrare, T.L. Mack, W. Welch, L.R. Izquierdo, and F.E. Hovis, *Airborne High Spectral Resolution Lidar for profiling aerosol optical properties.* Applied Optics, 2008. **47**(36): p. 6734-6752.
3. Kattawar, G.W. and G.N. Plass, *Time of Flight Lidar Measurements as an Ocean Probe.* Applied Optics, 1972. **11**(3): p. 662-666.
4. Scott, R.D., D.R. Scott, J. Seth, H.A. Michael, and W.Y. Anthony. *Liquid crystal clad waveguide laser scanner and waveguide amplifier for LADAR and sensing applications*. in *Proc.SPIE*. 2015.
5. Busch, T.E., Sr., *Beam steering techniques for free space laser communication*. 1997, State University of New York at Binghamton: Ann Arbor. p. 190.
6. Saghaye Polkoo, S. and C.K. Renshaw, *Imaging-based beam steering for free-space optical communication.* Applied Optics, 2019. **58**(13): p. D12-D21.
7. Raj, A.A.B., J.A.V. Selvi, D. Kumar, and S. Raghavan, *Design of Cognitive Decision Making Controller for Autonomous Online Adaptive Beam Steering in Free Space Optical Communication System.* Wireless Personal Communications, 2015. **84**(1): p. 765-799.

8. Feng, F., I.H. White, and T.D. Wilkinson, *Free Space Communications With Beam Steering a Two-Electrode Tapered Laser Diode Using Liquid-Crystal SLM.* Journal of Lightwave Technology, 2013. **31**(12): p. 2001-2007.

9. Xiong, J., Y. Li, K. Li, and S.-T. Wu, *Aberration-free pupil steering Maxwellian display with wide-view broadband polarization converters.* Journal of the Society for Information Display, 2021. **n/a**(n/a).

10. Lee, Y.-H., T. Zhan, and S.-T. Wu, *Enhancing the resolution of a near-eye display with a Pancharatnam- Berry phase deflector.* Optics Letters, 2017. **42**(22): p. 4732-4735.

11. Kessel, P.F.V., L.J. Hornbeck, R.E. Meier, and M.R. Douglass, *A MEMS-based projection display.* Proceedings of the IEEE, 1998. **86**(8): p. 1687-1704.

12. Komanduri, R.K., W.M. Jones, C. Oh, and M.J. Escuti, *Polarization-independent modulation for projection displays using small-period LC polarization gratings.* Journal of the Society for Information Display, 2007. **15**(8): p. 589-594.

13. Betzig, E. and J.K. Trautman, *Near-Field Optics: Microscopy, Spectroscopy, and Surface Modification Beyond the Diffraction Limit.* Science, 1992. **257**(5067): p. 189.

14. Neuman, K.C. and S.M. Block, *Optical trapping.* Review of Scientific Instruments, 2004. **75**(9): p. 2787-2809.

15. Goodman, J.L., *History of Space Shuttle Rendezvous and Proximity Operations.* Journal of Spacecraft and Rockets, 2006. **43**(5): p. 944-959.

16. Næsset, E., T. Gobakken, J. Holmgren, H. Hyyppä, J. Hyyppä, M. Maltamo, M. Nilsson, H. Olsson, Å. Persson, and U. Söderman, *Laser scanning of forest resources: the nordic experience.* Scandinavian Journal of Forest Research, 2004. **19**(6): p. 482-499.

17. Lefsky, M.A., W.B. Cohen, G.G. Parker, and D.J. Harding, *Lidar Remote Sensing for Ecosystem Studies: Lidar, an emerging remote sensing technology that directly measures the three-dimensional distribution of plant canopies, can accurately estimate vegetation structural attributes and should be of particular interest to forest, landscape, and global ecologists.* BioScience, 2002. **52**(1): p. 19-30.

18. Paul, F.M. and A. Abtin, *Progress and opportunities in the development of nonmechanical beam steering for electro-optical systems.* Optical Engineering, 2019. **58**(12): p. 1-15.

19. DeGennes, P. and J. Prost, *The Physics of liquid crystals.* Oxford Science Publications, 1993.

20. McManamon, P.F., T.A. Dorschner, D.C. Corkum, L.J. Friedman, D.S. Hobbs, M.K.O. Holz, S. Liberman, H. Nguyen, D.P. Resler, R.C. Sharp, and E.A. Watson, *Optical phased array technology.* Proc. IEEE, 1996. **842**: p. 268–298.

21. McManamon, P.F., P.J. Bos, M.J. Escuti, J. Heikenfeld, S. Serati, H. Xie, and E.A. Watson, *A Review of Phased Array Steering for Narrow-Band Electrooptical Systems.* Proceedings of the IEEE, 2009. **97**(6): p. 1078-1096.

22. McManamon, P.F., J. Shi, and P.J. Bos, *Broadband optical phased-array beam steering.* Optical Engineering, 2005. **44**(12): p. 1-5, 5.

23. Blanche, P.-A., P. Gailly, S.L.M. Habraken, P.C. Lemaire, and C.A.J. Jamar, *Volume phase holographic gratings: large size and high diffraction efficiency.* Optical Engineering, 2004. **43**(11): p. 2603-2612, 10.

24. Ziqian, H., L. Yun-Han, Y. Kun, and W. Shin-Tson. *Recent advances in liquid-crystal polarization volume gratings*. in *Proc.SPIE*. 2019.

25. Tabiryan, N.V., S.R. Nersisyan, D.M. Steeves, and B.R. Kimball, *The Promise of Diffractive Waveplates.* OSA, 2010. **1047-6938**: p. 41.

26. Shi, L., P.F. McManamon, and P.J. Bos, *Liquid crystal optical phase plate with a variable in-plane gradient.* Journal of Applied Physics 2008. **104**(033109).

27. Oh, C. and M.J. Escuti, *Achromatic diffraction from polarization gratings with high efficiency.* Optics Letters, 2008. **33**(20): p. 2287-2289.

28. Shi, L., J. Shi, P.F. McManamon, and P.J. Bos, *Design considerations for high efficiency liquid crystal decentered microlens arrays for steering light.* Applied Optics, 2010. **49**(3): p. 409-421.

29. Nys, I., M. Stebryte, Y.Y. Ussembayev, J. Beeckman, and K. Neyts, *Tilted Chiral Liquid Crystal Gratings for Efficient Large-Angle Diffraction.* Advanced Optical Materials, 2019. **7**(22): p. 1901364.

30. Reo Amanoa, P.S., Shunsuke Yokokawaa, Fumiaki Kobayashia, Yuji Sasaki, Shuji Fujii, Ágnes Bukab, Fumito Araoka and Hiroshi Orihara, *Tunable two-*

dimensional polarization grating using a self-organized micropixelated liquid crystal structure. RSC Adv, 2018. **8**: p. 41472-41479.

31. Magallanes, H. and E. Brasselet, *Macroscopic direct observation of optical spin-dependent lateral forces and left-handed torques.* Nature Photonics, 2018. **12**(8): p. 461-464.

32. Honma, M. and T. Nose, *Liquid-Crystal Fresnel Zone Plate Fabricated by Microrubbing.* Jpn. J. Appl. Phys, 2005. **44(1A)**: p. 287–290.

33. Crawford, G.P., J.N. Eakin, M.D. Radcliffe, A. Callan-Jones, and R.A. Pelcovits, *Liquid-crystal diffraction gratings using polarization holography alignment techniques.* J. Appl. Phys., 2005. **98(12)**: p. 123102.

34. Marrucci, L., C. Manzo, and D. Paparo, *Pancharatnam-Berry phase optical elements for wave front shaping in the visible domain: Switchable helical mode generation.* Applied Physics Letters, 2006. **88**(22): p. 221102.

35. Xu, D., G. Tan, and S.-T. Wu, *Large-angle and high-efficiency tunable phase grating using fringe field switching liquid crystal.* Optics Express, 2015. **23**(9): p. 12274-12285.

36. Tabiryan, N., H. Xianyu, D. Roberts, Z. Liao, D. Steeves, B. Kimball, E. Serabyn, and D. Mawet. *4G optics for communications and astronomy*. in *2016 IEEE Aerospace Conference*. 2016.

37. James, E.H. and N.P. Richard, *Understanding diffraction grating behavior: including conical diffraction and Rayleigh anomalies from transmission gratings.* Optical Engineering, 2019. **58**(8): p. 1-21.

38. Chou, J., L. Parameswaran, B. Kimball, and M. Rothschild, *Electrically switchable diffractive waveplates with metasurface aligned liquid crystals.* Optics Express, 2016. **24**(21): p. 24265-24273.

39. Steven, S., L.H. Christopher, H. Lance, K. Kelly, S. Jay, and H. Charles, *Large-aperture, wide-angle nonmechanical beam steering using polarization gratings.* Optical Engineering, 2016. **56**(3): p. 1-9.

40. Warriner, N.Z. and J.E. Michael. *Fabrication of liquid crystal binary polarization gratings (bin-PGs)*. in *Proc.SPIE*. 2019.

41. Jihwan, K., O. Chulwoo, J.E. Michael, H. Lance, and S. Steve. *Wide-angle nonmechanical beam steering using thin liquid crystal polarization gratings*. in *Proc.SPIE*. 2008.

42. Ramanujam, L.N.a.P.S., *Polarization Holography.* Cambridge University, 2009.

43. Larouche, S., Y.-J. Tsai, T. Tyler, N.M. Jokerst, and D.R. Smith, *Infrared metamaterial phase holograms.* Nature Materials, 2012. **11**(5): p. 450-454.

44. Crawford, G.P., J.N. Eakin, M.D. Radcliffe, A. Callan-Jones, and R.A. Pelcovits, *Liquid-crystal diffraction gratings using polarization holography alignment techniques.* Journal of Applied Physics, 2005. **98**(12): p. 123102.

45. Sarkissian, H., B. Park, N. Tabirian, and B. Zeldovich, *Periodically Aligned Liquid Crystal: Potential Application for Projection Displays.* Molecular Crystals and Liquid Crystals, 2006. **451**(1): p. 1-19.

46. Todorov, T., L. Nikolova, K. Stoyanova, and N. Tomova, *Polarization holography. 3: Some applications of polarization holographic recording.* Applied Optics, 1985. **24**(6): p. 785-788.

47. Escuti, M.J. and W.M. Jones, *A polarization-independent liquid crystal spatial light modulator*. SPIE Optics + Photonics. Vol. 6332. 2006: SPIE.

48. Shi, L., *Tunable liquid crystal polarization gratings*. 2009, Kent State University.

49. Rynbach, C.Y.P.J.B.A.V., *Optical phase control elements based on pancharatnam phase.* US Patent, 2020

50. Yun, H.J., M.H. Jo, I.W. Jang, S.H. Lee, S.H. Ahn, and H.J. Hur, *Achieving high light efficiency and fast response time in fringe field switching mode using a liquid crystal with negative dielectric anisotropy.* Liquid Crystals, 2012. **39**(9): p. 1141-1148.

51. Sharp, R.C., D.P. Resler, D.S. Hobbs, and T.A. Dorschner, *Electrically tunable liquid-crystal wave plate in the infrared.* Optics Letters, 1990. **15**(1): p. 87-89.

52. Roy, M.M. *Blazed phase liquid crystal beam steering*. in *Proc.SPIE*. 1994.

53. Resler, D.P., D.S. Hobbs, R.C. Sharp, L.J. Friedman, and T.A. Dorschner, *High-efficiency liquid-crystal optical phased-array beam steering.* Optics Letters, 1996. **21**(9): p. 689-691.

54. Weng, Y., D. Xu, Y. Zhang, X. Li, and S.-T. Wu, *Polarization volume grating with high efficiency and large diffraction angle.* Optics Express, 2016. **24**(16): p. 17746-17759.

55. Yin, K., Y.-H. Lee, Z. He, and S.-T. Wu, *Stretchable, flexible, rollable, and adherable polarization volume grating film.* Optics Express, 2019. **27**(4): p. 5814-5823.

56. Feng, X., L. Lu, O. Yaroshchuk, and P. Bos, *Closer look at transmissive polarization volume holograms: geometry, physics, and experimental validation.* Applied Optics, 2021. **60**(3): p. 580-592.

57. McManamon, P.F., *Agile Nonmechanical Beam Steering.* Optics and Photonics News, 2006. **17**(3): p. 24-29.

58. Gao, K., C. McGinty, H. Payson, S. Berry, J. Vornehm, V. Finnemeyer, B. Roberts, and P. Bos, *High-efficiency large-angle Pancharatnam phase deflector based on dual-twist design.* Optics Express, 2017. **25**(6): p. 6283-6293.

59. Nocentini, S.M., D.; Wiersma, D.S.; Parmeggiani, C., *Beam steering by liquid crystal elastomer fibres.* Soft Matter, 2017. **13**: p. 8590-8596

60. Li, C.-C., C.-W. Chen, C.-K. Yu, H.-C. Jau, J.-A. Lv, X. Qing, C.-F. Lin, C.-Y. Cheng, C.-Y. Wang, J. Wei, Y. Yu, and T.-H. Lin, *Arbitrary Beam Steering Enabled by Photomechanically Bendable Cholesteric Liquid Crystal Polymers.* Advanced Optical Materials, 2017. **5**(4): p. 1600824.

61. Pancharatnam, S., *Generalized theory of interference and its applications.* Proceedings of the Indian Academy of Sciences - Section A, 1956. **44**(6): p. 398-417.

62. Berry, M.V., *Quantal phase factors accompanying adiabatic changes.* Proceedings of the Royal Society of London. A. Mathematical and Physical Sciences, 1984. **392**(1802): p. 45-57.

63. Cohen, E., H. Larocque, F. Bouchard, F. Nejadsattari, Y. Gefen, and E. Karimi, *Geometric phase from Aharonov–Bohm to Pancharatnam–Berry and beyond.* Nature Reviews Physics, 2019. **1**(7): p. 437-449.

64. Snik, F., M. Rodenhuis, M.J. Escuti, L. Brickson, K. Hornburg, J. Kim, C. Kievid, S. Groenhuijsen, and D. Roosegaarde, *Producing true-color rainbows with patterned multi-layer liquid-crystal polarization gratings.* Optical Materials Express, 2019. **9**(4): p. 1583-1589.

65. Escuti, M.J. and W.M. Jones, *39.4: Polarization-Independent Switching With High Contrast from a Liquid Crystal Polarization Grating.* SID Symposium Digest of Technical Papers, 2006. **37**(1): p. 1443-1446.

66. Loewen, C.P.E., *DIFFRACTION GRATING HANDBOOK.* Newport Corporation, 2005.

67. Kim, J. and M.J. Escuti, *Polarization grating exposure method with easily tunable period via dual rotating polarization grating masks.* Journal of the Optical Society of America B, 2019. **36**(5): p. D42-D46.

68. Komanduri, R.K. and M.J. Escuti, *High efficiency reflective liquid crystal polarization gratings.* Applied Physics Letters, 2009. **95**(9): p. 091106.

69. Lee, Y.-H., K. Yin, and S.-T. Wu, *Reflective polarization volume gratings for high efficiency waveguide-coupling augmented reality displays.* Optics Express, 2017. **25**(22): p. 27008-27014.

70. Zhao, Z.-W., C.-M. Wang, S.-Z. Li, W. Chen, Y.-G. Liu, Q.-Q. Mu, Z.-H. Peng, Q.-D. Wang, L. Xuan, and R.-d. Wei, *High-efficiency large-angle reflective composite polarization grating.* Liquid Crystals, 2019. **47**(2): p. 191-198.

71. Guo, Q., L. Xu, J. Sun, X. Yang, H. Liu, K. Yan, H. Zhao, V.G. Chigrinov, and H.S. Kwok, *Fast switching beam steering based on ferroelectric liquid crystal phase shutter and polarisation grating.* Liquid Crystals, 2019. **46**(9): p. 1383-1388.

72. Wu, S.-T., U. Efron, and T.-Y. Hsu, *Near-infrared-to-visible image conversion using a Si liquid-crystal light valve.* Optics Letters, 1988. **13**(1): p. 13-15.

73. De Sio, L., T. Placido, S. Serak, R. Comparelli, M. Tamborra, N. Tabiryan, M.L. Curri, R. Bartolino, C. Umeton, and T. Bunning, *Nano-Localized Heating Source for Photonics and Plasmonics.* Advanced Optical Materials, 2013. **1**(12): p. 899-904.

74. Gou, F., F. Peng, Q. Ru, Y.-H. Lee, H. Chen, Z. He, T. Zhan, K.L. Vodopyanov, and S.-T. Wu, *Mid-wave infrared beam steering based on high-efficiency liquid crystal diffractive waveplates.* Optics Express, 2017. **25**(19): p. 22404-22410.

75. Elena, O., R. David, T. Nelson, D.M. Steeves, and B.R. Kimball. *Diffractive waveplates for long wave infrared*. in *Proc.SPIE*. 2017.

76. Yousefzadeh, C., A. Van Rynbach, and P.J. Bos, *Design of a large aperture, tunable, Pancharatnam phase beam steering device.* Optics Express, 2020. **28**(2): p. 991-1001.

77. Yousefzadeh, C., A. Van Rynbach, D. Bryant, and P. Bos, *High-efficiency, tunable, fringe-field switching-mode beam steering based on a liquid crystal Pancharatnam phase.* Applied Optics, 2020. **59**(34): p. 10706-10718.

78. Yousefzadeh, C., A. Van Rynbach, and P.J. Bos. *Tunable liquid crystal beam steering device based on Pancharatnam phase*. in *Proc.SPIE*. 2020.

79. Jamali, A.J., P. Bos, OhioLINK Electronic Theses and Dissertations Center; Department of Chemical Physics, and Kent State University, *LARGE AREA TUNABLE LIQUID CRYSTAL LENS*.

80. Jamali, A., D. Bryant, Y. Zhang, A. Grunnet-Jepsen, A. Bhowmik, and P.J. Bos, *Design of a large aperture tunable refractive Fresnel liquid crystal lens.* Applied Optics, 2018. **57**(7): p. B10-B19.

81. Liwei, L., B. Doug, H. Tony Van, D. Dwight, and J.B. Philip, *Near-diffraction-limited tunable liquid crystal lens with simplified design.* Optical Engineering, 2013. **52**(3): p. 1-8.

82. Jung, J.H., K.S. Ha, M. Chae, A.K. Srivastava, S.H. Lee, S.E. Lee, and H.K. Lee, *Light efficiency of the dependence of fringe-field switching mode on the dielectric anisotropy of liquid crystal for various values of the cell gap and the rubbing angle.* Journal of the Korean Physical Society, 2010. **56**(2): p. 548-553.

83. Kim, J.H., W.S. Kang, H.S. Choi, K. Park, J.H. Lee, S. Yoon, S. Yoon, G.-D. Lee, and S.H. Lee, *Effect of surface anchoring energy on electro-optic characteristics of a fringe-field switching liquid crystal cell.* Journal of Physics D: Applied Physics, 2015. **48**(46): p. 465506.

84. Chen, H., Z. Luo, D. Xu, F. Peng, S.-T. Wu, M.-C. Li, S.-L. Lee, and W.-C. Tsai, *A fast-response A-film-enhanced fringe field switching liquid crystal display.* Liquid Crystals, 2015. **42**(4): p. 537-542.

85. Xu, D., L. Rao, C. Tu, and S. Wu, *Nematic Liquid Crystal Display With Submillisecond Grayscale Response Time.* Journal of Display Technology, 2013. **9**(2): p. 67-70.

86. Gao, K., H.-H. Cheng, A.K. Bhowmik, and P.J. Bos, *Thin-film Pancharatnam lens with low f-number and high quality.* Optics Express, 2015. **23**(20): p. 26086-26094.

87. Gao, K., H.-H. Cheng, A. Bhowmik, C. McGinty, and P. Bos, *Nonmechanical zoom lens based on the Pancharatnam phase effect.* Applied Optics, 2016. **55**(5): p. 1145-1150.

88. Jamali, A., C. Yousefzadeh, C. McGinty, D. Bryant, and P. Bos. *A Continuous Variable Lens System to Address the Accommodation Problem in VR and 3D Displays*. in *Imaging and Applied Optics 2018 (3D, AO, AIO, COSI, DH, IS, LACSEA, LS&C, MATH, pcAOP)*. 2018. Orlando, Florida: Optical Society of America.

89. Yousefzadeh, C., A. Jamali, C. McGinty, and P.J. Bos, *Achromatic limits of Pancharatnam phase lenses.* Applied Optics, 2018. **57**(5): p. 1151-1158.

90. Afsoon, J., Y. Comrun, M. Colin, B. Douglas, and B. Philip, *LC lens systems to solve accommodation/convergence conflict in three-dimensional and virtual reality displays.* Optical Engineering, 2018. **57**(10): p. 1-8.

91. Yousefzadeh, C., A. Jamali, C. McGinty, and P.J. Bos, *45-2: Limits of Pancharatnam Phase lens for 3D/VR/AR Applications.* SID Symposium Digest of Technical Papers, 2019. **50**(1): p. 616-619.

92. Yousefzadeh, C., A. Jamali, C. McGinty, and P.J. Bos. *Achromatic Test of Pancharatnam Phase Lens for VR/AR*. in *Imaging and Applied Optics 2018 (3D, AO, AIO, COSI, DH, IS, LACSEA, LS&C, MATH, pcAOP)*. 2018. Orlando, Florida: Optical Society of America.

93. Kim, J., Y. Li, M.N. Miskiewicz, C. Oh, M.W. Kudenov, and M.J. Escuti, *Fabrication of ideal geometric-phase holograms with arbitrary wavefronts.* Optica, 2015. **2**(11): p. 958-964.

94. Sarkissian, H., S.V. Serak, N.V. Tabiryan, L.B. Glebov, V. Rotar, and B.Y. Zeldovich, *Polarization-controlled switching between diffraction orders in transverse-periodically aligned nematic liquid crystals.* Optics Letters, 2006. **31**(15): p. 2248-2250.

95. Lee, Y.-H., G. Tan, Y. Weng, and S.-T. Wu, *72-4: Switchable Lens based on Cycloidal Diffractive Waveplate for AR and VR Applications.* SID Symposium Digest of Technical Papers, 2017. **48**(1): p. 1061-1064.

96. Escuti, M.J., J. Kim, and M.W. Kudenov, *Controlling Light with Geometric-Phase Holograms.* Optics and Photonics News, 2016. **27**(2): p. 22-29.

97. D. Voelz, *Computational Fourier Optics: A Matlab Tutorial.* SPIE, 2011.

98. Hecht, E., *Optics.* Addison Wesley, 2001. **4th ed**.

99. Goodman, J.W., *Introduction to Fourier Optics.* McGraw-Hill, 1988. **2nd ed.**

100. Girod, B., *Image and video compression in Rate-Distortion Theory.* Stanford University, 2000. **EE368b**(No.5).

101. Gao, K., *OPTICAL SIMULATION AND FABRICATION OF PANCHARATNAM (GEOMETRIC) PHASE DEVICES FROM LIQUID CRYSTALS*. 2017, Kent State University.

102. Wang, J., C. McGinty, J. West, D. Bryant, V. Finnemeyer, R. Reich, S. Berry, H. Clark, O. Yaroshchuk, and P. Bos, *Effects of humidity and surface on photoalignment of brilliant yellow.* Liquid Crystals, 2017. **44**(5): p. 863-872.

103. Akeley, K., S.J. Watt, A.R. Girshick, and M.S. Banks, *A stereo display prototype with multiple focal distances.* ACM Trans. Graph., 2004. **23**(3): p. 804–813.

104. Love, G.D., D.M. Hoffman, P.J.W. Hands, J. Gao, A.K. Kirby, and M.S. Banks, *High-speed switchable lens enables the development of a volumetric stereoscopic display.* Optics Express, 2009. **17**(18): p. 15716-15725.

105. Lanman, D. and D. Luebke, *Near-eye light field displays.* ACM Trans. Graph., 2013. **32**(6): p. Article 220.

106. Li, G., D. Lee, Y. Jeong, J. Cho, and B. Lee, *Holographic display for see-through augmented reality using mirror-lens holographic optical element.* Optics Letters, 2016. **41**(11): p. 2486-2489.

107. He, Z., X. Sui, G. Jin, and L. Cao, *Progress in virtual reality and augmented reality based on holographic display.* Applied Optics, 2019. **58**(5): p. A74-A81.

108. Kramida, G., *Resolving the Vergence-Accommodation Conflict in Head-Mounted Displays.* IEEE Transactions on Visualization and Computer Graphics, 2016. **22**(7): p. 1912-1931.

109. Yousefzadeh, C., A. Jamali, C. McGinty, and P.J. Bos, *"Achromatic limits of Pancharatnam phase lenses".* Applied Optics, 2018. **57**(5): p. 1151-1158.

110. Pancharatnam, S., *Achromatic combinations of birefringent plates.* Proc Indian Acad. Sci, 1955. **Sect. A 41(4)**: p. 137–144.

111. *https://www.youtube.com/watch?v=sOCi5DcOIQE&t=2259s*.